University of Melbourne

LOW-REYNOLDS-NUMBER TURBULENT BOUNDARY LAYERS

by

Lincoln Paul Erm

A thesis submitted for the degree of

Doctor of Philosophy

December 1988

ABSTRACT

This thesis documents an extensive experimental investigation into low-Reynolds-number turbulent boundary layers flowing over a smooth flat surface in nominally zero pressure gradients.

The way in which these layers are affected by variations in R_θ, i.e. the Reynolds number based on the boundary-layer momentum thickness, type of tripping device used and variations in freestream velocity, each considered independently, are investigated.

The types of tripping devices used are a circular wire, distributed grit and cylindrical pins. An empirical technique is devised for matching device height and velocity so that the resulting flows are correctly stimulated, i. e. they follow Coles' (1962) $\Delta U/U_\tau$-versus-R_θ characteristic, at the nominal design velocity, which for this investigation is chosen to be 10.0 m/s.

For each of the three devices, measurements are taken at this nominal velocity, as well as at nominal velocities of 8.0 and 14.0 m/s. The use of three different devices at each of three different nominal velocities means that nine different flows are studied. However, most effort is concentrated on the design flows.

The measurements taken comprise mean-flow characteristics, broadband-turbulence characteristics and spectra. Emphasis is placed on obtaining good accurate experimental data. For the design flows, most of the measurements correspond to values of R_θ of about 713, 1020, 1544, 2175 and 2810, whereas for the off-design flows, the measurements are mainly restricted to values of R_θ of about 1020 and 2175.

The mean-flow measurements include longitudinal and transverse skin-friction coefficients as well as velocity profiles. Broadband-turbulence measurements correspond to the u, v and w components of the turbulence, although for the off-design flows the measurements are limited to the u component of the turbulence. The broadband-turbulence measurements consist

of basic quantities comprising Reynolds normal and shear stresses and triple and quadruple products. These basic quantities are used to derive other quantities consisting of anisotropy parameters, skewness and flatness factors, terms in the balances of turbulent kinetic energy and Reynolds shear stress, eddy viscosities and mixing lengths, dissipation length parameters and turbulent transport velocities. The spectra correspond to all three components of the turbulence and match the broadband-turbulence measurements described above.

Considering the mean-flow characteristics, it is shown that for the design flows, the mean-flow characteristics for the three devices are dependent on R_θ, which is consistent with the findings of other researchers. It is also shown that the type of device used has only a small effect on mean-flow characteristics, except perhaps at $R_\theta \approx 713$. For the three devices, variations in freestream velocity are shown to have an appreciable effect on mean-flow behaviour for $R_\theta \approx 1020$, but only a small effect at $R_\theta \approx 2175$.

The broadband-turbulence quantities for the design flows for the three devices are likewise shown to be affected by variations in R_θ. There is a general tendency for the absolute values of the basic quantities of Reynolds stresses and triple products to diminish with increasing R_θ. It is shown that the basic and derived quantities associated with the three devices often show large variations for $R_\theta \approx 713$, unlike the corresponding mean-flow characteristics, but for $R_\theta \approx 1020$ and above, the type of device used does not significantly affect these quantities. It is shown that for $R_\theta \approx 1020$, variations in freestream velocity generally have a significant effect upon u-component broadband-turbulence characteristics for each of the devices and although the effects of the different velocities are generally less pronounced for $R_\theta \approx 2175$, appreciable differences still exist at this value of R_θ.

Low-Reynolds-number spectra are compared with established models of spectral behaviour, developed for high-Reynolds-number flows, and good agreement between predictions and experiment is often obtained. Deviations from predictions for the different devices arise as a result of variations in R_θ. It is shown that the type of device used can have an appreciable effect on spectral behaviour for $R_\theta \approx 713$, but for $R_\theta \approx 1020$ and above, the type of device used is shown to have little effect on spectral behaviour. For the three

devices it is shown that variations in freestream velocity often have a marked effect on spectral behaviour for $R_\theta \approx 1020$, with the effects being mainly evident at the lower wavenumbers. Spectra corresponding to $R_\theta \approx 2175$ are affected very little by variations in freestream velocity.

ACKNOWLEDGEMENTS

The work described in this thesis was carried out under the supervision of Professor P. N. Joubert, whose guidance, encouragement and support throughout the duration of the project is deeply appreciated. His help in his capacity as Chairman of the Department of Mechanical and Manufacturing Engineering is also gratefully acknowledged.

I would also like to express my thanks to Professor A. J. Smits, now of Princeton University, who was a co-supervisor during the early stages of the project.

Thanks are due to Professor A. E. Perry for his interest in the project and his help in many ways.

The author is indebted to Aeronautical Research Laboratory, Melbourne, for granting part-time study leave and providing continued support. I would particularly like to thank Dr. G. L. Brown, Mr. F. G. Blight, Dr. W. H. Schofield, Mr. D. G. Stewart, Mr. T. S. Keeble and Mr. S. A. Fisher for the help that they have given.

The Department of Defence provided assistance in the form of a Postgraduate Study Award during the latter stages of the project and for this I am very grateful.

I would particularly like to thank Mr. S. G. Saddoughi, a co research student, for many stimulating discussions and his loyal friendship.

The staff of the Engineering workshop, headed by Messrs W. Simpson, J. Rogers and N. Massey, provided assistance by skillfully manufacturing the dynamic calibrator as well as other equipment, and their help and cooperation is much appreciated.

Past and present staff and postgraduate students have provided companionship and have helped in a variety of different ways. Thanks are due to Drs. M. S. Chong, T. T. Lim, J. H. Watmuff, S. M. Henbest, V. Baskaran, H. T. Witt, K. L. Lim and T. R. Steiner as well as Messrs J. Noonan, D. Jaquest,

H. Shaw, M. H. Wong, R. Kelso, L. J. Li, S. Hafez, G. Ibal, I. Marusic and T. Nickels.

Finally, I would like to express my deep gratitude to my wife Megan, our children Rohan and Rachel, and to my parents for all of their support and understanding. For this I will be forever grateful.

TABLE OF CONTENTS

NOMENCLATURE

a_1	Anisotropy parameter $a_1 = -\overline{uv}/\overline{q^2}$
A	Additive constant in logarithmic law
C	Additive constant in logarithmic law
C_f	Local skin-friction coefficient
C_{fm}	Mean value of C_f
E_U, E_V	Output voltage signals associated with hot wire anemometers
f	Function
f_r	Frequency
f_1, f_2, f_3	Functions
F_u, F_v, F_w	Flatness factors corresponding to the fluctuating components of velocity in the x, y and z directions respectively
g	function
G	Clauser parameter $G = \sqrt{2/C_f}(H-1)/H$
H	Boundary-layer shape factor $H = \delta^*/\theta$
k	Diameter of wire
k_1	Streamwise wavenumber $k_1 = 2\pi f_r/U_{cn}$
L	Dissipation length parameter
M	Molecular weight of air used when calculating density M = 28.9644
p	Fluctuating component of pressure
P	Mean value of pressure
q_1	Function
$\overline{q^2}$	Twice kinetic energy of turbulence per unit mass $\overline{q^2} \equiv \overline{u^2}+\overline{v^2}+\overline{w^2}$
R_{rf}	Reference Reynolds number/metre $R_{rf} = \rho U_{rf}/\mu$

R_{12}	Shear correlation coefficient $R_{12} \equiv -\overline{uv}/(\sqrt{\overline{u^2}}\sqrt{\overline{v^2}})$
R^*	Universal gas constant used when calculating air density $R^* = 8.31432 \times 10^3$ J/(K.kg Mol)
R_θ	Reynolds number based on momentum thickness
S	Sutherlands constant used when calculating dynamic viscosity of air S = 110.4 K
S_u, S_v, S_w	Skewness factors corresponding to the fluctuating components of velocity in the x, y and z directions respectively
t	Time
T	Temperature
u	Fluctuating component of velocity in longitudinal or x direction
U	Mean velocity in longitudinal or x direction
U_c	Mean velocity in longitudinal or x direction at $y = \delta_c$
U_{cn}	Local convection velocity
U_e	Freestream velocity at edge of boundary layer
U_k	Velocity in undisturbed boundary layer at the position of a wire and at a distance k from the wall, where k is the wire diameter
U_i	Instantaneous velocity in longitudinal or x direction
U_{rf}	Reference velocity
U_τ	Friction velocity $U_\tau = \sqrt{\tau_w/\rho}$
v	Fluctuating component of velocity in normal or y direction
V	Mean velocity in normal or y direction
V_i	Instantaneous velocity in normal or y direction
V_q	Turbulent transport velocity
V_τ	Turbulent transport velocity
w	Fluctuating component of velocity in transverse or z direction
$w[y/\delta]$	Coles' law of the wake

W	Mean velocity in transverse or z direction
W_i	Instantaneous velocity in transverse or z direction
x	Distance from tripping device in longitudinal direction
y	Distance from wall in normal direction
y^+	yU_τ/ν
z	Distance from wind tunnel centreline in transverse direction
β	Variable used when calculating dynamic viscosity of air $\beta = 1.458 \times 10^{-6}$ kg/(s.m.K$^{0.5}$)
δ	Boundary-layer thickness in general, or when used for the data of the current investigation, boundary-layer thickness corresponding to location where velocity has 99.5% of its asymptotic value. δ_{995} is sometimes used to denote such a thickness when showing data of other researchers.
δ_c	Boundary-layer thickness corresponding to the value of y at which the slope of the velocity profile $\partial(U/U_\tau)/\partial \ln y$ near the edge of the layer is equal to the slope of the logarithmic-law line
δ_s	Boundary-layer thickness based on shear stress profile
δ^*	Boundary-layer displacement thickness
Δ	Incremental value of a quantity
Δ_E	Outer flow length scale that scales with boundary-layer thickness, as given by Perry, Henbest & Chong (1986) for their spectral theory
ε	Turbulent energy dissipation
ε_m	Eddy viscosity
η	Kolmogorov length scale $\eta = (\nu^3/\varepsilon)^{0.25}$
θ	Boundary-layer momentum thickness
θ_0	Boundary-layer momentum thickness for most upstream profile within a set
ι	Mixing length

κ	Constant used in logarithmic law
μ	Dynamic viscosity of air
ν	Kinematic viscosity of air
Π	Coles' profile parameter
ρ	Density of air
τ_w	Shear stress at wall
υ	Kolmogorov velocity scale $\upsilon = (\nu\varepsilon)^{0.25}$
$\Phi_{ii}[k_1 y]$	Power spectral density per unit non-dimensional wavenumber, $k_1 y$, where i = 1, 2 or 3 and repeated indices do not denote a summation
$\Phi_{ii}[k_1 \delta]$	as above except for $k_1 \delta$
$\Phi_{ii}[k_1 \eta]$	as above except for $k_1 \eta$
ψ	Parameter used to denote $U_\tau \delta / \nu$ when discussing work of Granville (1977)
$\overline{}$	Overbars denote time-averaged quantities
[ ]	Square brackets denote a functional dependence

CHAPTER 1

INTRODUCTION

A low-Reynolds-number turbulent boundary layer is said to exist when the Reynolds number based on momentum thickness, R_θ, is less than about 6000. Such flows play an important role in many fluid-flow problems including flow through turbomachinery, flow over wings, numerical modelling, heat transfer and model testing in wind tunnels. Despite the importance of these flows, there still remains many significant unanswered questions regarding their behaviour. The unanswered questions refer mainly to low-Reynolds-number turbulence behaviour, rather than mean-flow behaviour, since by now this is reasonably well established. Considering the turbulence behaviour, broadband-turbulence characteristics have received increasing attention in recent times but there has been very little work done on spectral behaviour.

In the past the problem of understanding the flows and answering some of the outstanding questions has been attacked on at least three different fronts. Firstly, researchers have taken measurements using pressure probes or hot-wire probes. Secondly, flow visualisation has been used to obtain an understanding of eddy structure and thirdly, flow prediction, using models of varying degrees of complexity, has been used. This investigation was concerned with the first of these approaches.

In fundamental low-Reynolds-number experimental studies, a tripping device is generally used to stabilise the transition to turbulent flow. Low-Reynolds-number flow behaviour is intimately connected with the type of device used since different devices impart different types of disturbances into the flow. In the past, researchers have not systematically compared the effects of different devices on low-Reynolds-number mean-flow or turbulence behaviour, so the extent to which the flow behaviour depends on the device used is unknown. Ultimately, when the flow is fully developed at high values of R_θ, flow behaviour is known to be invariant to the type of tripping device used.

Given the fact that the actual type of device used has at least some effect upon flow behaviour in the very early stages of development, researchers want to know the limiting value of R_θ at which the flow ceases to be affected by the type of device used. In this investigation, the effects of device were investigated for three commonly used devices.

In the past, researchers have often presented low-Reynolds-number measurements corresponding to a given device, but different freestream velocities, and the assumption has been that it is only the value of R_θ that is important and not how R_θ was formed, i.e. the combination of velocity and momentum thickness used to determine R_θ. However, such an assumption has not been systematically tested and researchers want to know the extent to which variations in freestream velocity for a given device affect flow behaviour at low R_θ. In this study, this uncertainty was investigated for three different freestream velocities for each of the three devices.

The experimental results taken were diverse and included skin-friction coefficients measured with a Preston tube, mean-flow velocity profiles taken with a Pitot-static probe, broadband-turbulence measurements taken with both a single and a crossed hot-wire probe and spectral measurements which were also taken with both of these probes. Emphasis was placed on obtaining good accurate experimental data.

A broad outline of the structure of the thesis will now be given. A survey of relevant literature as well as associated background theory is presented in Chapter 2. The purpose of this chapter is to summarize the current state of knowledge and to indicate areas of critical concern where effort would be most fruitful. Chapter 3 outlines the experimental apparatus and techniques used in the investigation. Chapter 4 gives the details of an empirical technique that was devised to match device height and velocity so that the resulting flows were correctly stimulated. The mean-flow results are analysed in Chapter 5, the broadband-turbulence results in Chapter 6 and the spectra in Chapter 7. Finally, a general summary and the conclusions of the investigation are given in Chapter 8.

CHAPTER 2

LITERATURE SURVEY AND ASSOCIATED BACKGROUND THEORY

In this chapter relevant underlying theory and published data associated with the investigation is critically reviewed. The topics covered are mean-flow similarity laws, broadband-turbulence behaviour, spectral behaviour and flow prediction.

2.1 Mean-Flow Similarity Laws for Moderate to High Reynolds Numbers

The behaviour of a two-dimensional turbulent boundary layer flowing over a smooth surface in a zero or slight pressure gradient for moderate to high Reynolds numbers can be represented by two distinct types of similarity. These are (1) "inner-flow" similarity in which the mean velocity component, U, can be expressed functionally as

$$U = f\,[y,\tau_w,\rho,\nu] \tag{2.1}$$

or alternatively

$$\frac{U}{U_\tau} = f\left[\frac{yU_\tau}{\nu}\right] \qquad 0 < y < 0.1\delta \text{ to } 0.2\delta \tag{2.2}$$

where

$$U_\tau = \sqrt{\frac{\tau_w}{\rho}} \tag{2.3}$$

and (2) "outer-flow" similarity in which the velocity defect (U_e-U) can be expressed functionally as

$$U_e - U = g\,[y, \delta, \tau_w, \rho] \tag{2.4}$$

or alternatively

$$\frac{U_e - U}{U_\tau} = g\left[\frac{y}{\delta}\right] \qquad \frac{50\nu}{U_\tau} < y < \delta \text{ (approx.)} \tag{2.5}$$

Equation (2.2) is termed the "law of the wall" or "inner velocity law" and was introduced by Prandtl (1933). Equation (2.5), which is generally attributed to von Karman (1930), is known as the "velocity-defect law" or the "outer velocity law".

In the extremely thin viscous sublayer, equation (2.2) has the special form

$$\frac{U}{U_\tau} = \frac{yU_\tau}{\nu} \qquad 0 < y < \frac{5\nu}{U_\tau} \text{ (approx.)} \tag{2.6}$$

An overlap region exists in the flow where equations (2.2) and (2.5) both apply. The only form of the functions f and g which can satisfy these two equations simultaneously in this region is a logarithmic one. For the overlap region, equation (2.2) expressed in terms of inner-flow variables becomes

$$\frac{U}{U_\tau} = \frac{1}{\kappa}\ln\left(\frac{yU_\tau}{\nu}\right) + C \qquad \frac{50\nu}{U_\tau} < y < 0.1\delta \text{ to } 0.2\delta \text{ (approx.)} \tag{2.7}$$

and equation (2.5) expressed in terms of outer-flow variables becomes

$$\frac{U_e - U}{U_\tau} = -\frac{1}{\kappa}\ln\left(\frac{y}{\delta}\right) + A \qquad \frac{50\nu}{U_\tau} < y < 0.1\delta \text{ to } 0.2\delta \text{ (approx.)} \tag{2.8}$$

κ, C and A are empirical constants whose exact values are somewhat controversial, even for the moderate to high Reynolds numbers considered so far. However, for such Reynolds numbers, the value of κ is generally quoted as varying between 0.40 (Coles 1956) and 0.42 (Patel 1965), C between 5.0 (Coles 1968) and 5.45 (Patel 1965) and A between 2.19 (Granville 1977) and 2.50 (Clauser 1956).

The different regions of a typical turbulent boundary layer are shown in figure 2.1 using U/U_τ and $\log(yU_\tau/\nu)$ coordinates. This figure is based on figure 6.6 given by Cebeci & Bradshaw (1977).

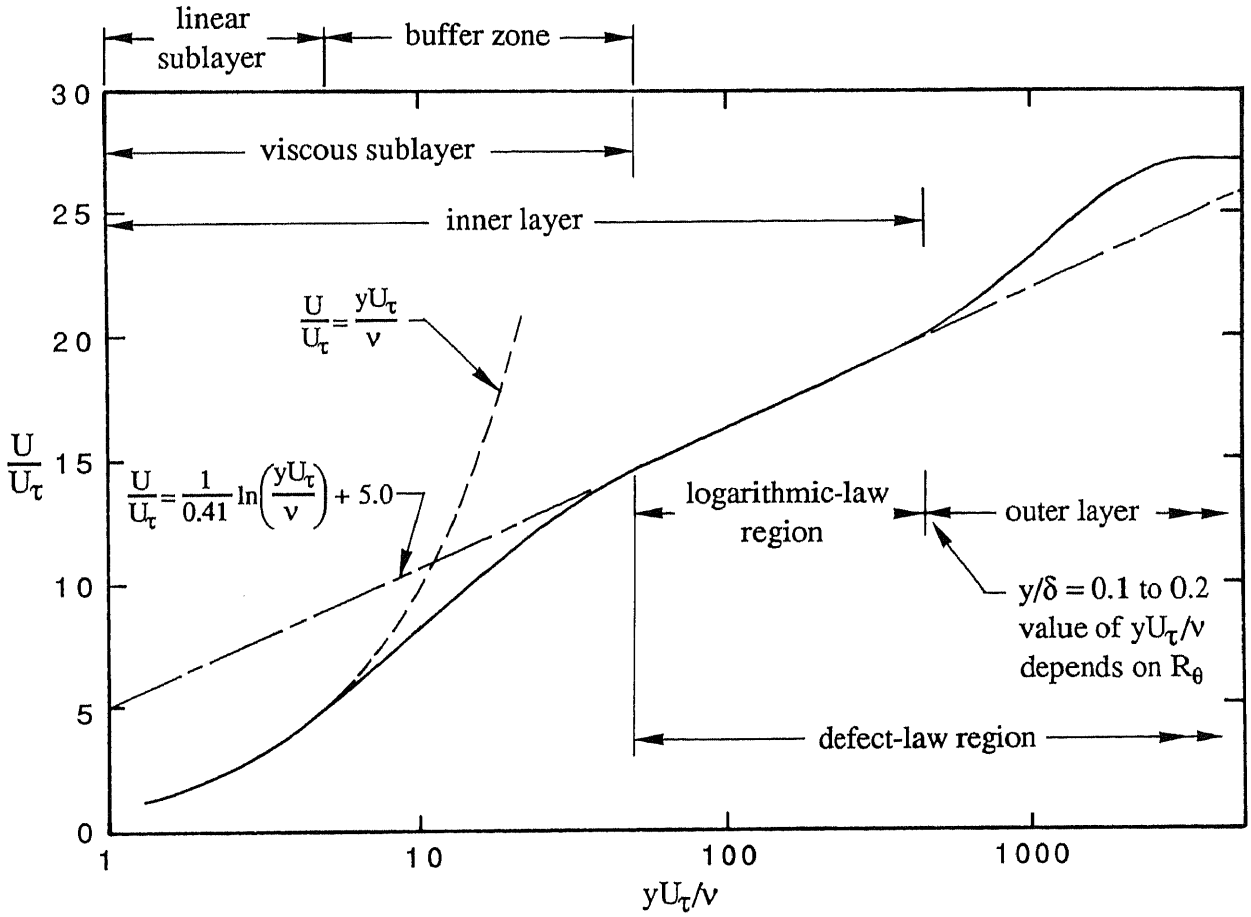

FIGURE 2.1. Different regions of a typical turbulent boundary layer.

Coles (1956) carried out an extensive survey of mean velocity profile measurements at high Reynolds numbers and proposed that the velocity profile outside the viscous sublayer could be accurately described by the expression

$$\frac{U}{U_\tau} = \frac{1}{\kappa}\ln\left(\frac{yU_\tau}{\nu}\right) + C + \frac{\Pi}{\kappa} w\left[\frac{y}{\delta}\right] \qquad (2.9)$$

where $\kappa = 0.40$ and $C = 5.1$. Π is a profile parameter and for flows at constant pressure it has a value of approximately 0.55. The function $w[y/\delta]$ is apparently universal and is termed the "law of the wake" because of its similarity with a half wake profile. Coles (1956) defined $w[y/\delta]$ numerically with normalising conditions, one of which was $w = 2.0$ when $y = \delta$. The function has been approximated by Hinze (1959) as

$$w\left[\frac{y}{\delta}\right] = 1 - \cos\left(\frac{\Pi y}{\delta}\right) \qquad 0 \le y \le \delta \qquad (2.10)$$

Equation (2.9) has an abrupt change of slope at the outer edge of the layer, where $d(U/U_\tau)/d(y/\delta)$ changes from $1/\kappa$ to 0.

Bull (1969) used equations (2.9) and (2.10) but with δ replaced by δ_c, where δ_c is the value of y at which the slope of the velocity profile $\partial(U/U_\tau)/\partial \ln y$ near the edge of the layer is equal to the slope of the logarithmic-law line as shown in figure 2.2, which is based on one of Bull's figures. He indicated that Coles (1956) effectively assumed that U_c, the velocity at $y = \delta_c$, was experimentally indistinguishable from U_e, the freestream velocity outside the boundary layer. Bull suggested a modified wake function having the form

$$w[\zeta_c] = 1 - \cos\left(\frac{\Pi(\zeta_c - a)}{1-a}\right) \qquad (2.11)$$

where $\zeta_c = y/\delta_c$ and $a = 0.08$.

2.2 Mean-Flow Behaviour at Low Reynolds Numbers

In the preceding section only moderate to high Reynolds numbers were considered. Low Reynolds numbers are known to affect the mean-flow behaviour, but different researchers have given differing opinions on how the flow changes. An area of controversy has been whether or not the logarithmic

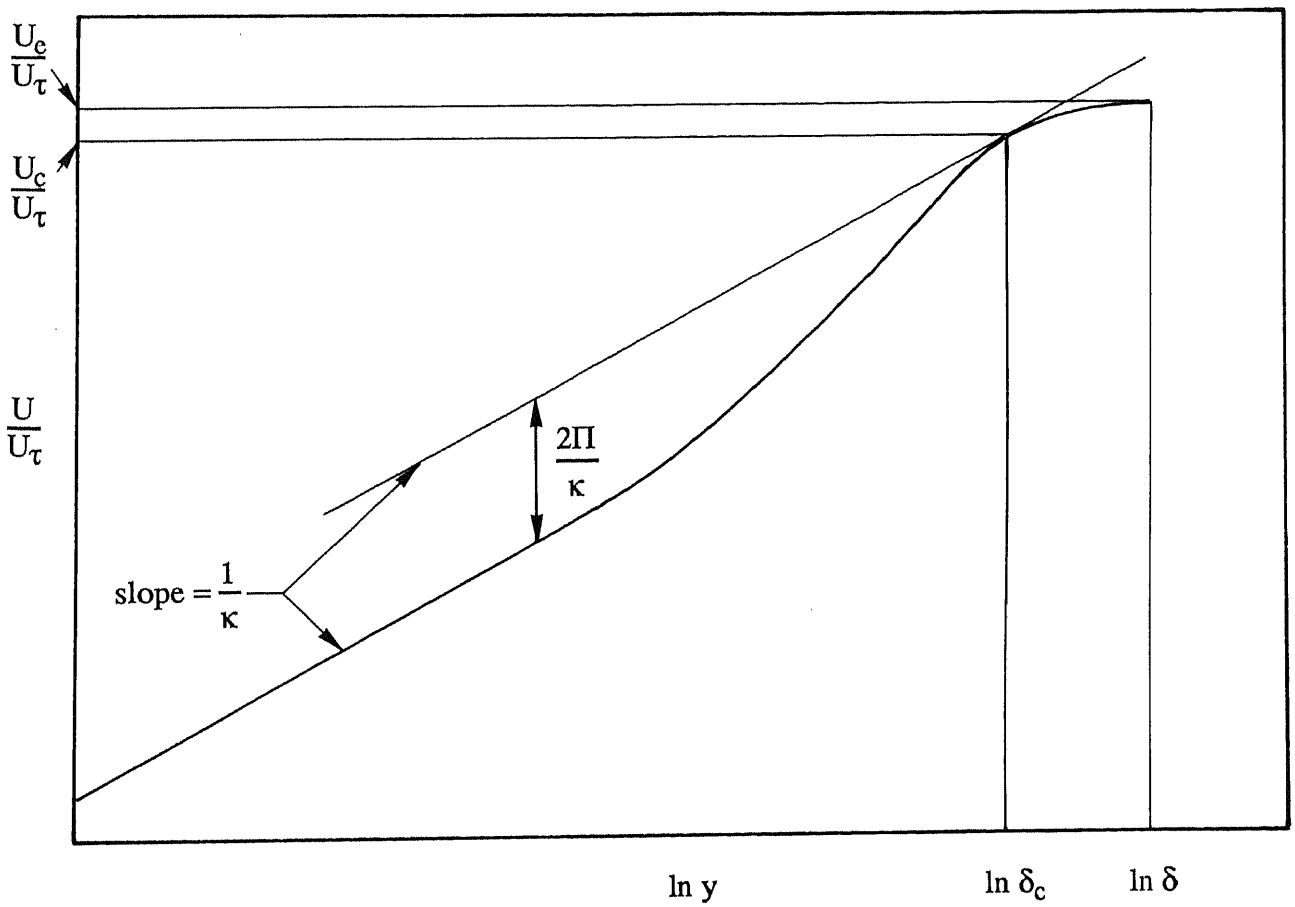

FIGURE 2.2. Velocity profile according to Bull (1969).

region disappears or has changing values of κ and C as the Reynolds number is decreased. The wake component of the flow is also known to change at low Reynolds numbers, but the changes have been interpreted in a number of different ways. The conclusions of different researchers on these and other aspects of low-Reynolds-number mean-flow behaviour are now considered.

The extent of the logarithmic region specified using U/U_τ and $\log(yU_\tau/\nu)$ is known to diminish for decreasing Reynolds numbers. Landweber (1953) examined the possible disappearance of this region by assuming that it had a lower limit given by $yU_\tau/\nu = 30$ and an upper limit given by $y/\delta = 0.16$. He found that for $C_f = 0.00524$, where C_f is given by

$$C_f = \frac{\tau_w}{0.5\rho U_e^2} \tag{2.12}$$

the logarithmic region contracted to zero thickness. Preston (1958) also examined the possible disappearance of this region and he used $yU_\tau/\nu = 30$ and $y/\delta = 0.2$ as the limiting conditions. He found that at $R_\theta = 389$, which corresponds to $C_f = 0.0048$, the logarithmic region disappeared. He also indicated that $R_\theta = 320$ was about the minimum Reynolds number for which fully developed turbulent flow was observed experimentally on a flat plate. Although Landweber did not actually state the limiting value of R_θ corresponding to the disappearance of the logarithmic law, it is obvious from the above two values of C_f that Landweber's limiting value of R_θ is less than that of Preston.

Coles (1962) extended his initial work by analysing virtually all of the published data on low-Reynolds-number turbulent boundary layers on smooth flat surfaces in nominally zero pressure gradients. He determined U_τ from velocity profiles by fitting the data in the logarithmic region of the profile to equation (2.7) as shown in figure 2.3. For the fitting process Coles chose $\kappa = 0.41$ and $C = 5.0$ for the logarithmic-law constants for every low-Reynolds-number profile and he also removed probe displacement corrections. The maximum deviation of a velocity profile from the logarithmic law, $\Delta U/U_\tau$ shown in figure 2.3, was referred to by Coles as the "strength of the wake component". Coles identified a normal state for the turbulent boundary layer at constant pressure and expressed this normal state in terms of a variation of $\Delta U/U_\tau$ with R_θ. Figure 2.4 shows the relationship plotted in this form as well as

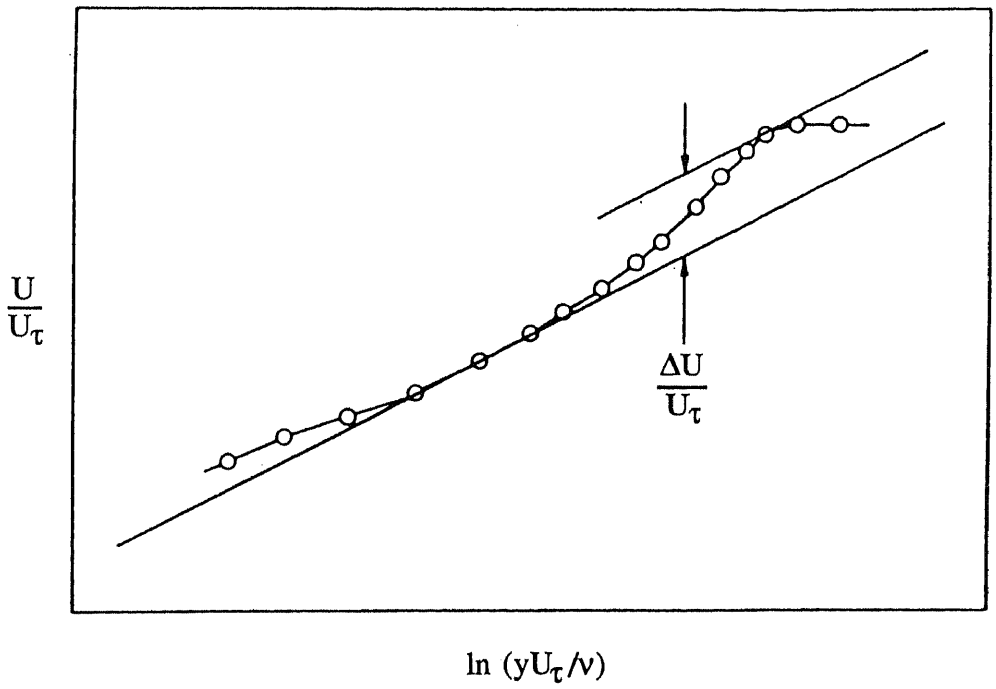

FIGURE 2.3. Fitting procedure used by Coles (1962) to determine $\Delta U/U_\tau$.

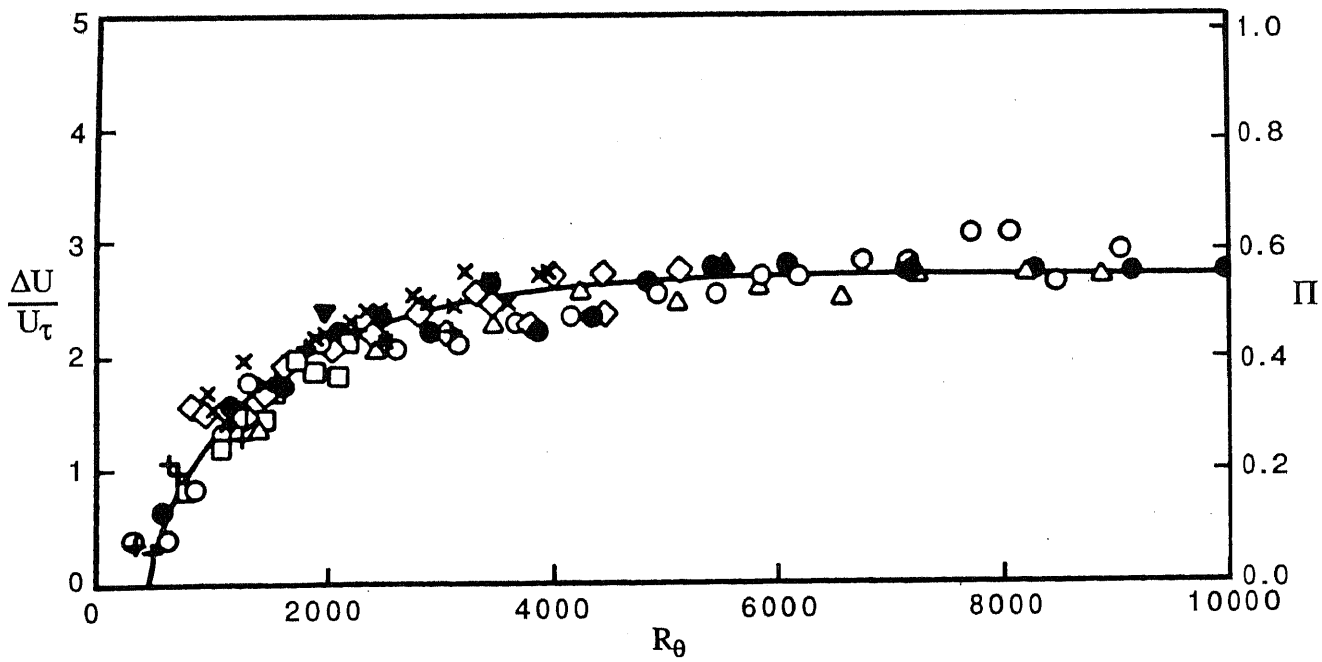

FIGURE 2.4. Variation of $\Delta U/U_\tau$ and Π with R_θ for a zero pressure gradient turbulent boundary layer as given by Coles (1962). For key to symbols corresponding to data of different researchers see Coles' publication.

the form Π versus R_θ, where Π is related to $\Delta U/U_\tau$ by $\Delta U/U_\tau = 2\Pi/\kappa$. Coles defined the Π versus R_θ relationship numerically and this has been approximated by Cebeci & Smith (1974) (page 221) by

$$\Pi = 0.55(1 - \exp(-0.243a^{0.5} - 0.298a)) \qquad (2.13)$$

where $a = ((R_\theta/425)-1)$. The decrease in $\Delta U/U_\tau$ with R_θ, for R_θ less than about 6000, led Coles to assert that the traditional momentum-defect law fails for these values of R_θ. The validity of this conclusion depended upon whether or not the logarithmic law with $\kappa = 0.41$ and $C = 5.0$, as chosen by Coles, applied at low Reynolds numbers. To check on this it was necessary to establish that the values of U_τ determined from the logarithmic region (see above) were in fact accurate. Coles did this by using the above values of U_τ and checking balances of momentum for the selected sets of data. He found that the balances were acceptable thus confirming the form of figure 2.4 and indicating that the logarithmic law, with the above values of κ and C, applied at low Reynolds numbers. He also physically explained the behaviour of the wake in terms of energy associated with eddies and he inferred that viscous effects were present in the outer layer.

Coles (1962) indicated that equation (2.9), which was developed for high Reynolds numbers, is still valid provided Π varies with R_θ in the manner shown in figure 2.4. The asymptotic value of $\Delta U/U_\tau$ given in this figure is approximately 2.7.

Coles (1968) used a different analytic technique when reanalysing data and he found that the asymptotic value of $\Delta U/U_\tau$ was now approximately 3.0. In this case $\Delta U/U_\tau$ was determined by fitting data in the logarithmic and wake regions of the profile to equation (2.9), rather than only fitting data in the logarithmic region of the profile to equation (2.7) as previously (Coles 1962). Coles (1968) also indicated that this modified fitting technique reduced the value of C_f by perhaps one or two percent compared with previously. The logarithmic-law constants used by Coles in 1968 were $\kappa = 0.41$ and $C = 5.0$, the same as he used in his 1962 publication. Although Coles' 1968 method of analysis superseded his 1962 method, the earlier Π versus R_θ relationship is still given prominence in the literature as a basis for comparison, as will be shown later in this section.

Simpson (1970) extended Coles' (1956) high-Reynolds-number work to low Reynolds numbers. Simpson showed that for $1000 < R_\theta < 6000$, his own earlier velocity profiles (Simpson 1967) and those of Wieghardt (1943) collapsed together outside the viscous sublayer when plotted as U/U_e versus y/δ. This led Simpson to propose that κ and C vary with R_θ. More specifically, Simpson assumed that κ was now given by

$$\kappa = 0.40 \left(\frac{R_\theta}{6000}\right)^{-0.125} \qquad R_\theta < 6000 \tag{2.14}$$

and C by

$$C = R_\theta^{0.125} \left(7.90 - 0.737 \ln\left|R_\theta\right|\right) \qquad R_\theta < 6000 \tag{2.15}$$

This led him to assert that the reduction of the wake with decreasing Reynolds number could be accounted for by varying κ and C in this manner and holding Π constant. This is in complete contrast to Coles (1962), who extended his earlier work (Coles 1956) and showed that the disappearance of the wake component at low Reynolds numbers could be explained by keeping κ and C constant but varying Π with R_θ. This contradiction requires some explanation.

Huffman & Bradshaw (1972) investigated this contradiction by analysing low-Reynolds-number duct flows. They chose these flows since they realised that the highly-turbulent outer region associated with them would presumably have a greater effect on the inner layer, and thus on the values of κ and C, than would the outer region of boundary-layer flows, which are much less turbulent, so therefore if κ and C were found to be constant for Reynolds number variation for duct flows, then κ and C would also be constant for boundary-layer flows. The method of analysis used by Huffman & Bradshaw was to adjust κ and C so as to optimise the agreement between the actual velocity profiles in the inner layer and those calculated from a mixing length formula. Their results showed that κ appeared to be a constant to good accuracy and that C was Reynolds number dependent. However, they indicated that even the variation of C is likely to be small in boundary layers unless the influence of the outer layer is extremely large.

Huffman & Bradshaw also showed that the velocity-defect profiles for duct flows appeared to follow equation (2.5) for low Reynolds numbers, whereas the boundary layer velocity-defect profiles of Coles (1962) did not. They hypothesized that it was the "viscous superlayer" at the interface separating turbulent and irrotational flow that was responsible for the low-Reynolds-number effects on the velocity-defect profiles documented by Coles (1962). This interface is present in boundary-layer flows but is non-existent in fully developed duct flows.

The work of Murlis (1975) and Murlis, Tsai & Bradshaw (1982) represents a very significant contribution to our understanding of the behaviour of low-Reynolds-number turbulent boundary-layers . Since both publications refer to the same general investigation, they will generally be treated together. An object of their research was to improve understanding of the mechanics behind the departure from high-Reynolds-number scaling laws in a fully-developed low-Reynolds-number turbulent boundary layer. Emphasis was placed on conditional sampling in the viscous superlayer separating the turbulent and non-turbulent regions. The researchers indicated that it appears that the key to understanding low-Reynolds-number effects is the behaviour of the viscous superlayer, and that the key to measuring the behaviour of the viscous superlayer is conditional sampling.

Mean-flow and turbulence measurements were taken in a zero pressure gradient for values of R_θ ranging from 791 to 4750. The tripping device used was a 0.03 in. (0.76 mm) wire and the nominal velocity was 50 ft/s (15.2 m/s). The mean-flow results are discussed in this section whereas the turbulence results will be considered in Sections 2.3 and 2.4.

Skin-friction coefficients were measured over the Reynolds number range by using both Preston and Stanton tubes and both sets of results agreed very closely. The researchers indicated that the Preston-tube calibration depends upon the validity of the inner logarithmic law, whereas the Stanton tube remains within the viscous sublayer and should therefore be independent of changes in the logarithmic law. Applying this to their results, they reasoned that the agreement between the two devices for all Reynolds numbers strongly suggests that the logarithmic law applies unchanged down to $R_\theta = 700$.

The $\Delta U/U_\tau$-versus-R_θ data of these researchers are shown in figure 2.5, where they are compared with Coles (1962) characteristic. The values of $\Delta U/U_\tau$ were determined using $\kappa = 0.41$ and $C = 5.2$ and also using $\kappa = 0.41$ and a best-fit value of C. The authors used this latter value of C because the data at the lower values of R_θ were slightly above the logarithmic-law line having $\kappa = 0.41$ and $C = 5.2$.

The publications by Purtell (1978) and Purtell, Klebanoff & Buckley (1981) both refer to the same experimental investigation of low-Reynolds-number turbulent boundary layers in a zero pressure gradient. The profiles presented, both for mean velocities and turbulence intensities, were taken with a hot wire. Even though both publications contain some data that are not contained in the other, they will still generally be referred to together. Once again only the mean-flow results will be discussed in this section.

The values of R_θ for which measurements were taken varied from 465 to 5200. These values of R_θ were obtained by using different combinations of velocity, tripping device and measuring station. The velocities ranged from 2.3 m/s to 11.6 m/s and two sandpaper tripping devices were used. These devices had a streamwise extent of 150 mm for 2.3 m/s and 610 mm for other velocities. Altogether at least six different boundary-layer flows were used for measurements, where the different flows corresponded to different combinations of tripping device and velocity. Often plots were given to show how a quantity varied with R_θ, but the experimental points on these plots corresponded to different flows, thus implying that only the value of R_θ was important and that it was immaterial how R_θ was obtained.

The above researchers matched their low-Reynolds-number velocity profiles with a logarithmic law having $\kappa = 0.41$ and $C = 5.0$ and found that the inferred values of U_τ agreed closely with values of U_τ determined by other means and thus showed that even at low Reynolds numbers, the law of the wall, and thus the values of κ and C, did not vary. The extent of the logarithmic region was found to decrease with decreasing Reynolds number but the logarithmic region did not disappear at low Reynolds numbers. In fact the extent of the logarithmic region was shown to remain a nearly constant fraction of the boundary-layer thickness. From this they concluded that the logarithmic

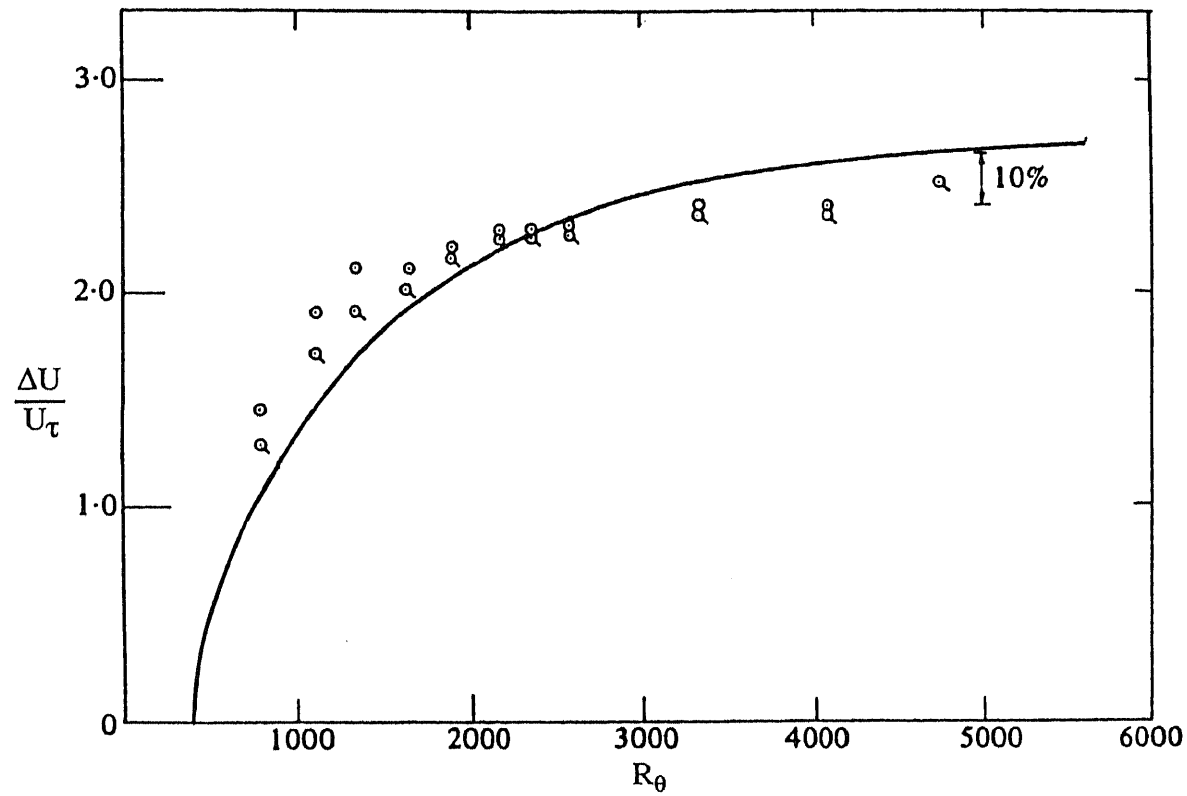

FIGURE 2.5. Variation of $\Delta U/U_\tau$ with R_θ as given by Murlis, Tsai & Bradshaw (1982): o, C = 5.2; q, best-fit C; ——, Coles (1962).

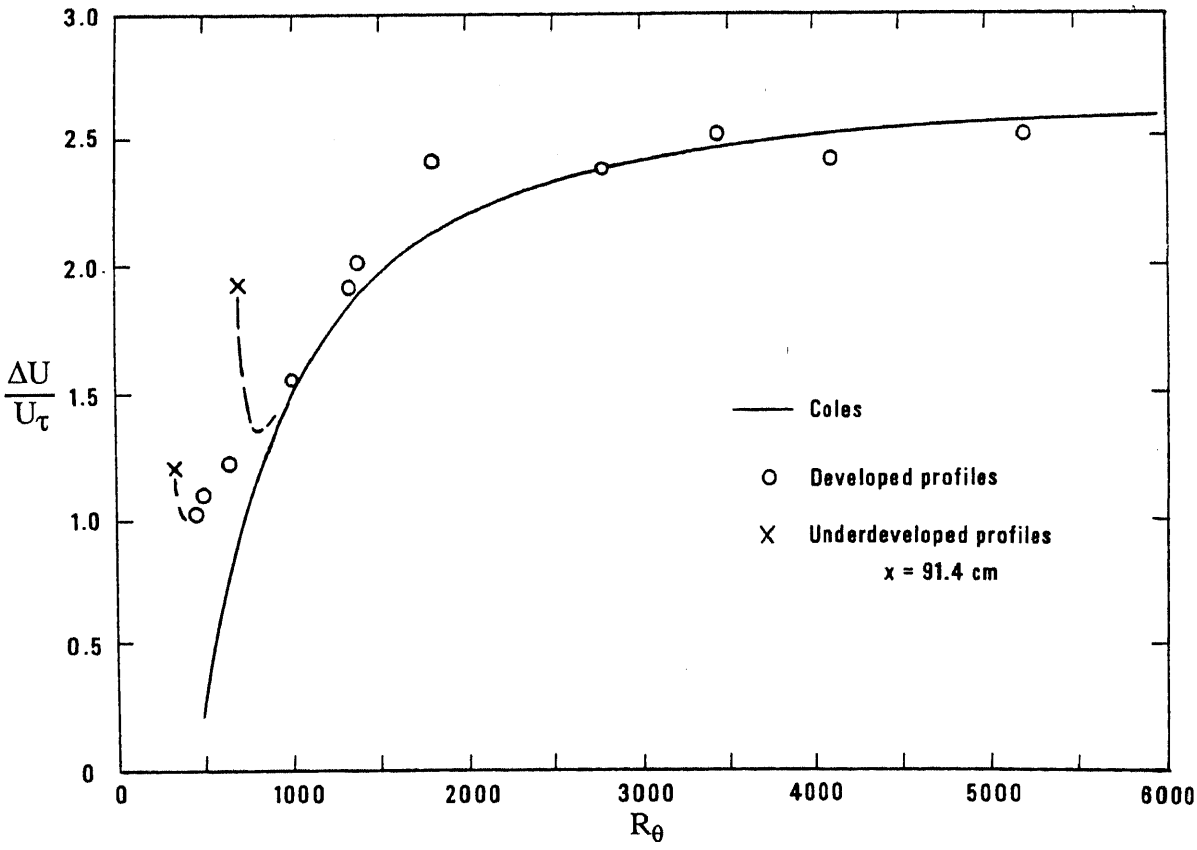

FIGURE 2.6. Variation of $\Delta U/U_\tau$ with R_θ as given by Purtell, Klebanoff & Buckley (1981).

region seems to be an inherent characteristic of the turbulent boundary layer. To examine boundary-layer development, a limited number of profiles of mean velocity were plotted using coordinates of U/U_e versus y/δ^*. This method of plotting the data was shown to be a sensitive indicator of flow development since the underdeveloped profiles deviated from the developed profiles in the outer-flow regions. The researchers also compared their $\Delta U/U_\tau$-versus-R_θ data with the relationship proposed by Coles (1962), as shown in figure 2.6. Included on this figure are underdeveloped profiles, which show a sharp increase in $\Delta U/U_\tau$ Considering the developed profiles, they noted that the asymptotic curve differs somewhat from that of Coles (1962) in that no disappearance of $\Delta U/U_\tau$ is found for low values of R_θ.

The above contradiction between Simpson (1970) and Coles (1962) was also addressed by these researchers. They studied Simpson's work very carefully and concluded that the assertion by Simpson that κ varies with Reynolds number is shown to imply either values of shear stress at the wall which do not agree with the measured values or to imply a line through the logarithmic region which does not fit the measured profiles nearly as well as the logarithmic-law line determined by using constant values of κ and C, viz. κ = 0.41 and C = 5.0.

Granville (1977) accounted for the effects of low Reynolds number by proposing that viscosity also affects the outer law, so that for low Reynolds numbers, equation (2.4) becomes

$$U_e - U = g[y,\delta,\tau_w,\rho,\nu] \tag{2.16}$$

or alternatively

$$\frac{U_e - U}{U_\tau} = g\left[\frac{y}{\delta},\psi\right] \tag{2.17}$$

where

$$\psi = \frac{U_\tau \delta}{\nu} \tag{2.18}$$

(Granville did not use ψ, but instead he used η). Equation (2.8), which applies to the logarithmic region of overlap, therefore becomes

$$\frac{U_e-U}{U_\tau} = -\frac{1}{\kappa}\ln\left(\frac{y}{\delta}\right) + A[\psi] \qquad \frac{50\nu}{U_\tau} < y < 0.1\delta \text{ to } 0.2\delta \text{ (approx.)} \qquad (2.19)$$

The value of A now depends on ψ, or alternatively on Reynolds number, for low Reynolds numbers, but is constant for moderate to high Reynolds numbers. Since κ is assumed invariant with Reynolds number, the effects of low Reynolds number are accounted for entirely by $A[\psi]$. The value of $A[\psi]$ was obtained from experimental results. Granville indicated that when $A[\psi] = 0$ the logarithmic region disappears and it can be shown that this corresponds to $R_\theta = 738$.

To justify physically the above modification, Granville referred to the work of Huffman & Bradshaw (1972), and indicated that the large eddies of the outer boundary-layer flow are affected by the viscous effects from the turbulent irrotational interface at low Reynolds numbers.

Barr (1980) performed low-Reynolds-number turbulent boundary-layer experiments on a flat plate in a zero pressure gradient for $200 < R_\theta < 7000$. The experiments were performed in the NASA Ames low-pressure wind tunnel using either air or carbon dioxide as the working fluid. The pressures were at least as low as about 300 kPa, which is about one third of a percent of atmospheric pressure. The purpose of using low pressures and carbon dioxide was to simulate atmospheric conditions on the planet Mars. With low pressures, the gas density was much lower and the kinematic viscosity was therefore much higher than at normal pressures. Thus higher freestream velocities could be used (up to at least 97.5 m/s), and the boundary layer was much thicker (typically from 170 to 210 mm) than for the same Reynolds number at normal pressures. Both of these factors improved experimental accuracy and enabled accurate measurements to be taken in the viscous sublayer. The boundary layer was tripped by a bed of small pebbles and mean-flow profiles were taken at different velocities but for the same values of x. No turbulence measurements were taken.

Within the range $600 < R_\theta < 2000$, Barr compared measured Clauser-chart values of C_f with values computed using well-known formulae. When using the Clauser chart, the logarithmic-law constants were assumed to be $\kappa = 0.418$ and $C = 5.45$ (as given by Patel 1965) and the validity of these was checked by calculating C_f by an alternative method. Since the measured values of C_f were significantly different from those computed from formulae, an expression for C_f was developed for the above range of R_θ.

Within the range $425 < R_\theta < 600$, the flow was found to deviate from the logarithmic law corresponding to $\kappa = 0.418$ and $C = 5.45$. Barr indicated that these flows could be modelled by making κ and C functions of R_θ for this range of R_θ, an idea similar to that proposed by Simpson (1970) for $R_\theta < 6000$. Barr found that for $425 < R_\theta < 600$, the viscous sublayer became a larger fraction of the boundary-layer thickness (sublayer up to about 10 mm thick) than at higher Reynolds numbers.

White (1981) presented an abridged version of Barr's publication. For $425 < R_\theta < 600$, he indicated that κ is given by

$$\kappa = 0.0013\, R_\theta - 0.362 \qquad (2.20)$$

and C appears to be a function of both R_θ and H. However, White also indicated that flows corresponding to this range of R_θ may not have been in equilibrium or fully developed.

Smits, Matheson & Joubert (1983) studied low-Reynolds-number turbulent boundary layers on a flat plate in both a zero and two favourable pressure gradients for $R_\theta < 3000$. The following discussion will apply to the zero-pressure-gradient results. An extensive range of mean-flow measurements, but no turbulence measurements, were presented. Measurements were taken for at least five different reference velocities and the boundary layers were generally tripped by using cylindrical pins of height 1.0 mm, diameter 3.2 mm and spacing 9.6 mm. It was assumed that $\kappa = 0.41$ and $C = 5.2$ and that both of these logarithmic-law parameters were unaffected by Reynolds number. These values of κ and C were confirmed since they were used when performing balances of momentum and these balances were found to be acceptable. The constancy of κ and C is in contrast to the conclusions of White (1981). A

logarithmic region was found to exist for R_θ as low as 354. The researchers indicated that the variation of Π, H, G and C_f, with R_θ, appeared to be independent of how R_θ was formed.

2.3 Broadband-Turbulence Behaviour at Low Reynolds Numbers

From the preceding section it can be seen that low-Reynolds-number mean-flow behaviour is reasonably well understood. However, relatively few low-Reynolds-number broadband-turbulence measurements have been published so obviously there has not been any in-depth analysis of such data comparable to Coles' (1962) analysis of the mean-flow data. Consequently there is no unifying framework which correlates low-Reynolds-number broadband-turbulence measurements from different sources. Also there does not seem to be any well-established scaling for plotting of such data. Different types of scaling that have been proposed in the literature will be outlined in the following with the intention of using some of these types of scaling when presenting and analysing the current results. The important contributions that have been made towards our understanding of low-Reynolds-number broadband-turbulence behaviour will now be reviewed.

Before this is done, however, it is first necessary to discuss some terminology used in this thesis. Quantities such as $\sqrt{\overline{u^2}}$ will be referred to as r.m.s. intensities, whereas quantities such as $\overline{u^2}$ and $\overline{uv}$ will be referred to as Reynolds normal stresses and Reynolds shear stresses respectively, even though strictly speaking they are kinematic Reynolds stresses. The above terminology is by no means universal in the literature.

Whenever researchers study this flow behaviour, they almost invariably refer to the classical work of Klebanoff (1954), who measured r.m.s. intensities for the three coordinate directions, as well as Reynolds shear stresses. In this work, the boundary layer was tripped by covering the first 2 feet (609.6 mm) of a smooth plate with sand roughness consisting of No. 16 floor-sanding paper and the freestream velocity at the measuring station was 50 ft/s (15.2 m/s). The value of R_θ at this station was about 7500, which is slightly above the upper limit of the low-Reynolds-number range. Klebanoff plotted values of $\sqrt{\overline{u^2}}/U_e$ against y/δ and similarly for the v and w components of the turbulence.

Normalized Reynolds shear stresses were expressed as $-2\overline{uv}/U_e^2$ and were also plotted against y/δ. The shear correlation coefficient, $-\overline{uv}/(\sqrt{\overline{u^2}}\sqrt{\overline{v^2}})$, was calculated by Klebanoff and it had a value of approximately 0.49 out to about $y/\delta = 0.8$. It is worth noting that Klebanoff does not seem to indicate the method that he used to define δ.

Murlis (1975) and Murlis, Tsai & Bradshaw (1982) complemented their mean-flow measurements referred to above with an extensive range of broadband-turbulence measurements for the u and v components of the turbulence. All of their turbulence measurements were outside the logarithmic region. The presentation of their results was designed to highlight Reynolds-number-dependent changes in the structure of the turbulence.

These researchers plotted values of $\overline{u^2}/U_\tau^2$ against y/δ for a range of values of R_θ, and similarly for the v component of the turbulence. The values of $\overline{u^2}/U_\tau^2$ were found to be dependent on R_θ and the corresponding v component terms were also found to be dependent on R_θ, but to a lesser extent. The manner in which the above parameters varied with R_θ as the flow developed were also presented for a number of fixed values of y/δ.

No measurements of the w components of the turbulence were actually taken by the researchers, although for the purpose of constructing the balances of turbulent kinetic energy, $\overline{w^2}$ terms were approximated from the measured $\overline{u^2}$ and $\overline{v^2}$ terms, as will be shown in Section 2.4.

Normalized Reynolds-shear-stress profiles, expressed in the form $\overline{uv}/U_e^2$ versus y/δ, were also presented for different values of R_θ and were shown to vary with R_θ. The ratio of Reynolds shear stress to wall shear stress was found to be higher at high values of R_θ. The four triple products for the u and v components of the turbulence were also presented by these researchers. When these triple products were normalized by U_e^3 and plotted against y/δ for a range of values of R_θ, their maximum values decreased as R_θ increased in all four cases. The four triple products were also normalized by U_τ^3 and plotted against R_θ for a number of values of y/δ to show streamwise development of the different terms. The triple products in this dimensionless form were shown to vary only slowly with R_θ.

The above researchers indicated that the best measure of structural changes in the turbulence is the behaviour of the Reynolds normal stress ratio, $\overline{u^2}/\overline{v^2}$, and the shear correlation coefficient, $-\overline{uv}/(\sqrt{\overline{u^2}}\sqrt{\overline{v^2}})$. They plotted these two anisotropy parameters against y/δ for a range of values of R_θ in order to indicate the changes. The Reynolds normal stress ratio was shown to vary considerably with R_θ. This parameter increased monotonically with R_θ to a roughly constant value by about $R_\theta = 2000$. At the higher values of R_θ, the parameter followed Klebanoff's (1954) results reasonably well. It was noted that the change took place principally in the same Reynolds number range as the increase in the profile parameter, Π, thus raising the possibility of a direct link between the two phenomena. Data for the shear correlation coefficient reached a weak maximum at about $R_\theta = 1900$ followed by a slow fall to a nearly asymptotic value at $R_\theta = 4750$. For $y/\delta = 0.6$, the shear correlation coefficient had a value of -0.42 at $R_\theta = 791$, -0.45 at $R_\theta = 1900$ and -0.40 at $R_\theta = 4750$.

Purtell (1978) and Purtell, Klebanoff & Buckley (1981) presented broadband-turbulence intensities for the u component of the turbulence to complement their low-Reynolds-number mean-velocity measurements. Normalized r.m.s intensities expressed as $\sqrt{\overline{u^2}}/U_\tau$ were plotted against both $\log(yU_\tau/\nu)$ and y/δ for a range of values of R_θ. Normalized r.m.s. intensities for the developed profiles plotted against yU_τ/ν showed approximate similarity out to about $yU_\tau/\nu = 15$, but beyond this range the profiles were strongly dependent on R_θ. On the other hand, profiles of mean velocity, plotted using coordinates of U/U_τ versus $\log(yU_\tau/\nu)$, showed similarity to the end of the logarithmic region. When the normalized r.m.s. intensities were plotted against y/δ they showed approximate similarity for nearly all values of y/δ. The researchers indicated that this approximate similarity for variations in R_θ was somewhat unexpected since profiles of mean velocity scaled in outer-flow variables are definitely functions of R_θ. Profiles of mean velocity plotted as U/U_e versus y/δ^* had been shown to be a sensitive indicator of flow development, and this was also found to be the case when turbulence data were plotted using coordinates of $\sqrt{\overline{u^2}}/U_e$ versus y/δ^*

2.4 Balances of Energy and Shear Stress

For a steady, two-dimensional flow field having velocity components U,V[x,y] and u,v,w[x,y,z,t], the general Navier-Stokes equations reduce to

$$\frac{\partial u}{\partial t} + (U+u)\frac{\partial (U+u)}{\partial x} + (V+v)\frac{\partial (U+u)}{\partial y} + w\frac{\partial u}{\partial z} =$$

$$-\frac{1}{\rho}\frac{\partial (P+p)}{\partial x} + \nu\left(\frac{\partial^2 U}{\partial x^2} + \frac{\partial^2 U}{\partial y^2} + \nabla^2 u\right) \qquad (2.21)$$

$$\frac{\partial v}{\partial t} + (U+u)\frac{\partial (V+v)}{\partial x} + (V+v)\frac{\partial (V+v)}{\partial y} + w\frac{\partial v}{\partial z} =$$

$$-\frac{1}{\rho}\frac{\partial (P+p)}{\partial y} + \nu\left(\frac{\partial^2 V}{\partial x^2} + \frac{\partial^2 V}{\partial y^2} + \nabla^2 v\right) \qquad (2.22)$$

$$\frac{\partial w}{\partial t} + (U+u)\frac{\partial w}{\partial x} + (V+v)\frac{\partial w}{\partial y} + w\frac{\partial w}{\partial z} =$$

$$-\frac{1}{\rho}\frac{\partial p}{\partial z} + \nu\,\nabla^2 w \qquad (2.23)$$

Also, continuity considerations necessitate that

$$\frac{\partial U}{\partial x} + \frac{\partial V}{\partial y} = 0 \qquad (2.24)$$

and

$$\frac{\partial u}{\partial x} + \frac{\partial v}{\partial y} + \frac{\partial w}{\partial z} = 0 \qquad (2.25)$$

If equation (2.21) is multiplied by u, equation (2.22) multiplied by v and equation (2.23) multiplied by w, and each of the three resulting equations averaged and added together, then after the use of continuity and introduction of the boundary-layer simplifications, the following equation for turbulent kinetic energy can be shown to exist.

$$\underbrace{\frac{1}{2}\left(U\frac{\partial\overline{q^2}}{\partial x}+V\frac{\partial\overline{q^2}}{\partial y}\right)}_{1}+\underbrace{\overline{uv}\frac{\partial U}{\partial y}+(\overline{u^2}-\overline{v^2})\frac{\partial U}{\partial x}}_{2}+\underbrace{\frac{\partial}{\partial y}\left(\frac{\overline{pv}}{\rho}+\frac{\overline{q^2}v}{2}\right)}_{3}$$

$$+\underbrace{\varepsilon}_{4}-\underbrace{\nu\frac{\partial^2}{\partial y^2}\left(\frac{\overline{q^2}}{2}+\overline{v^2}\right)}_{5}=0 \qquad (2.26)$$

As can be seen, terms in this equation have been conveniently grouped together and the different groups have the following physical interpretations:

(1) Advection of turbulent energy by the x and y components of the mean motion

(2) Production of turbulent energy from the mean motion

(3) Diffusion by fluctuating pressure and turbulence velocity

(4) Turbulent energy dissipation to heat

(5) Transport of turbulent energy by viscous forces.

When obtaining an energy balance for a particular flow, terms in groups 1 and 2 can be easily measured and thus these groups present no difficulties. According to Rotta (1962) (page 64), group 5 is negligible outside the viscous sublayer, so therefore for the remainder of the boundary layer this group can be neglected. Groups 3 and 4, corresponding to diffusion and dissipation respectively, can present problems and different researchers have dealt with these groups in different ways. Klebanoff (1955) measured the dissipation directly by measuring the microscales and obtained the diffusion by difference. Bradshaw (1967), on the other hand, determined diffusion and obtained dissipation by difference. He assumed that $\overline{pv}/\rho$ could be neglected and also that $0.5\overline{q^2v} \approx 0.75(\overline{u^2v}+\overline{v^3})$, which in effect meant that $\overline{vw^2}$, which is one of the terms comprising $\overline{q^2v}$, is equal to $0.5(\overline{u^2v}+\overline{v^3})$. Murlis (1975) and Murlis, Tsai and Bradshaw (1982) did not measure the w component of the turbulence but instead determined $\overline{w^2}$ by means of the relationship $\sqrt{\overline{w^2}} \approx 0.5(\sqrt{\overline{u^2}}+\sqrt{\overline{v^2}})$, which was based on Klebanoff's (1954) data. When obtaining an energy balance, these researchers also determined diffusion and obtained dissipation by difference. They also assumed that $(\overline{pv}/\rho)+0.5\overline{q^2v} \approx 0.75(\overline{u^2v}+\overline{v^3})$. Murlis (1975) indicated that this expression could also be obtained using approximations given by Lawn

(1970) (see also Lawn 1971), viz. $\overline{vw^2} \approx 0.5\overline{v^3} \approx 0.5\overline{u^2v}$ and $\overline{pv}/\rho \approx 0.125\overline{q^2v}$.

The equation for Reynolds shear stress can be obtained in a similar manner to the energy equation after first multiplying equation (2.21) by v and equation (2.22) by u. The resulting equation is

$$\underbrace{U\frac{\partial \overline{uv}}{\partial x} + V\frac{\partial \overline{uv}}{\partial y}}_{1} + \underbrace{\overline{v^2}\frac{\partial U}{\partial y}}_{2} - \underbrace{\overline{\frac{1}{\rho}p\left(\frac{\partial u}{\partial y} + \frac{\partial v}{\partial x}\right)}}_{3} + \underbrace{\frac{\partial \overline{uv^2}}{\partial y}}_{4} + \underbrace{\frac{1}{\rho}\frac{\partial \overline{pu}}{\partial y}}_{5} - \underbrace{\nu\overline{(u\nabla^2 v + v\nabla^2 u)}}_{6} = 0 \qquad (2.27)$$

Once again terms have been grouped together and the different groups have the following physical interpretations:

(1) Transport of Reynolds shear stress by the mean flow

(2) Generation of Reynolds shear stress by interaction with mean flow

(3) Redistribution by pressure fluctuations

(4) Transport by velocity fluctuations

(5) Transport by pressure fluctuations

(6) Transport and destruction of Reynolds shear stress by viscous forces.

When obtaining a shear-stress balance, terms in groups 1, 2 and 4 can be easily measured. According to Bradshaw (1972), groups 5 and 6 can be neglected, and so therefore group 3, the remaining group, can be determined by difference.

For the energy balance for the current investigation, the advection and production were calculated directly using equation (2.26). The diffusion was calculated using the method of Bradshaw (1967) and Murlis, Tsai & Bradshaw (1982) outlined above, in which approximations were used. The dissipation was determined by difference after neglecting other terms in equation (2.26). For the shear-stress balance for the current investigation, the procedure outlined above was followed.

Murlis (1975) and Murlis, Tsai & Bradshaw (1982) present comprehensive data on energy and shear stress balances for low-Reynolds-number flows and

consequently these results will be used as a basis for comparison with the current results.

2.5 Spectral Behaviour

Spectra of fluctuating turbulence signals give an indication of how turbulent energy is distributed among the eddy length scales and thus can be used to help interpret turbulence structure.

Over the years a large amount of spectral data have been presented in the literature but only a relatively small amount of these have been for low-Reynolds-number flows. Purtell (1978) did present three families of spectra for the u component of the turbulence, corresponding to values of R_θ of 500, 1300 and 1800, which were associated with three different flows. The spectra were plotted using coordinates of $\log\Phi[\omega']$ versus $\log[\omega']$ where $\omega' = 2\Pi\nu f_r/U_\tau^2$, and were shown to be independent of R_θ. Apart from this contribution, very little low-Reynolds-number spectral data are available. Murlis (1975) and Murlis, Tsai & Bradshaw (1982) did not present any spectral measurements.

In the current investigation, spectra are analysed according to the theory of Perry, Henbest & Chong (1986). Details of their work are not given here, but instead are given in Chapter 7 which deals with spectra.

2.6 Flow Prediction by Numerical Simulation

Spalart (1988) and Spalart & Leonard (1987) used numerical simulation to predict boundary-layer flow for a low-Reynolds-number turbulent boundary layer and presented both mean-flow and turbulence results for values of R_θ of 300, 670 and 1410. The three-dimensional time-dependent Navier-Stokes equations were solved using a spectral method with up to about 10^7 grid points and the computations were performed on the NASA Ames Cray computer. Although numerical simulations such as this are beyond the scope of this thesis, the work is mentioned here since it will be referred to periodically and also some early results of the current investigation, documented by Erm, Smits & Joubert (1985) (see also Erm, Smits & Joubert 1987), were used by Spalart and Spalart & Leonard when they were verifying their predictions by comparing them with experimental data.

2.7 Scope of Current Investigation

The preceding literature survey broadly outlines our current understanding of low-Reynolds-number turbulent boundary layers. Some aspects of these flows have by now been firmly established whereas in other areas doubts remain ranging from differences of opinion to an almost complete lack of knowledge. In the light of this survey, an experimental programme was developed. This programme was basically comprised of mean-flow velocity profiles taken with a Pitot-static probe, skin-friction coefficients measured with a Preston tube and turbulence measurements taken with hot-wire probes. The aim of the programme was to concentrate on critical areas of concern and attempt to clarify some of the outstanding questions. In addition, the programme was devised to investigate areas that have not received much attention in the past. All of this will help extend the available low-Reynolds-number data base which hopefully will be of benefit to future researchers such as those looking for data to test their prediction methods. The broad experimental programme, together with the reasoning behind its development, is now outlined.

A question that had to be answered was what type of tripping device to use. A tripping device is used in investigations such as this one to stabilise boundary-layer transition from laminar to turbulent flow and stop the transition region moving back and forth along the measuring surface as it would with no tripping device,i.e. natural transition. Low-Reynolds-number turbulent boundary layers are intimately connected with the tripping device since such flows occur in close proximity to the device and also different types of devices introduce different types of disturbances into the flow. Thus devices must be selected very carefully.

The above survey indicates that different researchers have used a variety of different types of devices, including wires, pins, sandpaper and pebbles, to trip their boundary layers, which tends to suggest that researchers have thought that the actual type of device used is not all that important. This assumption is consistent with the fact that Coles' (1962) $\Delta U/U_\tau$-versus-R_θ characteristic, shown in figure 2.4, was based on data from nine different investigations in which a variety of different tripping devices were used. However, the fact remains that

even though this characteristic may not depend on the device used, other mean-flow characteristics and turbulence characteristics may depend upon the device. To investigate this possibility, three different tripping devices, representative of those used by others, were chosen for use in this investigation. The devices were a circular wire, distributed silicon carbide grit and cylindrical pins. Further details of these will be given in Chapter 4.

The general consensus of most researchers after Coles (1962) is that his criterion for a normal state for a low-Reynolds-number turbulent boundary layer at constant pressure, as shown in figure 2.4, is basically correct. Thus the flows of the current investigation were established so that they also followed this characteristic and such flows were regarded to be correctly stimulated. To meet this requirement it was necessary that the sizes of the tripping devices were selected with considerable care. Appendix 1 briefly outlines some formulae to determine the heights of tripping devices necessary to cause transition to turbulence. It is indicated in Appendix 1 that the formulae have limitations and can only be used as a guide when determining the heights of tripping devices. As a consequence of these limitations, an empirical technique was devised to determine the heights of the devices to match a velocity so that the resultant flows followed Coles' characteristic.

When a flow velocity is changed from its value corresponding to correct stimulation, i.e. is changed from its design value, the resulting $\Delta U/U_\tau$-versus-R_θ relationship is known to depart from the ideal form suggested by Coles (1962). However, the degree to which this relationship changes and also how other mean-flow and turbulence characteristics change with changes in flow velocity for different devices has not been systematically investigated in the past. This is of importance to researchers setting up low-Reynolds-number turbulent boundary-layer experiments since they would like to know just how precisely their flow velocity has to be matched to the tripping device to obtain acceptable flow. Perhaps some devices are more stable to velocity changes away from the design value and are thus more suitable for fundamental research. Consequently a limited experimental investigation was undertaken to study both mean-flow and turbulence behaviour for operation both below and above the design velocity using the three different tripping devices. However, this was

not the most important part of the study and most experimental effort was concentrated on the design flows.

So far the details of the experimental programme have only been outlined in general terms, referring only to mean-flow measurements or turbulence measurements. The programme will now be considered in more specific terms.

Landweber (1953), Preston (1958) and Granville (1977) have given differing opinions regarding the actual value of R_θ at which the logarithmic region disappeared. Since this matter was controversial, measurements were taken in the current investigation to address this problem. This was done for all three tripping devices.

The existence of a logarithmic region at low Reynolds numbers with $\kappa = 0.41$ and $C = 5.0$ or 5.2 has by now been well established by Coles (1962), Huffman & Bradshaw (1972), Murlis (1975), Murlis, Tsai & Bradshaw (1982), Purtell (1978), Purtell, Klebanoff & Buckley (1981), and Smits, Matheson & Joubert (1983), so there was no need to investigate this matter any further except to decide whether to use $C = 5.0$ or $C = 5.2$ in the current investigation.

Brederode & Bradshaw (1974) investigated the values of κ and C by analysing their Preston-tube (see Section 3.6) and velocity-profile measurements, as well as similar sets of measurements from different sources within the Department of Aeronautics, Imperial College. The Preston-tube results were reduced by using Patel's (1965) calibration and the values of the skin-friction coefficients were used to non-dimensionalise velocity profiles. They suggested that to obtain agreement in the linear region between the profiles and a logarithmic line, then the constants used for the line should be $\kappa = 0.41$ and $C = 5.2$, provided the velocity profiles have been corrected for shear displacement effect. Since Preston-tube results are known to be reliable, the above values of κ and C carry considerable weight.

In the current investigation, the value of κ was assumed to be 0.41 and the value of C was assumed to be either 5.0 or 5.2, depending upon the particular application, for all values of R_θ. Whenever the data of the current investigation were compared with the work of Coles (1962), then the values of the constants associated with this data were $\kappa = 0.41$ and $C = 5.0$, the same as those used by Coles (1962), since it would not have been strictly correct to use other values,

even though Brederode & Bradshaw (1974) have shown that $\kappa = 0.41$ and $C = 5.2$ are better choices. In other cases, when values of U_τ were required to non-dimensionalise the current data when they were plotted, then the values of U_τ were almost invariably determined by means of a Clauser chart using $\kappa = 0.41$ and $C = 5.2$, the method shown by Brederode & Bradshaw to give the same values of U_τ as those determined using Preston tubes. Throughout this thesis it will be made perfectly clear what values of κ and C are being used in each particular application.

A method used to check on the two-dimensionality of a flow is to take transverse C_f measurements. Very few measurements of this type for low-Reynolds-number flows have been reported in the literature. Murlis (1975) did present some of these measurements, but only for $R_\theta = 4750$. In the current study, measurements were taken for several different values of R_θ for correctly-stimulated flows for all three tripping devices, thus providing checks on two-dimensionality and also enabling a comparison to be made between how different devices distort the flow and how long it takes these flows to settle down after being tripped.

When deciding upon which broadband-turbulence characteristics to measure in the current investigation, the main consideration was to verify and extend results that had already been presented in the literature. Purtell (1978) and Purtell, Klebanoff & Buckley (1981) presented broadband-turbulence measurements for a range of values of R_θ, but these were only for the u component of the turbulence and were restricted to normalized r.m.s intensities. Murlis (1975) and Murlis, Tsai & Bradshaw (1982) presented a wide range of the important broadband-turbulence measurements for the u and v components of the turbulence up to quadruple products. These latter two publications contain the most comprehensive set of low-Reynolds-number broadband-turbulence results available. It is significant that none of the above four publications present any measurements of the w component of the turbulence. In the current investigation, broadband-turbulence terms up to quadruple products were measured for a range of values of R_θ for all three components of the turbulence for the three different tripping devices for correctly-stimulated flows. Additional broadband-turbulence terms for the u component of the

turbulence were also measured for two values of R_θ for the three tripping devices in flows both above and below the design velocity.

An analysis of the literature indicates that there is a scarcity of spectral data for low-Reynolds-number turbulent boundary layers. Despite this scarcity of data, spectral measurements are very important since they facilitate interpretation of the structure of the turbulence at low Reynolds numbers. In fact Murlis (1975) specifically states that a spectral analysis is an outstanding possibility for an extension of his work. In view of this, spectra corresponding to all of the above broadband-turbulence measurements were taken.

CHAPTER 3

EXPERIMENTAL APPARATUS AND TECHNIQUES

Details of the experimental apparatus used in the investigation as well as other information relevant to the measurement and reduction of the experimental data are described in the following.

3.1 Description of Wind Tunnel

The wind tunnel used for the experiments was an open-return suction type of conventional design and is depicted in figure 3.1.

The inlet section had cross-sectional dimensions of 1219 mm by 914 mm and contained six polyester screens and an aluminium honeycomb. These suppressed turbulence and straightened the flow. The honeycomb had hexagonal cells of width 6.5 mm (distance between flat surfaces) and depth 50 mm and was situated between the first and second screens. Screens of two different sizes, having open to total area ratios of 57% and 58%, were used and these were placed alternatively along the inlet section with the 57% screen most upstream. These sizes were based on a recommendation by Bradshaw (1965). The inlet section and the working section were connected by a three-dimensional contraction.

The working section had cross-sectional dimensions of 613 mm by 309 mm at the inlet and was 2.5 m long. It had three fixed walls and an adjustable straight wall which was used to alter the pressure gradient. The smooth flat vertical surface upon which measurements were taken formed one of the walls of the working section. This wall, which was opposite the adjustable wall, had pressure tappings placed every 40.0 mm along its centreline. Corner fillets having a radius of about 33 mm were used on the inlet section, the contraction and the working section, to reduce secondary flow. The freestream turbulence intensity in the working section for a freestream velocity of about 9.5 m/s was

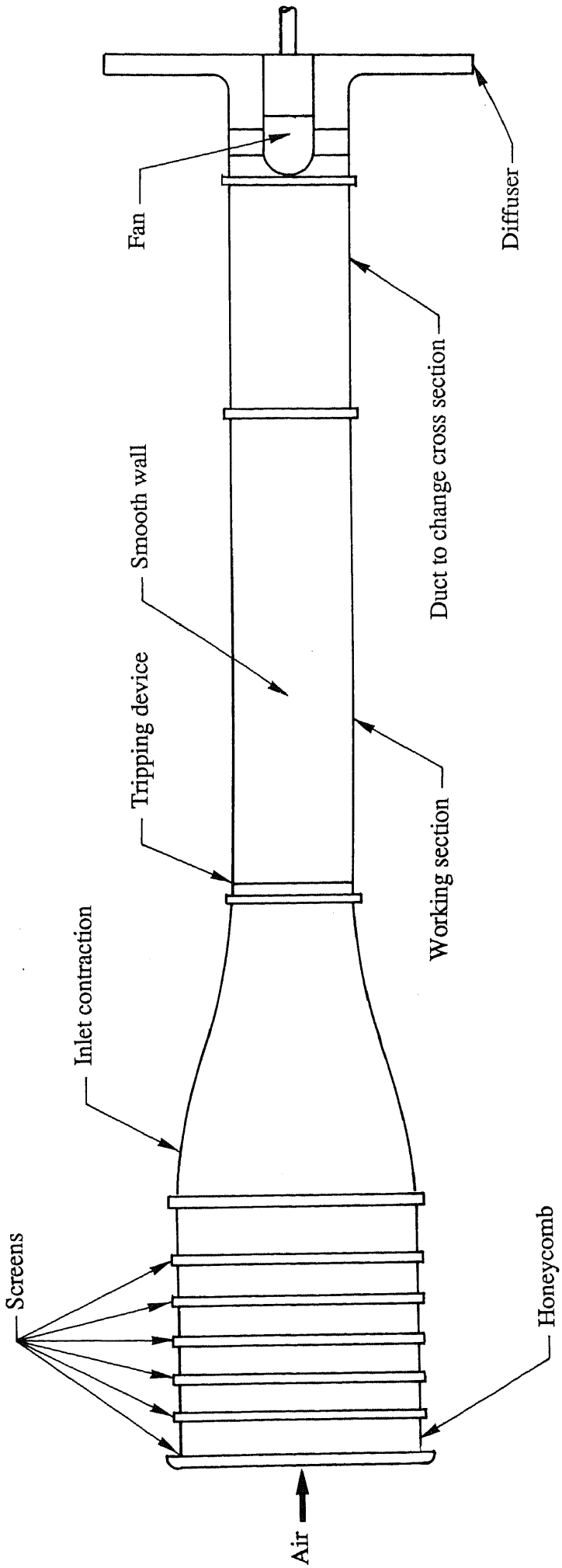

FIGURE 3.1. Diagrammatic representation of wind tunnel

about 0.0032. An intensity of this level is close to the midpoint of the "moderate" range as classified by Coles (1962).

Downstream of the working section was a duct which changed the cross-section from a rectangle to a circle of diameter 613 mm, thus slightly diffusing the flow. The duct was connected to an axial-flow fan and this was followed by a radial-flow diffuser which contained some straightening vanes. Additional details of the wind tunnel are given in figure 3.1.

The fan speed was controlled by a thyristor speed controller which produced a virtually constant fan angular velocity over many hours operation.

3.2 Tripping Devices

The tripping devices used in this investigation were glued onto an accurately-machined metal insert that could be bolted into a recess in the smooth wall so that the outer surface of the insert was flush with the smooth wall to high accuracy. The arrangement is shown in figure 3.2. The insert and tripping devices extended right across the smooth wall. The use of the metal insert meant that not only could the devices be changed quickly, but also that a device was exactly the same as previously each time its insert was repositioned. These capabilities were invaluable since it was continually necessary to change from one tripping device to another throughout the course of the experiments.

When inserts were bolted into position, the centrelines of the wire and pins and the upstream extremity of the silicon carbide grit were located 80 mm downstream of the contraction outlet. This was the origin for all x distances.

3.3 Calculation of Density and Viscosity

In the course of the experimental investigation it was necessary to calculate the air density, ρ, and the air kinematic viscosity, ν, for specified values of air temperature and pressure. The formulae used to calculate these variables are given in Appendix 2.

3.4 Constant Reynolds Number Reference Conditions

When undertaking the current experimental programme, the data were collected over a long period of time, so in order to obtain a consistent set of

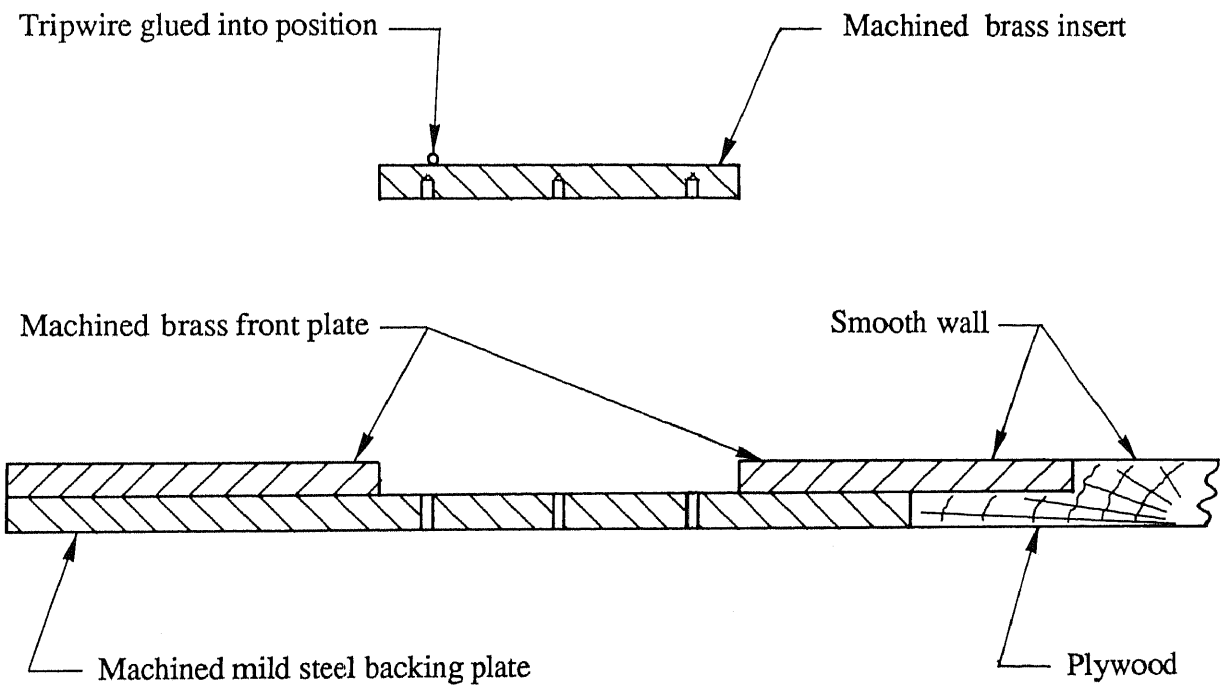

FIGURE 3.2. Tripping device glued to metal insert and corresponding recess in smooth wall.

measurements an allowance had to be made for the variations in atmospheric temperature and pressure that occurred from day to day. One possible way of doing this was to always set the reference velocity to a specified value for each set of measurements. A better way, however, and one with a sounder physical basis, was to choose a nominal reference velocity and always set the reference Reynolds number/metre, $R_{rf} = \rho U_{rf}/\mu$, to a specified value. This method was the one used in these experiments. When determining the specified values of R_{rf}, the temperature used was 22° C, i.e. 295.15 K, which is the approximate average temperature in the laboratory throughout the year, and the pressure used was 101325 Pa, which is standard atmospheric pressure.

The value of R_{rf} depended upon temperature, pressure and U_{rf} (i.e. fan speed), which all varied throughout an experiment, so it was impractical to maintain R_{rf} precisely at a specified value. Consequently, some variation of R_{rf} from its specified value had to be accepted. The tolerance band for R_{rf} was arbitrarily selected to be ±1.0% of the specified value. This was an extremely rigid requirement since, for example, a change in air temperature of only 1.8° C (approximate value), for constant pressure and constant fan speed, would cause R_{rf} to change by 1.0%. Despite the fact that R_{rf} could vary throughout an experiment, it did not deviate by more than ±1.0% from its required value for any of the measurements in the entire experimental investigation, even for mean-flow velocity profiles which took up to four hours to measure.

The numerical values of R_{rf} used in the experiments are large and unwieldy and also the expression "reference Reynolds number/metre" is itself cumbersome. Consequently, in order to simplify presentation throughout this thesis, reference conditions are generally referred to in terms of nominal reference velocities even though the reference conditions are in fact always based on Reynolds numbers/metre. This simplification gives the reader a better insight into the actual reference conditions since velocities are easier to comprehend than Reynolds numbers/metre, and in addition the simplification means that the text can be presented more concisely with less likelihood of confusion arising as a result of being too wordy.

3.5 Measurement of Pressures

Throughout the experimental programme it was necessary to measure accurately differences between two pressures arising from the use of Pitot-static probes, Preston tubes and pressure tappings. This was accomplished by using either a Baratron or Barocel electronic manometer that gave output voltages directly proportional to pressure differences. The full-scale reading of the Baratron corresponded to a pressure difference of 1.0 mm of mercury (133.3 Pa), which is the dynamic head associated with a velocity of about 14.9 m/s. Corresponding figures for the Barocel are 10.0 inches of water (2491 Pa) and 64.5 m/s. Pressure differences were not read directly from scales on these instruments, but instead the output voltages were fed into an electronic integrator and integrated for 40 s. To obtain greater accuracy, successive integrations were taken until the average value was repeatable to within acceptable limits. The actual number of integrations necessary to obtain convergence depended upon the size of the fluctuations in the output voltage in relation to the mean voltage.

3.6 Measurement of Skin-Friction Coefficients with a Preston Tube

Preston (1954) proposed a simple method of measuring C_f which makes use of a Pitot tube (the so-called Preston tube) resting on the surface. Preston made use of the idea that within the wall region a kind of local dynamical similarity existed, so that measurements of Pitot pressure, P, and local surface static pressure, p_w, in this region could be presented in a non-dimensional form as follows:

$$\frac{(P-p_w)d^2}{\rho\nu^2} = f\left[\frac{\tau_w d^2}{\rho\nu^2}\right] \tag{3.1}$$

where d is the outside diameter of the Pitot tube. Preston's original calibration has been revised by Patel (1965), and this revised calibration was the one used in the current investigation. All of this work is well known and no further details will be given here.

The Preston-tube values of C_f presented in this thesis all correspond to a tube diameter of 1.00 mm. Checks with other tubes having diameters of 1.26

mm and 1.60 mm showed typically about 2% total variation between the three devices.

3.7 Measurement of Velocity Profiles

Velocity profiles were taken with a specially made Pitot-static probe. Some features of the probe, as well as the associated velocity profiles, are now described.

3.7.1 Details of Probe

The probe used had a round head of diameter 0.722 mm for the measurement of total pressures and it also had another arm for the measurement of static pressures. Probes used by other researchers often only measure total pressure and the static pressure is measured by using a wall pressure tapping (e.g. Murlis, Tsai & Bradshaw 1982). The probe was calibrated against a National Physical Laboratory probe for a wide range of freestream velocities. It passed through clearance holes drilled through the smooth wall and was connected to a manual traversing mechanism. Modelling clay was used on the back of the wall to seal the holes and also to provide additional support for the probe.

3.7.2 Spacing of Points on Profiles and Setting of Probe on Wall

A velocity profile can be used to determine many parameters (see Sections 3.8.1 to 3.8.3) and the accuracy to which these can be determined is affected by the spacing of the points on the profiles. The technique used to calculate the values of y for the different points and to set the probe on the wall are explained in Appendix 3.

3.7.3 Wall Proximity Corrections

The y values of the experimental points on the velocity profiles were corrected to allow for the proximity of the wall. The correction used was that proposed by Macmillan (1956) which assumes that a value of y is equal to the sum of the distance from the wall to the centre of the probe tip plus 15% of the probe tip diameter.

3.8 Determination of Parameters From a Mean Velocity Profile

3.8.1 Profile Parameters and Skin-Friction Coefficients

A number of alternative methods are available for determining Π and U_τ, or equivalently C_f, from velocity profiles. Values of these parameters can be determined by using the two different techniques given by Coles (1962) and Coles (1968), which have already been described in Section 2.2. It will be recalled that in the former technique data is only fitted to the logarithmic-law line while in the latter technique data is fitted to both the logarithmic-law line and the wake-law line. The effects of this change is to increase the resultant value of Π and decrease the resultant value of C_f.

It is worth indicating that Π is an extremely sensitive variable. A check on one of the velocity profiles showed that if the velocity at the location where Π is computed is varied by say 1%, then the computed value of Π for R_θ about 1000 changes by about 15%. A 1% variation in velocity could be associated with experimental error or the flow may be imperfect to the extent that a velocity is 1% away from its ideal value. The sensitivity of Π to changes in velocity is even greater for lower values of R_θ.

Clauser (1954) proposed a technique for determining C_f from a velocity profile. The basis of Clauser's technique was to rearrange equations (2.3), (2.7) and (2.12) so as to obtain the following expression

$$\frac{U}{U_e} = \sqrt{\frac{C_f}{2}}\frac{1}{\kappa}\ln\left(\frac{yU_e}{\nu}\right) + \sqrt{\frac{C_f}{2}}\frac{1}{\kappa}\ln\sqrt{\frac{C_f}{2}} + C\sqrt{\frac{C_f}{2}} \qquad (3.2)$$

When U/U_e is plotted against $\ln(yU_e/\nu)$ for different values of C_f, then a series of straight lines is produced and this is known as a Clauser chart. To determine a value of C_f by using this chart, it is necessary to take a velocity profile and plot the different combinations of U and y on the chart. The value of C_f is determined by noting which straight line the plotted data follow.

3.8.2 Velocity Profile Integral Parameters

Close to the wall there may be some uncertainty in the measured experimental data and to reduce the likelihood of errors in the computed values

of displacement and momentum thicknesses, δ^* and θ respectively, the standard integrals proposed by Coles (1968) were used for $yU_\tau/\nu < 50$. These integrals are

$$\int_0^{50} \left(\frac{U}{U_\tau}\right) d\left(\frac{yU_\tau}{\nu}\right) = 540.6 \tag{3.3}$$

and

$$\int_0^{50} \left(\frac{U}{U_\tau}\right)^2 d\left(\frac{yU_\tau}{\nu}\right) = 6546 \tag{3.4}$$

Thus the formulae for calculating displacement and momentum thicknesses become

$$\delta^* = \int_{\frac{50\nu}{U_\tau}}^{\delta} \left(1-\frac{U}{U_e}\right) dy + \frac{50\nu}{U_\tau} - \frac{540.6\nu}{U_e} \tag{3.5}$$

and

$$\theta = \int_{\frac{50\nu}{U_\tau}}^{\delta} \frac{U}{U_e}\left(1-\frac{U}{U_e}\right) dy + \frac{540.6\nu}{U_e} - \frac{6546U_\tau\nu}{U_e^2} \tag{3.6}$$

respectively. Beyond $yU_\tau/\nu = 50$, the contributions to δ^* and θ were determined by simple trapezoidal integration.

For the shape factor, H, the expression

$$H = \frac{\delta^*}{\theta} \tag{3.7}$$

was used, while the Clauser parameter, G, was determined by using

$$G = \frac{(H-1)}{H}\sqrt{\frac{2}{C_f}} \tag{3.8}$$

3.8.3 Boundary-Layer Thicknesses

Various definitions have been used in the literature to specify the outer edge of a boundary layer and the differences between them is not always insignificant. Often the definition used is not clearly stated and this makes comparison between such data and other data more difficult. The location where a velocity attains a specified percentage, such as 99% or 99.5%, of its asymptotic value is commonly used. Purtell (1978) used the 99% definition and Murlis (1975) the 99.5% definition. For the data of the current investigation, the 99.5% definition was used and this thickness is denoted simply by δ. Its value was determined by joining the outer points of a y-versus-U plot by straight lines and noting where $U = 0.995\ U_e$

Spalart (1988) adopted a different approach and defined the boundary-layer thickness, δ_s, in terms of a "stress thickness", which meant that the value of U/U_e, defining the edge of the boundary layer, varied with R_θ. At the edge of the boundary layer, where $y = \delta_s$, the value of U/U_e was equal to 0.9965, 0.9974 and 0.9977 for $R_\theta = 300$, 670 and 1410 respectively.

3.9 Momentum Balance

For a zero pressure gradient turbulent boundary layer, the momentum integral equation is given by

$$\frac{d\theta}{dx} = \frac{C_f}{2} \tag{3.9}$$

A check on the balance of this equation was performed by evaluating $(U_e^2/U_\tau^2)(d\theta/dx)$ for the developing flows as was done by Coles (1962). This method of checking on the balance incorporated a curve-fitting procedure to determine $d\theta/dx$ and inherent difficulties were involved in doing this. An alternative method of performing the balance was therefore adopted. Equation (3.9) was integrated to yield

$$\frac{\theta-\theta_0}{\theta_0}=\frac{1}{\theta_0}\int_{x_0}^{x}\frac{C_f}{2}dx \qquad (3.10)$$

and both terms of this equation were evaluated and compared at all stations. θ_0 is the boundary-layer momentum thickness of the most-upstream profile within a set and x_0 is the corresponding x distance. This method was used by Murlis (1975). In the current investigation, the integral was evaluated by connecting the experimental points with a series of straight lines. Although the above two methods are in effect equivalent, differences can occur in practice as a consequence of limitations in the curve fitting.

3.10 Hot-Wire Anemometers and Probes

Constant-temperature hot-wire anemometers of Melbourne-University design (see Perry 1982) were used for all of the turbulence measurements. The frequency response of the anemometers was set using a square-wave injection so that optimum damping was obtained. At zero velocity the frequency response was about 20 kHz and the response was set such that second-order behaviour occurred over the range of velocities encountered by the hot wires during the experiments.

For the single-wire measurements, a DISA 55P05 probe and corresponding chuck and leads were used. A home-made mounting tube was used to hold the chuck. For the crossed-wire measurements, a DISA 55P51 probe was used, but instead of using a DISA chuck, the leads were home made and were soldered straight onto the four short pins connected to the prongs, and the probe was mounted in a 4 mm diameter tube that could be rotated through 90° thus enabling measurements to be taken in both the uv and uw planes. For both probes, the DISA tungsten filaments were replaced by Wollaston-wire filaments having a platinum core of 5 μm diameter and an etched length of 0.8 to 1.0 mm. For the crossed-wire probe, the filaments were nominally ±45° to the streamwise direction. Before use, the wires were annealed for at least 24 hours at a resistance ratio of 2.0 to strengthen them and make them more stable.

It will be shown in Chapter 4 that most of the measurements in the current investigation were taken at nominal reference velocities of 8.0, 10.0 and 14.0

m/s. For all of the hot-wire measurements taken at these nominal velocities, the filaments on the crossed-wire probe remained intact and it was not necessary to replace them, whereas the filament on the single-wire probe only had to be replaced once. Thus any uncertainties arising from variations in filament geometry were eliminated for the crossed-wire measurements and would have been small for the single-wire measurements, where the geometry is easier to control.

3.11 Measurement of Broadband-Turbulence Profiles

3.11.1 Spacing of Points on Profiles and Measurement of Wall Distance

The spacing of the experimental points on the turbulence profiles was based upon the spacing used for the corresponding mean-flow velocity profiles. To enable turbulence profiles to be completed reasonably quickly, and thus minimize the effects of drifting of the hot wires, turbulence measurements were only taken at every second point compared with the mean-flow profiles. For the single wire, values of y as small as 0.47 mm were used, which corresponds to the corrected value of y when the mouth of the Pitot probe was touching the wall. For the crossed wire, the minimum value of y was restricted to 1.97 mm.

The distances of the hot wires from the wall were measured with a microscope using the method outlined by Witt, Watmuff & Joubert (1983). With this method the hot wires were positioned close to the wall and the distances between the wires and their images measured by using a graticule scale superimposed on the field of view. For the single wire, the wall distance was simply the distance from the wall to the axis of the wire filament. For the crossed wires in uv mode, the wall distance was the distance from the wall to the centre of the cross formed by the two wires and for the crossed wires in uw mode, the wall distance was the distance from the wall to a point midway between the planes containing the two wires. When the crossed-wire probe was rotated from one mode to the other, the wall distance did not change.

3.11.2 Dynamic Calibration

Both the single- and crossed-wire probes were calibrated by using the dynamic calibration technique developed at the University of Melbourne by Perry and his co-workers. The technique has been documented in detail by Perry (1982) and consequently it will only be outlined here.

The technique makes use of a dynamic calibrator to oscillate the hot-wire probes in an air stream. A new version of such a calibrator was designed by the author and this is shown in figure 3.3. The design of the calibrator was an extension of earlier designs at the University of Melbourne by Perry & Morrison (1971) and Perry & Watmuff (1981). The calibrator incorporated a Murray cycloidal drive, which is a unit used in the weaving industry to impart simple harmonic motion to a device attached to its output. For this unit the stroke was 3 inches (76.2 mm). The calibrator could be easily set to oscillate the probes at any angle between the horizontal and vertical references axes. Shown on the calibrator is a slotted disc, containing 120 slots, which was used in conjunction with LED-phototransistor pairs to enable the angular velocity of the calibrator and the phase of its motion to be determined accurately.

The calibration procedure will be described for the crossed-wire probe. The same procedure, but in a simplified form, was used for the single-wire probe. Prior to calibration, it was necessary to process the signals from the hot-wire anemometers by using the electronic circuitry shown in figure 3.4. The hot-wire probe was placed in the calibrator and oscillated horizontally in a steady air stream. The output voltage signals E_U and E_V were observed on an oscilloscope and the potentiometer P_4 was adjusted until the voltage signal E_V remained virtually constant and was thus insensitive to fluctuations in velocity U. The probe was then oscillated vertically and the potentiometer P_3 adjusted until E_U was virtually insensitive to fluctuations in velocity V. This process is termed "matching" of the hot wires. The calibrator was then stopped and potentiometers P_1 and P_2 adjusted to remove excessive offset voltages. This did not affect the matching. The signals were then amplified to improve resolution and since the signals were later to be sampled by a digital computer, checks were made to ensure that E_U and E_V would not exceed ± 5.0 Volts, which was a

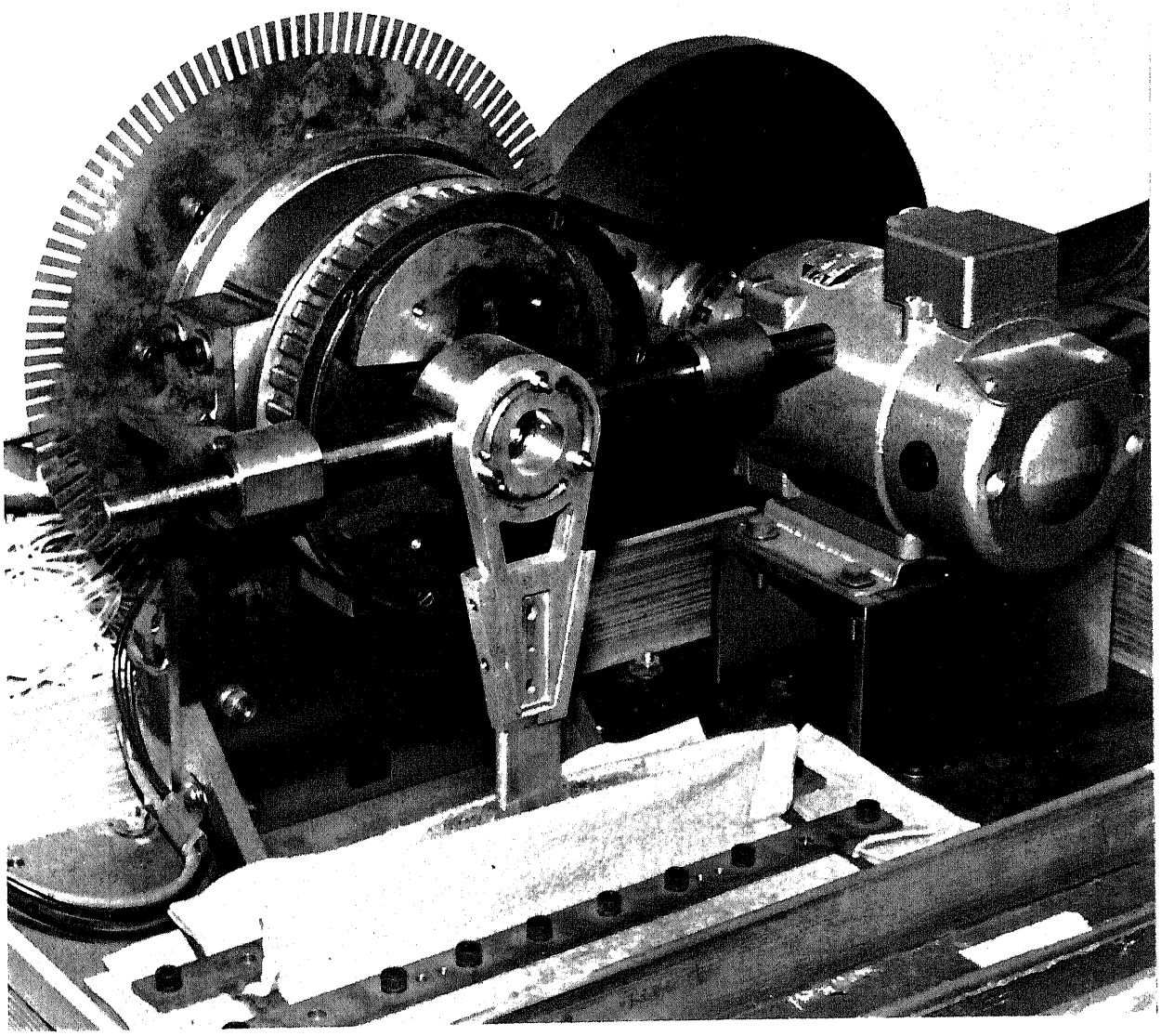

FIGURE 3.3. Dynamic calibrator mounted on wind tunnel.

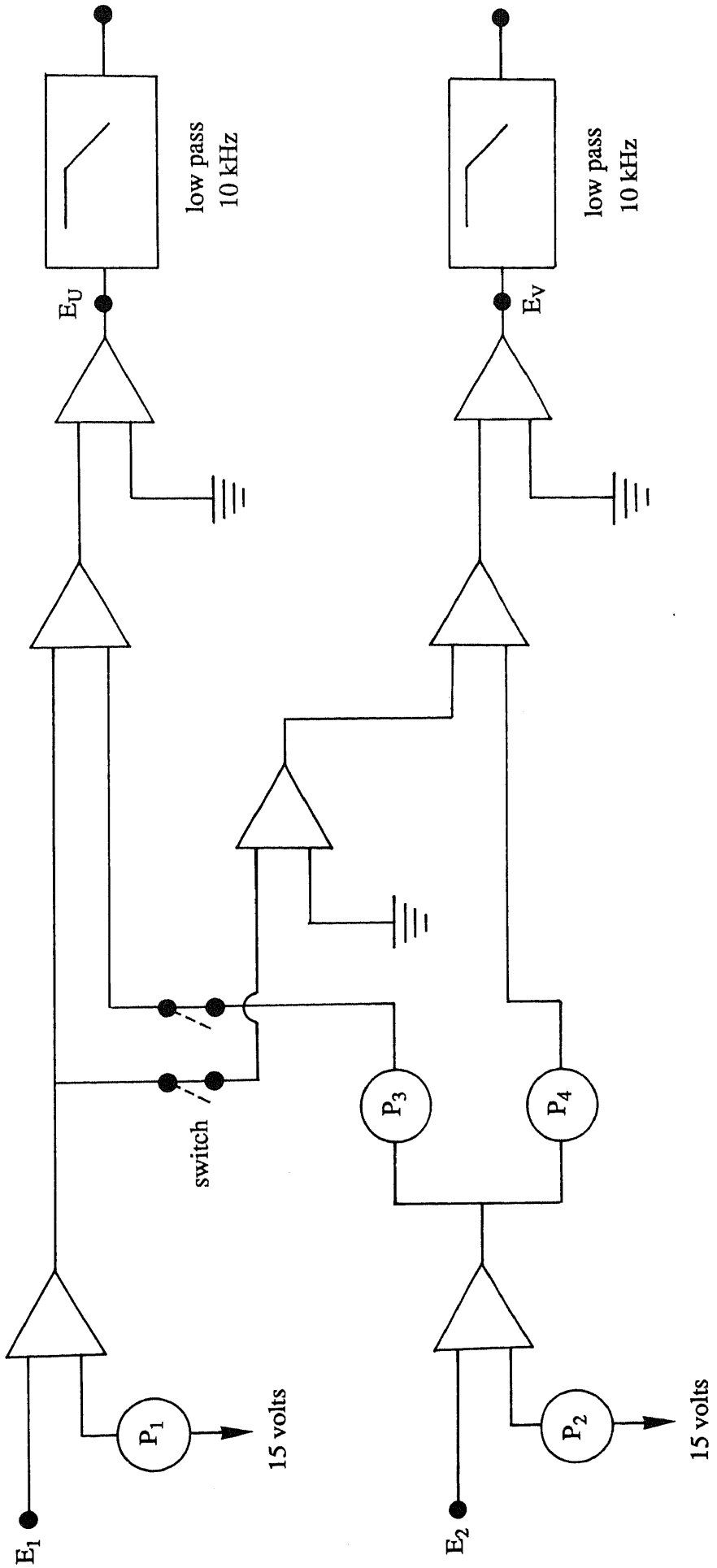

FIGURE 3.4. Hot-wire signal processing circuit.

requirement of the computer, during the subsequent calibration and the sampling of the turbulence profile.

To perform a dynamic calibration, the freestream velocity was set and the hot-wire probe was oscillated in the freestream at 45° to the longitudinal direction. The x-component velocity perturbations given to the probe were small, being less than 10% of the freestream velocity. The analogue voltage signals, E_U and E_V, were low-pass filtered at 30 Hz and then sampled by a PDP 11/10 digital computer using a 12 bit analogue-to-digital convertor and the sampling was controlled by the slotted disc referred to above. Sampling was performed for 50 cycles of the probe oscillation and the sensitivities, $\partial u/\partial E_U$ and $\partial v/\partial E_V$, and mean voltages, E_U and E_V, were determined for the particular freestream velocity, U. The above procedure was repeated for seven other freestream velocities so that the calibration covered the velocity range to be encountered by the hot wires during the subsequent profile measurements.

Perry (1982) has shown that

$$U_i = A_0 + A_1E_U + A_2E_U^2 + A_3E_U^3 + \ldots\ldots \qquad (3.11)$$

and

$$V_i = B_0 + B_2E_U + B_3E_V + B_4E_UE_V + B_5E_U^2E_V + \ldots\ldots \qquad (3.12)$$

where U_i and V_i are the instantaneous velocities at a point in the flow, measured with respect to a fixed coordinate system and the A and B quantities are constants. According to Perry (1982), these equations have been found to be extremely robust. The coefficients in the above two equations were determined by using the measured values of $\partial u/\partial E_U$, $\partial v/\partial E_V$, E_U, E_V and U obtained during the dynamic calibration.

After the coefficients had been determined, the accuracy of the calibration was checked. This was done by comparing the value of U measured with the hot-wire probe with that measured with the Pitot-static probe. The crossed-wire probe was also oscillated in the freestream at 45° to the flow direction and the value of $\overline{uv}$ measured using the hot-wire probe was compared with that calculated using the known stroke of the calibrator and the frequency of oscillation of the hot-wire probe. If the calibration was acceptable, the hot-wire

probe was removed from the calibrator and repositioned in readiness for the profile sampling.

From the above it can be seen that the dynamic calibration technique yields simple relationships between velocity and voltage which take account of the non-linearities of the hot-wire response and do not depend on any particular heat-transfer law.

3.11.3 Data Sampling and Reduction for Profiles

To take a broadband-turbulence profile, the hot-wire voltage signals were low-pass filtered at 10 kHz and sampled as previously and the sampled voltages were stored on magnetic tape for subsequent processing. Sampling was in bursts of 8000 samples and the sampling frequency was 200 Hz. The number of bursts taken for each experimental point was selected to ensure that the resulting turbulence terms would converge to within acceptable limits after the profile had been processed. The number of bursts necessary to achieve this depended upon the location of the point within the boundary layer. For points close to the wall it was necessary to sample six bursts, but this was reduced to four or sometimes three bursts by the time the freestream had been reached. The fact that the data were placed on magnetic tape and not processed on line meant that the number of bursts necessary to achieve acceptable convergence had to be chosen from experience. The main virtue of sampling all of the data of a profile before processing meant that the sampling could be completed quicker and thus the effects of the drifting of the hot wires were minimized.

The reduction programme read the sampled voltages from magnetic tapes and determined the U_i, V_i and W_i quantities by using the appropriate hot-wire calibration (see equations 3.11 and 3.12). The mean velocities, U and V (or W), were then calculated and then the fluctuating components of velocity, u and v (or w) were determined. Various turbulence terms were then calculated from the u, v and w quantities. In theory it was possible to calculate turbulence terms to any degree of complexity required, but in this investigation only terms up to quadruple products were calculated.

3.11.4 Wall Proximity Corrections

The presence of a wall close to a hot-wire filament can cause changes in the rate of heat loss from the wire for a given local velocity. This problem has been examined in detail by Wills (1962), who showed that heat loss depends upon the diameter of a hot wire and its distance from a wall. A check against Will's analysis indicated that it was not necessary to apply any corrections in the current investigation for the presence of a wall.

3.12 Measurement of Spectra

3.12.1 Spacing of Spectra

All spectra within each family were spaced at fixed values of y/δ. The complete range of values of y/δ used were 0.015, 0.02, 0.03, 0.04, 0.06, 0.08, 0.10, 0.15, 0.20, 0.25, 0.35, 0.45, 0.55, 0.70 and 0.85. Since the boundary-layer thickness was variable and also since there was a limit to how close the single-wire and the crossed-wire probes could be taken to the wall (see Section 3.11.1), the lower values of y/δ were not obtainable for most families.

3.12.2 Data Sampling and Reduction for Spectra

The u spectra were measured with an uncalibrated single-wire probe and the v and w spectra with a dynamically matched but uncalibrated crossed-wire probe. The power spectral density of a hot-wire signal was calculated digitally using a fast-Fourier-transform algorithm. The signal was sampled at three different sampling rates to improve the frequency bandwidth of the spectrum at low frequencies and was low-pass filtered at half the digital sampling rate to avoid aliasing of the measured spectrum. The three resulting spectral files were matched and joined to form a single spectral file and the final spectrum covered a frequency range of 0.1 Hz to 10 kHz. To transform the spectral argument from frequency, f_r, to streamwise wavenumber, k_1, Taylor's (1938) hypothesis of frozen turbulence was used, i.e. $k_1 = 2\pi f_r / U_c$, where U_c is the local convection velocity, which was assumed to be equal to the local mean velocity at that point in the flow. In actual fact there is a spread in convection velocities at a given wavenumber and the implications of this will be discussed in Chapter 7, when the spectra are being analysed.

All spectra were smoothed and normalized such that

$$\int_0^\infty \Phi_{11}[k_1]\, dk_1 = \overline{u^2} \tag{3.13}$$

$$\int_0^\infty \Phi_{22}[k_1]\, dk_1 = \overline{v^2} \tag{3.14}$$

$$\int_0^\infty \Phi_{33}[k_1]\, dk_1 = \overline{w^2} \tag{3.15}$$

where Φ_{11}, Φ_{22} and Φ_{33} are power spectral densities per unit streamwise wavenumber, k_1, for velocity fluctuations u, v and w respectively.

The technique described above for measuring and reducing spectra is virtually identical to that used by Perry, Lim & Henbest (1987), the only difference being that for the current investigation, the method of smoothing the spectra was slightly different.

CHAPTER 4

THE ESTABLISHMENT OF ACCEPTABLE LOW-REYNOLDS-NUMBER TURBULENT BOUNDARY LAYERS IN A ZERO PRESSURE GRADIENT

Researchers setting up low-Reynolds-number turbulent boundary layers in a zero pressure gradient for fundamental studies are invariably confronted with the question of whether or not their boundary layer has been stimulated correctly so that they have an acceptable low-Reynolds-number flow. It is generally agreed that for such a flow to be classified as normal, it must follow the $\Delta U/U_\tau$-versus-R_θ characteristic suggested by Coles (1962), which is depicted in figure 2.4. Boundary layers following this characteristic are assumed to be correctly stimulated. As well as this, it is essential that the flow satisfy the momentum integral equation balance. Thus in any fundamental study of flow behaviour at low Reynolds number, it is essential that these conditions be satisfied before proceeding. Only if they are satisfied can any subsequent measurements, such as turbulence measurements, have any credibility attached to them.

In this chapter a technique is proposed for obtaining low-Reynolds-number turbulent boundary layers that show good agreement with Coles $\Delta U/U_\tau$-versus-R_θ characteristic. In addition the concepts of under and overstimulation are discussed and the $\Delta U/U_\tau$-versus-R_θ data resulting from under and over-stimulating the flow are also shown.

4.1 Selection of Types of Tripping Devices

Coles (1962) obtained his $\Delta U/U_\tau$-versus-R_θ characteristic by using the data of many different researchers, who used a variety of tripping devices and velocities, so it appears that numerous combinations of tripping device and

velocity will produce the desired characteristic provided that the tripping device and velocity are matched so that the boundary layer is correctly stimulated.

Three different types of tripping devices, viz. (a) a circular wire, (b) distributed silicon carbide grit of streamwise extent 50 mm and (c) cylindrical pins of diameter 3.0 mm and spacing 9.0 mm, were selected for use in the current investigation. These were chosen since they were representative of the different types of tripping devices commonly used in practice. They are respectively a two-dimensional device, a three-dimensional uniformly distributed device and a three-dimensional linearly distributed device. It is important to note that although the types of devices to be used were chosen at the outset, the actual heights of the devices corresponding to correctly-stimulated flows were initially unspecified.

Although, according to Coles (1962), different types of device produce the same $\Delta U/U_\tau$-versus-R_θ characteristic when matched with an appropriate velocity, the three types of device were used so as to investigate any possible effects of device on other mean-flow characteristics and, more importantly, on turbulence characteristics. The possible effects of the different devices on both the mean-flow and turbulence characteristics when the devices were operating at velocities away from the design value could also be studied.

4.2 Selection of a Nominal Design Reference Velocity

A nominal design reference velocity of 10.0 m/s was chosen for use with the three different types of tripping device since this choice offered a reasonable compromise between the conflicting requirements of having a low velocity for thick boundary layers and a high velocity for large pressure differences. Furthermore, the choice of this velocity meant that it was still possible to use a lower velocity for understimulated flow without this latter velocity being impractically low.

4.3 Determination of Heights of Tripping Devices for Correctly-Stimulated Boundary Layers

For the above three types of tripping devices, it was necessary to determine their actual heights so that the boundary layers were correctly stimulated at the

nominal design reference velocity of 10.0 m/s. It will be recalled from Section 2.7 that published formulae for determining the heights necessary to cause transition to turbulence can only be used as a guide. Consequently, an empirical technique was devised for determining the velocity corresponding to correct stimulation for a device of a given height. However, since the requirement was to determine the stimulator height necessary to produce correct stimulation at the nominal design reference velocity of 10.0 m/s, the stimulator height had to be determined iteratively by using this technique. This point will be dealt with in more detail after the technique has been explained. The reasoning behind the development of the technique is now outlined.

It was seen to be logical that for a given tripping device there must be some particular velocity at which the device produces correctly-stimulated flow. Also, it was realised that the effectiveness of a given device in tripping a flow could be gauged to some extent by an examination of a plot of the associated C_f versus x relationship. Thus it was reasoned that if a given device was subjected to a series of discrete velocities covering the range of say 8.0 to 14.0 m/s, and plots of C_f versus x made for each velocity within the range, then an examination of the entire family of plots may indicate a velocity that will later on, after further testing, be shown to be the velocity that leads to Coles' (1962) characteristic being satisfied by the flow. This line of reasoning was validated by actual measurements.

Figure 4.1 depicts three families of curves of C_f versus x for different nominal velocities for the three different tripping devices and in each case turbulent flow commences just downstream of the peaks of the curves. The parts of the curves that are broken correspond to regions of transition from laminar to turbulent flow. The values of C_f represented by these broken parts are not true values since, along with the rest of the data, they were computed by applying Patel's (1965) calibration to Preston-tube measurements and of course this calibration does not apply in transition regions. When interpreting these curves to select the nominal reference velocity corresponding to correct stimulation, some latitude is allowed for the case of the pins. The curves for the pins display some unusual behaviour and it is shown in Section 5.8 that this behaviour is almost certainly related to the transverse distribution of C_f. Considering all three tripping devices, as the nominal velocity is increased from

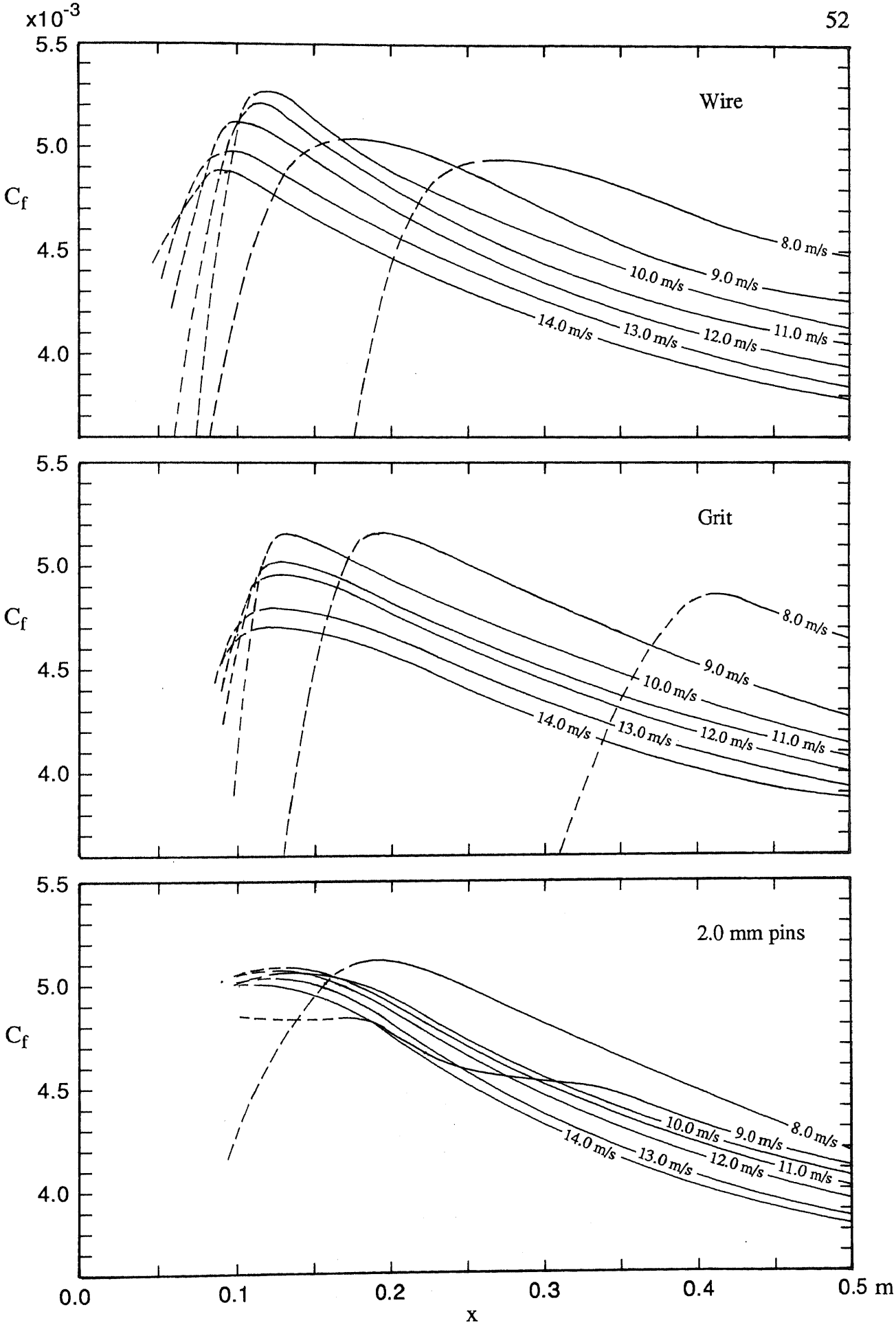

FIGURE 4.1. Families of centreline values of C_f versus x for three tripping devices and for nominal reference velocities varying from 8.0 to 14.0 m/s.

8.0 m/s then the laminar-to-turbulent transition region moves upstream. It is conjectured that correct stimulation is associated with a particular curve when the peaks of successive curves, corresponding to higher nominal velocities, do not advance significantly upstream. Since the velocity corresponding to the particular curve establishes a turbulent boundary layer almost to the possible upstream limit of turbulent flow, it seems reasonable to assume that the main effect of higher velocities will be to overstimulate the flow. Velocities lower than that corresponding to the particular curve are obviously associated with understimulated flows since the peaks of the curves are well downstream of the device and thus the device is therefore not completely effective in tripping the flow. It is apparent from figure 4.1 that, for all three devices, the above condition for correct stimulation is satisfied when the nominal reference velocity is 10.0 m/s. It is a matter of interest that the peaks of the curves of C_f versus x for this velocity for the three devices correspond to the highest, or almost the highest, values of C_f indicated by the families of curves for the three cases. The heights of devices necessary to achieve correct stimulation at a nominal reference velocity of 10.0 m/s were arrived at iteratively as explained in the following.

When using the above technique for determining the nominal velocity corresponding to correct stimulation for the different devices, nominal velocity was a dependent variable and could not be prespecified. Consequently, for the different devices, it was generally necessary to try several different heights before finally arriving at the height corresponding to correct stimulation at a nominal velocity of 10.0 m/s, and some effort was involved in achieving this. It was felt worthwhile to do this for all three devices, however, since this meant that they all would be subjected to the same incident flow and consequently it would be possible to obtain a more meaningful comparison between their stimulating abilities. If all three types of device had been matched with different nominal design reference velocities, then unnecessary complications would have been introduced.

If future researchers wanted to use this method, then it would not in general be necessary for them to go to all this effort since probably they would only use one tripping device and they could judiciously choose its height and

settle for the resultant velocity whose precise value would probably not be all that important.

The heights of the tripping devices determined by the technique for correct stimulation at a nominal reference velocity of 10.0 m/s are given in table 4.1, where the important details of the devices are summarized. The only other details that need be given are that the grit was purchased in the form of a very coarse powder and not a coarse sandpaper and was glued straight onto the metal insert (see Section 3.2). The grit was commercially specified as grade 16.

Table 4.1 Details of Tripping Devices

Wire:	Diameter = 1.2 mm.
Grit::	Height ≈ 1.6 mm (dimension refers to distance from smooth surface to outermost peaks). Streamwise extent = 50 mm.
Pins:	Height = 2.0 mm. Diameter = 3.0 mm. Spacing = 9.0 mm. Pins are of circular cylindrical form.

4.4 Understimulated and Overstimulated Boundary Layers

Before the above empirical technique is verified, the concepts of under and overstimulated boundary layers will first be considered. For this particular study it was assumed that understimulated flow was associated with nominal velocities less than the design value and overstimulated flow with nominal velocities greater than the design value. The selection of the actual discrete nominal velocities used in these experiments for the under and overstimulated flows was based on the C_f versus x distributions shown in figure 4.1. When choosing these velocities it was necessary that two conditions were simultaneously satisfied for all devices. Firstly the C_f-versus-x curves corresponding to the under and overstimulation velocities had to have acceptable shapes and secondly the locations of the maximum values of C_f on these curves,

and thus the locations of the commencement of the fully turbulent boundary layers, had to be within acceptable distances from the tripping devices.

An analysis of the curve for a nominal velocity of 9.0 m/s for the cylindrical pins tripping device indicated that this nominal velocity was obviously unsuitable for the understimulated flows since it did not satisfy the first condition. A nominal velocity of 8.0 m/s was seen to satisfy both conditions for all devices, although the agreement with the second condition for the wire and grit tripping devices was only tolerably acceptable, and consequently this nominal velocity was chosen for the understimulated flows. Any nominal velocity above the design reference velocity of 10.0 m/s could have been chosen for the overstimulated flows since both conditions were always simultaneously satisfied for all three devices. A nominal velocity of 14.0 m/s was actually chosen since this nominal velocity was the maximum used in the range and consequently gave the greatest amount of overstimulation.

4.5 Verification of Technique

To verify the above technique it was necessary to check that the tripping devices produced acceptable low-Reynolds-number flows when subjected to a nominal design reference velocity of 10.0 m/s. This basically involved checking that data followed Coles' (1962) curve and that the momentum balances were within acceptable limits. Coles (1962) did not go as far as saying that for a low-Reynolds-number flow to be normal it must follow his mean $\Delta U/U_\tau$-versus-R_θ line precisely, but instead he classified data having some degree of scatter about this line as normal. It therefore seemed reasonable to assume that a flow had an acceptable $\Delta U/U_\tau$-versus-R_θ characteristic provided it fell within the general scatter of Coles' data. The $\Delta U/U_\tau$-versus-R_θ characteristics for the three design flows are shown in figure 4.2 and when this data are compared with Coles' data shown in figure 2.4, then it can be seen that the current data are acceptable, at least as far as their $\Delta U/U_\tau$-versus-R_θ characteristics are concerned. The corresponding balances of momentum were determined by using the second of the two alternative techniques outlined in Section 3.9 and were found to be acceptable, as will be shown in figure 4.4, where the balances for the design flows are presented together with the balances for the under and overstimulated flows. The second technique of computing the balance was used in preference

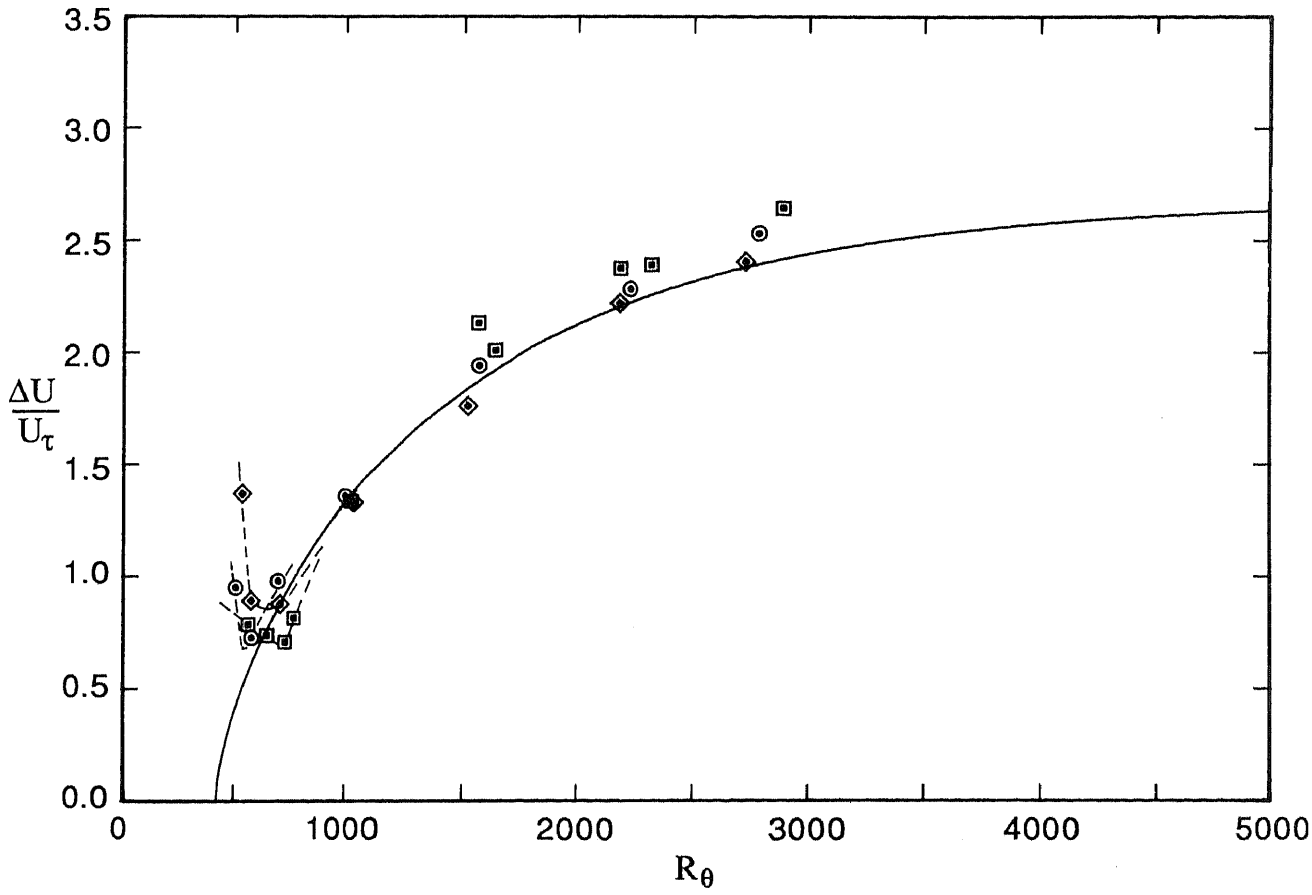

FIGURE 4.2. Variation of $\Delta U/U_\tau$ with R_θ.
———, Coles' (1962) curve.
Data of current investigation for design flows;
⊙, wire; ◈, grit; ⊡, 2.0 mm pins.

to the first technique because of difficulties of accurately curve fitting data using the first method. Throughout this chapter, the method of determining U_τ and $\Delta U/U_\tau$ for the current data was exactly the same as that used by Coles (1962).

Even though the above checks showed that the flows were acceptable at the nominal design reference velocity of 10.0 m/s, it was still necessary to determine whether or not the under and overstimulated flows showed similar agreement with Coles' characteristic and had acceptable balances of momentum, since if this were the case there probably would not have been any point in using the technique because most likely a whole range of velocities could have been used to obtain acceptable flows. The $\Delta U/U_\tau$-versus-R_θ plots for the three tripping devices for understimulated, correctly-stimulated and overstimulated flows are shown in figure 4.3 where they are compared with Coles' characteristic. The reasoning behind the selection of symbols used in this figure, as well as other figures throughout this thesis, is given in Section 4.6. An analysis of figure 4.3 indicates that in all cases the under and overstimulated $\Delta U/U_\tau$-versus-R_θ data differ noticeably from the design data and clearly do not fit Coles' characteristic as well as the design data. The balances of momentum for these nine flows calculated using the second of the two alternative techniques outlined in Section 3.9, are shown in figure 4.4 where they can be seen to be acceptable. Even for the worst case, which is for the grit for correctly-stimulated flow, the imbalance in the momentum equation at the last measuring station is only about 8%, which is within the bounds of acceptability.

The above strongly suggests that the empirical technique is in fact valid, at least for the limited amount of data presented here, but as further confirmation, the current data were compared with other low-Reynolds-number flow characteristics published by Coles (1962) to check on possible differences between the current data and these characteristics.

Figure 4.5 shows the current data for each of the devices compared with Coles' C_f-versus-C_fR_θ characteristic. The data for the nine flow cases agree well with Coles' characteristic at the higher values of R_θ, but show some scatter at the lower values of R_θ, thus indicating that the degree of stimulation has more effect on the plotted data at low values of R_θ than at high values of R_θ, as was

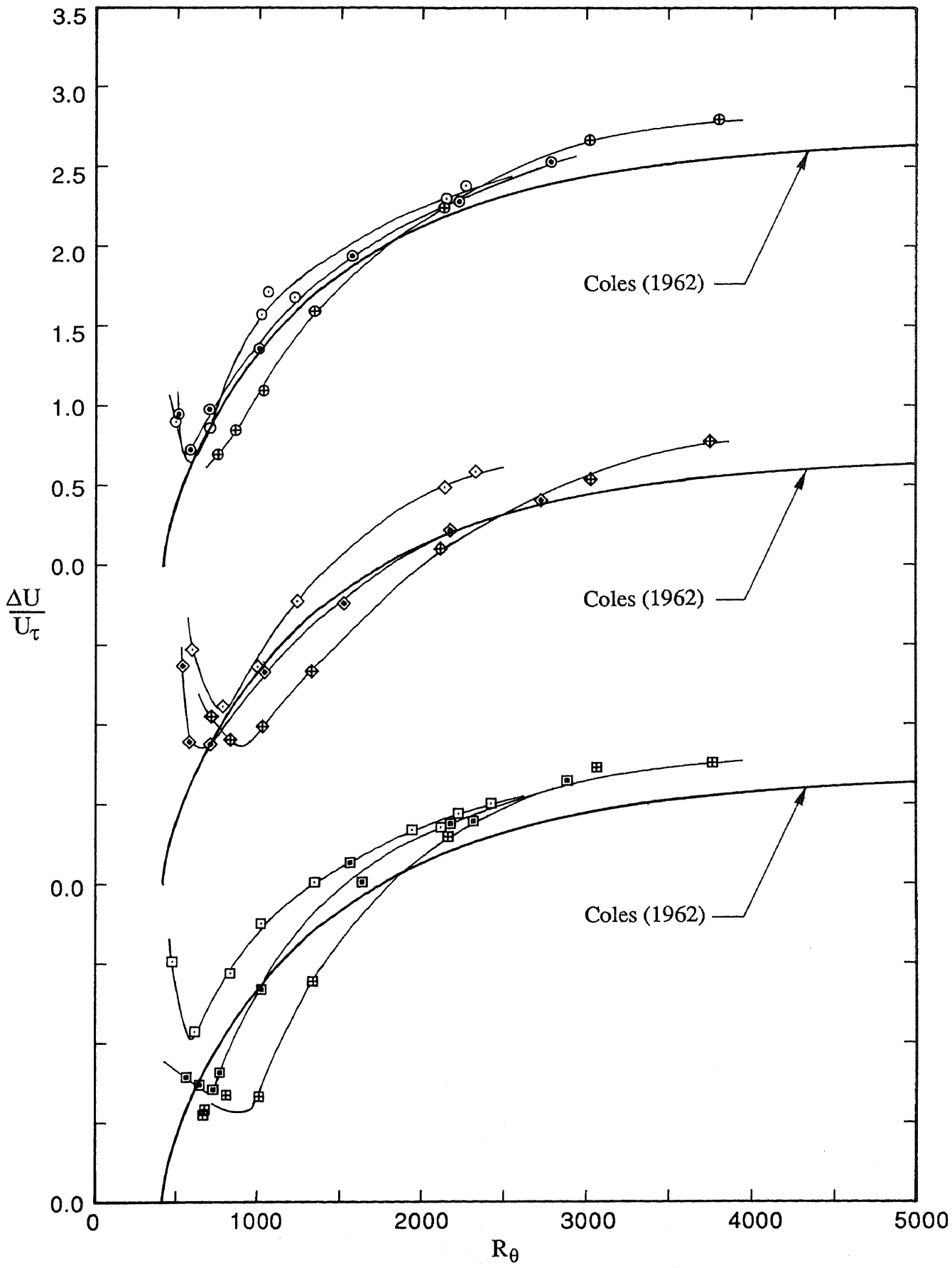

FIGURE 4.3. Variation of $\Delta U/U_\tau$ with R_θ. Note shift in ordinate. Velocities given below are nominal values.

Wire:	⊙, 8.0 m/s;	⊙, 10.0 m/s;	⊕, 14.0 m/s.
Grit:	◇, 8.0 m/s;	◈, 10.0 m/s;	⊕, 14.0 m/s.
2.0 mm pins:	⊡, 8.0 m/s;	⊞, 10.0 m/s;	⊞, 14.0 m/s.

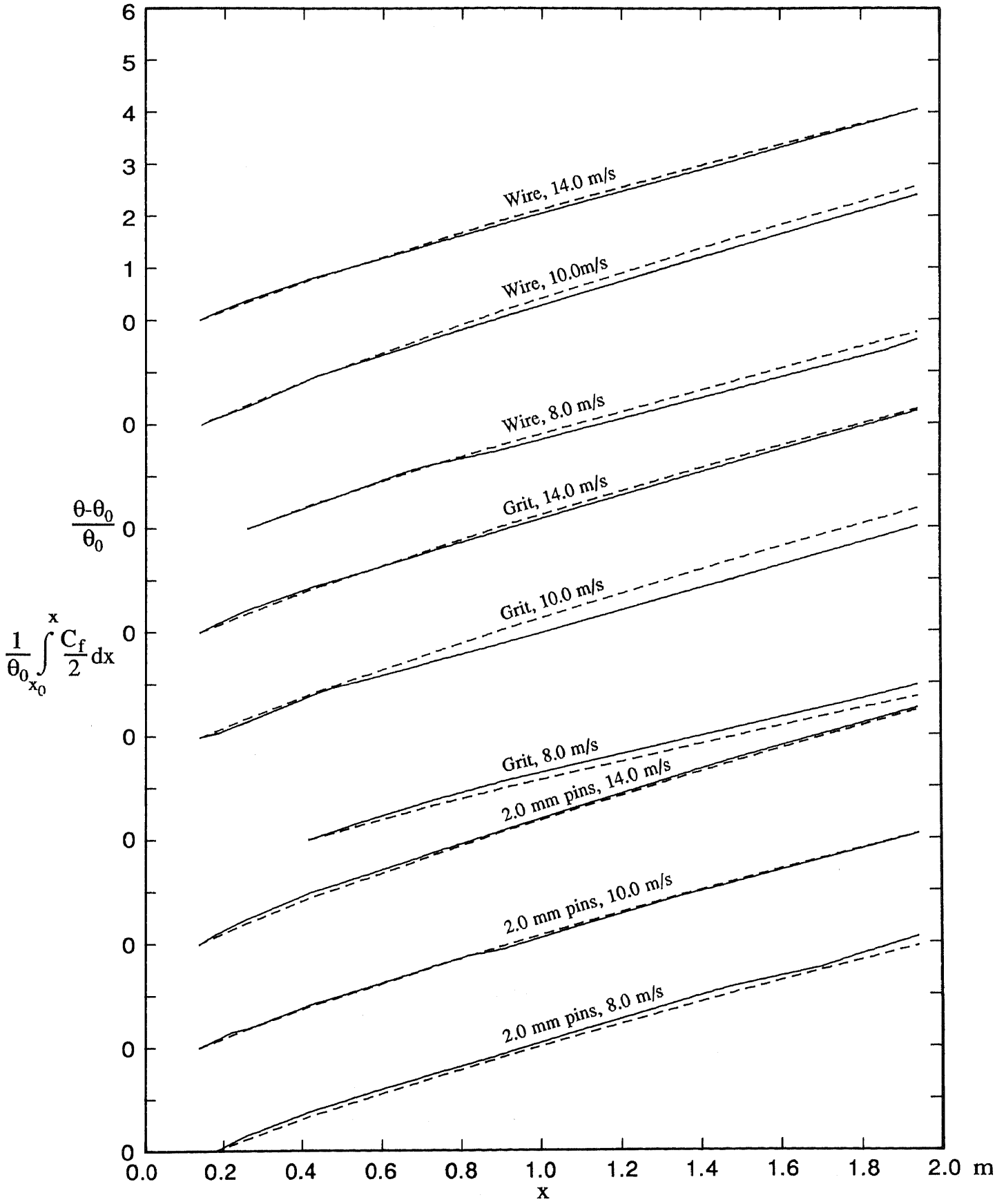

FIGURE 4.4. Balances of momentum. Note shift in ordinate.

——, $(\theta-\theta_0)/\theta_0$; – – –, $(1/\theta_0)\int(C_f/2)dx$.

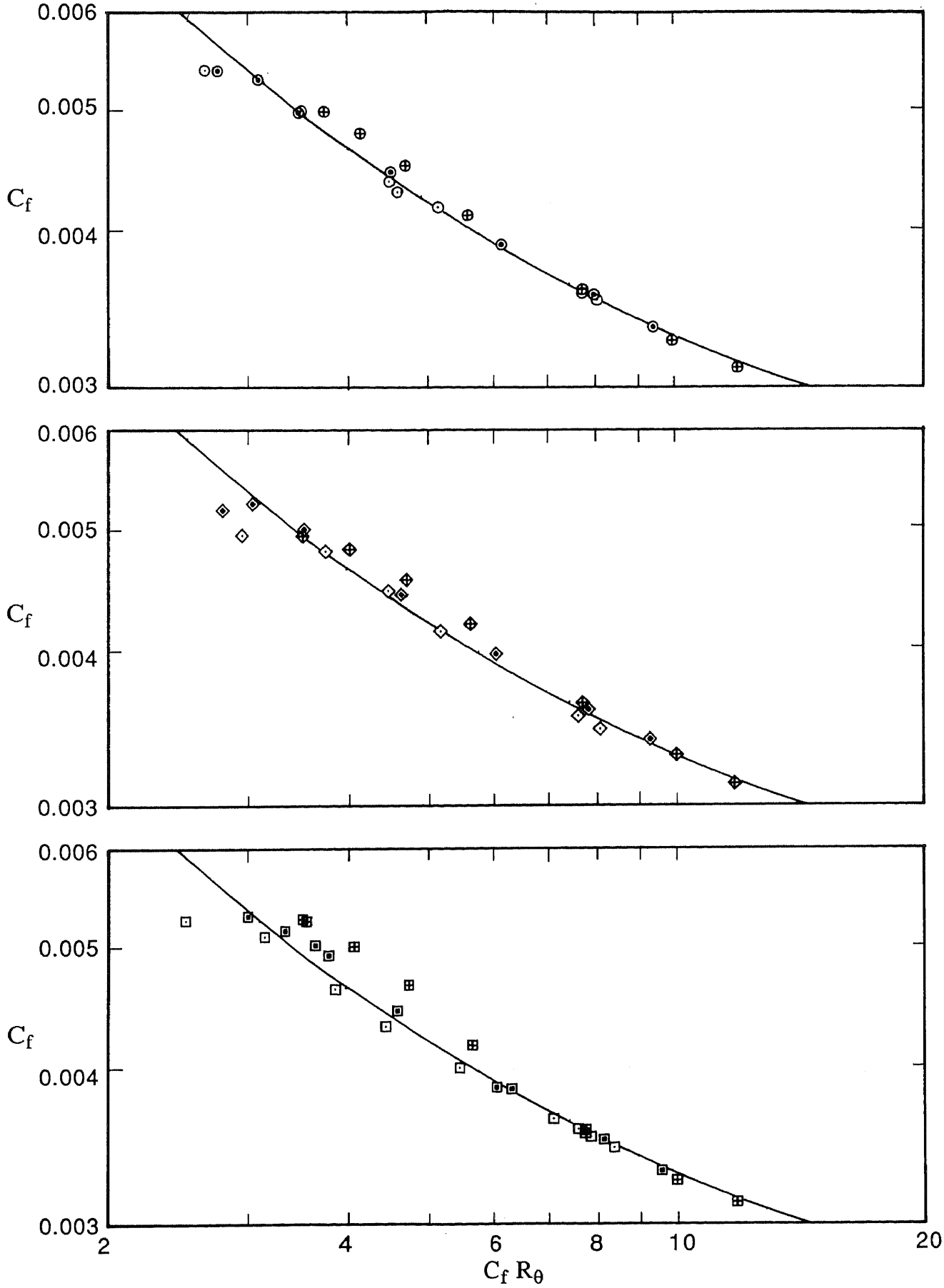

FIGURE 4.5. C_f versus $C_f R_\theta$. Velocities given below are nominal values.
———, Coles' (1962) curve.

Wire:	⊙, 8.0 m/s;	⊙, 10.0 m/s;	⊕, 14.0 m/s.
Grit:	◇, 8.0 m/s;	◈, 10.0 m/s;	◈, 14.0 m/s.
2.0 mm pins:	⊡, 8.0 m/s;	⊡, 10.0 m/s;	⊞, 14.0 m/s.

the case for the $\Delta U/U_\tau$-versus-R_θ data shown in figure 4.3. For these lower values of R_θ, the design flows generally show good agreement with Coles' characteristic, except perhaps for the pins where some discrepancies do occur. In this R_θ range, the data for the design flows clearly exhibit a better overall agreement with Coles' characteristic than do the data for the corresponding overstimulated flows and the overall agreement with Coles' characteristic for the design flows is about the same as for the understimulated flows. At the lowest values of R_θ, data points often deviate noticeably below Coles' characteristic and a close examination of these data points indicates that they correspond to the data points of figure 4.3 that show sharp rises in the values of $\Delta U/U_\tau$ on the $\Delta U/U_\tau$-versus-R_θ characteristics.

The values of shape factor, H, for each of the devices are shown plotted against R_θ in figure 4.6 where they are compared against the characteristic given by Coles (1962). It is apparent from this figure that for all three devices, the degree of stimulation has more effect on the value of H at low values of R_θ than it does at high values of R_θ, which is consistent with earlier trends. Also, a close examination of figure 4.6 indicates that for the three devices, the data for the design flows agree with Coles' curve better than do the data for the understimulated and overstimulated flows, except perhaps for the wire, where the design flows and the understimulated flows show about the same agreement with Coles' curve. Thus different amounts of stimulation, but for a given value of R_θ, can affect the shapes of the profiles. Although none of the data show a large variation from Coles' curve, as can be gauged from the tolerance bands included on figure 4.6, the design flows nevertheless give the best overall agreement with Coles' curve.

The values of the Clauser parameter, G, for each of the devices are shown plotted against R_θ in figure 4.7. An analysis of this figure leads to essentially the same conclusions as for the plots of H versus R_θ. In a similar manner, the degree of stimulation has more effect on the value of G at low values of R_θ than it does at high values of R_θ. For all three devices, the design-flow data show better agreement with Coles' curve than do the under- and overstimulated-flow data. At the lowest values of R_θ, the values of G rise noticeably in a number of cases and as discussed above for the C_f-versus-C_fR_θ plots, these data points can be matched to the data points displaying unusual behaviour on the $\Delta U/U_\tau$-

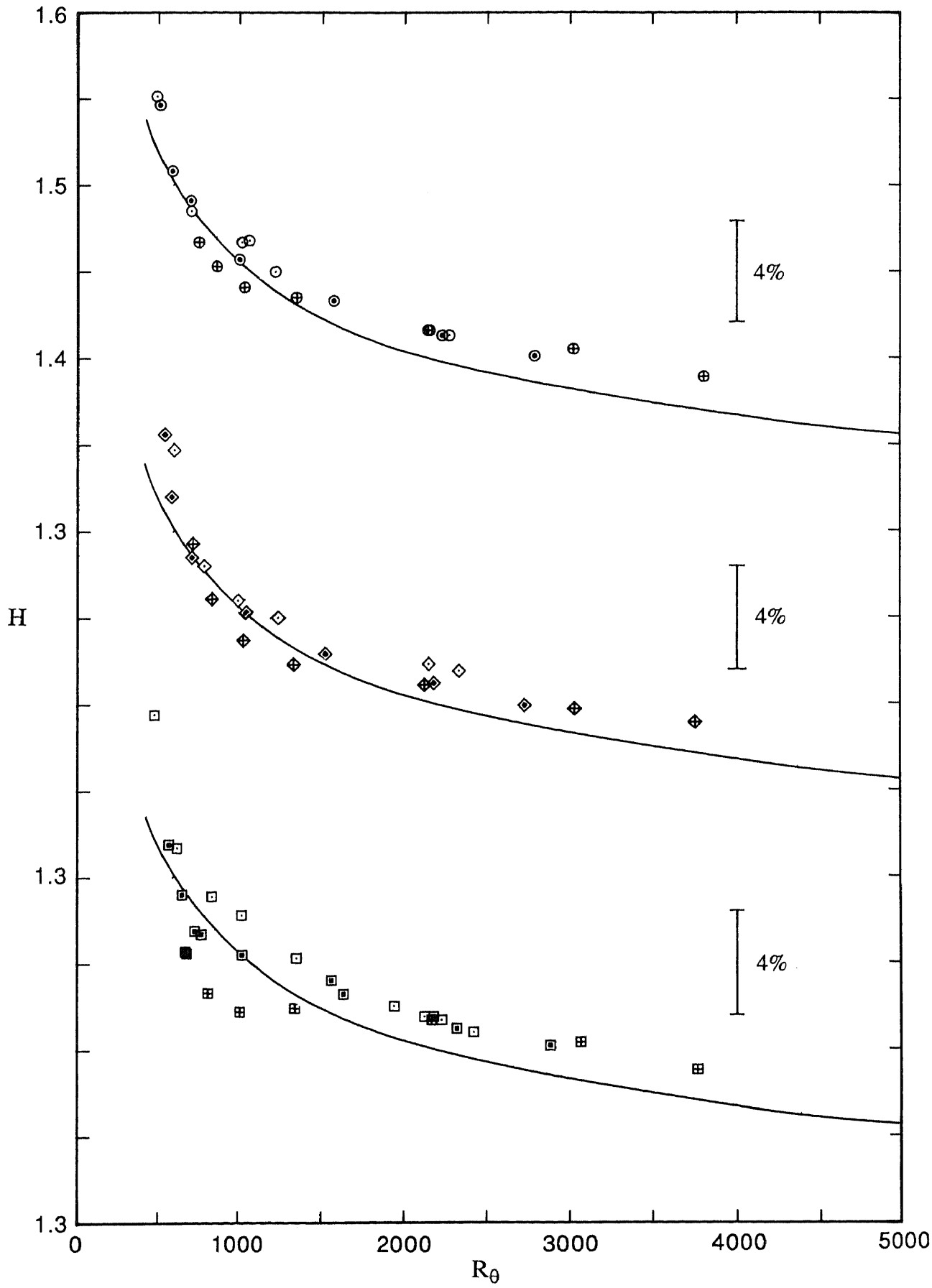

FIGURE 4.6. Variation of H with R_θ. Note shift in ordinate. Velocities given below are nominal values.

———, Coles' (1962) curve.

Wire:	⊙, 8.0 m/s;	⊙, 10.0 m/s;	⊕, 14.0 m/s.
Grit:	◇, 8.0 m/s;	◈, 10.0 m/s;	✥, 14.0 m/s.
2.0 mm pins:	⊡, 8.0 m/s;	▣, 10.0 m/s;	⊞, 14.0 m/s.

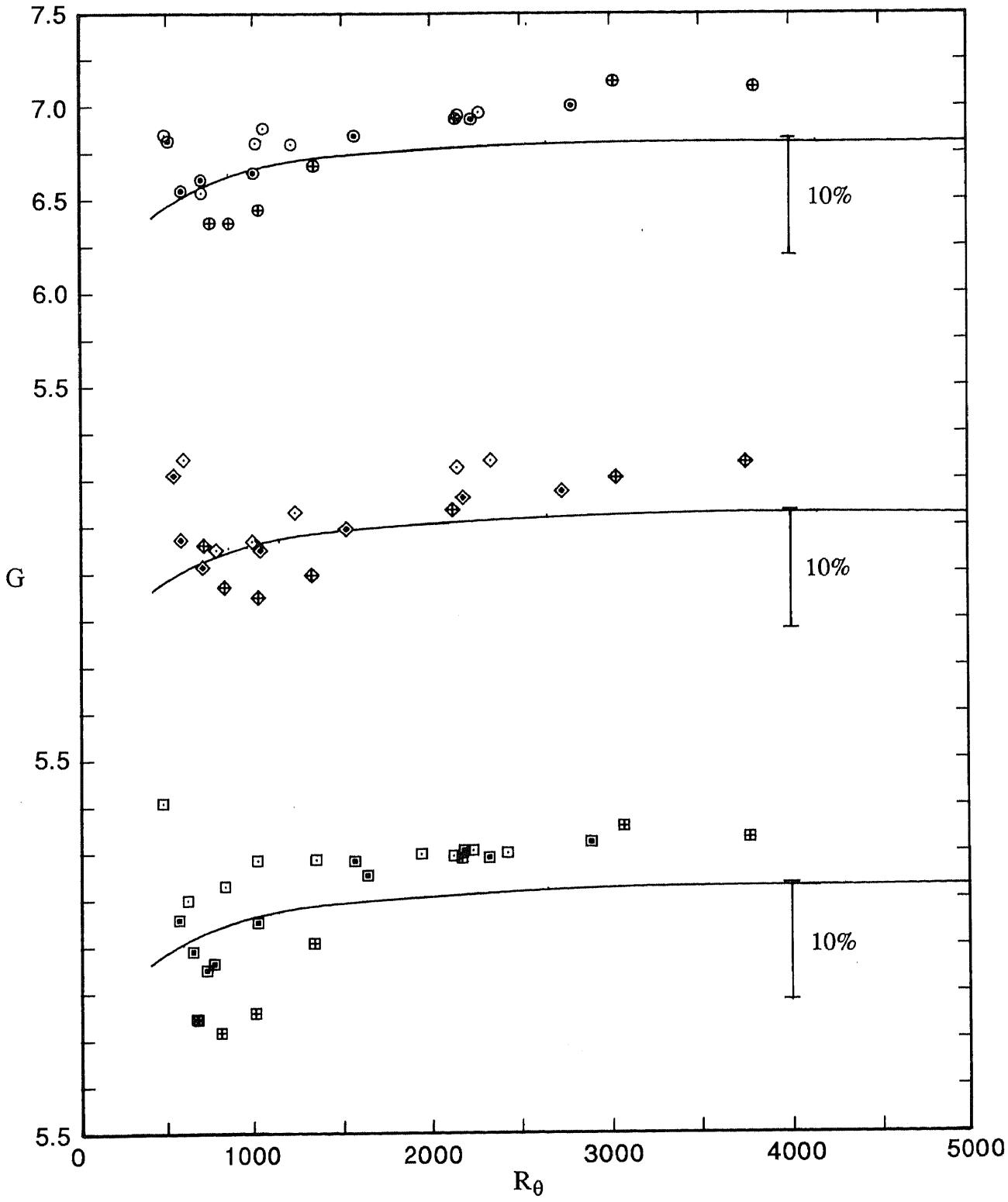

FIGURE 4.7. Variation of G with R_θ. Note shift in ordinate. Velocities given below are nominal values.

———, Coles' (1962) curve.

Wire: ⊙, 8.0 m/s; ⊙, 10.0 m/s; ⊕, 14.0 m/s.
Grit: ◇, 8.0 m/s; ◈, 10.0 m/s; ◈, 14.0 m/s.
2.0 mm pins: ⊡, 8.0 m/s; ⊞, 10.0 m/s; ⊞, 14.0 m/s.

versus-R_θ plots shown in figure 4.3. This behaviour seems to be present in the H versus R_θ data shown in figure 4.6, but the fact that H is expected to rise sharply for low values of R_θ tends to mask any such behaviour. Tolerance bands are shown on figure 4.7 to help gauge the agreement of the current data with Coles' curve. In percentage terms, there is more spread in the data for G than for H, but this is not surprising since G and H are related by $G = \sqrt{(2/C_f)}\,(H-1)/H$.

From the above it can be seen that the current data for C_f versus C_fR_θ, H versus R_θ and G versus R_θ further supports the validity of the empirical technique described earlier for obtaining correctly-stimulated boundary layers.

Since the above design flows had acceptable low-Reynolds-number characteristics and satisfied momentum balance requirements they were used for further mean-flow and turbulence measurements. Additional mean-flow and turbulence measurements were also taken using the off-design flows to study the effects on the flow of under and overstimulation.

4.6 Selection of Symbols

Before completing this chapter, the reasoning behind the selection of symbols used when plotting data will be discussed. Throughout this thesis the symbols used are of three different types, each type having a distinctive extremity but a variable inner portion. The three types of extremities have been chosen so that they resemble the side view, roughly speaking, of the device that they represent. Thus circles (○) have been chosen for data associated with the wire, diamonds (◇) for the grit and squares (□) for the cylindrical pins. The inner portions of the symbols have variable forms, such as a plus or a small dot, generally to indicate either changing degrees of stimulation for a given device or else changing values of R_θ for a given device. Such a system will facilitate the interpretation of data and will hopefully reduce the need to continually refer to figure captions.

CHAPTER 5

ANALYSIS OF MEAN-FLOW RESULTS

An extensive set of mean-flow measurements were taken for nine different flows, which were obtained by using three different tripping devices at each of three different nominal reference velocities, viz. 8.0 m/s (understimulated flows), 10.0 m/s (correctly-stimulated or design flows) and 14.0 m/s (overstimulated flows). The details of the devices and the concepts of the different amounts of stimulation are given in the previous chapter.

Mean-flow profiles were systematically taken so that the effects on the mean-flow characteristics of R_θ, tripping device and amount of stimulation, each considered separately, could be determined when the results were plotted using some common types of scaling.

Some of the mean-flow characteristics, viz. C_f versus x, $\Delta U/U_\tau$ versus R_θ, balances of momentum, C_f versus C_fR_θ, H versus R_θ and G versus R_θ have, by necessity, already been presented in the previous chapter. These will be discussed still further where necessary and other aspects of the mean flow will also be considered.

5.1 Nominal Zero Pressure Gradients

All of the measurements reported in the thesis were taken in nominally constant pressure flows. The moveable wall on the wind tunnel was not altered once it had been set which meant that although the pressure distributions for each of the above nine flows were nominally constant, they did change slightly from flow to flow due to the different tripping devices and velocities in the different cases. The variations were, however, only minor, and the variation in U_e for any given flow was typically about 1.3%.

5.2 $\Delta U/U_\tau$-versus-R_θ Relationships

The $\Delta U/U_\tau$-versus-R_θ plots for the nine flows are shown in figure 4.3 where they are compared with Coles' (1962) characteristic. These plots have been briefly discussed in Section 4.5 when verifying an empirical technique for obtaining correctly-stimulated boundary layers. They will now be discussed in more detail.

It is clearly apparent from these plots that for the three tripping devices, the degree of stimulation often has a noticeable effect on the $\Delta U/U_\tau$-versus-R_θ characteristic. At the nominal design reference velocity, however, all three devices have approximately the same characteristic and these show good agreement with the characteristic proposed by Coles (see also figure 4.2). For each tripping device, the three $\Delta U/U_\tau$-versus-R_θ characteristics associated with nominal reference velocities of 8.0, 10.0 and 14.0 m/s often differ noticeably at the lower values of R_θ, but there is a general tendency for the three characteristics for each device to merge together by about R_θ = 2500 to 3000. For a change in the nominal reference velocity from 8.0 to 14.0 m/s for all devices, the amount of variation in the characteristics is greatest for the pins. Thus on the basis of the $\Delta U/U_\tau$-versus-R_θ characteristics, the wire and distributed grit are less sensitive to changes in the reference velocity than the pins, but it must be pointed out that the opposite trend applies when the devices are compared on the basis of their C_f-versus-x distributions (see figure 4.1).

An interesting feature of most of the $\Delta U/U_\tau$-versus-R_θ characteristics shown in figure 4.3 is their unusual behaviour at their left hand extremities where they turn around and have the opposite trend to Coles' characteristic. This phenomenon has also been noticed by Purtell, Klebanoff & Buckley (1981), who indicated that the behaviour is due to underdevelopment of the flow (see figure 2.6). A careful examination of the data used by Coles to establish his characteristic (see figure 2.4) indicates that, in three cases at least, this trend may be just starting to develop, but not enough data have been plotted to be sure of this. All of the plotted points on figure 4.3 in the regions of the reversals of the characteristics were computed for boundary layers that had become turbulent, as verified by the skin-friction measurements shown in figure 4.1, and also the fact that linear regions existed on the mean velocity profiles, as

will be shown in Section 5.4 for the wire and the grit, so therefore the flows in this region are definitely low-Reynolds-number turbulent boundary-layer flows and are thus worthy of being studied for turbulence behaviour.

5.3 Constant Values of R_θ for Comparison Between Different Flows

In order that the mean-flow characteristics of any of the above nine flows could be systematically compared with each other, it was essential that mean-flow profiles were taken in each flow for the value of R_θ at which the comparison was to be made. Since the value of R_θ was not accurately known until after a profile had actually been taken, the requirement could only be satisfied by taking more profiles than the minimum number required for the comparison. Practical limitations meant that some tolerance be allowed on the values of R_θ in the flows being compared. Mean-flow profiles corresponding to five different ranges of values of R_θ were taken and the tolerance bands for the five ranges of values of R_θ are shown to scale on a plot of $\Delta U/U_\tau$ versus R_θ in figure 5.1, where all of the data of figure 4.3 have been replotted on one set of axes. Profiles taken to correspond to one of these five groups, but which were not ultimately selected for use in a group, do not have their details given in this thesis. There are twenty seven mean-flow profiles represented within these five groups and details of these are given for convenience in table 5.1. As can be seen, the mid point values of R_θ for groups 1 to 5 are respectively 713, 1020, 1544, 2175 and 2810. For the three design flows, mean-flow profiles were associated with each of these five nominal values of R_θ, while for the three understimulated and the three overstimulated flows, mean-flow profiles were associated with nominal values of R_θ of 1020 and 2175.

Also shown in table 5.1 are details of mean-flow profiles having $R_\theta = 509$ and $R_\theta = 537$. These profiles which are associated with correctly-stimulated flow using the wire and grit respectively as tripping devices, were the most upstream taken for these flow conditions. As can be seen from figure 4.3, the associated $\Delta U/U_\tau$-versus-R_θ data points display unusual behaviour (see Section 5.2). A profile for the pins was not grouped with these two profiles since only a limited range of measurements were taken in the regions of unusual behaviour.

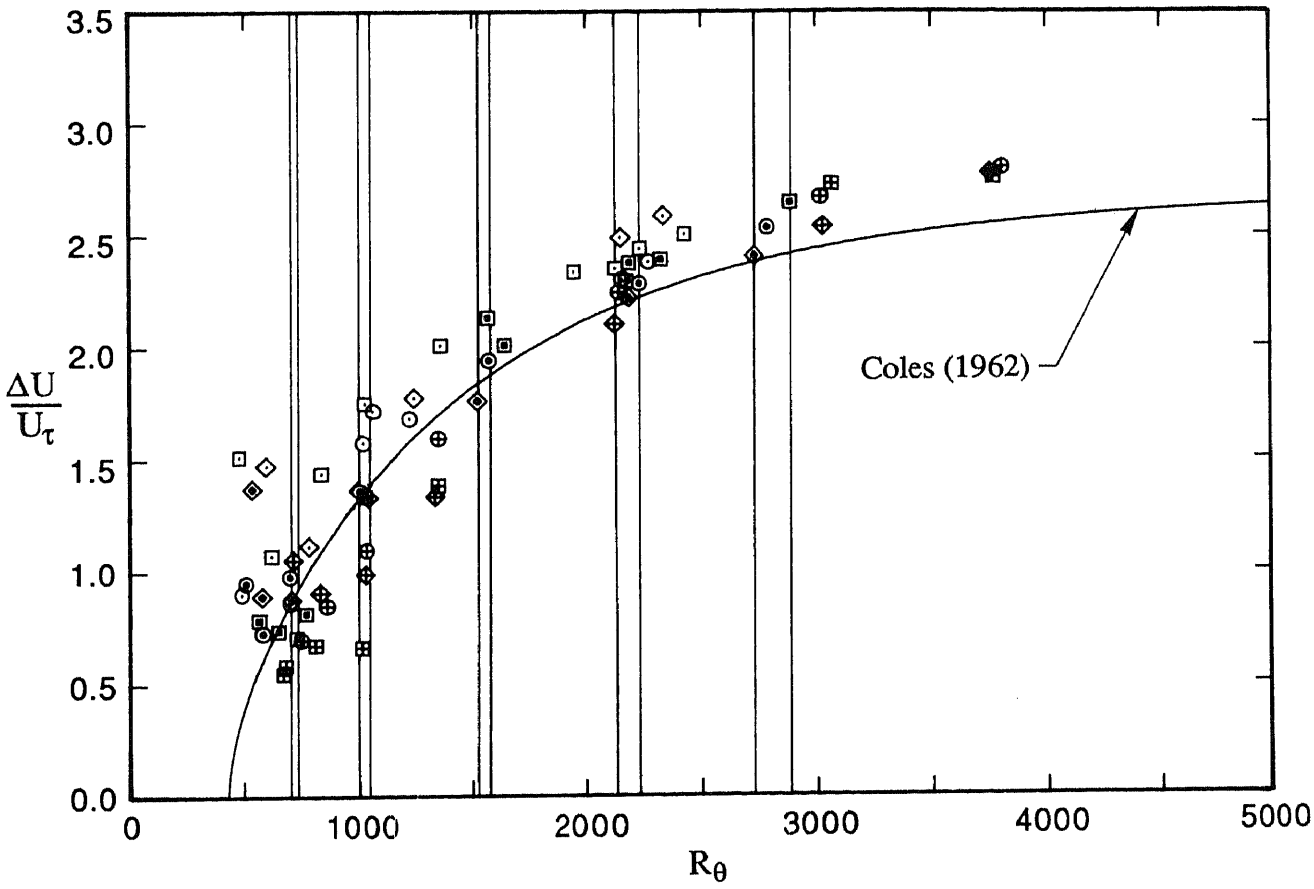

FIGURE 5.1. Variation of $\Delta U/U_\tau$ with R_θ. Tolerance bands, which are used when comparing different flows, are shown for five different ranges of values of R_θ. Velocities given below are nominal values.

Wire:	⊙, 8.0 m/s;	⊛, 10.0 m/s;	⊕, 14.0 m/s.
Grit:	◇, 8.0 m/s;	◈, 10.0 m/s;	⧫, 14.0 m/s.
2.0 mm pins:	⊡, 8.0 m/s;	▣, 10.0 m/s;	⊞, 14.0 m/s.

Table 5.1. Details of Mean Flow Profiles, Broadband Turbulence Profiles and Spectra.

Group	R_θ From Mean Flow Profiles	Nominal Reference Velocity m/s	Tripping Device	x m	Broadband Turbulence Profiles	Spectral Measurements
	509	10.0	1.2 mm wire	0.140	u	
	537	10.0	Grit	0.140		
	697	10.0	1.2 mm wire	0.260	u uv uw	u v w
1	706	10.0	Grit	0.260	u uv uw	u v w
	729	10.0	2.0 mm pins	0.220	u uv uw	u v w
	Mid pt.=713					
	Var'n=±2.2%					
	1017	8.0	1.2 mm wire	0.660	u	u
	997	8.0	Grit	0.700	u	u
	1024	8.0	2.0 mm pins	0.580	u	u
	1003	10.0	1.2 mm wire	0.440	u uv uw	u v w
2	1042	10.0	Grit	0.460	u uv uw	u v w
	1027	10.0	2.0 mm pins	0.420	u uv uw	u v w
	1033	14.0	1.2 mm wire	0.260	u	u
	1029	14.0	Grit	0.260	u	u
	1013	14.0	2.0 mm pins	0.260	u	u
	Mid pt.=1020					
	Var'n=±2.2%					
	1568	10.0	1.2 mm wire	0.900	u uv uw	u v w
3	1520	10.0	Grit	0.900	u uv uw	u v w
	1565	10.0	2.0 mm pins	0.820	u uv uw	u v w
	Mid pt.=1544					
	Var'n=±1.6%					
	2151	8.0	1.2 mm wire	1.860	u	u
	2146	8.0	Grit	1.780	u	u
	2230	8.0	2.0 mm pins	1.780	u	u
	2226	10.0	1.2 mm wire	1.460	u uv uw	u v w
4	2178	10.0	Grit	1.460	u uv uw	u v w
	2181	10.0	2.0 mm pins	1.340	u uv uw	u v w
	2137	14.0	1.2 mm wire	0.900	u	u
	2119	14.0	Grit	0.900	u	u
	2169	14.0	2.0 mm pins	0.900	u	u
	Mid pt.=2175					
	Var'n=±2.6%					
	2788	10.0	1.2 mm wire	1.940	u uv uw	u v w
5	2730	10.0	Grit	1.940	u uv uw	u v w
	2889	10.0	2.0 mm pins	1.940	u uv uw	u v w
	Mid pt.=2810					
	Var'n=±2.8%					

The mean-flow experimental programme summarized in table 5.1 formed the basis of the broadband-turbulence and spectral experimental programmes. For convenience, details of the turbulence measurements presented in this thesis are also given in table 5.1. Considering only the measurements within the five groups, u broadband-turbulence profiles and u spectra were taken for each of the twenty seven cases but uv and uw broadband-turbulence profiles and v and w spectra were limited to the three design flows.

By appropriately selecting the profiles given in table 5.1, it was possible to compare the different flows in such a manner that the effects of R_θ, tripping device and different amounts of stimulation, each considered independently, could be determined. Considering the three profiles for correctly-stimulated flows within any of the five groups, all such profiles within each group have the same degree of stimulation and approximately the same value of R_θ, thus eliminating degree of stimulation and R_θ as variables, so therefore the only difference between such flows within each group is the tripping device. Thus if such flows within any of the groups are compared, the effects of tripping device on the flow for correctly-stimulated flows at the given value of R_θ will be indicated. In a similar manner, considering profiles for a given device and correctly-stimulated flows from any of the five groups, it is possible to compare profiles to indicate the effects of R_θ on the flows for a particular device for correctly-stimulated flows. Likewise, considering profiles for the understimulated, correctly-stimulated and overstimulated flows for a particular device from either group 2 or group 4, it is possible to compare profiles to indicate the effects that different amounts of stimulation have on the flow for a particular device at each of two values of R_θ. The above comparisons are the main ones of interest but it is possible to make additional comparisons if desired. Considering all profiles in groups 2 or 4, the profiles within each group all have different combinations of tripping device and amount of stimulation, but have approximately the same value of R_θ, so therefore it is possible to compare profiles to indicate the complete range of variation of the flows at each of two values of R_θ.

5.4 Velocity Profiles for Correctly-Stimulated Flows

Mean-flow velocity profiles for the wire of diameter 1.2 mm for the design flow and for different values of R_θ are shown plotted in figure 5.2 using the familiar U/U_τ-versus-$\log(yU_\tau/\nu)$ coordinates. Corresponding plots for the grit grade 16 and the pins of height 2.0 mm are shown in figures 5.3 and 5.4 respectively. The logarithmic-law constants used for these three plots are $\kappa = 0.41$ and $C = 5.2$.

When each of these design-flow profiles are presented on their own set of axes such as they are in figures 5.2 to 5.4, it is not readily apparent how variations in both R_θ and device affect the profiles. To assess the effects on the profiles of variation in R_θ for each of the three devices, it is necessary to superimpose all profiles for a given device on a single set of axes as has been done in figure 5.5 for each of the devices. Likewise, to assess the effects on the profiles of variations of device at each of the five nominal values of R_θ, it is necessary to superimpose all profiles associated with a given nominal value of R_θ on a single set of axes as has been done in figure 5.6 for each of the five nominal values of R_θ. This plotting procedure for design flows will be used on many occasions when presenting data in this thesis.

An analysis of figure 5.5 indicates that for each of the three devices, the data in the wall region collapse, but the data in the outer region depend strongly on the value of R_θ. The behaviour of these profiles is completely as expected for low-Reynolds-number flows.

An analysis of figure 5.6 indicates that for the five nominal values of R_θ, the type of device used has only a very minor effect upon the profiles when they are plotted using these coordinates. The maximum differences between the three profiles in each group, expressed as a percentage difference between maximum and minimum values of U/U_τ in the freestream for profiles within that group, are 1.1%, 0.4%, 1.3%, 0.6% and 1.1% for nominal values of R_θ of 713, 1020, 1544, 2175 and 2810 respectively. The good agreement between corresponding profiles is not completely unexpected, since the associated design-flow $\Delta U/U_\tau$-versus-R_θ characteristics shown in figures 4.2 and 4.3 agree very well. It must be pointed out, however, that the data plotted in figures 5.2 to 5.6 correspond to $\kappa = 0.41$ and $C = 5.2$, whereas the data in figures 4.2 and

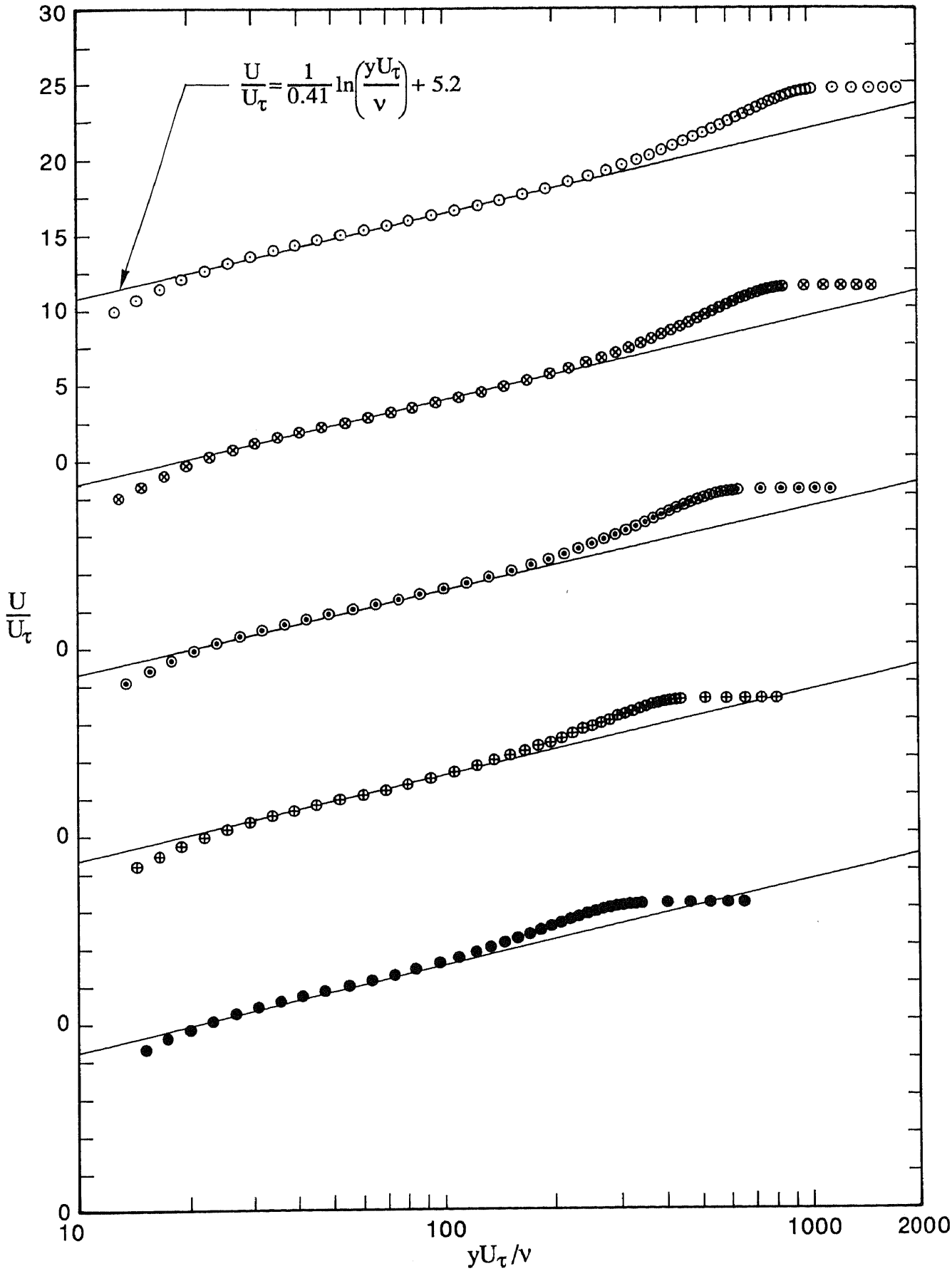

FIGURE 5.2. Mean-flow velocity profiles of U/U_τ versus $\log(yU_\tau/\nu)$ for wire for design flow. Note shift in ordinate.

●, R_θ=697; ⊕, 1003; ⊙, 1568; ⊗, 2226; ⊙, 2788.

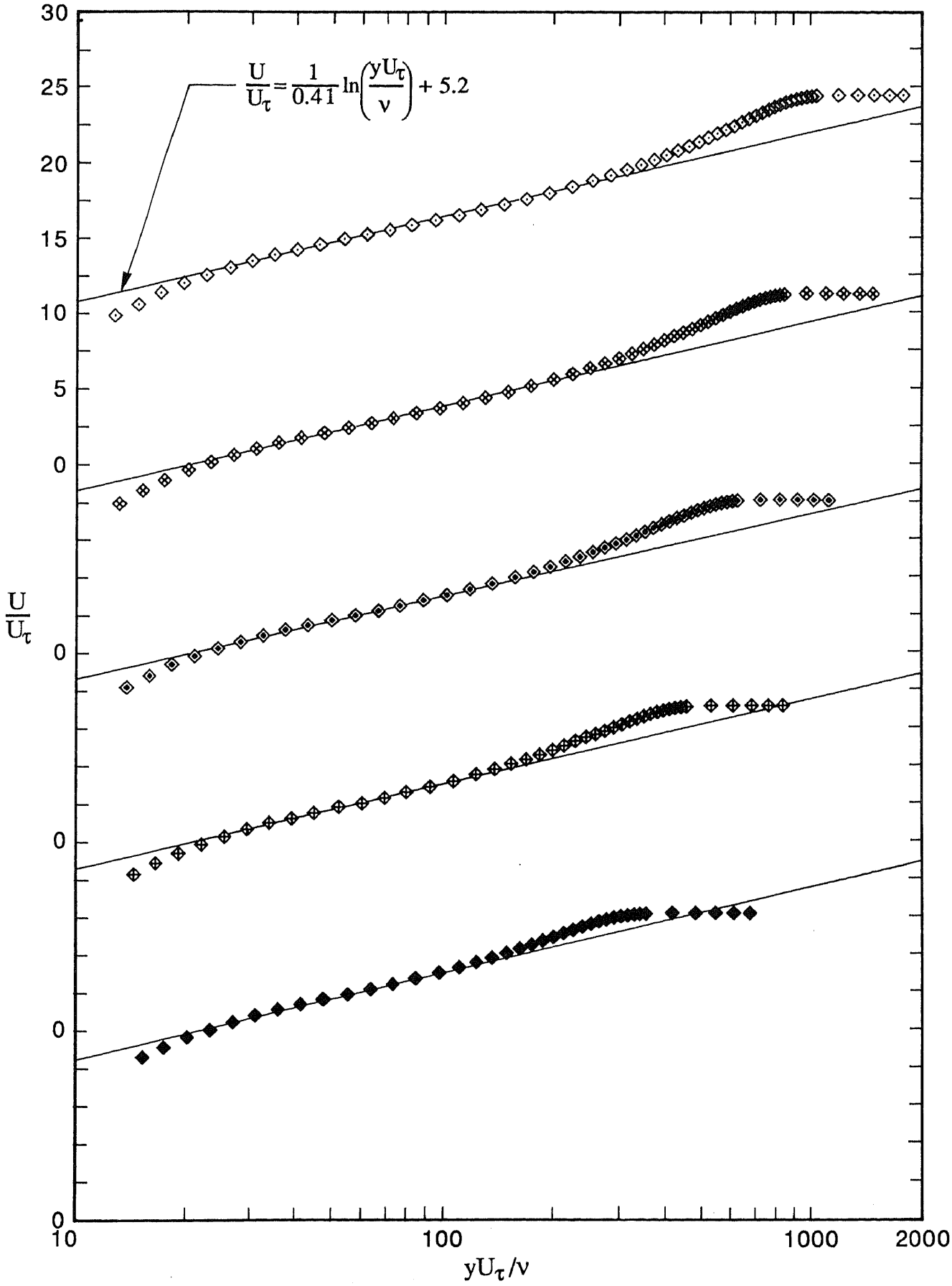

FIGURE 5.3. Mean-flow velocity profiles of U/U_τ versus $\log(yU_\tau/\nu)$ for grit for design flow. Note shift in ordinate.

◆, R_θ=706; ◈, 1042; ◇, 1520; ◈, 2178; ◇, 2730.

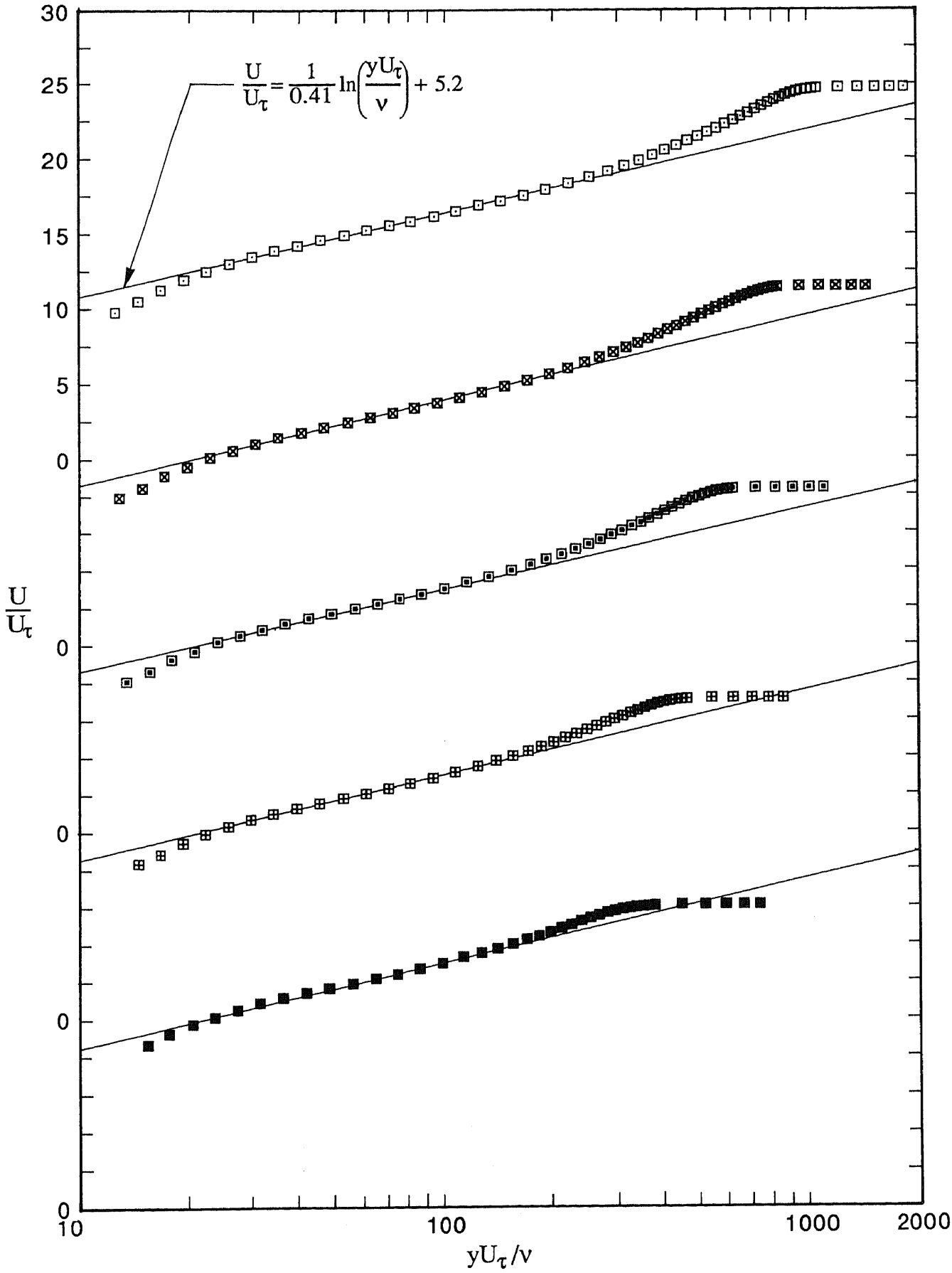

FIGURE 5.4. Mean-flow velocity profiles of U/U_τ versus $\log(yU_\tau/\nu)$ for 2.0 mm pins for design flow. Note shift in ordinate.

■, R_θ=729; ⊞, 1027; ▣, 1565; ⊠, 2181; ⊡, 2889.

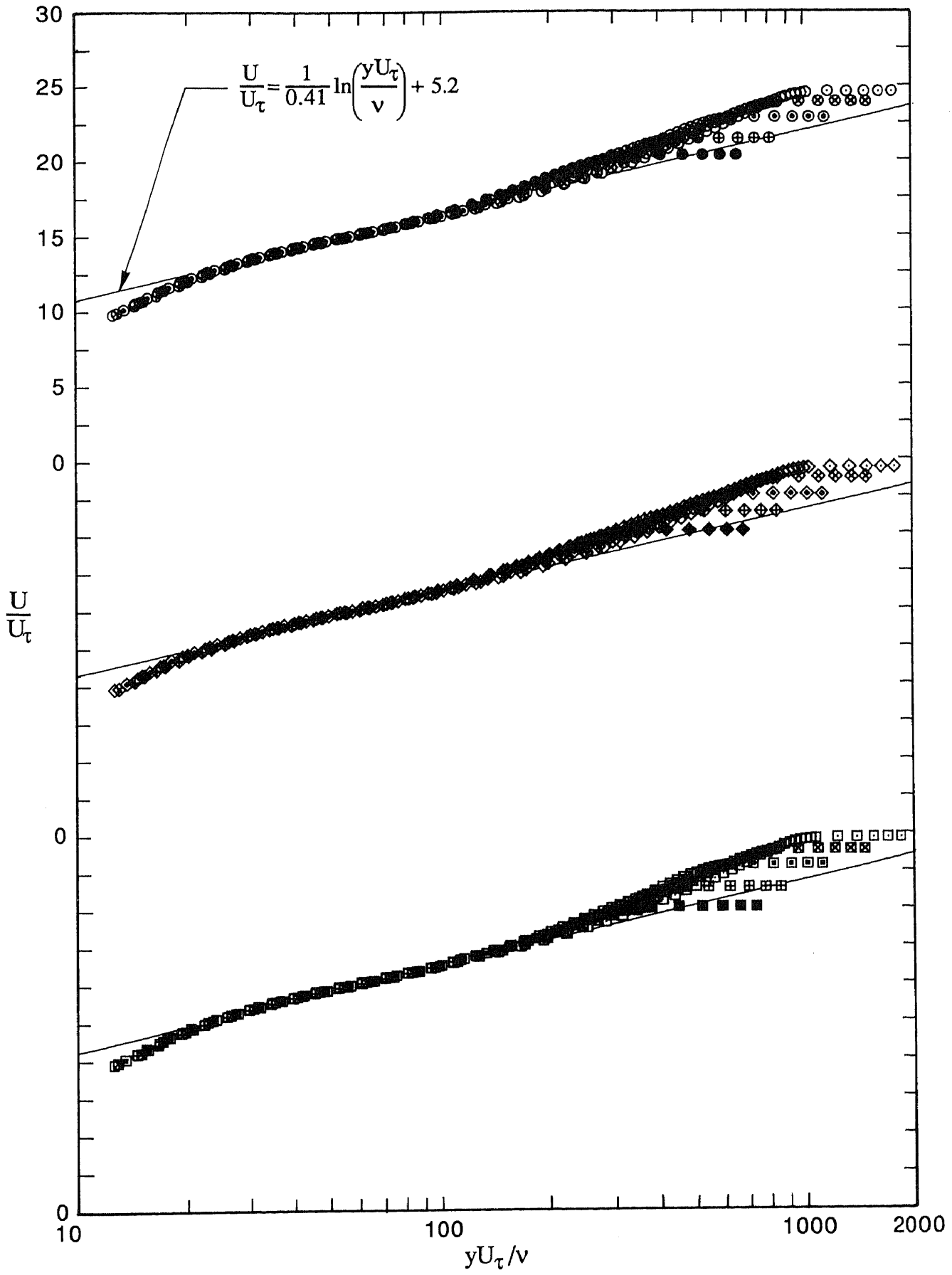

FIGURE 5.5. Mean-flow velocity profiles of U/U_τ versus $\log(yU_\tau/\nu)$ for design flows showing effects of R_θ for three devices. Note shift in ordinate.

Wire: ●, R_θ=697; ⊕, 1003; ⊙, 1568; ⊗, 2226; ⊙, 2788.
Grit: ◆, R_θ=706; ◈, 1042; ◇, 1520; ◈, 2178; ◇, 2730.
2.0 mm pins: ■, R_θ=729; ⊞, 1027; ⊡, 1565; ⊠, 2181; ⊡, 2889.

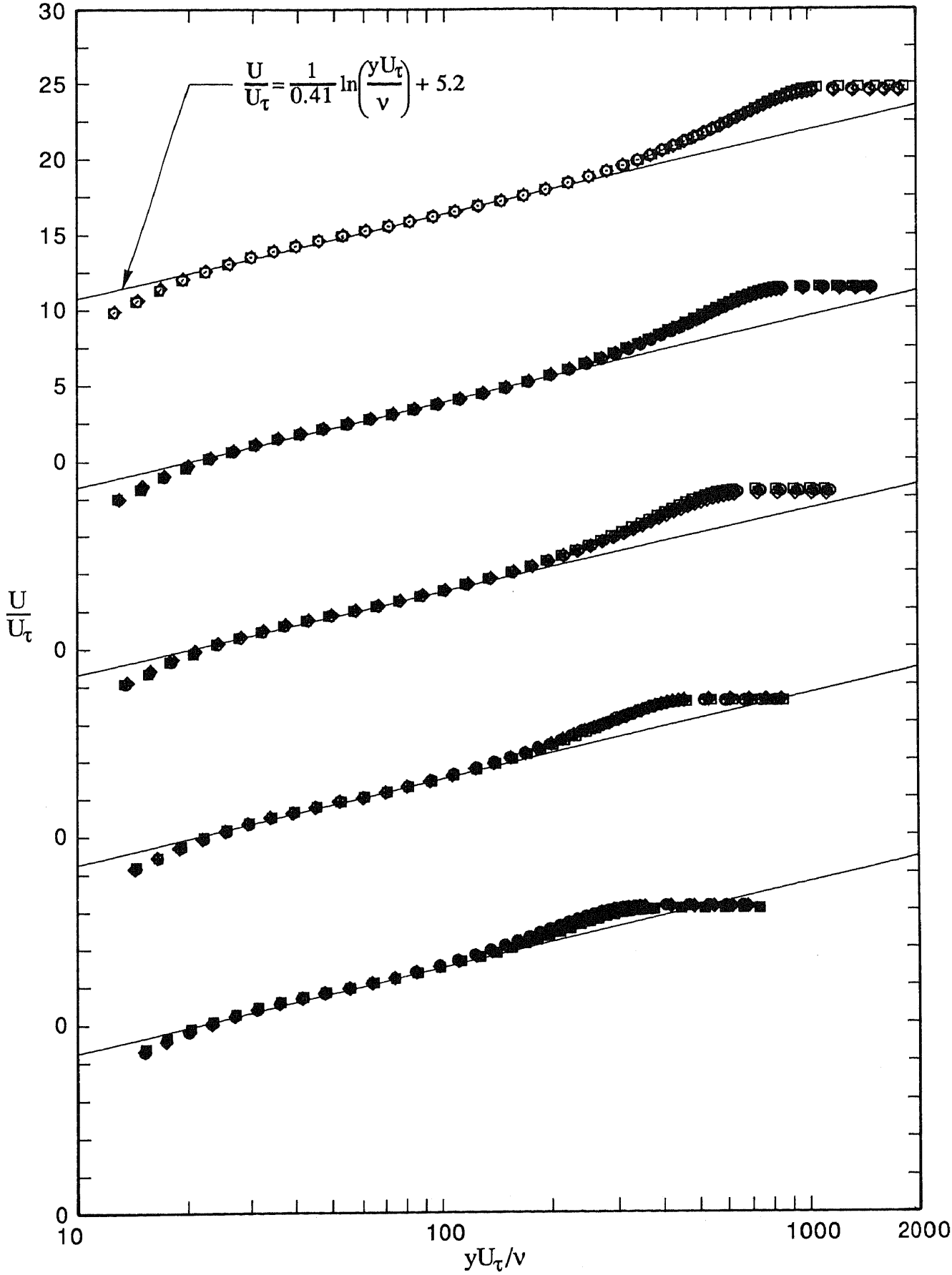

FIGURE 5.6. Mean-flow velocity profiles of U/U_τ versus $\log(yU_\tau/\nu)$ for design flows showing effects of device for five nominal values of R_θ. Note shift in ordinate.

Wire: ●, R_θ=697; ⊕, 1003; ⊙, 1568; ⊗, 2226; ⊙, 2788.
Grit: ◆, R_θ=706; ⊕, 1042; ◇, 1520; ◈, 2178; ◇, 2730.
2.0 mm pins: ■, R_θ=729; ⊞, 1027; ⊡, 1565; ⊠, 2181; ⊡, 2889.

4.3 were determined using $\kappa = 0.41$ and $C = 5.0$ for reasons given in Section 2.7. It is often difficult to pick out individual symbols in figures 5.5 and 5.6, but this is inevitable in the regions where the data collapse. In figure 5.6 it may be necessary to interpret the symbols of the collapsed profiles in the context of figures 5.2 to 5.4.

The good agreement between the design flows for the three devices at five nominal values of R_θ when the flows are compared on the basis of their U/U_τ-versus-$\log(yU_\tau/\nu)$ characteristics, means that whenever the flows are compared to see whether or not the type of device used affects other flow behaviour, such as turbulence characteristics or spectra, then the comparisons can be made on a sound basis.

The mean-flow profiles corresponding to $R_\theta = 509$ for the wire and $R_\theta = 537$ for the grit for the design flows are shown in figure 5.7 plotted using U/U_τ-versus-$\log(yU_\tau/\nu)$ coordinates. For comparison purposes, data for the wire and grit from figure 5.5 have been appropriately replotted on figure 5.7. The replotted profiles are in the form of lines to avoid confusion and to emphasize the behaviour of the profiles for $R_\theta = 509$ and 537. As can be seen, the outer flow region of the profiles for $R_\theta = 509$ and 537 have a different form compared with profiles having higher values of R_θ, and the reason for the increased values of $\Delta U/U_\tau$ shown in figures 4.2 and 4.3 now becomes apparent. The flows corresponding to $R_\theta = 509$ and 537 exhibit characteristics of turbulence, viz. linear logarithmic regions on the profiles shown in figure 5.7 and also the Preston-tube values of C_f correspond to turbulent flow, as shown in figure 4.1. It will be recalled from Section 2.2 that Coles (1968) determined $\Delta U/U_\tau$ and C_f by fitting data in the logarithmic and wake regions of a profile to equation (2.9). Thus, the unusual shape of the wakes of the profiles for $R_\theta = 509$ and 537 means that it is questionable whether accurate values of C_f would be obtained if Coles' technique were applied to profiles such as these.

In Section 2.2 it was mentioned that Landweber (1953) and Preston (1958) quoted different values of C_f corresponding to the disappearance of the logarithmic region. Preston's value of C_f corresponded to $R_\theta = 389$ and Landweber's value of R_θ, although unspecified, was less than this. In the current study, the lowest value of R_θ at which a logarithmic region was found to

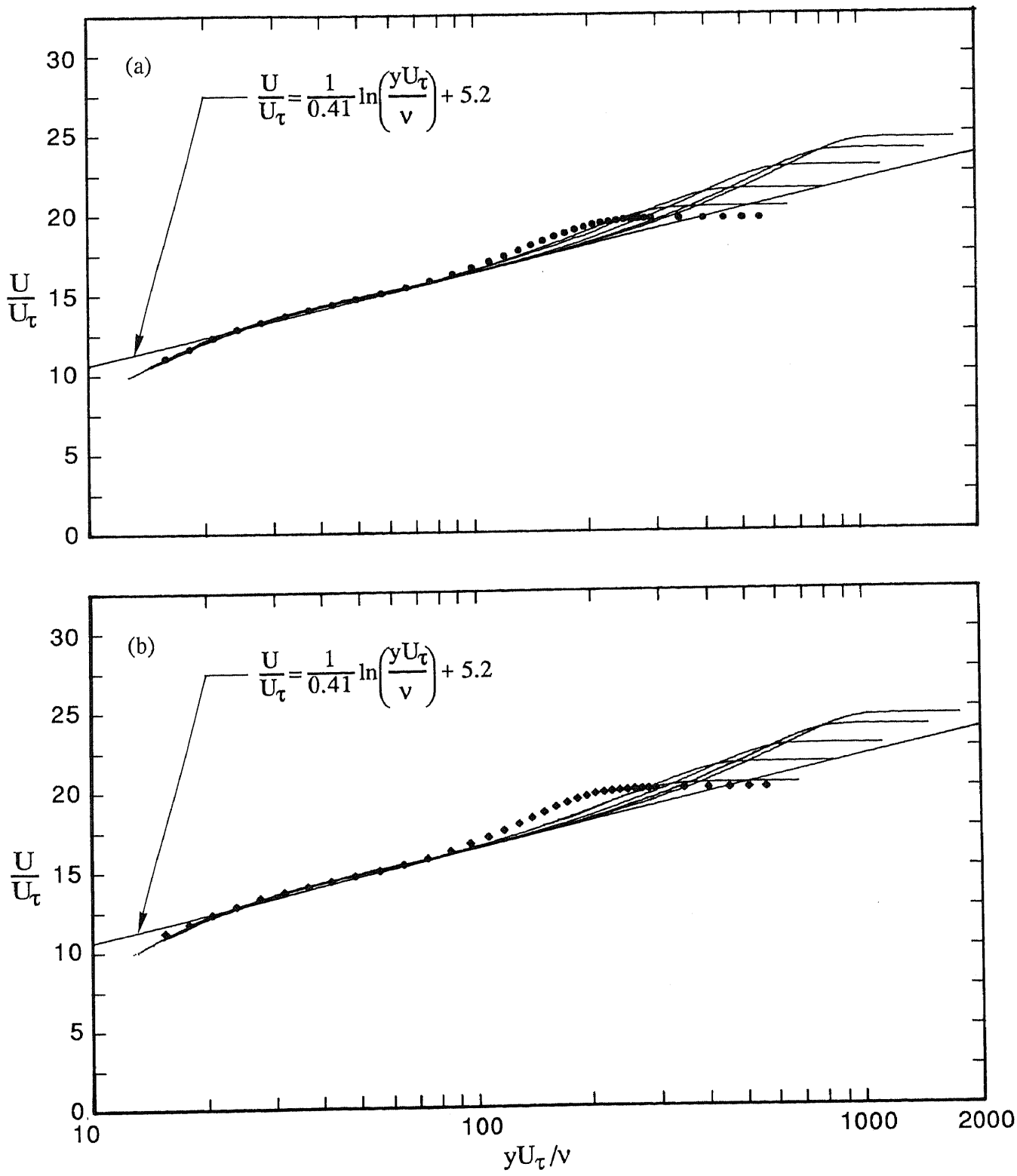

FIGURE 5.7. Mean-flow velocity profiles of U/U_τ versus $\log(yU_\tau/\nu)$ for various values of R_θ for design flows.

(a) wire: • , $R_\theta = 509$; ———, various R_θ, based on figure 5.5.

(b) Grit: ◆ , $R_\theta = 537$; ———, various R_θ, based on figure 5.5.

exist for a design-flow profile whose $\Delta U/U_\tau$-versus-R_θ characteristic followed the trend of Coles' (1962) relationship, was $R_\theta = 581$. The profile was for the wire. The extreme design-flow profiles shown in figure 5.7 displayed logarithmic regions down to $R_\theta = 509$ and 537 for the wire and grit respectively, but these profiles had an unusual form for the wake as explained above.

The data contained in figures 5.5 and 5.6 were replotted using $(U-U_e)/U_\tau$-versus-y/δ coordinates as shown in figures 5.8 and 5.9 respectively. Figure 5.8 clearly shows that for each of the three devices, the velocity-defect profiles are not universal at low values of R_θ but change monotonically with R_θ. In each case, there is a tendency for the profiles to converge at the higher values of R_θ. For each of the devices, the profiles near the edges of the boundary layers collapse for all five values of R_θ, unlike the profiles plotted as in figure 5.5.

An analysis of figure 5.9 indicates that for each of the five nominal values of R_θ, the type of device used does not greatly affect the velocity defect profiles. Contributing factors to any differences are the same as those discussed above for the profiles plotted semi-logarithmically.

5.5 Velocity Profiles for Under and Overstimulated Flows

The effects that under and overstimulation had on mean-flow behaviour for different devices were investigated by simply comparing mean-flow profiles, at nominal values of R_θ of 1020 and 2175, for each of the devices for flows having different amounts of stimulation. Details of these profiles are given in table 5.1. The mean-flow profiles used in the comparisons were plotted using coordinates of U/U_τ versus $\log(yU_\tau/\nu)$ and $(U-U_e)/U_\tau$ versus y/δ, both of which were used for the correctly-stimulated flows.

Considering the first type of scaling, the mean-flow velocity profiles are shown in figures 5.10 and 5.11 for $R_\theta \approx 1020$ and $R_\theta \approx 2175$ respectively. The profiles for $R_\theta \approx 1020$ are more affected by the degree of stimulation than the profiles for $R_\theta \approx 2175$, which are affected very little, and this is consistent with the behaviour of the associated $\Delta U/U_\tau$-versus-R_θ characteristics shown in figure 4.3. Any observed differences in the sets of profiles shown in figures 5.10 and 5.11 are confined to the outer flows and the degree of stimulation can be seen to

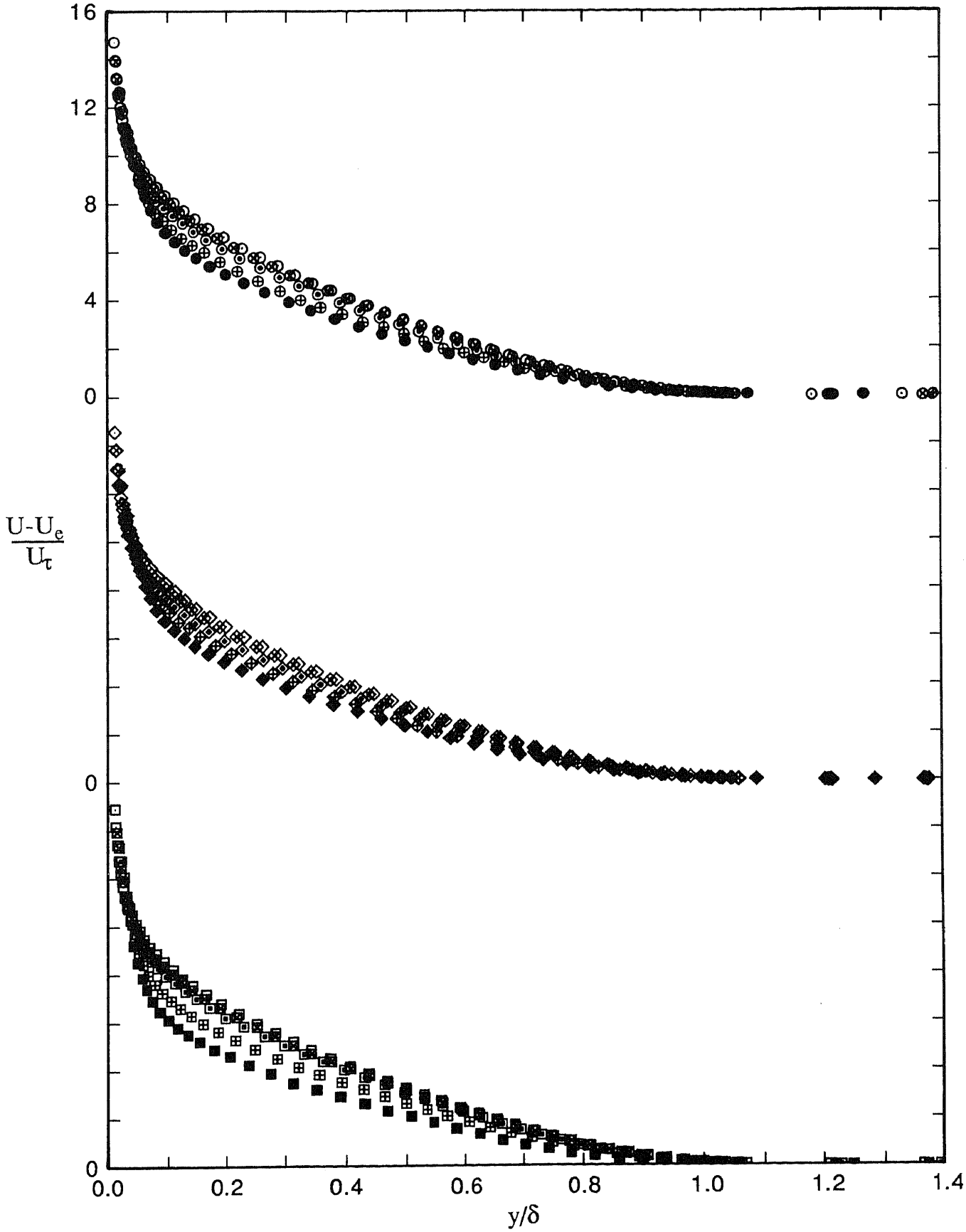

FIGURE 5.8. Mean-flow velocity profiles of $(U-U_e)/U_\tau$ versus y/δ for design flows showing effects of R_θ for three devices. Note shift in ordinate.

Wire: ●, R_θ=697; ⊕, 1003; ⊙, 1568; ⊗, 2226; ⊙, 2788.
Grit: ◆, R_θ=706; ⊕, 1042; ◇, 1520; ◈, 2178; ◇, 2730.
2.0 mm pins: ■, R_θ=729; ⊞, 1027; ⊡, 1565; ⊠, 2181; ⊡, 2889.

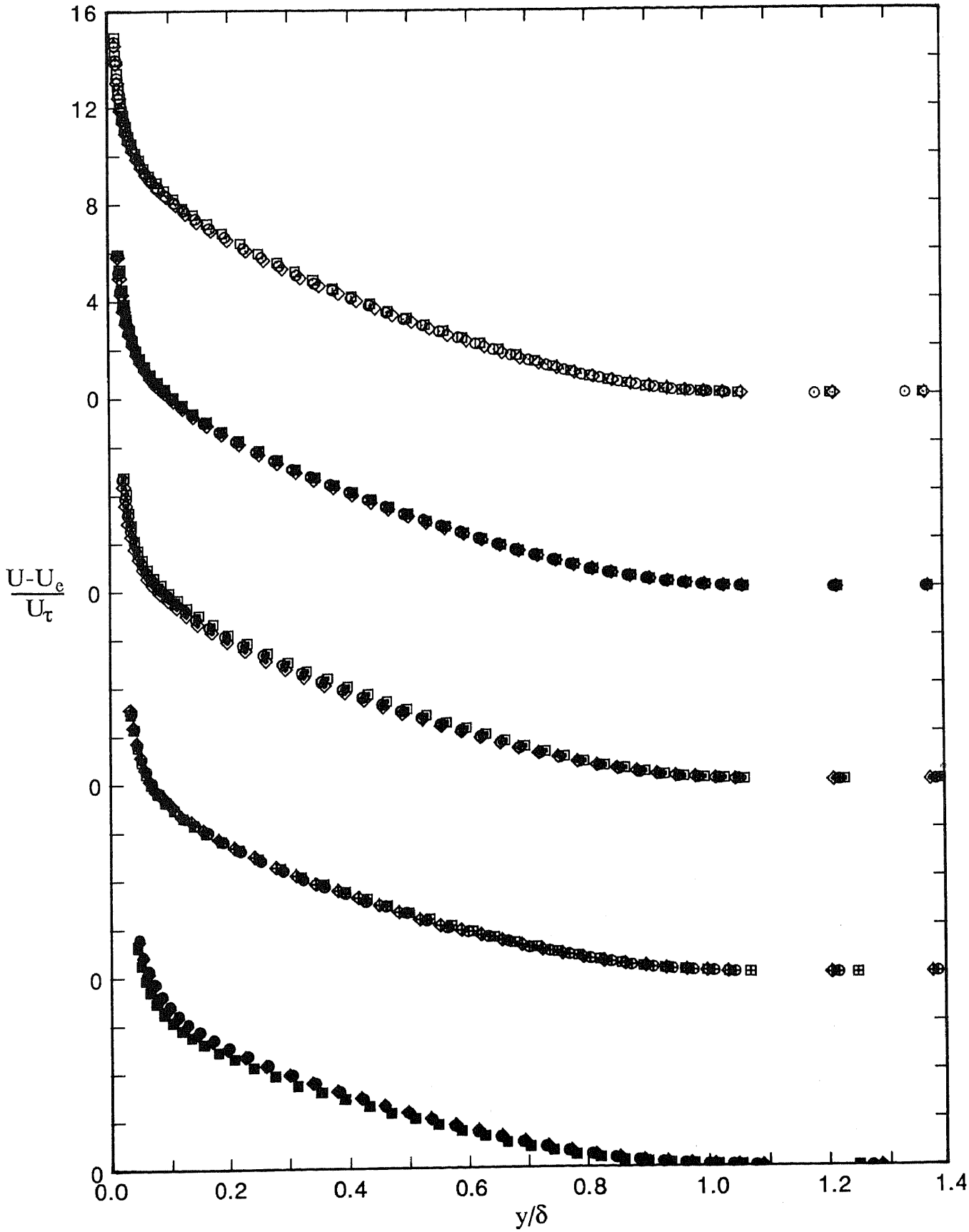

FIGURE 5.9. Mean-flow velocity profiles of $(U-U_e)/U_\tau$ versus y/δ for design flows showing effects of device for five nominal values of R_θ. Note shift in ordinate.

Wire: ●, R_θ=697; ⊕, 1003; ⊙, 1568; ⊗, 2226; ⊙, 2788.
Grit: ◆, R_θ=706; ⊕, 1042; ◇, 1520; ◈, 2178; ◇, 2730.
2.0 mm pins: ■, R_θ=729; ⊞, 1027; ⊡, 1565; ⊠, 2181; ⊡, 2389.

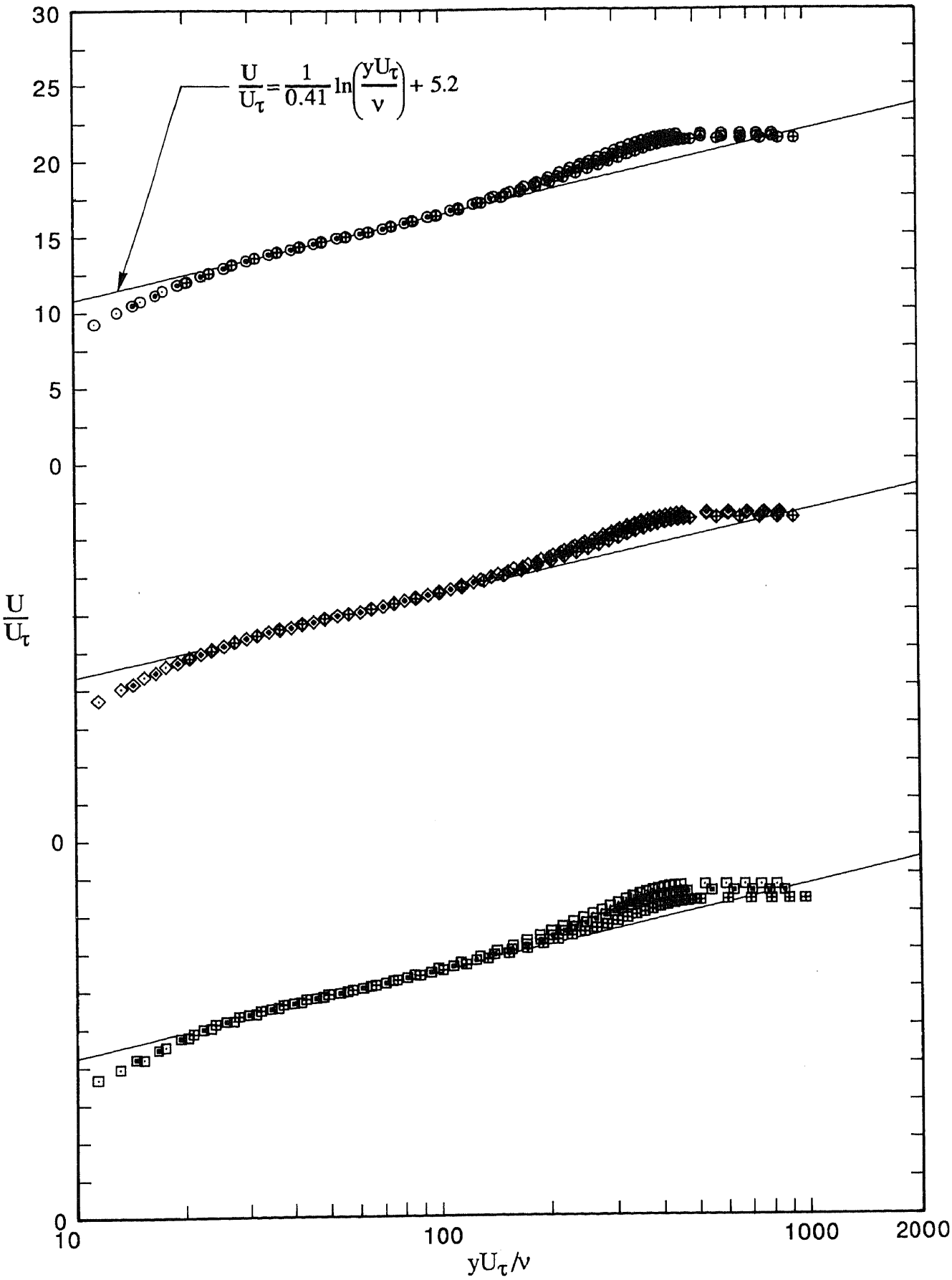

FIGURE 5.10. Mean-flow velocity profiles of U/U_τ versus $\log(yU_\tau/\nu)$ for three devices showing effects of different amounts of stimulation. Note shift in ordinate. Velocities given below are nominal values.

Wire:	⊙, 8.0 m/s, R_θ=1017;	⊙, 10.0 m/s, R_θ=1003;	⊕, 14.0 m/s, R_θ=1033.
Grit:	◇, 8.0 m/s, R_θ= 997;	◇, 10.0 m/s, R_θ=1042;	◈, 14.0 m/s, R_θ=1029.
2.0 mm pins:	⊡, 8.0 m/s, R_θ=1024;	⊡, 10.0 m/s, R_θ=1027;	⊞, 14.0 m/s, R_θ=1013.

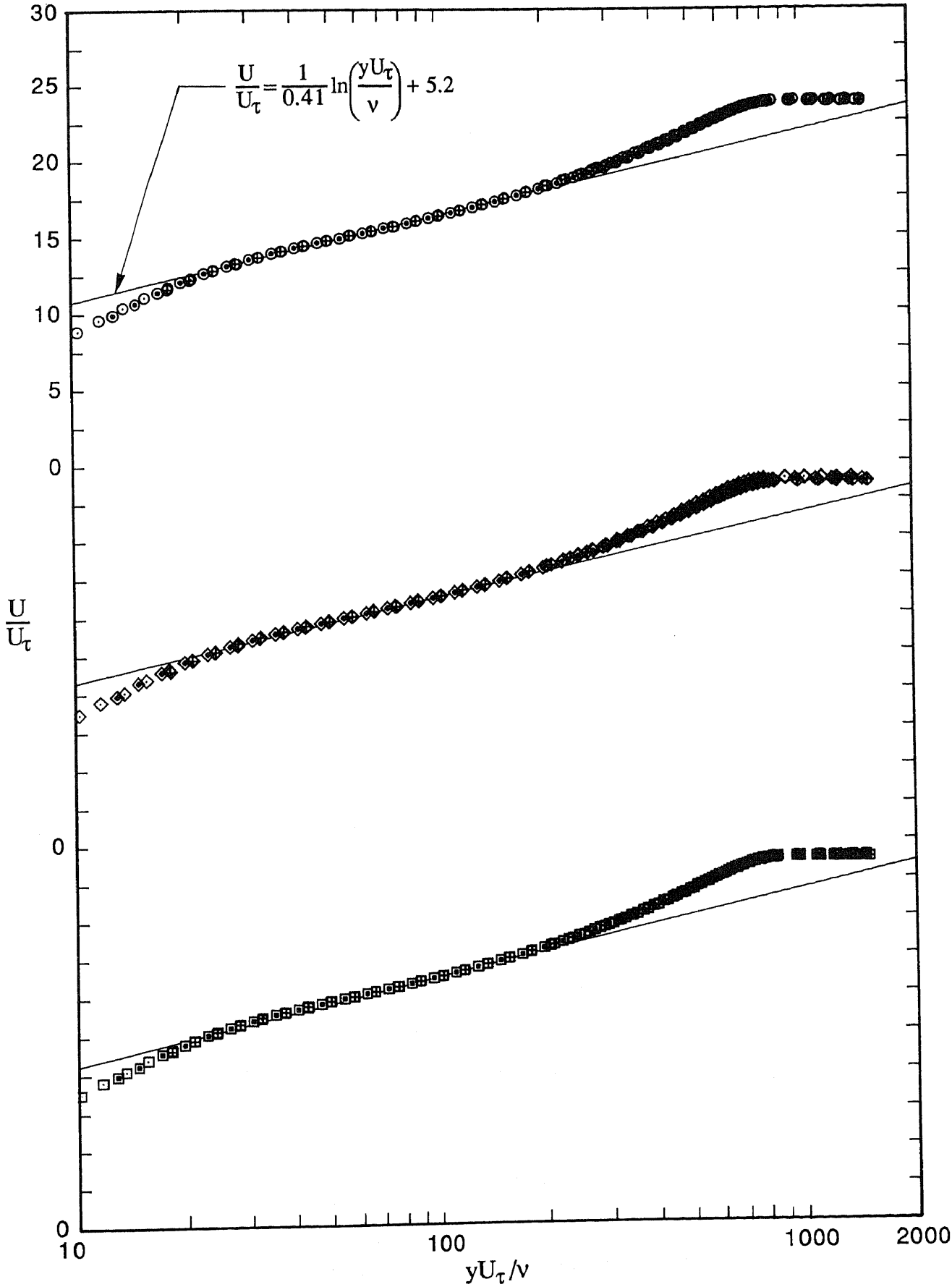

FIGURE 5.11. Mean-flow velocity profiles of U/U_τ versus $\log(yU_\tau/\nu)$ for three devices showing effects of different amounts of stimulation. Note shift in ordinate. Velocities given below are nominal values.

Wire:	⊙, 8.0 m/s, R_θ=2151;	⊙, 10.0 m/s, R_θ=2226;	⊕, 14.0 m/s, R_θ=2137.
Grit:	◇, 8.0 m/s, R_θ=2146;	◈, 10.0 m/s, R_θ=2178;	⊕, 14.0 m/s, R_θ=2119.
2.0 mm pins:	⊡, 8.0 m/s, R_θ=2230;	▣, 10.0 m/s, R_θ=2181;	⊞, 14.0 m/s, R_θ=2169.

have negligible effect on the wall regions of the flows. For $R_\theta \approx 1020$, the maximum differences between the three profiles in each group, expressed as a percentage difference between the maximum and minimum values of U/U_τ in the freestream for profiles within that group, are 1.5%, 1.6% and 4.5% for the wire, grit and pins respectively. Corresponding differences for the profiles corresponding to $R_\theta \approx 2175$ are 0.3%, 1.0% and 0.5% respectively. Although these differences are generally within the experimental uncertainty of the measurements, the trends of the $\Delta U/U_\tau$-versus-R_θ characteristics shown in figure 4.3 suggest that real differences can exist in the shapes of velocity profiles having approximately the same value of R_θ, but different amounts of stimulation. However, presenting data as in figures 5.10 and 5.11 is not as good an indicator of the effects of different amounts of stimulation as presenting data as in figure 4.3.

The data appearing in figures 5.10 and 5.11 are replotted in figures 5.12 and 5.13 respectively using $(U-U_e)/U_\tau$-versus-y/δ coordinates. As expected, the replotted data reflects the behaviour of the data plotted semi-logarithmically. The profiles for $R_\theta \approx 1020$ are more affected by the amount of stimulation than are the profiles for $R_\theta \approx 2175$, which are affected very little. Also, for $R_\theta \approx 1020$, the profiles for the pins show more variation with the amount of stimulation than do the profiles for the other two devices.

5.6 Skin-Friction Coefficients from a Preston Tube and from Velocity Profiles

The complete set of skin-friction coefficients taken with a 1.00 mm diameter Preston tube for the three tripping devices for understimulated, design and overstimulated flows are shown plotted against x in figure 5.14. Some of these Preston-tube values of C_f have already been presented in figure 4.1. These plots do not exhibit any unusual behaviour from what could reasonably be expected and no further comment on them is necessary.

Values of C_f were also determined from velocity profiles by using a Clauser chart with $\kappa = 0.41$ and $C = 5.2$. These values of C_f are also shown plotted in figure 5.14 for the same nine flows for the complete set of velocity profiles and not just those specified in table 5.1.

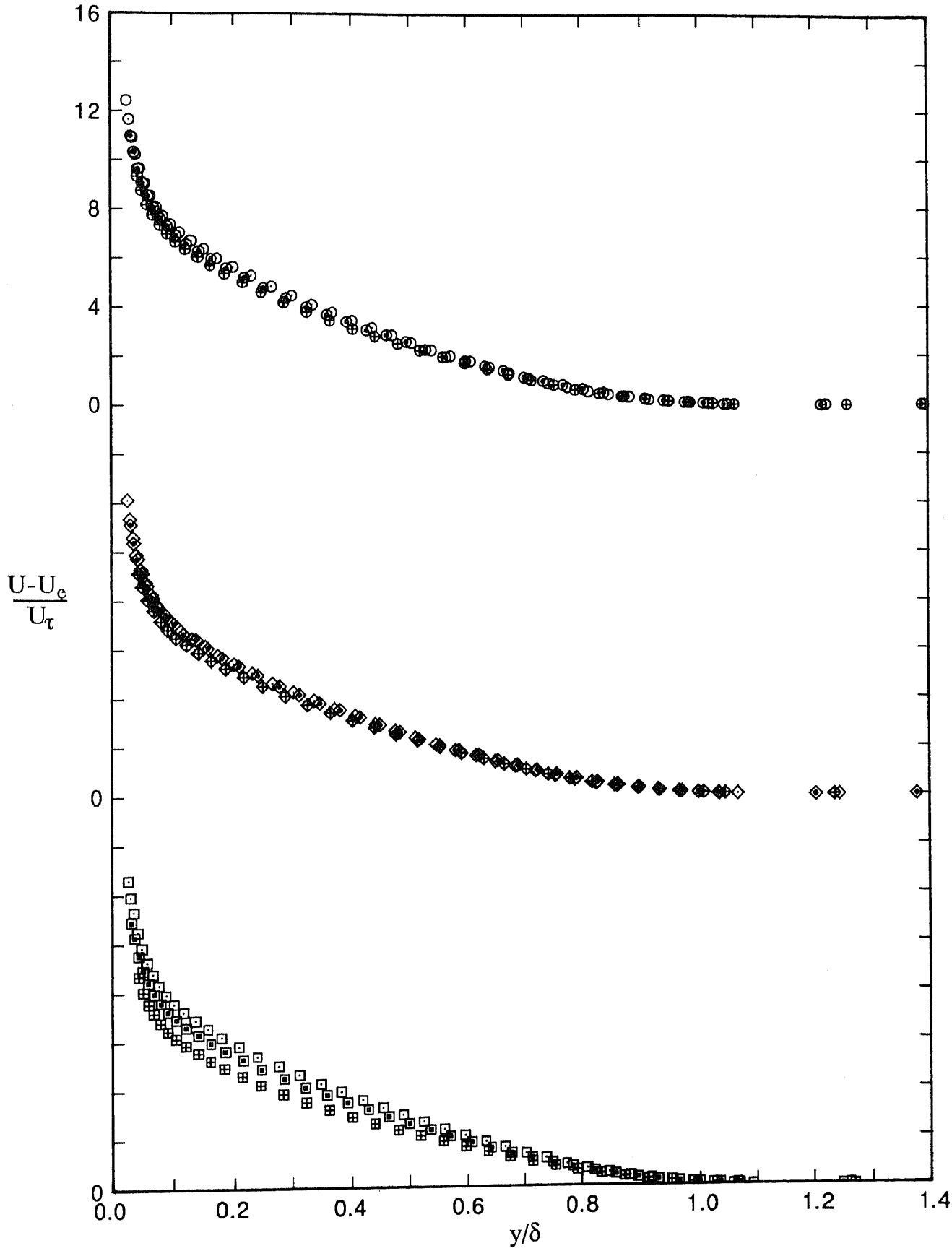

FIGURE 5.12. Mean-flow velocity profiles of $(U-U_e)/U_\tau$ versus y/δ for three devices showing effects of different amounts of stimulation. Note shift in ordinate. Velocities given below are nominal values.

Wire:	⊙, 8.0 m/s, R_θ=1017;	⊙, 10.0 m/s, R_θ=1003;	⊕, 14.0 m/s, R_θ=1033.
Grit:	◇, 8.0 m/s, R_θ=0997;	◈, 10.0 m/s, R_θ=1042;	✥, 14.0 m/s, R_θ=1029.
2.0 mm pins:	⊡, 8.0 m/s, R_θ=1024;	▣, 10.0 m/s, R_θ=1027;	⊞, 14.0 m/s, R_θ=1013.

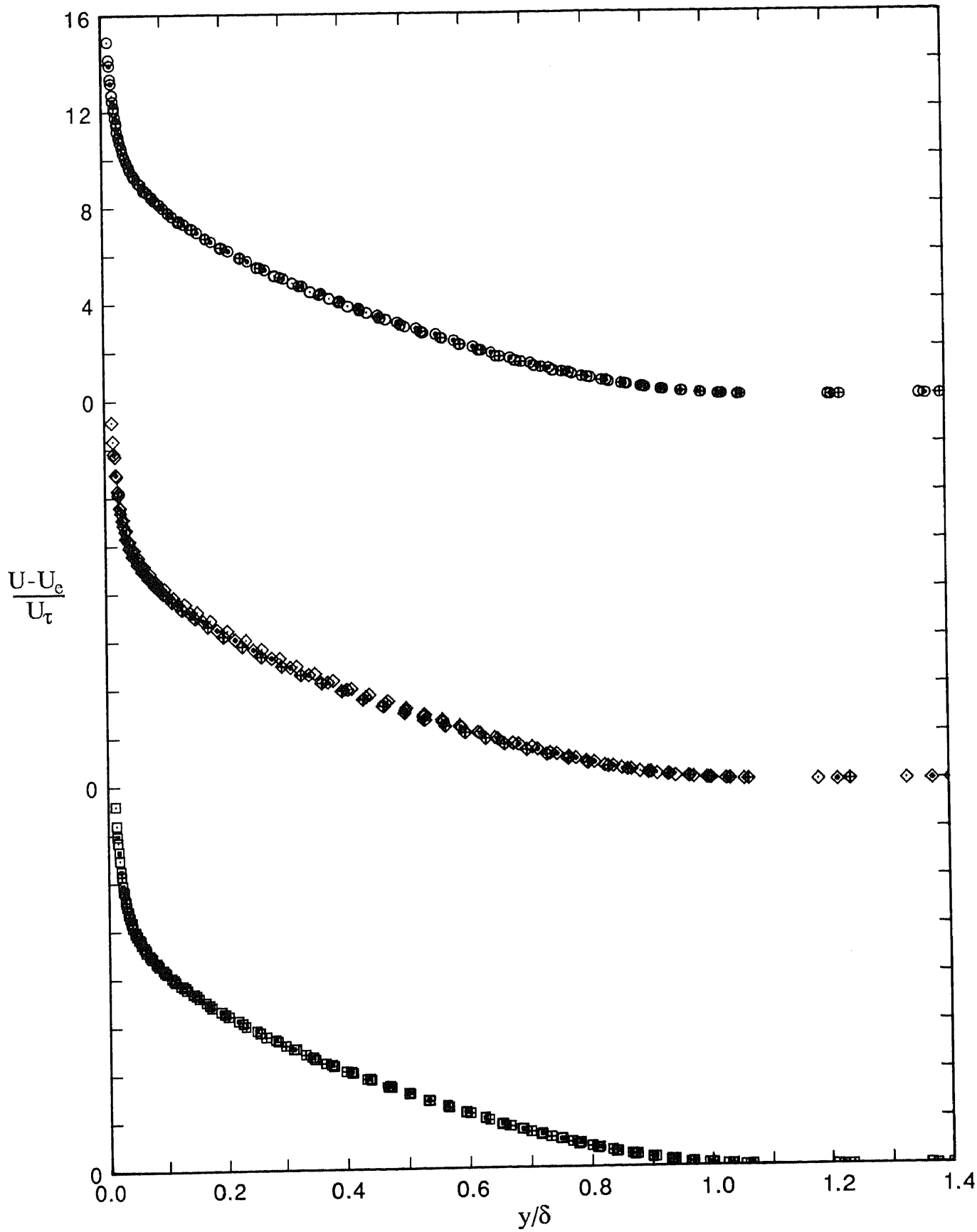

FIGURE 5.13. Mean-flow velocity profiles of $(U-U_e)/U_\tau$ versus y/δ for three devices showing effects of different amounts of stimulation. Note shift in ordinate. Velocities given below are nominal values.

Wire:	⊙, 8.0 m/s, R_θ=2151;	⊙, 10.0 m/s, R_θ=2226;	⊕, 14.0 m/s, R_θ=2137.
Grit:	◇, 8.0 m/s, R_θ=2146;	◈, 10.0 m/s, R_θ=2178;	◈, 14.0 m/s, R_θ=2119.
2.0 mm pins:	⊡, 8.0 m/s, R_θ=2230;	▣, 10.0 m/s, R_θ=2181;	⊞, 14.0 m/s, R_θ=2169.

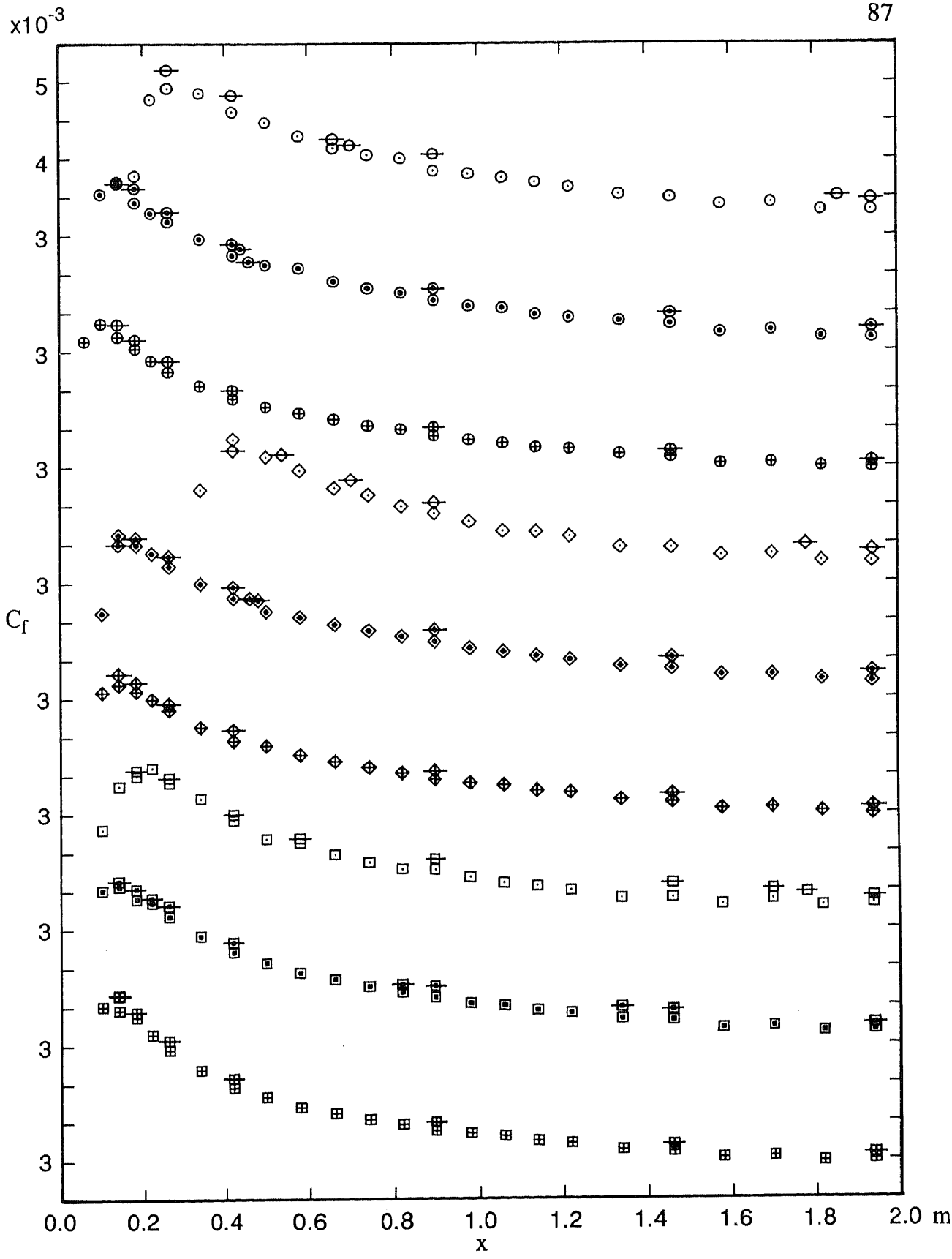

FIGURE 5.14. Variation of C_f with x. Note shift in ordinate. Velocities given below are nominal values.

Wire: ⊙, ⊖, 8.0 m/s; ⊙, ⊖, 10.0 m/s; ⊕, ⊕, 14.0 m/s.

Grit: ◇, ◈, 8.0 m/s; ◇, ◈, 10.0 m/s; ◈, ◈, 14.0 m/s.

2.0 mm pins: ⊡, ⊟, 8.0 m/s; ⊡, ⊟, 10.0 m/s; ⊞, ⊞, 14.0 m/s.

For each pair of symbols shown above, symbol on left corresponds to C_f measured with a Preston tube and symbol on right corresponds to C_f measured with a Clauser chart, using κ = 0.41 and C = 5.2

As can be seen, the Clauser-chart values of C_f are generally above the corresponding Preston-tube values by about 3.5% on average. Since skin-friction coefficients are inherently difficult to measure, no significance is attached to these differences.

5.7 Velocity Profile Integral Parameters

The momentum thicknesses, θ, are shown plotted against x in figure 5.15 for the complete set of velocity profiles. The individual experimental points for each particular flow have been joined by straight lines so as to make the results easier to interpret. The plotted values of θ were determined by using standard integrals for $yU_\tau/\nu < 50$ and trapezoidal integration beyond this range, as discussed in Section 3.8.2. The values of θ shown were used when checking on the balance of the momentum integral equation.

Other integral parameters, viz. the shape factor, H, and the Clauser parameter, G, have already been discussed in Section 4.5 and will not be considered here.

Flow variables associated with the profiles appearing in groups 1 to 5 of table 5.1 are listed in table 5.2.

5.8 Transverse Measurements of Skin-Friction Coefficients

To help obtain an understanding of transverse flow behaviour, transverse C_f measurements were taken with a Preston tube for different values of R_θ, different devices and different nominal velocities. The measurements were spaced at intervals of 4.5 mm and extended 108 mm both sides of the wind-tunnel centreline so that they covered approximately the central third of the smooth wall. The above spacing was chosen so that measurements would be taken at locations both directly behind the cylindrical pins and also at locations halfway between these. Although this spacing was only relevant to the pins, the same spacing was used for all devices. All of the transverse C_f measurements within a particular set were divided by C_{fm}, the mean value of C_f within that set, and the values of C_f/C_{fm} are shown in figures 5.16 and 5.17. These results will now be discussed.

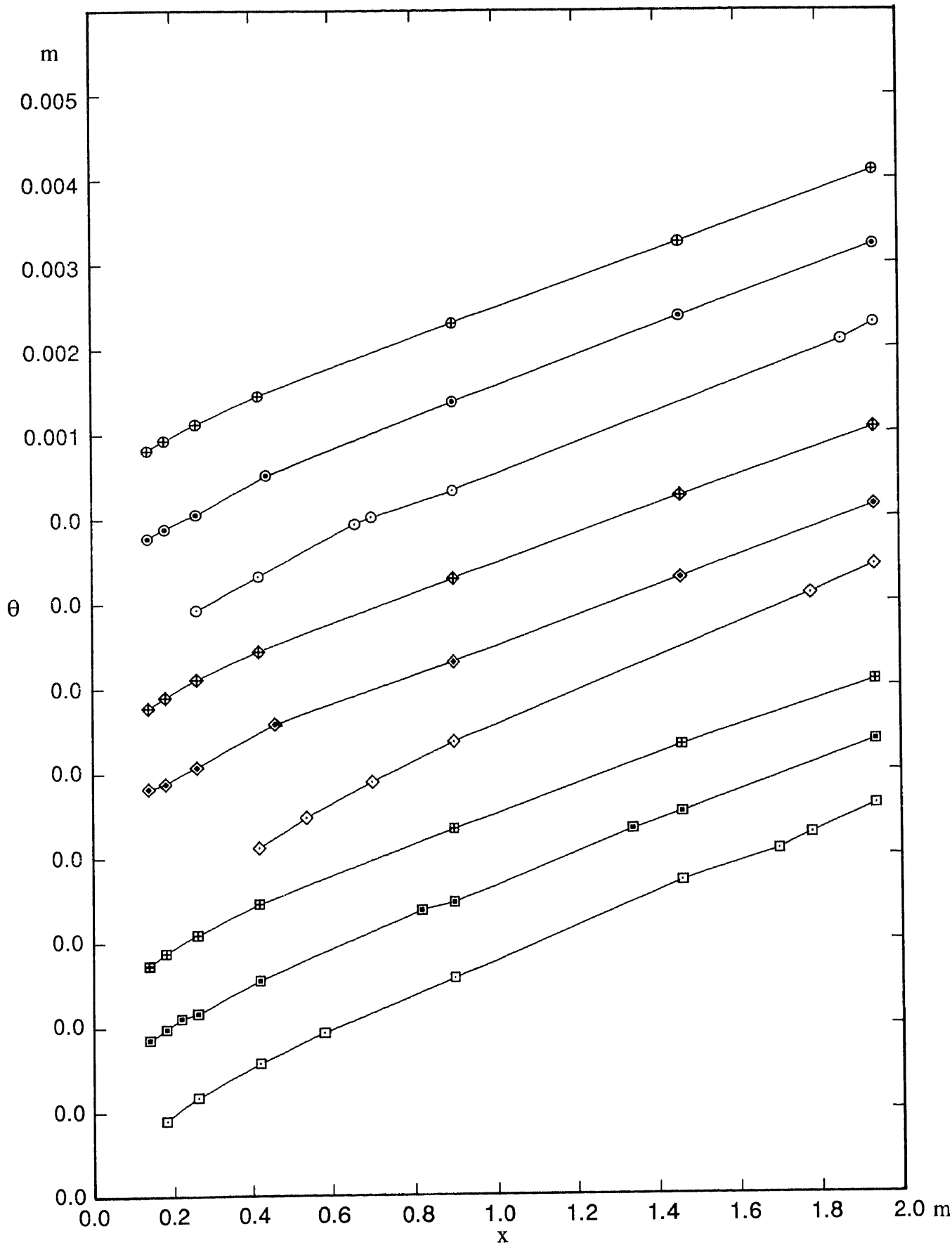

FIGURE 5.15. Variation of θ with x. Note shift in ordinate. Velocities given below are nominal values.

Wire:	⊙, 8.0 m/s;	⊙, 10.0 m/s;	⊕, 14.0 m/s.
Grit:	◇, 8.0 m/s;	◈, 10.0 m/s;	◈, 14.0 m/s.
2.0 mm pins:	⊡, 8.0 m/s;	⊞, 10.0 m/s;	⊞, 14.0 m/s.

Table 5.2. Flow variables corresponding to plotted profiles.

x m	U_e m/s	C_{f_1}	C_{f_2}	δ mm	θ mm	H	R_θ	$(U_{rf}/\nu)_{av}$ 1/m
			1.2 mm wire					
0.660	8.157	0.004380	0.004252	17.533	1.934	1.467	1017	522808
1.860	7.859	0.003566	0.003513	35.754	4.087	1.416	2151	524542
0.140	9.867	0.005374	0.005181	7.304	0.775	1.546	509	654270
0.260	10.194	0.004972	0.004812	9.934	1.056	1.491	697	656317
0.440	10.027	0.004457	0.004332	13.901	1.518	1.457	1003	656036
0.900	10.107	0.003901	0.003815	21.036	2.374	1.433	1568	656818
1.460	10.180	0.003556	0.003495	29.266	3.375	1.413	2226	656333
1.940	10.147	0.003349	0.003302	36.666	4.212	1.401	2788	658194
0.260	14.113	0.004511	0.004382	10.588	1.120	1.441	1033	916241
0.900	14.139	0.003591	0.003516	20.090	2.301	1.416	2137	920599
			Grit					
0.700	8.194	0.004456	0.004331	17.443	1.889	1.460	997	524485
1.780	8.094	0.003536	0.003483	35.107	4.088	1.423	2146	523907
0.260	10.039	0.004995	0.004849	10.097	1.072	1.485	706	656460
0.460	10.238	0.004424	0.004298	14.529	1.581	1.453	1042	654556
0.900	10.218	0.003967	0.003882	20.624	2.300	1.429	1520	657054
1.460	10.302	0.003580	0.003520	28.627	3.284	1.412	2178	660129
1.940	10.250	0.003388	0.003331	36.016	4.134	1.399	2730	656771
0.260	14.148	0.004550	0.004435	10.520	1.111	1.437	1029	920703
0.900	14.523	0.003624	0.003550	20.346	2.286	1.411	2119	919577
			2.0 mm pins					
0.580	7.943	0.004319	0.004183	16.847	1.930	1.478	1024	525271
1.780	7.879	0.003521	0.003463	36.767	4.257	1.417	2230	521730
0.220	9.755	0.005018	0.004913	11.035	1.107	1.469	729	654350
0.420	10.386	0.004446	0.004336	14.092	1.551	1.455	1027	656505
0.820	10.139	0.003860	0.003781	20.347	2.370	1.440	1565	654975
1.340	9.895	0.003546	0.003481	28.553	3.318	1.419	2181	653016
1.940	10.313	0.003308	0.003260	37.485	4.355	1.402	2889	657778
0.260	14.336	0.004663	0.004569	10.680	1.092	1.422	1013	920554
0.900	14.274	0.003568	0.003494	20.236	2.332	1.417	2169	921548

C_{f_1} denotes that C_f was determined using the method of Coles (1962) in which $\kappa = 0.41$ and $C = 5.0$.
C_{f_2} denotes that C_f was determined using a Clauser chart with $\kappa = 0.41$ and $C = 5.2$.

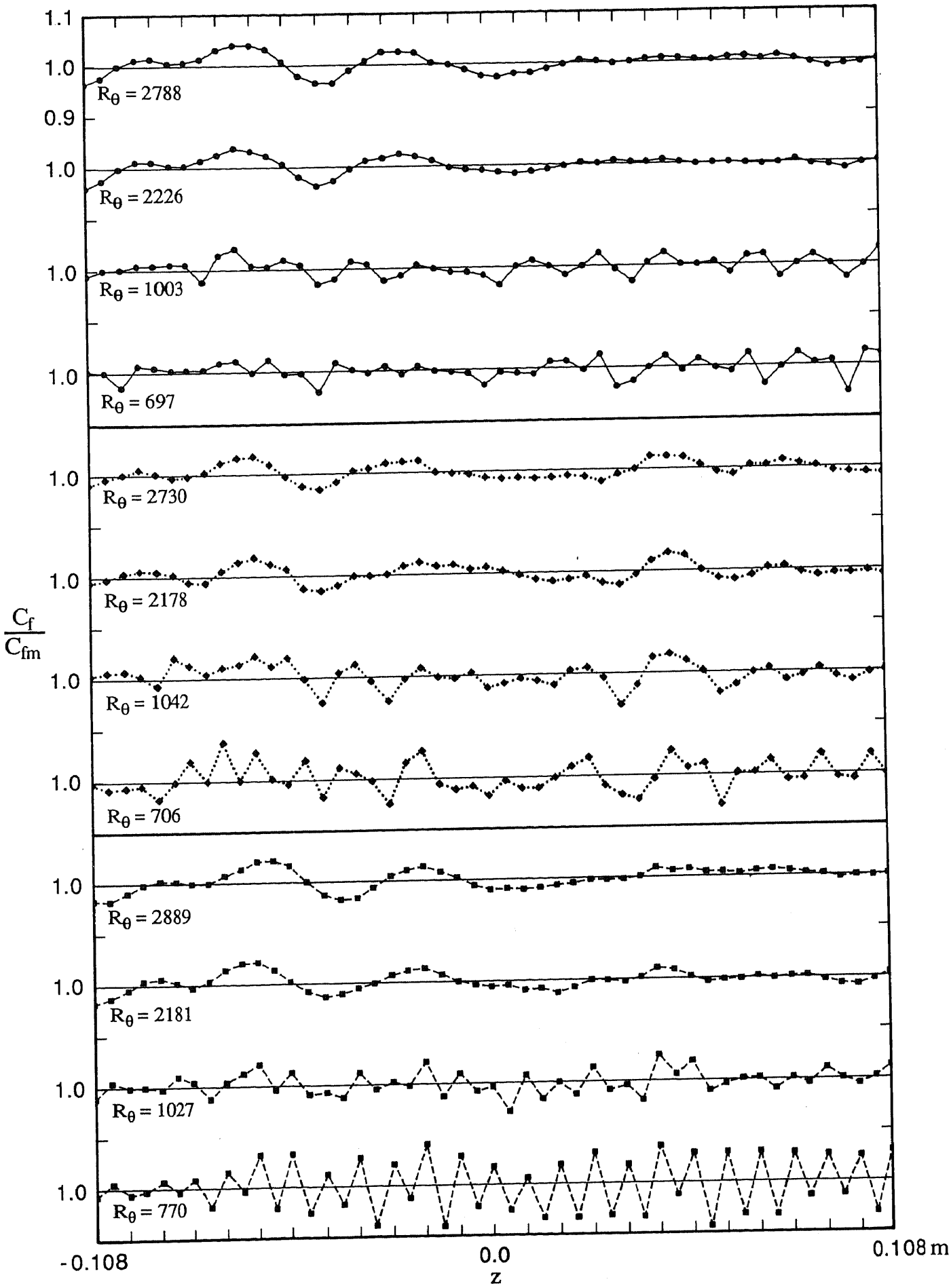

FIGURE 5.16. Variation of C_f/C_{fm} with z for design flows for different values of R_θ. Note shift in ordinate.

———, wire; ·····, grit; — — —, 2.0 mm pins.

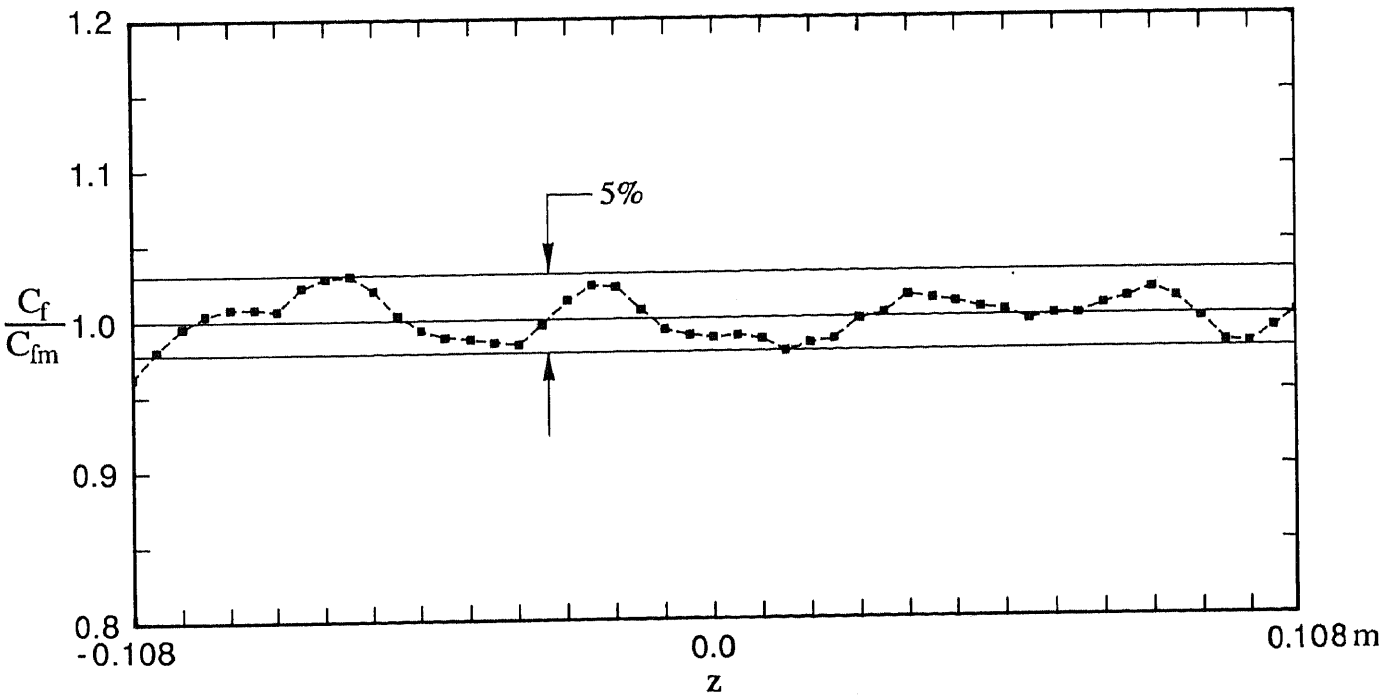

FIGURE 5.17. Variation of C_f / C_{fm} with z for pins of height 0.6 mm for R_θ = 5010 corresponding to a nominal reference velocity of 20.0 m/s.

Measurements for the design flows for different values of R_θ using the wire, grit and pins of height 2.0 mm as tripping devices are shown in figure 5.16. The actual experimental points are shown on these figures, and as an aid to interpreting the results, the experimental points have been joined by straight lines. The grid marks on the abscissa have been plotted so that they correspond to pin locations.

From figure 5.16 it is apparent that in each case the spanwise values of C_f/C_{fm} fluctuate the most rapidly at the lowest values of R_θ, but the fluctuations become less pronounced with increasing R_θ. Also the overall range of variation in the values of C_f/C_{fm} is greatest at the lowest values of R_θ but diminishes with increasing R_θ, except perhaps for the wire, where the range of variation of C_f/C_{fm} does not change all that much for changes in R_θ. As can be seen, the above behaviour is particularly noticeable for the 2.0 mm pins. For this device the configuration of peaks and valleys of the values of C_f/C_{fm} at the lowest value of R_θ show a strong correlation with pin position, but the correlation can be seen to disappear as the flow develops. The correlation is undoubtedly related to the fact that wedges of turbulent flow form behind the pins. There does not seem to be any pattern in the transverse variation of C_f/C_{fm} for the wire and the grit.

The most notable feature of figure 5.16 is that the curves for the three devices, although dissimilar in the early stages of development, show some remarkable similarities at the higher values of R_θ. In this region the peaks and valleys of the curves for the three devices correspond quite closely in most cases and the type of device used clearly now has little influence on the transverse C_f/C_{fm} distribution. The perturbations in C_f/C_{fm} that remain are most likely a consequence of the characteristics of the wind tunnel itself. There is a tendency in some cases for the configurations of peaks and valleys to move downstream and to maintain their forms with respect to the wind-tunnel centreline as the flows develop.

When an attempt was made to compare the current transverse C_f measurements with the results of other researchers, it was found that very little published data on low-Reynolds-number transverse C_f measurements were available. However, Watmuff, Witt & Joubert (1985) (see also Witt 1986) have

presented a comprehensive set of such measurements for a range of reference velocities using a wire as the tripping device and these measurements can be readily compared with the current data for the wire. The measurements of Watmuff, Witt & Joubert were for the zero-rotation reference condition in their rotating boundary-layer experiments. An analysis of their measurements for 10 m/s for five values of R_θ varying between about 880 and 2080 indicated that the range of variation of C_f/C_{fm} did not change appreciably from station to station, as was the case for the current results for the wire. For both investigations, the transverse values of C_f/C_{fm} within a given set varied by about ±3 %, with some minor excursions beyond this range. The limits of these excursions were about the same for the two investigations. Barlow & Johnston (1985), (1988) also presented some transverse C_f measurements. They found that C_f/C_{fm} varied by about ±3% for R_θ = 1140. Although the experiments of Barlow & Johnston were primarily concerned with the effects of concave curvature on turbulent boundary-layer structure, some of their upstream measurements before the start of the wall curvature are in good agreement with published zero pressure gradient boundary layers at similar Reynolds number.

To investigate the transverse variation of C_f close to the upper limit of the low-Reynolds-number range, a single set of measurements was taken at x = 1.94 m for a nominal reference velocity of 20.0 m/s using cylindrical pins of height 0.6 mm, diameter 3.0 mm and spacing 9.0 mm as the tripping device, and in this case the value of R_θ was 5010. These measurements are shown in figure 5.17, which has an enlarged ordinate scale compared with previously. As can be seen from this figure, the transverse variation of C_f/C_{fm} over virtually the entire z range given is about 5% overall. This is comparable with the results of Murlis (1975), who measured the transverse distribution of surface pressure over a distance of 6 inches (152.4 mm) both sides of the wind-tunnel centreline at the location where R_θ = 4750 and he found the overall variation to be almost 6 %.

A question that must be addressed is whether or not the non-uniform transverse flow distributions shown in figures 5.16 and 5.17 for the current results remained stable when considered on a time-averaged basis. Evidence based mainly on the centreline results suggests that this was in fact the case. Spot checks showed that results were repeatable to within close limits and also

values of quantities determined independently showed good agreement, e.g. values of C_f determined using Preston tubes of different diameters agreed quite closely. In addition, when quantities such as C_f and θ were plotted against x, they produced smooth curves. Furthermore, the configurations of peaks and valleys in the transverse C_f/C_{fm} measurements often maintained their form with respect to the wind-tunnel centreline as the flows developed. If in fact the mean transverse flow pattern had varied significantly with time, then this would have meant that it would not have been possible to obtain repeatable results and under these circumstances a study such as this one would have been made much more difficult.

It will be recalled from figure 4.1 that the longitudinal C_f-versus-x distributions for the 2.0 mm pins displayed unusual behaviour for a nominal velocity of 9.0 m/s. Now that transverse C_f/C_{fm} measurements for this device have been presented, a possible explanation for this unusual behaviour can be given. An analysis of figure 4.1 indicates that in the regions where the curve displays unusual behaviour, the difference between the actual curve and that which could reasonably be expected in the absence of imperfections is only about 6%. Furthermore, an analysis of figure 5.16 indicates that in the region of unusual behaviour, the transverse variation of C_f/C_{fm} for a nominal velocity of 10.0 m/s is quite large. For example, at $R_\theta = 770$, which corresponds to x = 0.26 m, C_f/C_{fm} decreases by about 8% on both sides of the wind tunnel centreline over a distance of only 4.5 mm. Assuming that a similar variable flow field also applies for a nominal velocity of 9.0 m/s, then this could account for the unusual behaviour shown in figure 4.1.

CHAPTER 6

ANALYSIS OF BROADBAND-TURBULENCE RESULTS

In this chapter the broadband-turbulence results are presented and analysed. The results are for the u, v and w components of the turbulence and were measured with either the single-wire probe or the rotatable crossed-wire probe. The results comprise profiles of turbulence terms of varying degrees of complexity as well as balances of turbulent kinetic energy and Reynolds shear stress. The methods used to sample and reduce the broadband-turbulence data have been explained in Section 3.11.

As was done for the mean flows, the effects on the broadband-turbulence characteristics of R_θ, tripping device and amount of stimulation, each considered separately, were investigated. This was done by systematically taking broadband-turbulence profiles so that they matched the mean-flow profiles, as shown in table 5.1, and then comparing the turbulence profiles in the manner outlined in Section 5.3. Broadband-turbulence profiles for the u component of the turbulence were taken for understimulated, design and overstimulated flows, whereas profiles for the v and w components of the turbulence were limited to the design flows.

6.1 Verification of Measured Broadband-Turbulence Data

To give some credibility to the broadband-turbulence measurements from these experiments, it was necessary to perform a number of spot checks to verify their accuracy. This involved comparing current results, obtained in different ways, to see if they were consistent amongst themselves, as well as comparing current results with those of other researchers.

The checks on the internal consistency of the results were made using the measurements taken with the Pitot probe and the single- and crossed-hot wire probes for the 1.2 mm wire for the design flow for the most downstream location where the value of R_θ was 2788.

Figure 6.1 shows mean velocities determined using the single hot-wire probe compared with those using the Pitot probe. As can be seen, the agreement between the results for the two instruments is very good. Close to the wall there is a discrepancy of about 3% between the velocities measured by the two instruments, but these differences diminish as y increases. This behaviour is consistent with the use of slightly inaccurate measurements of wall distance in one or both cases. Accurate wall distances for points close to the wall are especially significant when data are plotted semi-logarithmically as in figure 6.1. Uncertainties exist in applying Pitot-probe displacement corrections and difficulties can be encountered in accurately measuring the distance between the hot-wire filament and the wall. For example, a change in the wall distance measurement of about 0.1 mm for the single wire could explain the differences shown for points close to the wall.

Profiles of $\sqrt{\overline{u^2}}/U_\tau$ versus $\log(yU_\tau/\nu)$ for the single-wire probe, the crossed-wire probe in uv mode and the crossed-wire probe in uw mode, are shown superimposed in figure 6.2. As previously, the alternative sets of results agree very well, and in this case the agreement between the three sets of results is generally within 1 or 2%.

For the purpose of comparing the current results with other published data, a turbulence profile was taken with the single-wire probe at x = 1.94 m (the most downstream station) for a nominal reference velocity of 20.0 m/s using the 0.6 mm cylindrical pins tripping device described in Section 5.8. The combination of high velocity and large value of x gave $R_\theta = 5010$, which was the highest value of R_θ measured in these experiments. The profile, plotted as $\sqrt{\overline{u^2}}/U_\tau$ versus $\log(yU_\tau/\nu)$, is shown in figure 6.3 where it is compared with a profile of Purtell, Klebanoff & Buckley (1981) for which $R_\theta = 5100$. Once again there is very good agreement between the alternative sets of results.

The good agreement in the above checks gives credibility to the current data and thus subsequent conclusions can be made on a sound basis.

6.2 Scaling used when Plotting Broadband-Turbulence Data

The broadband-turbulence behaviour may or may not be affected by either the value of R_θ, the tripping device used or the amount of stimulation, but

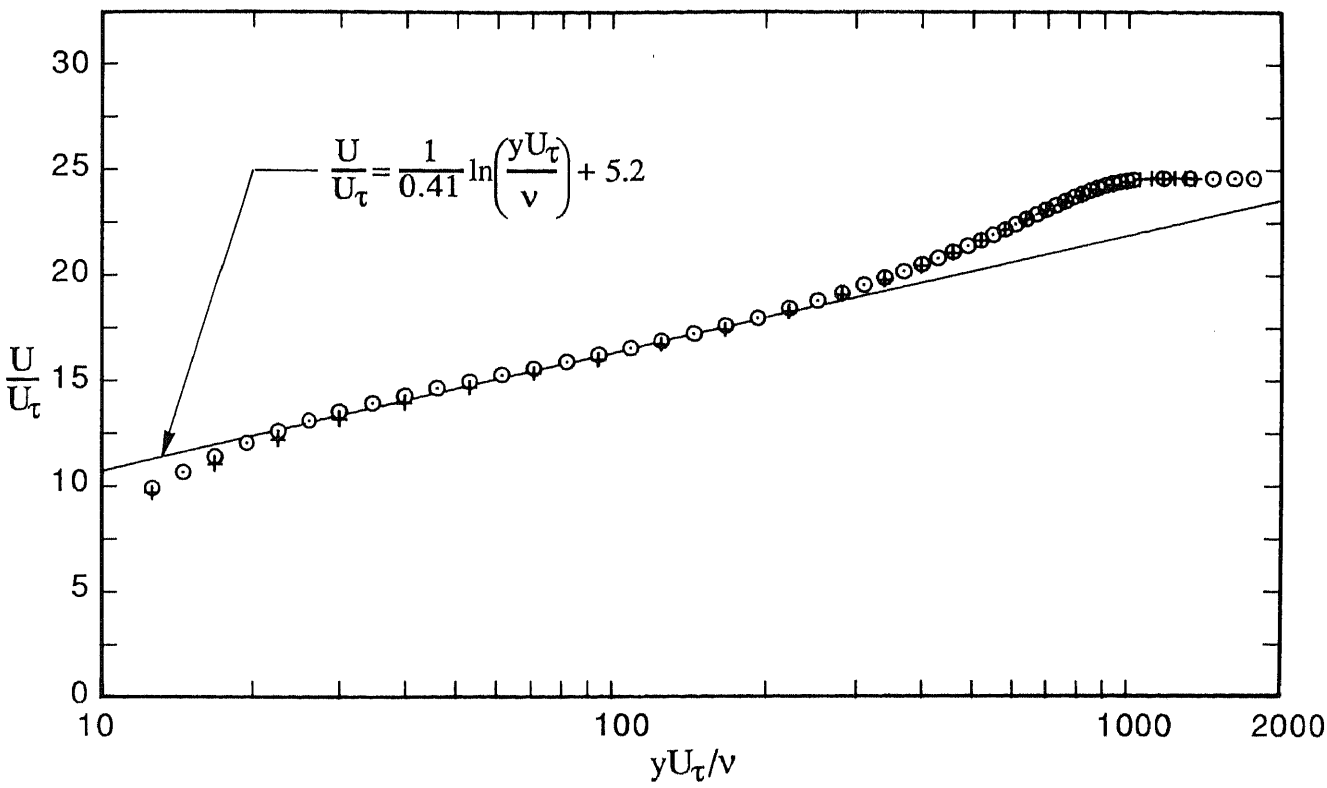

FIGURE 6.1. Profiles of U/U_τ versus $\log(yU_\tau/\nu)$ for the mean velocity for $R_\theta = 2788$ for wire tripping device for design flow.
⊙, Pitot probe measurements; +, single-hot-wire measurements.

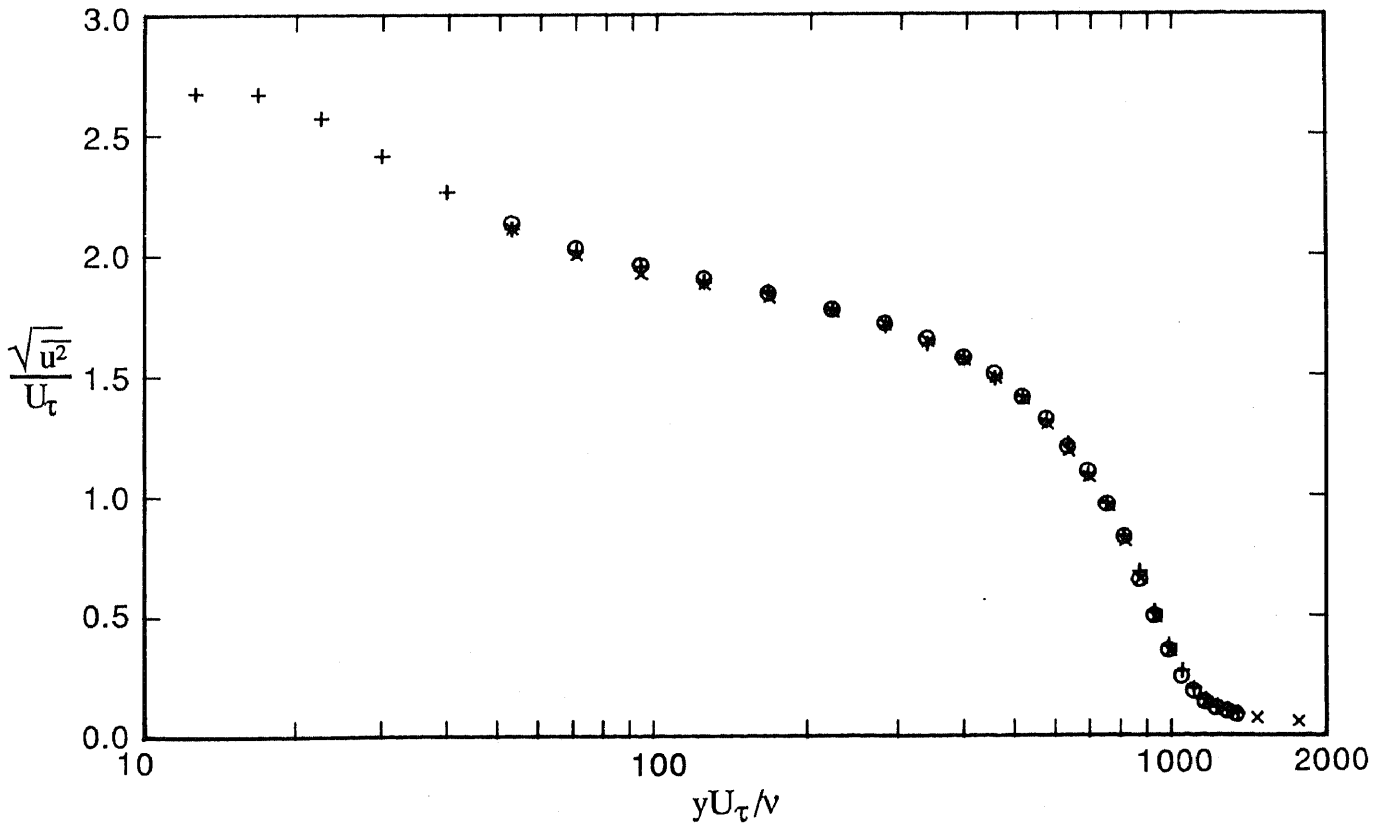

FIGURE 6.2. Profiles of $\sqrt{\overline{u^2}}/U_\tau$ versus $\log(yU_\tau/\nu)$ for $R_\theta = 2788$ for wire tripping device for design flow.
+, single-hot-wire measurements; ×, uv mode crossed-hot-wire measurements;
⊙, uw mode crossed-hot-wire measurements.

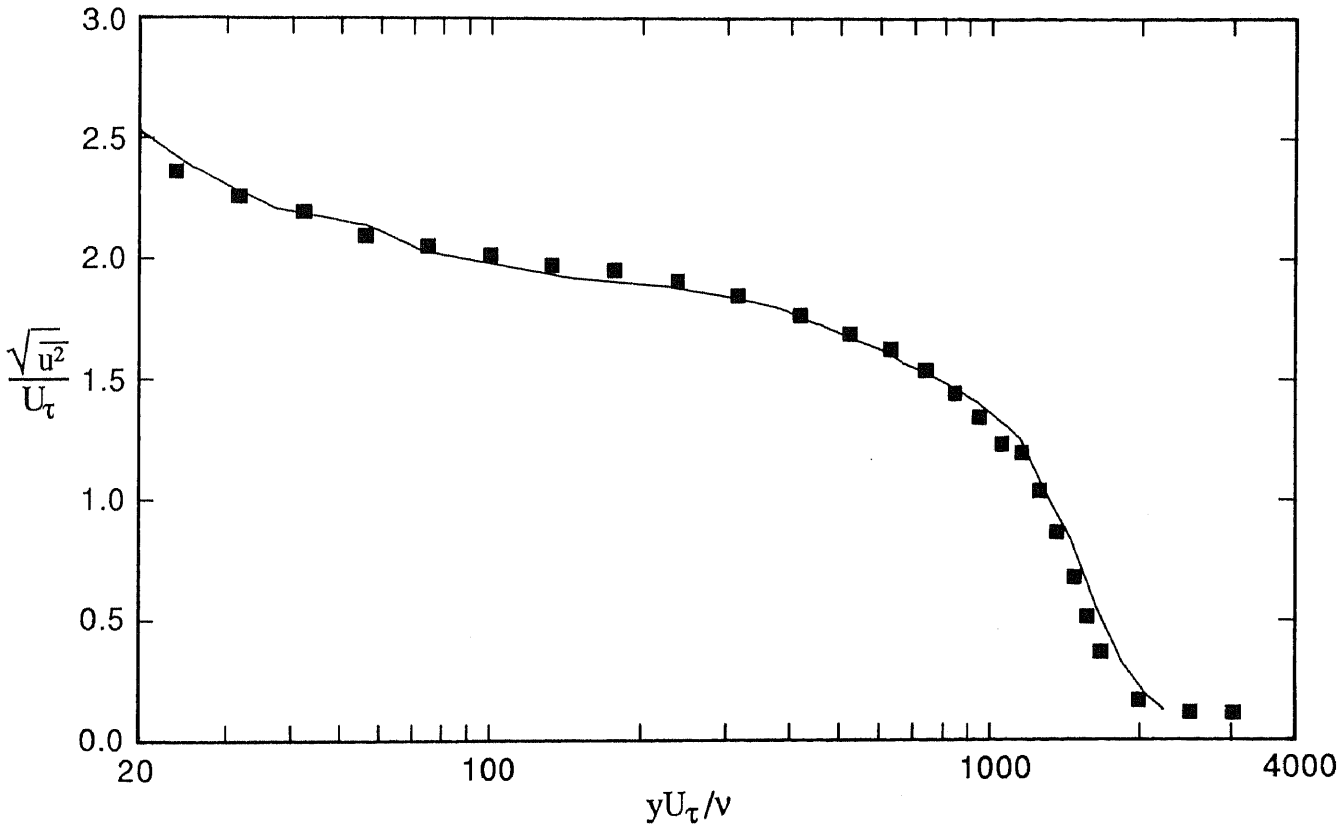

FIGURE 6.3. Profile of $\sqrt{\overline{u^2}}/U_\tau$ versus $\log(yU_\tau/\nu)$ for current investigation, having R_θ = 5010, compared with profile of Purtell, Klebanoff & Buckley (1981), having R_θ = 5100.

———, profile of Purtell, Klebanoff & Buckley.

■, profile of current investigation.

whether or not the effects of these different factors are apparent when the data are plotted, can depend upon the scaling used on that plot. In the following, the broadband-turbulence profiles are plotted using different types of scaling. The velocity scaling factor used is either U_e or U_τ, with these velocities used either as single quantities or else quantities raised to some power. Both types of scaling have their merits. U_e is constant for a given zero pressure gradient flow, so the use of this scaling factor means that profiles corresponding to different values of x for such a flow have the same velocity scaling factor applied to them. Thus such profiles are effectively compared as if they have no velocity scaling at all. On the other hand, U_τ varies with x in a zero pressure gradient flow, so the use of this scaling factor means that profiles corresponding to different values of x for such a flow are each factored differently. When U_e is used as a scaling factor, uncertainties arising out of possible inaccuracies in the measurement of U_τ are eliminated. The length scaling factor used is a boundary-layer thickness, such as δ or δ^*, or alternatively ν/U_τ.

If different profiles do not collapse for a particular type of scaling, then this will highlight how the flow depends upon either the value of R_θ, the tripping device or the degree of stimulation. Such a presentation of data may be of help when giving a physical explanation of flow behaviour. Alternatively, if different profiles do show a good degree of collapse, then this information will be useful to researchers such as those devising prediction methods. A relationship that is independent of one or more of the above three factors will be more useful in prediction methods than one that is dependent on these factors.

6.3 Broadband-Turbulence Characteristics for Correctly-Stimulated Flows

It was shown in Section 5.4 that the mean-flow characteristics for the three devices for the design flows were dependent on R_θ and virtually independent of device, when the data were plotted using coordinates of U/U_τ-versus-$\log(yU_\tau/\nu)$ (figures 5.5 and 5.6) and $(U-U_e)/U_\tau$ versus y/δ (figures 5.8 and 5.9). Thus it was of interest to see whether or not the broadband-turbulence characteristics for these flows displayed similar behaviour when plotted using different types of scaling.

To check on similarity for the design flows, forty five broadband-turbulence profiles were taken and details of these are documented in groups 1 to 5 of table 5.1. The forty five turbulence profiles consisted of fifteen taken with the single-wire probe, fifteen taken with the crossed-wire probe in uv mode and fifteen taken with the crossed-wire probe in uw mode.

Initially Reynolds normal stresses for the three coordinate directions will be presented, followed by Reynolds shear stresses and triple products. These basic quantities will be followed by derived quantities consisting of anisotropy parameters, skewness and flatness factors, terms in the balances of turbulent kinetic energy and Reynolds shear stress, eddy viscosities and mixing lengths, dissipation length parameters and turbulent transport velocities.

6.3.1 Reynolds Normal Stresses

Profiles of $\overline{u^2}/U_e^2$ versus y/δ are shown plotted in figure 6.4 so as to indicate the effects on the profiles of variations in R_θ for each of the three devices. This figure is analogous to figure 5.5 for the mean flow. The profiles shown in figure 6.4 were all taken with the single-wire probe. It is apparent from figure 6.4 that with this scaling, the profiles for the three devices depend on R_θ, but the extent of the dependency varies throughout the y/δ range. For the three devices, the variation of the profiles with R_θ is greatest near the wall, but diminishes with increasing y/δ. If the measurements for $R_\theta \approx 713$ for each of the devices are disregarded, then beyond $y/\delta \approx 0.3$, the profiles collapse well for each of the devices and exhibit an approximately linear variation with y/δ out to $y/\delta \approx 0.9$. Since the wall region, as determined from a mean-flow plot of U/U_τ versus $\log(yU_\tau/\nu)$ (see figure 5.5), was found to extend to $y/\delta \approx 0.25$ for $R_\theta \approx 713$ and to $y/\delta \approx 0.2$ for $R_\theta \approx 2810$, then when the scaling of figure 6.4 is used, the effects of R_θ are most pronounced in the wall region or slightly beyond. For the three devices, the profiles show a monotonic trend with R_θ, except for the pins for $R_\theta = 729$ for y/δ greater than about 0.2, and in each case the differences between the profiles for $R_\theta \approx 2175$ and $R_\theta \approx 2810$ are quite small.

To investigate the possible dependency of the profiles of $\overline{u^2}/U_e^2$ versus y/δ upon the device, at each of five nominal values of R_θ, the data in figure 6.4 were replotted as shown in figure 6.5. The replotted data has the same scaling

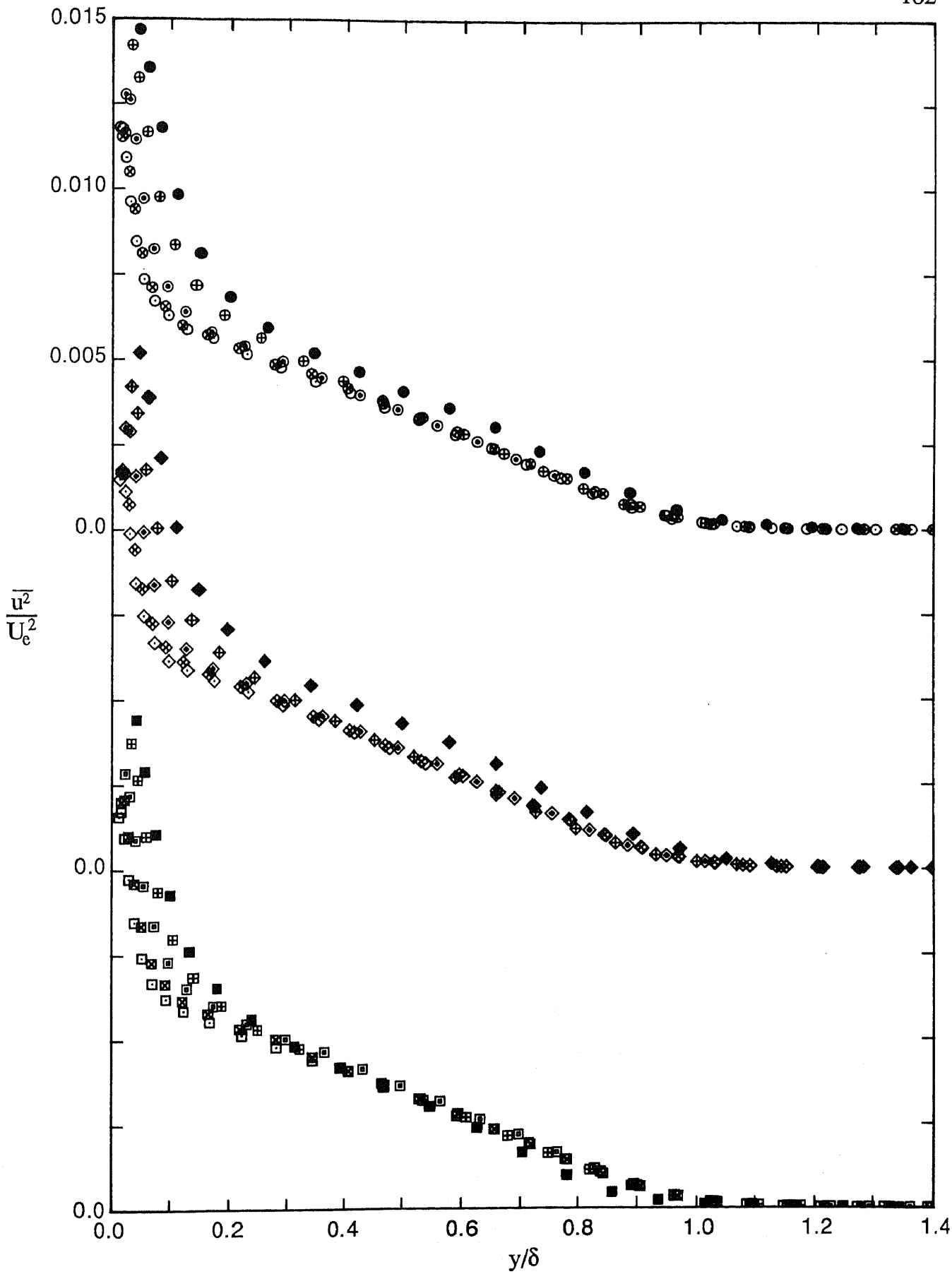

FIGURE 6.4. Profiles of $\overline{u^2}/U_e^2$ versus y/δ for design flows showing effects of R_θ for three devices. Note shift in ordinate.

Wire:	●, R_θ=697;	⊕, 1003;	⊙, 1568;	⊗, 2226;	⊙, 2788.
Grit:	◆, R_θ=706;	◈, 1042;	◇, 1520;	◈, 2178;	◇, 2730.
2.0 mm pins:	■, R_θ=729;	⊞, 1027;	⊡, 1565;	⊠, 2181;	⊡, 2889.

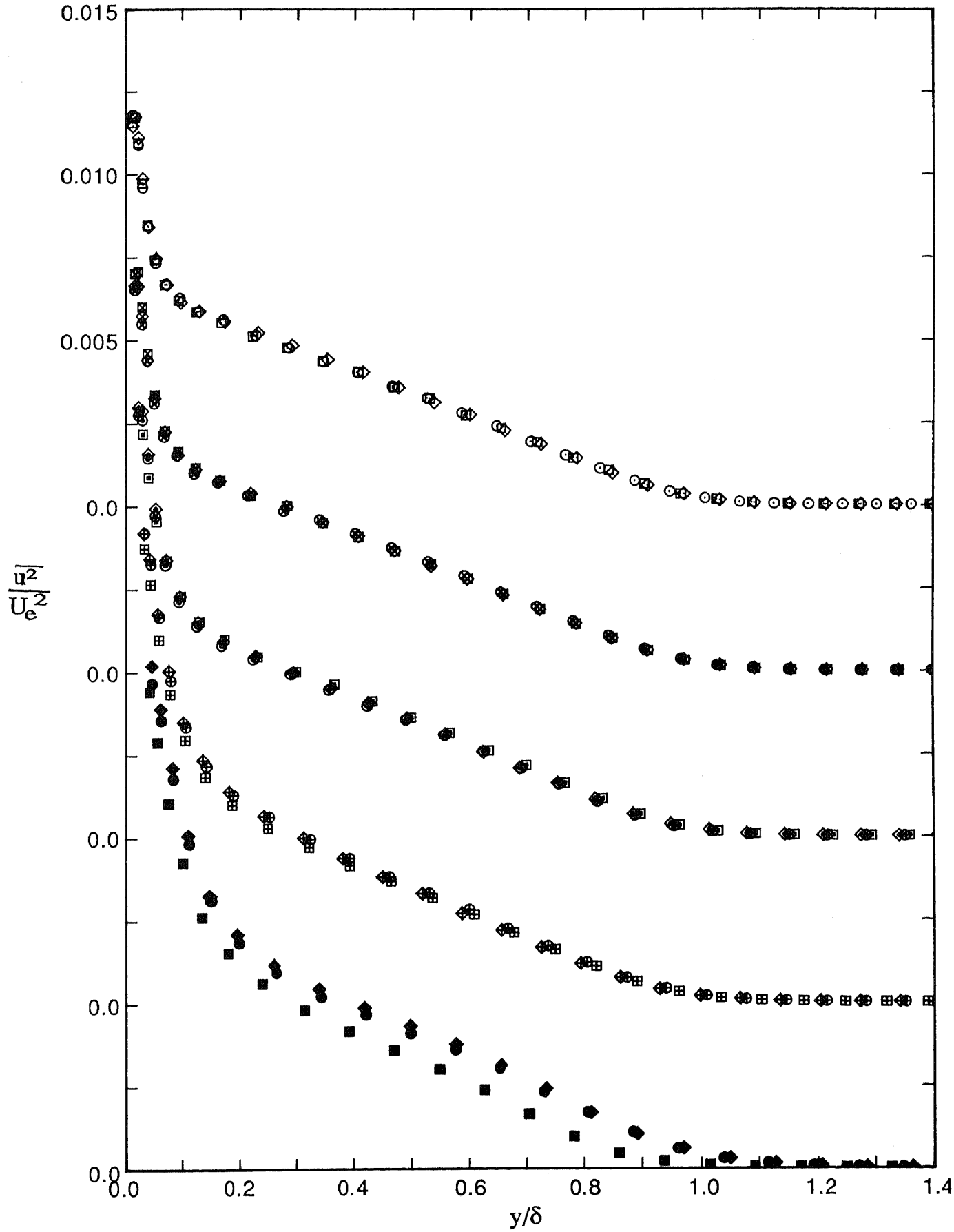

FIGURE 6.5. Profiles of $\overline{u^2}/U_e^2$ versus y/δ for design flows showing effects of device for five nominal values of R_θ. Note shift in ordinate.

Wire:	●, R_θ=697;	⊕, 1003;	⊙, 1568;	⊗, 2226;	⊙, 2788.
Grit:	◆, R_θ=706;	◈, 1042;	◇, 1520;	◈, 2178;	◇, 2730.
2.0 mm pins:	■, R_θ=729;	⊞, 1027;	⊡, 1565;	⊠, 2181;	⊡, 2889.

as previously, but is now in a form that enables corresponding $\overline{u^2}/U_e^2$ profiles for the different devices to be readily compared. Figure 6.5 is analogous to figure 5.6 for the mean flow. An analysis of figure 6.5 indicates that with this scaling, the profiles for the three devices do not agree at $R_\theta \approx 713$, but for $R_\theta \approx 1020$ and above, the type of device used has only a small or negligible effect on the profiles. For $R_\theta \approx 713$, the overall variation of the profiles is far greater in percentage terms than that for the corresponding mean-flow profiles shown in figures 5.6 and 5.9. This matter will be discussed in detail at the end of Section 6.3.3, which deals with triple products.

It is desirable to extend the above analysis using different types of scaling. The data contained in figure 6.4 are shown replotted in figure 6.6 using coordinates of $\overline{u^2}/U_\tau^2$ versus y/δ but with other features of figure 6.4 unaltered. It is apparent from figure 6.6 that the use of the different scaling significantly alters the appearance of the plotted data compared with that shown in figure 6.4. The data for the lower values of R_θ have been factored down relative to the data for the higher values of R_θ, according to the variations in U_τ throughout the R_θ range. The profiles for the three devices still, however, depend upon the value of R_θ. With the change in scaling, the profiles for y/δ less than 0.2 or 0.3 have far less variation than previously for each of the devices. The profiles for the different devices show monotonic trends with R_θ, except for $R_\theta = 697$ for the wire and $R_\theta = 706$ for the grit for y/δ greater than about 0.4 in both cases. Once again, for the three devices, the differences between the profiles for $R_\theta \approx 2175$ and $R_\theta \approx 2810$ are quite small.

It is also possible to replot the data contained in figure 6.5 and obtain a corresponding plot having coordinates of $\overline{u^2}/U_\tau^2$ versus y/δ. However, it was not worthwhile doing this since the replotted data would convey essentially the same information as that shown in figure 6.5. If the replotting were done, then for each of the five nominal values of R_θ, the profiles for the three devices would exhibit approximately the same relationship with each other as they do in figure 6.5, since values of U_τ for the three devices for a given value of R_θ are approximately the same. However, since U_τ varies with R_θ, profiles associated with a given set would be factored significantly differently from profiles within other sets, unlike when the data are plotted as in figure 6.5, where U_e is nominally the same for all profiles.

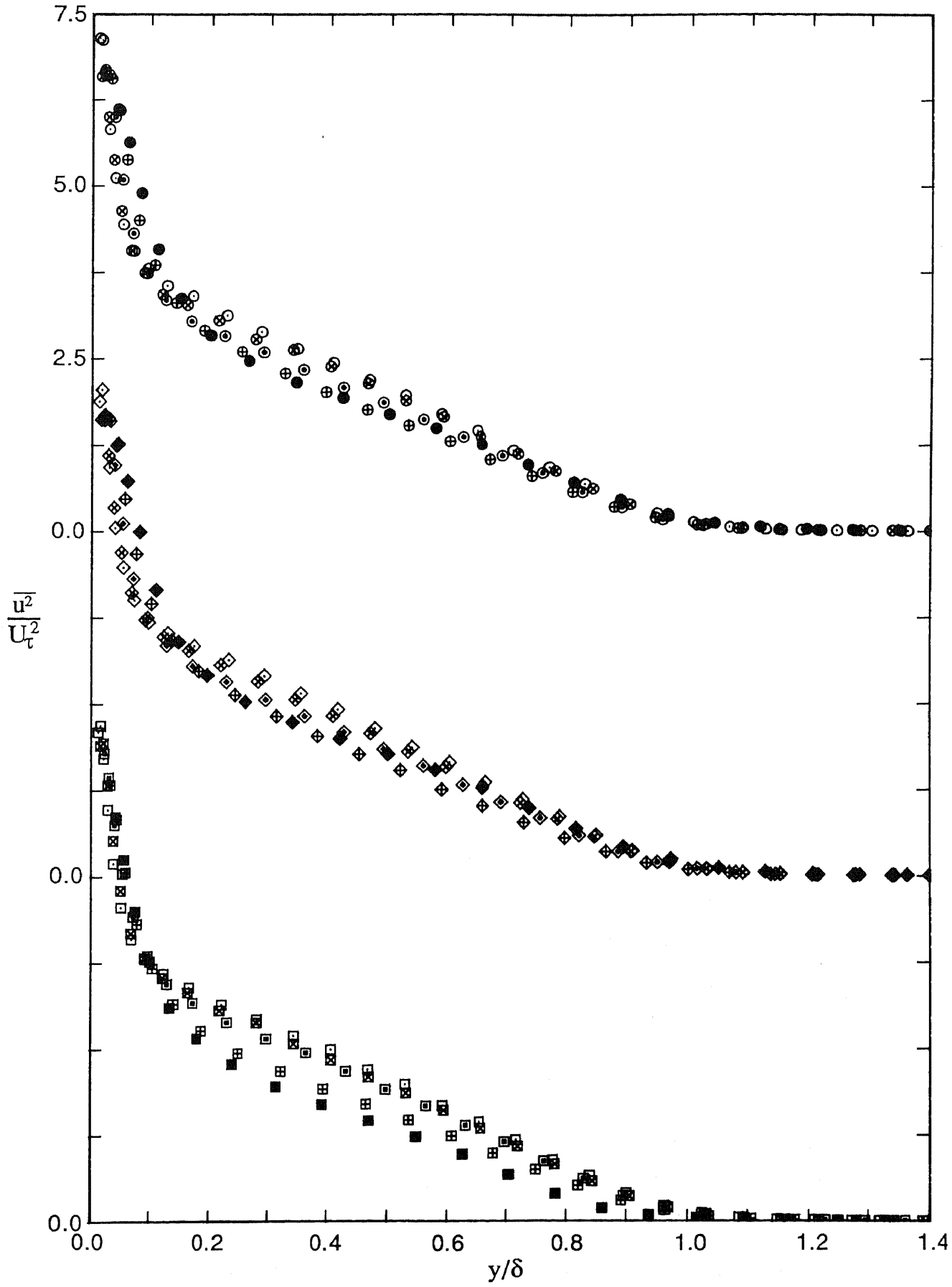

FIGURE 6.6. Profiles of $\overline{u^2}/U_\tau^2$ versus y/δ for design flows showing effects of R_θ for three devices. Note shift in ordinate.

Wire: ●, R_θ=697; ⊕, 1003; ⊙, 1568; ⊗, 2226; ⊙, 2788.
Grit: ◆, R_θ=706; ⊕, 1042; ◇, 1520; ◈, 2178; ◇, 2730.
2.0 mm pins: ■, R_θ=729; ⊞, 1027; ▣, 1565; ⊠, 2181; ⊡, 2889.

The $\overline{v^2}$ Reynolds normal stresses were scaled and plotted as in figures 6.4 to 6.6 for the $\overline{u^2}$ normal stresses.

Figure 6.7 shows profiles of $\overline{v^2}/U_e^2$ versus y/δ and this figure corresponds to figure 6.4 for the u-component data. From figure 6.7 it can be seen that, with this scaling, the profiles for the three devices are strongly Reynolds number dependent near the wall, but the dependency decreases as y/δ increases. Since the v- and w-component broadband-turbulence data were measured with the crossed-wire probe, it was not possible to take v- and w-component measurements as close to the wall as for the u-component measurements. Similarities can be seen to exist between the u and v component data. In particular, for each of the devices, the $\overline{v^2}/U_e^2$ profiles show monotonic trends with R_θ, except for the profile for the pins for $R_\theta = 729$. Also, the differences between the profiles for $R_\theta \approx 2175$ and $R_\theta \approx 2810$ are once again quite small.

Profiles of $\overline{v^2}/U_e^2$ versus y/δ are shown in figure 6.8 and this figure corresponds to figure 6.5 for the u-component data. It can be seen from figure 6.8 that the collapse of the $\overline{v^2}/U_e^2$ profiles for different values of R_θ for the three devices is not as good as for the corresponding $\overline{u^2}/U_e^2$ profiles shown in figure 6.5, but except for $R_\theta \approx 713$, corresponding $\overline{v^2}/U_e^2$ profiles still collapse reasonably well, indicating that for $R_\theta \approx 1020$ and above, the effect of device on the profiles is reasonably small. In fact the slight variations for $R_\theta \approx 1020$ and above could well be due to the fact that it is more difficult to obtain accurate measurements using a crossed-wire probe than using a single-wire probe.

Figure 6.9 shows profiles of $\overline{v^2}/U_\tau^2$ versus y/δ and this figure corresponds to figure 6.6 for the u-component data. When the data are expressed in the form $\overline{v^2}/U_\tau^2$, rather than the form $\overline{v^2}/U_e^2$, shown in figure 6.7, then the appearance of the plotted data changes and the dependency of the data on R_θ is now different from previously. It is apparent from figure 6.9 that the profiles show deviations from monotonic trends with R_θ. Figure 6.9 also shows that there are often appreciable differences between the profiles corresponding to $R_\theta \approx 2175$ and $R_\theta \approx 2810$, and the same trend is evident for all three devices.

The $\overline{w^2}$ Reynolds normal stresses were scaled and plotted in the same way as both the $\overline{u^2}$ and $\overline{v^2}$ normal stresses. The w-component data are shown plotted

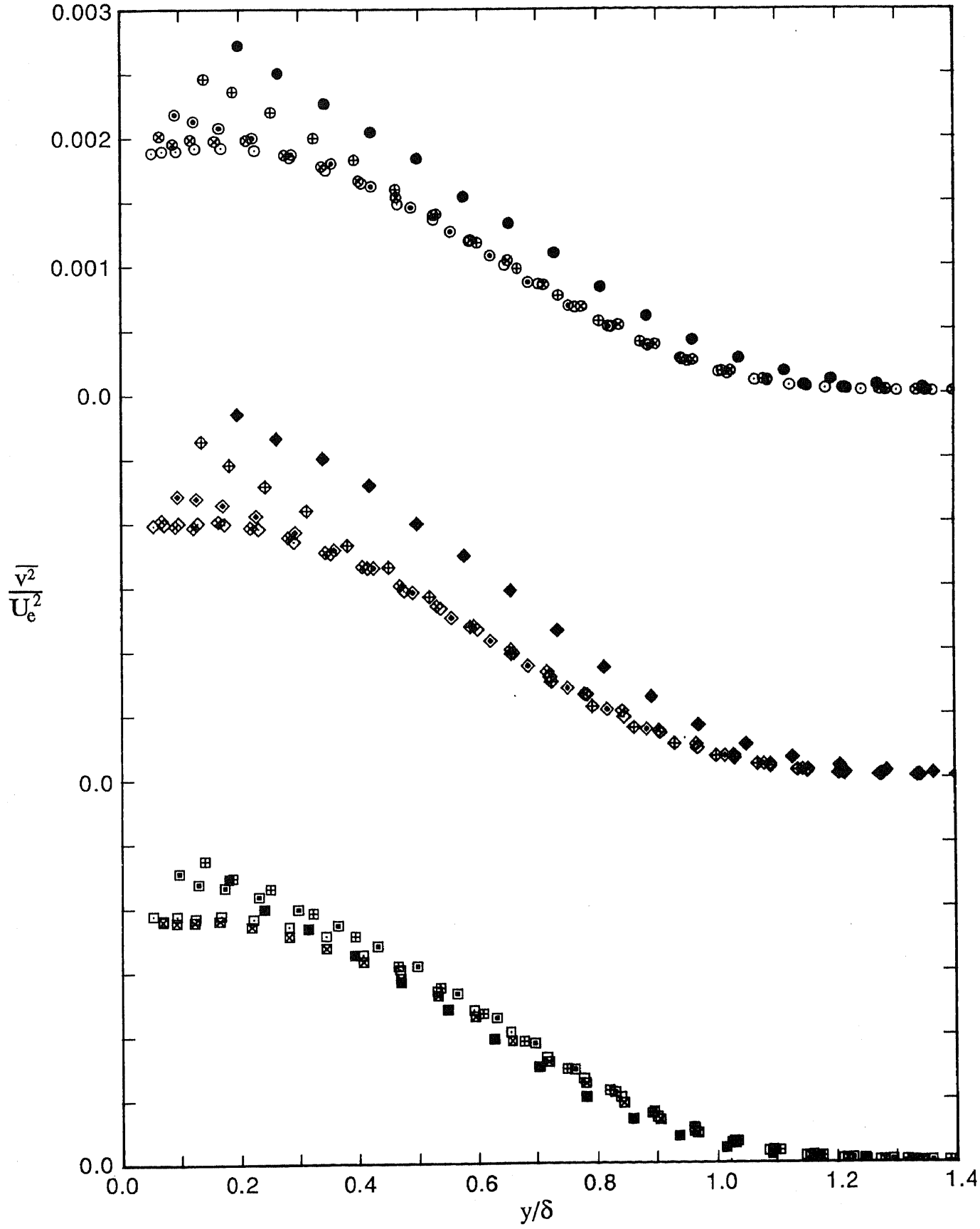

FIGURE 6.7. Profiles of $\overline{v^2}/U_e^2$ versus y/δ for design flows showing effects of R_θ for three devices. Note shift in ordinate.

Wire: ●, R_θ=697; ⊕, 1003; ⊙, 1568; ⊗, 2226; ⊙, 2788.
Grit: ◆, R_θ=706; ⊕, 1042; ◇, 1520; ◈, 2178; ◇, 2730.
2.0 mm pins: ■, R_θ=729; ⊞, 1027; ⊡, 1565; ⊠, 2181; ⊡, 2889.

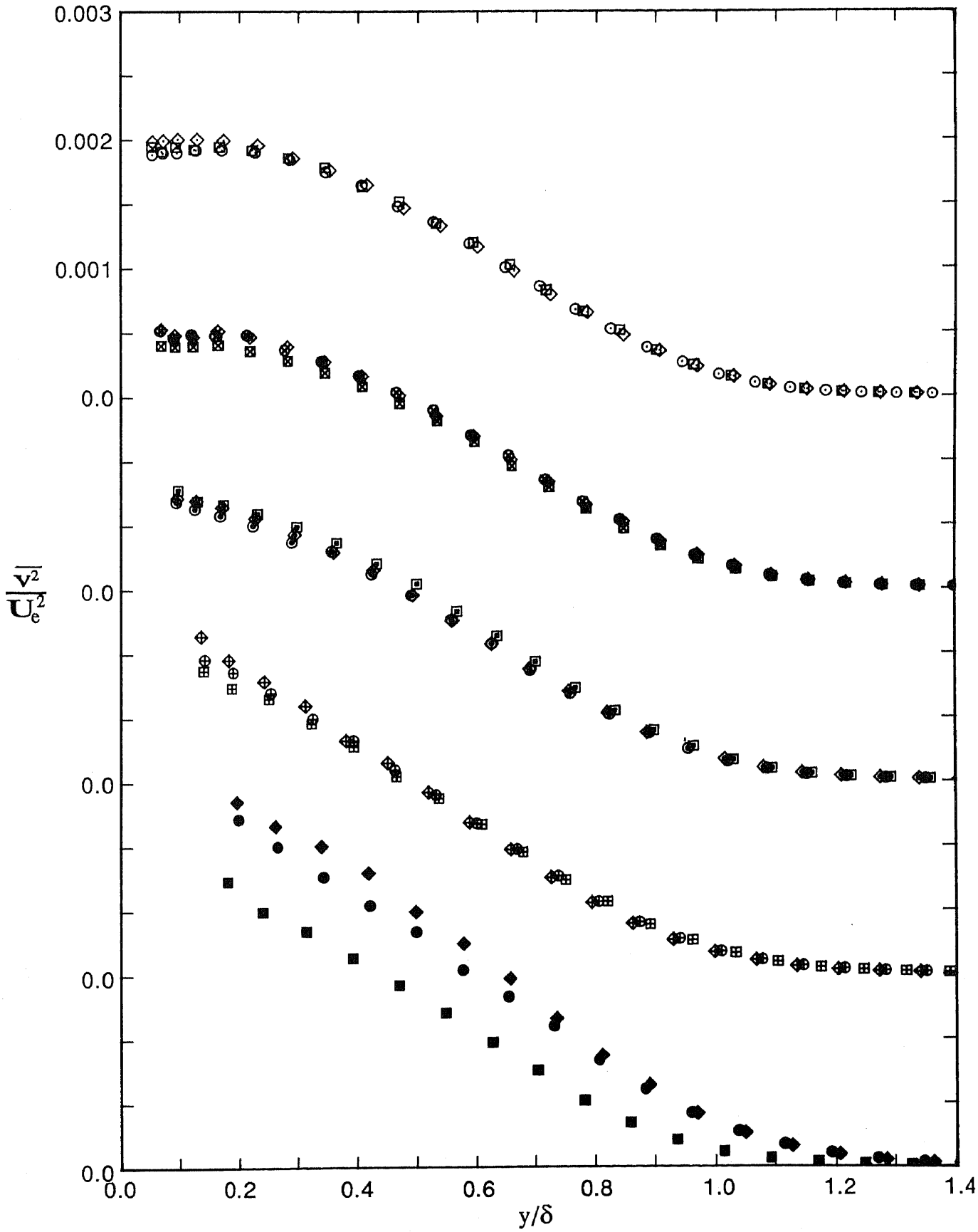

FIGURE 6.8. Profiles of $\overline{v^2}/U_e^2$ versus y/δ for design flows showing effects of device for five nominal values of R_θ. Note shift in ordinate.

Wire:	●, R_θ=697;	⊕, 1003;	⊙, 1568;	⊗, 2226;	⊙, 2788.
Grit:	◆, R_θ=706;	◈, 1042;	◇, 1520;	◈, 2178;	◇, 2730.
2.0 mm pins:	■, R_θ=729;	⊞, 1027;	⊡, 1565;	⊠, 2181;	⊡, 2889.

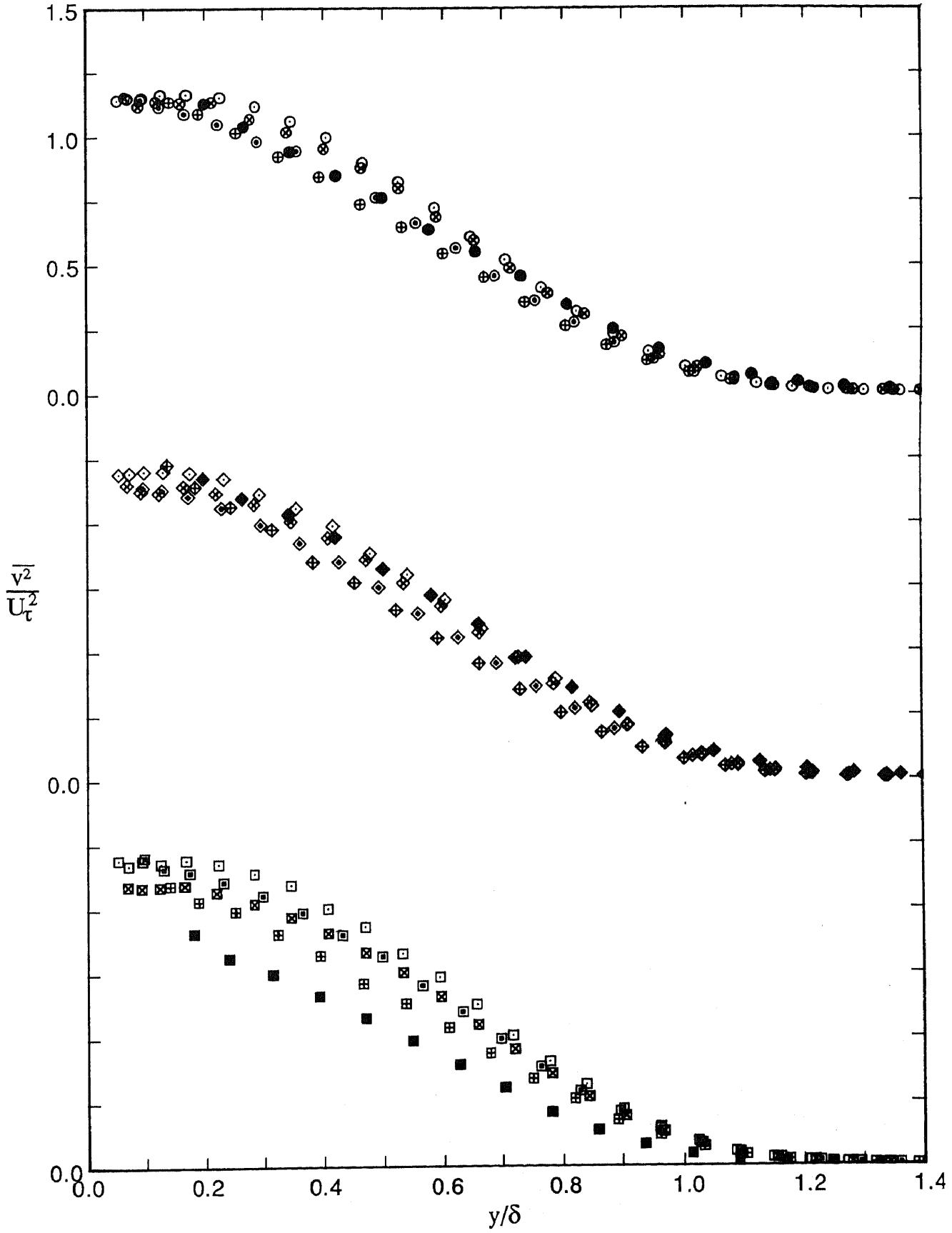

FIGURE 6.9. Profiles of $\overline{v^2}/U_\tau^2$ versus y/δ for design flows showing effects of R_θ for three devices. Note shift in ordinate.

Wire:	●, R_θ=697;	⊕, 1003;	⊙, 1568;	⊗, 2226;	⊙, 2788.
Grit:	◆, R_θ=706;	◈, 1042;	◇, 1520;	◈, 2178;	◇, 2730.
2.0 mm pins:	■, R_θ=729;	⊞, 1027;	▣, 1565;	⊠, 2181;	⊡, 2889.

in figures 6.10 to 6.12 and these figures correspond to figures 6.4 to 6.6 respectively for the u-component data.

An analysis of figures 6.10 to 6.12 indicates that the shapes and sizes of the profiles of $\overline{w^2}/U_e^2$ versus y/δ or $\overline{w^2}/U_\tau^2$ versus y/δ are different from those for the corresponding v-component data shown in figures 6.7 to 6.9 respectively, but in other ways the behaviour of both the w- and v-component data is substantially the same. Since discussion already given for the v-component data also applies to the w-component data, then to avoid repetition, no such discussion on the behaviour of the w-component data will be given. However, it is worth reiterating that very few measurements involving $\overline{w^2}$ normal stresses, such as those shown in figures 6.10 to 6.12, have been published in the literature.

Often profiles are plotted using $\sqrt{\overline{u^2}}/U_\tau$ as the ordinate, rather than $\overline{u^2}/U_\tau^2$, and likewise for the v- and w-component data. Figures 6.13 and 6.14 show profiles of $\sqrt{\overline{u^2}}/U_\tau$ versus y/δ and these profiles were all taken using the single-wire probe. The use of this scaling causes the profiles to have less variation than when the data are plotted using coordinates of $\overline{u^2}/U_\tau^2$ versus y/δ, but this is obviously a consequence of representing the same scaling in an alternative way rather than the introduction of new physical considerations.

The data contained in figures 6.13 and 6.14 were replotted using coordinates of $\sqrt{\overline{u^2}}/U_\tau$ versus $\log(yU_\tau/\nu)$ as shown in figures 6.15 and 6.16 respectively.

It is apparent from figure 6.15, that with this type of scaling, the profiles for each of the devices are strongly Reynolds number dependent. Also there is no obvious collapse of the data for any of the values of yU_τ/ν shown. This is in contrast to the behaviour of the corresponding mean-flow data shown in figure 5.5, in which the data within the wall regions for each of the devices collapse for all values of R_θ.

An analysis of figure 6.16 indicates that for this scaling, the type of device used has a small or negligible effect on the profiles for $R_\theta \approx 1020$ and above. When figure 6.16 is compared with figure 6.14 it can be seen that using

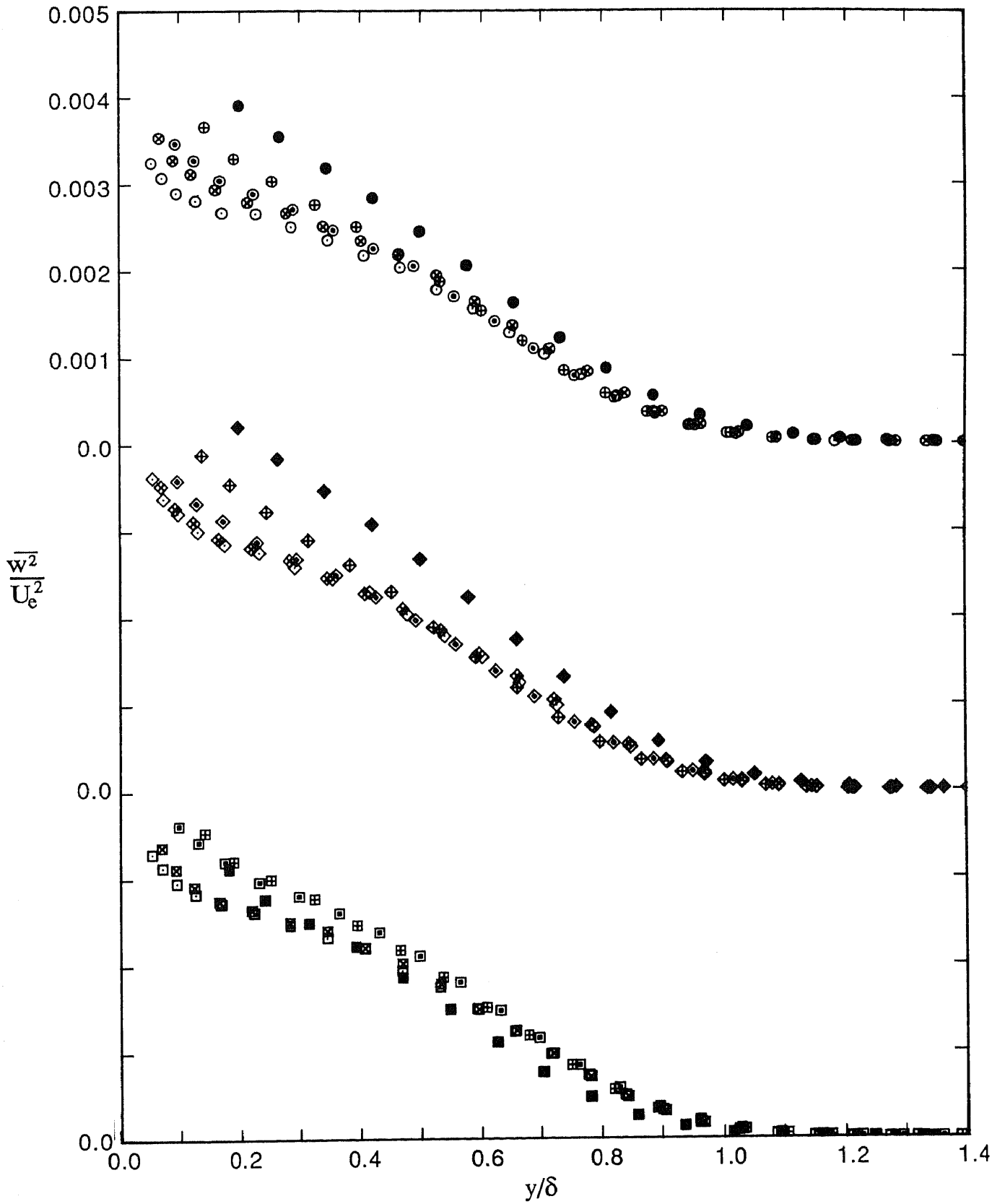

FIGURE 6.10. Profiles of $\overline{w^2}/U_e^2$ versus y/δ for design flows showing effects of R_θ for three devices. Note shift in ordinate.

Wire:	●, R_θ=697;	⊕, 1003;	⊙, 1568;	⊗, 2226;	⊙, 2788.
Grit:	◆, R_θ=706;	◈, 1042;	◇, 1520;	◈, 2178;	◇, 2730.
2.0 mm pins:	■, R_θ=729;	⊞, 1027;	⊡, 1565;	⊠, 2181;	⊡, 2889.

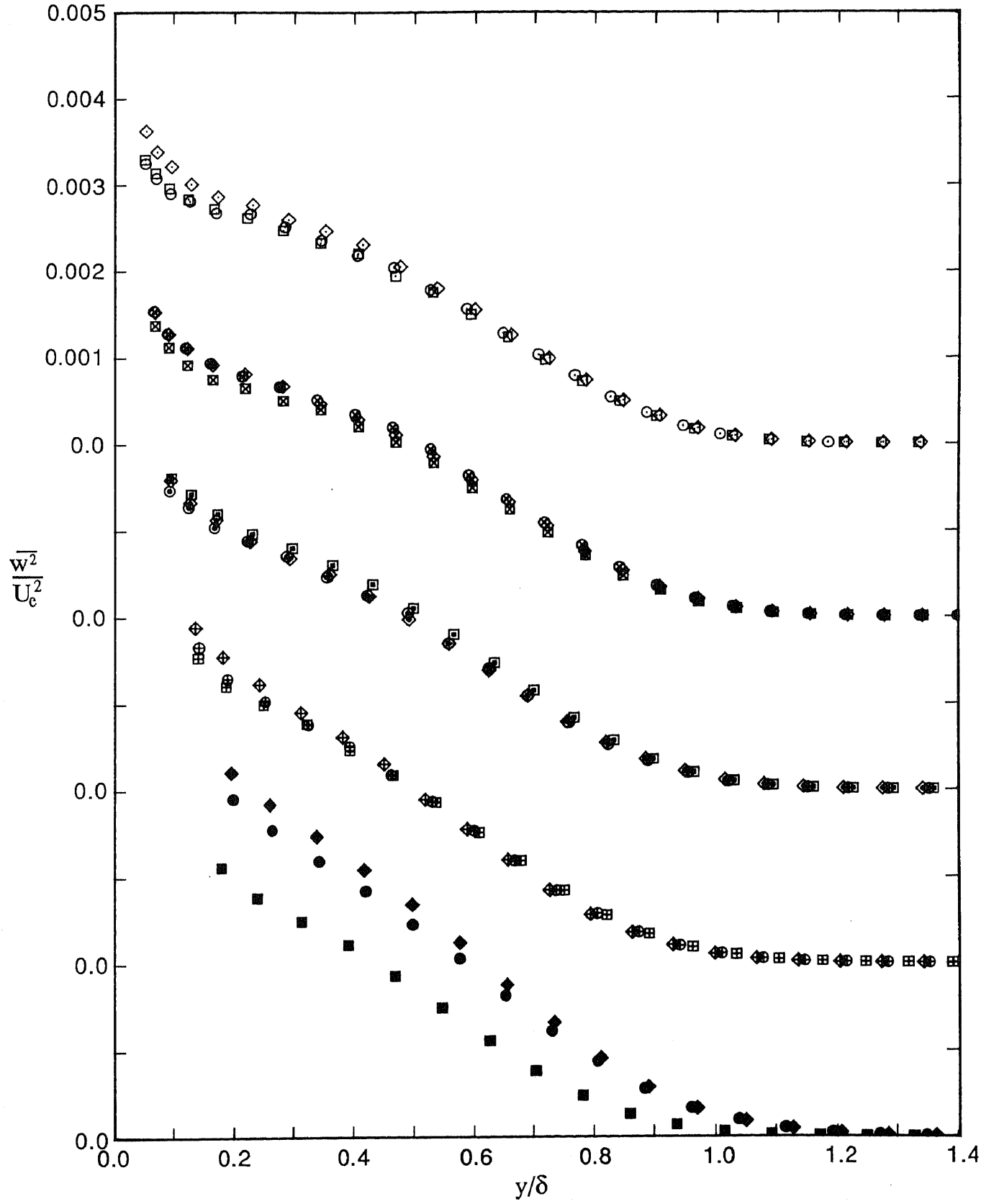

FIGURE 6.11. Profiles of $\overline{w^2}/U_e^2$ versus y/δ for design flows showing effects of device for five nominal values of R_θ. Note shift in ordinate.

Wire:	●, R_θ=697;	⊕, 1003;	⊙, 1568;	⊗, 2226;	⊙, 2788.
Grit:	◆, R_θ=706;	◈, 1042;	◇, 1520;	◈, 2178;	◇, 2730.
2.0 mm pins:	■, R_θ=729;	⊞, 1027;	⊡, 1565;	⊠, 2181;	⊡, 2889.

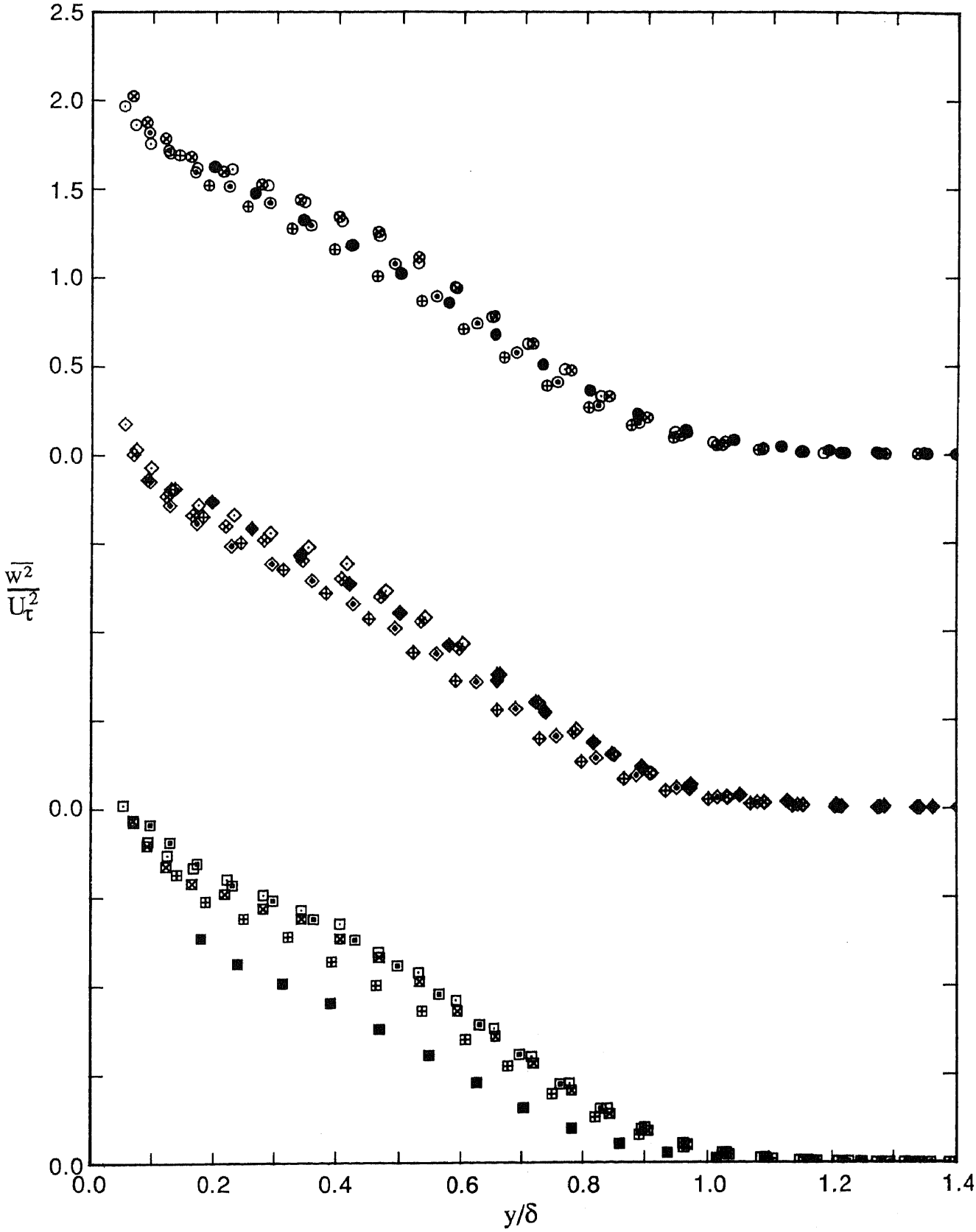

FIGURE 6.12. Profiles of $\overline{w^2}/U_\tau^2$ versus y/δ for design flows showing effects of R_θ for three devices. Note shift in ordinate.

Wire:	●, R_θ=697;	⊕, 1003;	⊙, 1568;	⊗, 2226;	⊙, 2788.
Grit:	◆, R_θ=706;	◈, 1042;	◈, 1520;	◈, 2178;	◇, 2730.
2.0 mm pins:	■, R_θ=729;	⊞, 1027;	⊡, 1565;	⊠, 2181;	⊡, 2889.

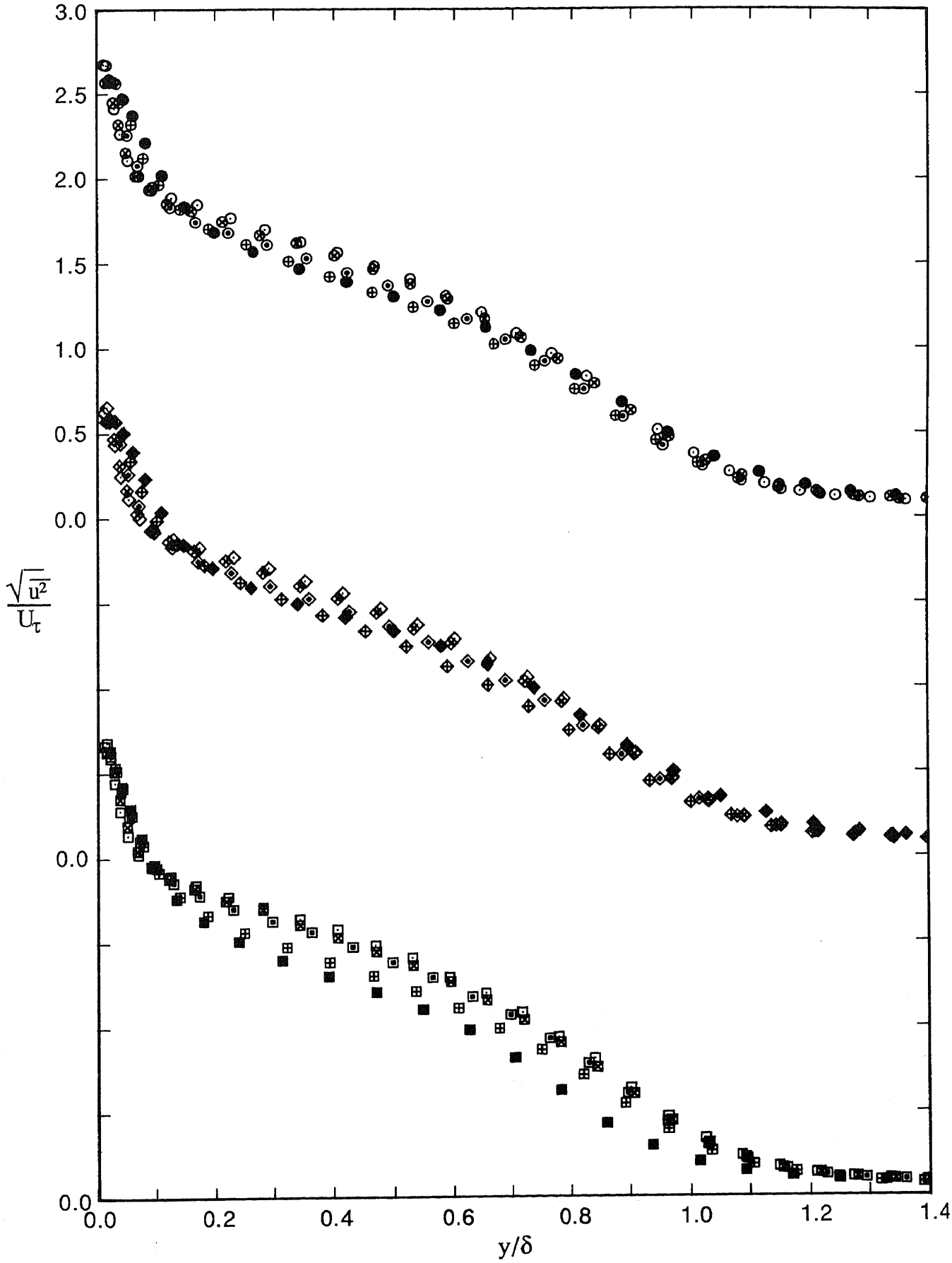

FIGURE 6.13. Profiles of $\sqrt{\overline{u^2}}/U_\tau$ versus y/δ for design flows showing effects of R_θ for three devices. Note shift in ordinate.

Wire:	●, R_θ=697;	⊕, 1003;	⊙, 1568;	⊗, 2226;	⊙, 2788.
Grit:	◆, R_θ=706;	◈, 1042;	◇, 1520;	◈, 2178;	◇, 2730.
2.0 mm pins:	■, R_θ=729;	⊞, 1027;	▣, 1565;	⊠, 2181;	⊡, 2889.

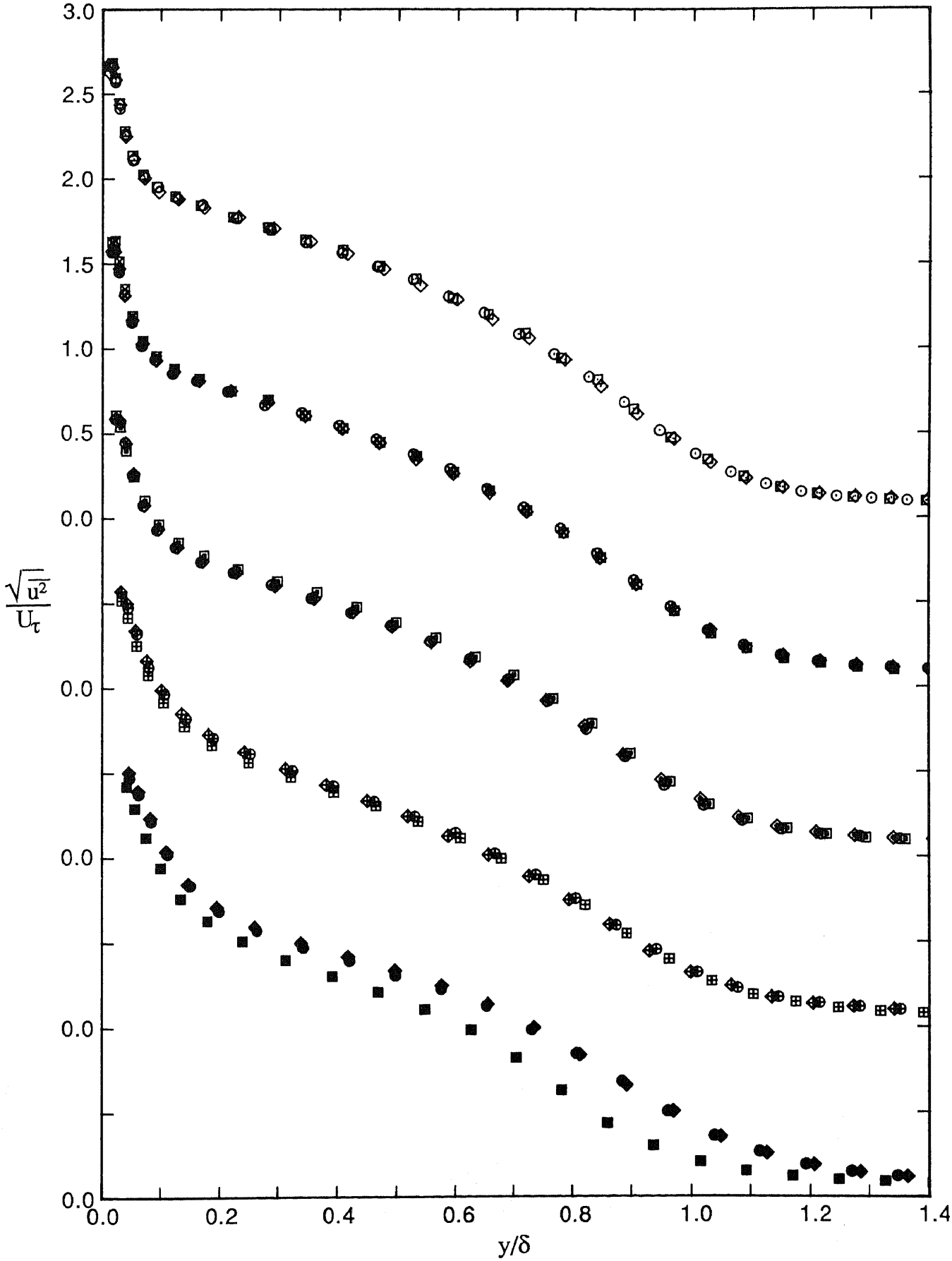

FIGURE 6.14. Profiles of $\sqrt{u^2}/U_\tau$ versus y/δ for design flows showing effects of device for five nominal values of R_θ. Note shift in ordinate.

Wire:	●, R_θ=697;	⊕, 1003;	⊙, 1568;	⊗, 2226;	⊙, 2788.
Grit:	◆, R_θ=706;	◈, 1042;	◇, 1520;	◈, 2178;	◇, 2730.
2.0 mm pins:	■, R_θ=729;	⊞, 1027;	▣, 1565;	⊠, 2181;	□, 2889.

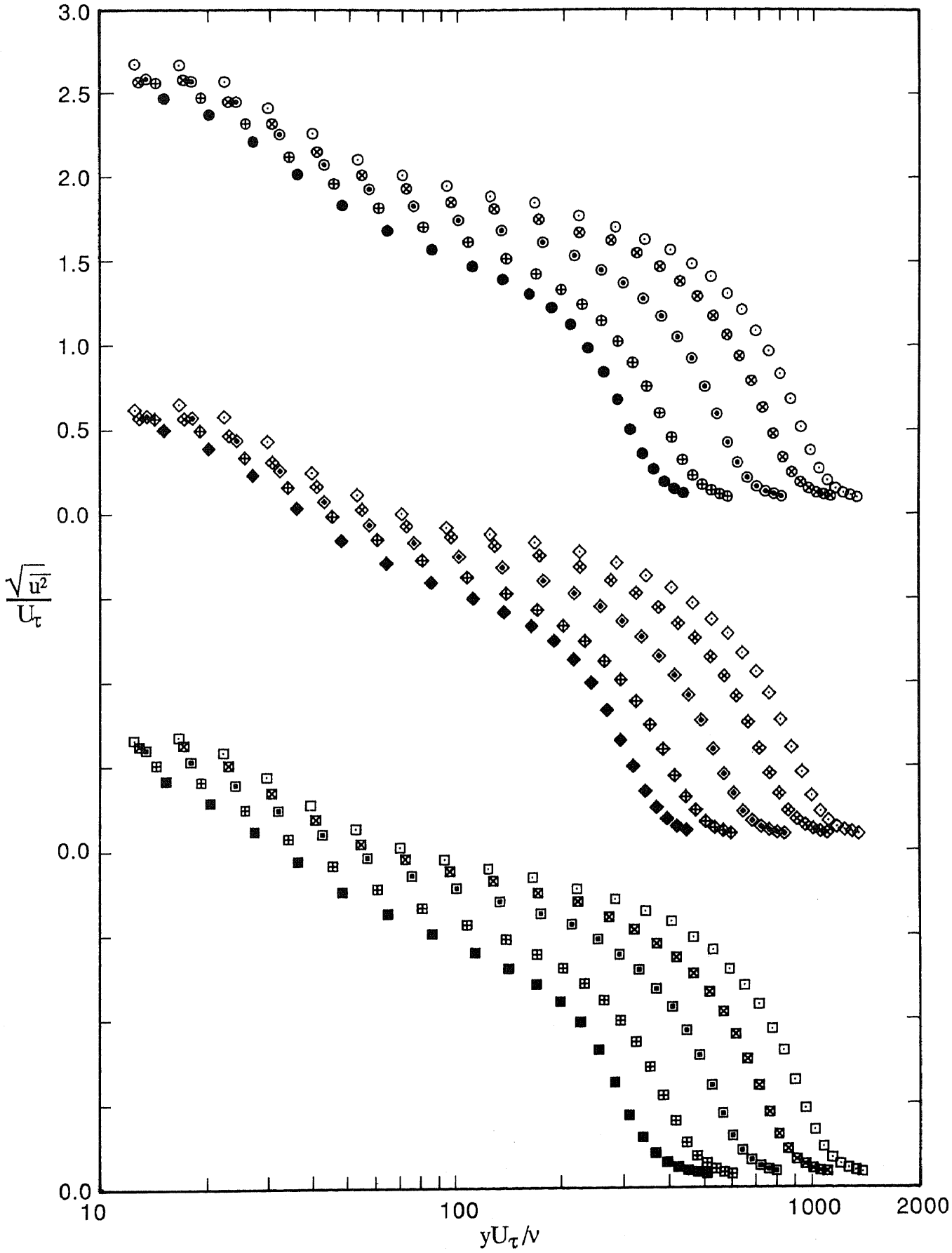

FIGURE 6.15. Profiles of $\sqrt{u^2}/U_\tau$ versus $\log(yU_\tau/\nu)$ for design flows showing effects of R_θ for three devices. Note shift in ordinate.

Wire:	●, R_θ=697;	⊕, 1003;	⊙, 1568;	⊗, 2226;	⊙, 2788.
Grit:	◆, R_θ=706;	◈, 1042;	◇, 1520;	◈, 2178;	◇, 2730.
2.0 mm pins:	■, R_θ=729;	⊞, 1027;	⊡, 1565;	⊠, 2181;	□, 2889.

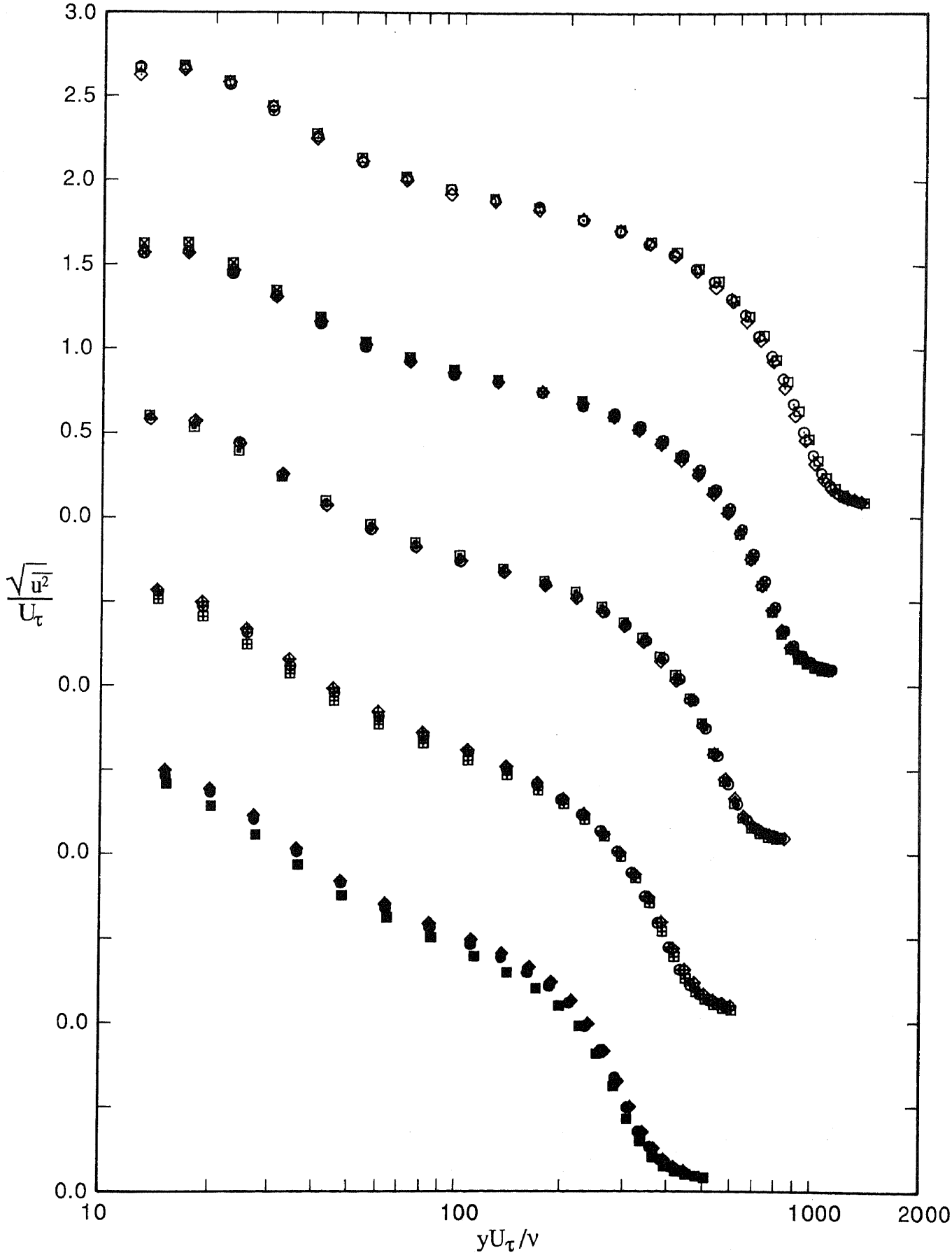

FIGURE 6.16. Profiles of $\sqrt{\overline{u^2}}/U_\tau$ versus $\log(yU_\tau/\nu)$ for design flows showing effects of device for five nominal values of R_θ. Note shift in ordinate.

Wire:	●, R_θ=697;	⊕, 1003;	⊙, 1568;	⊗, 2226;	⊙, 2788.
Grit:	◆, R_θ=706;	⊕, 1042;	◇, 1520;	⊗, 2178;	◇, 2730.
2.0 mm pins:	■, R_θ=729;	⊞, 1027;	⊡, 1565;	⊠, 2181;	⊡, 2889.

$\log(yU_\tau/\nu)$ as the abscissa rather than y/δ tends to suppress the differences between the data for the three devices for $R_\theta \approx 713$.

A turbulence profile for $R_\theta = 509$ for the design flow for the wire tripping device was also taken using the single-wire probe. Mean-flow measurements for this flow condition displayed unusual behaviour (see figure 5.7), and it was of interest to examine the turbulence characteristics. The profile is shown plotted in figure 6.17 using coordinates of $\sqrt{\overline{u^2}}/U_\tau$ versus $\log(yU_\tau/\nu)$. For comparison purposes, profiles for the wire from figure 6.15 have been replotted on this figure. The replotted profiles are in the form of lines to avoid confusion and highlight the behaviour of the profile for $R_\theta = 509$. From figure 6.17 it can be seen that the profile for $R_\theta = 509$ clearly shows the effects of underdevelopment, although the flow undoubtedly exhibits characteristics of turbulent flow as explained in Section 5.2. Purtell's (1978) data displayed behaviour similar to that shown in figure 6.17 for the current results.

It will be recalled from Section 2.4 that Murlis (1975) did not actually measure $\overline{w^2}$ normal stresses, necessary for calculating $\overline{q^2}$, but instead he approximated $\overline{w^2}$ using the expression $\sqrt{\overline{w^2}} = 0.5(\sqrt{\overline{u^2}}+\sqrt{\overline{v^2}})$. He based this approximation upon Klebanoff's (1954) data, for which $R_\theta \approx 7750$, and used it for his low R_θ measurements when calculating advection in his energy balances. Although Murlis indicated that this expression is a very close approximation to Klebanoff's data, the fact remains that it may not be accurate at low values of R_θ. It is appropriate, therefore, to use the actual measurements of the current investigation to see if the above expression still holds at low values of R_θ. Profiles of $\sqrt{\overline{u^2}}/U_e$, $\sqrt{\overline{v^2}}/U_e$ and $\sqrt{\overline{w^2}}/U_e$, versus y/δ, are shown in figure 6.18 for the wire for both $R_\theta = 1003$ and $R_\theta = 2226$. It can be seen that at low Reynolds numbers, the relativity of the w-component data to the u- and v-component data is different from that which applies at high Reynolds numbers. At $y/\delta = 0.5$, the actual measured value of $\overline{w^2}$ is about 21% smaller than that determined from the above approximation for $R_\theta = 1003$ and about 17% smaller for $R_\theta = 2226$.

To complete this section, it is appropriate to consider how twice the turbulent kinetic energy, $\overline{q^2} \equiv \overline{u^2}+\overline{v^2}+\overline{w^2}$, varies with R_θ. Profiles of $\overline{q^2}/U_e^2$ versus y/δ for three devices and different values of R_θ are shown in figure 6.19.

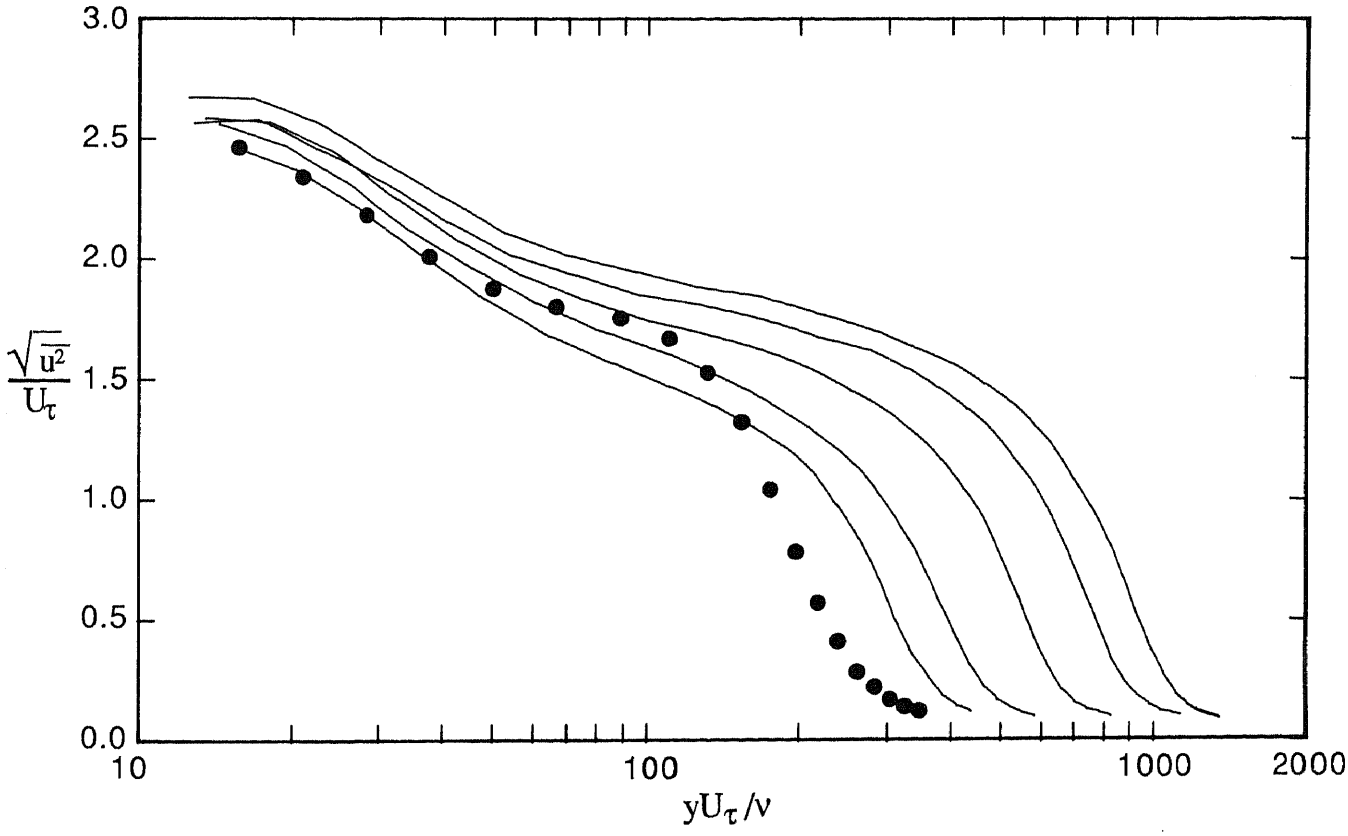

FIGURE 6.17. Profiles of $\sqrt{\overline{u^2}}/U_\tau$ versus $\log(yU_\tau/\nu)$ for various values of R_θ for wire for design flow.

●,$R_\theta = 509$

———, various R_θ, based on figure 6.15.

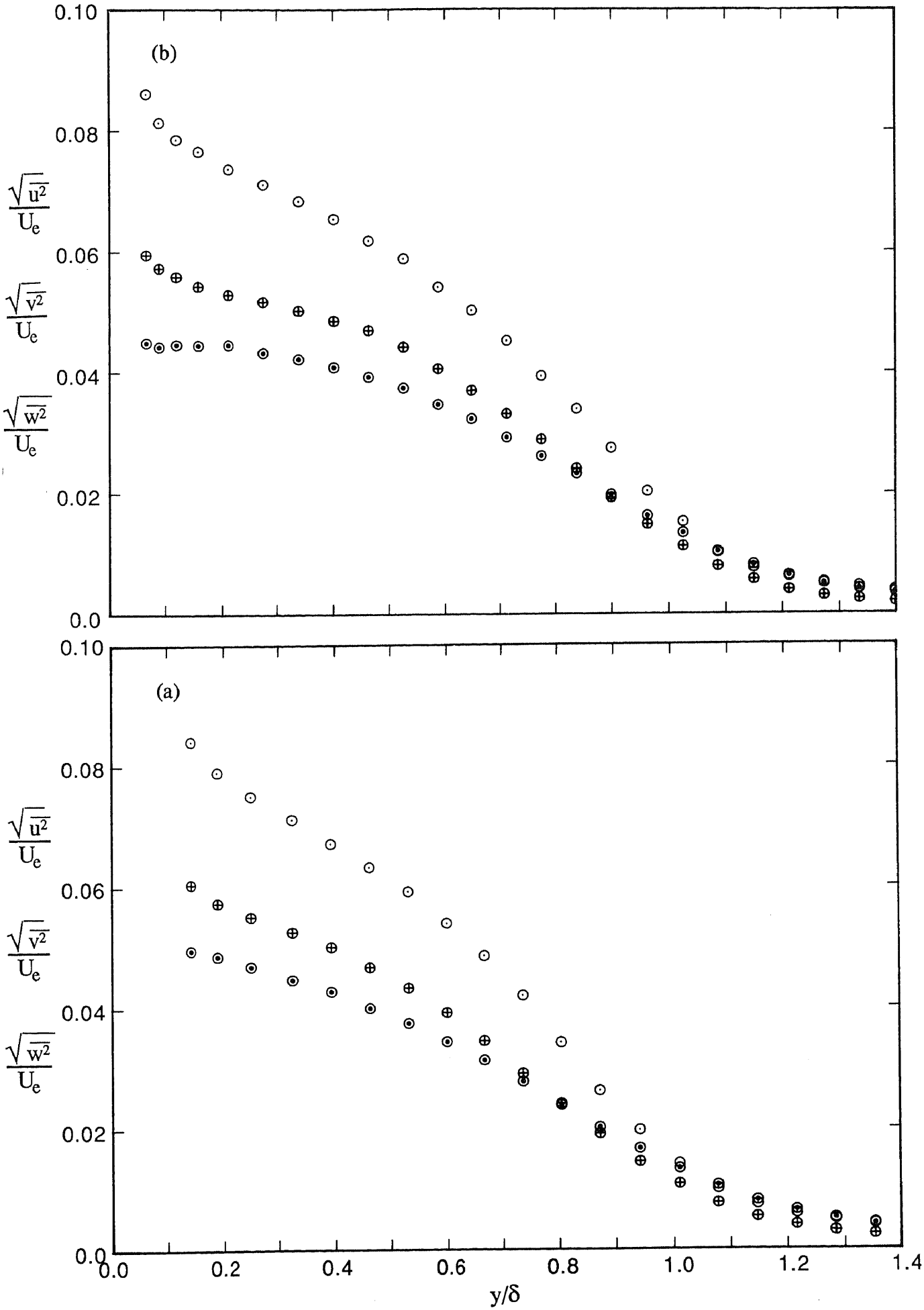

FIGURE 6.18. Profiles of $\sqrt{\overline{u^2}}/U_e$, $\sqrt{\overline{v^2}}/U_e$ and $\sqrt{\overline{w^2}}/U_e$, versus y/δ for wire for design flow. (a) $R_\theta = 1003$, (b) $R_\theta = 2226$

$\odot$, $\sqrt{\overline{u^2}}/U_e$; $\circledcirc$, $\sqrt{\overline{v^2}}/U_e$; $\oplus$, $\sqrt{\overline{w^2}}/U_e$

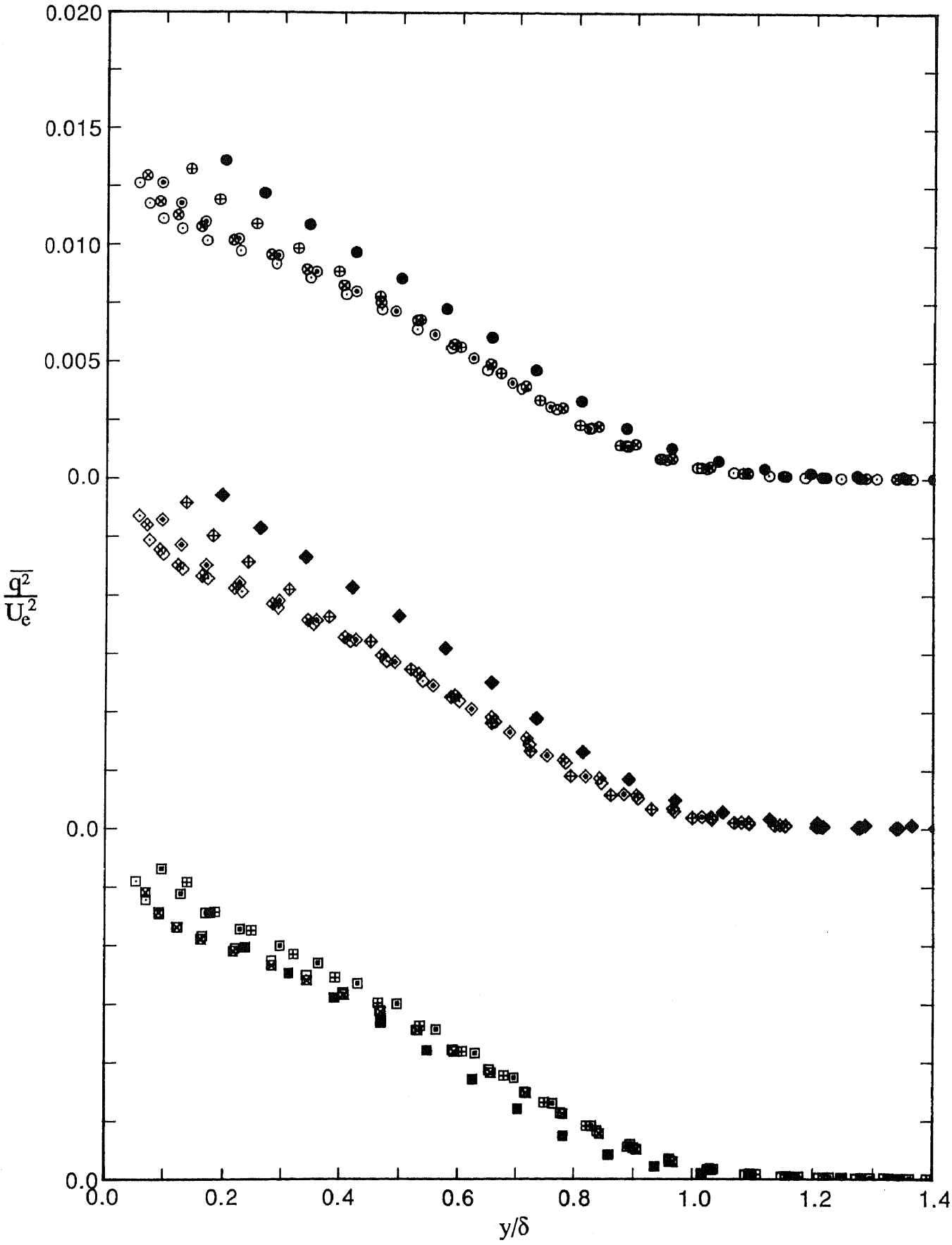

FIGURE 6.19. Profiles of $\overline{q^2}/U_e^2$ versus y/δ for design flows showing effects of R_θ for three devices. Note shift in ordinate.

Wire: ●, R_θ=697; ⊕, 1003; ⊙, 1568; ⊗, 2226; ⊙, 2788.
Grit: ◆, R_θ=706; ⊕, 1042; ◇, 1520; ⊗, 2178; ◇, 2730.
2.0 mm pins: ■, R_θ=729; ⊞, 1027; ⊡, 1565; ⊠, 2181; ⊡, 2889.

The $\overline{u^2}$ measurements, used when determining $\overline{q^2}$, were taken with the crossed-wire probe. All that need be noted is that the $\overline{q^2}/U_e^2$ profiles behave as expected, given the behaviour already described for the profiles of the component Reynolds normal stresses.

6.3.2 Reynolds Shear Stresses

The $\overline{uv}$ Reynolds shear stresses were scaled and plotted as in figures 6.4 to 6.6 for the $\overline{u^2}$ Reynolds normal stresses.

Figure 6.20 shows profiles of $-\overline{uv}/U_e^2$ versus y/δ. It is apparent from this figure that, with this scaling, the shear stresses for the three devices depend strongly on R_θ near the wall but the dependency becomes less as y/δ increases. For the three devices, the profiles show monotonic trends with R_θ, except for the profile for the pins for $R_\theta = 729$. Near the wall, the values of the shear stresses corresponding to the different profiles decrease with increasing R_θ, and this behaviour is consistent with the fact that the ordinate corresponds to $C_f/2$. Also, it is well known that for small values of y/δ, where the effects of viscosity become pronounced, the values of Reynolds shear stress should decrease. For increasing values of R_θ, the innermost points of the profiles correspond to successively smaller values of y/δ, and it is apparent from figure 6.20 that the values of $-\overline{uv}/U_e^2$ for small values of y/δ for the higher values of R_θ decrease from their maximum values as expected.

Figure 6.21 shows profiles of $-\overline{uv}/U_e^2$ versus y/δ, and it can be seen from this figure that for $R_\theta \approx 713$, the type of device used has a significant effect upon the shear stresses, but for $R_\theta \approx 1020$ and above, the effect of device on the shear stresses is reasonably small. This behaviour is consistent with that already described for the corresponding Reynolds normal stresses shown in figures 6.5, 6.8 and 6.11.

Profiles of $-\overline{uv}/U_\tau^2$ versus y/δ are shown in figure 6.22 and once again the change of scaling significantly alters the appearance of the plotted data. The profiles clearly do not exhibit monotonic trends with R_θ and it is a matter of interest that the profiles for $R_\theta \approx 2175$ for each of the devices correspond to higher values of $-\overline{uv}/U_\tau^2$ than the other profiles. From figure 6.22 it can be seen that close to the wall the normalized Reynolds shear stresses, $-\overline{uv}/U_\tau^2$, for the

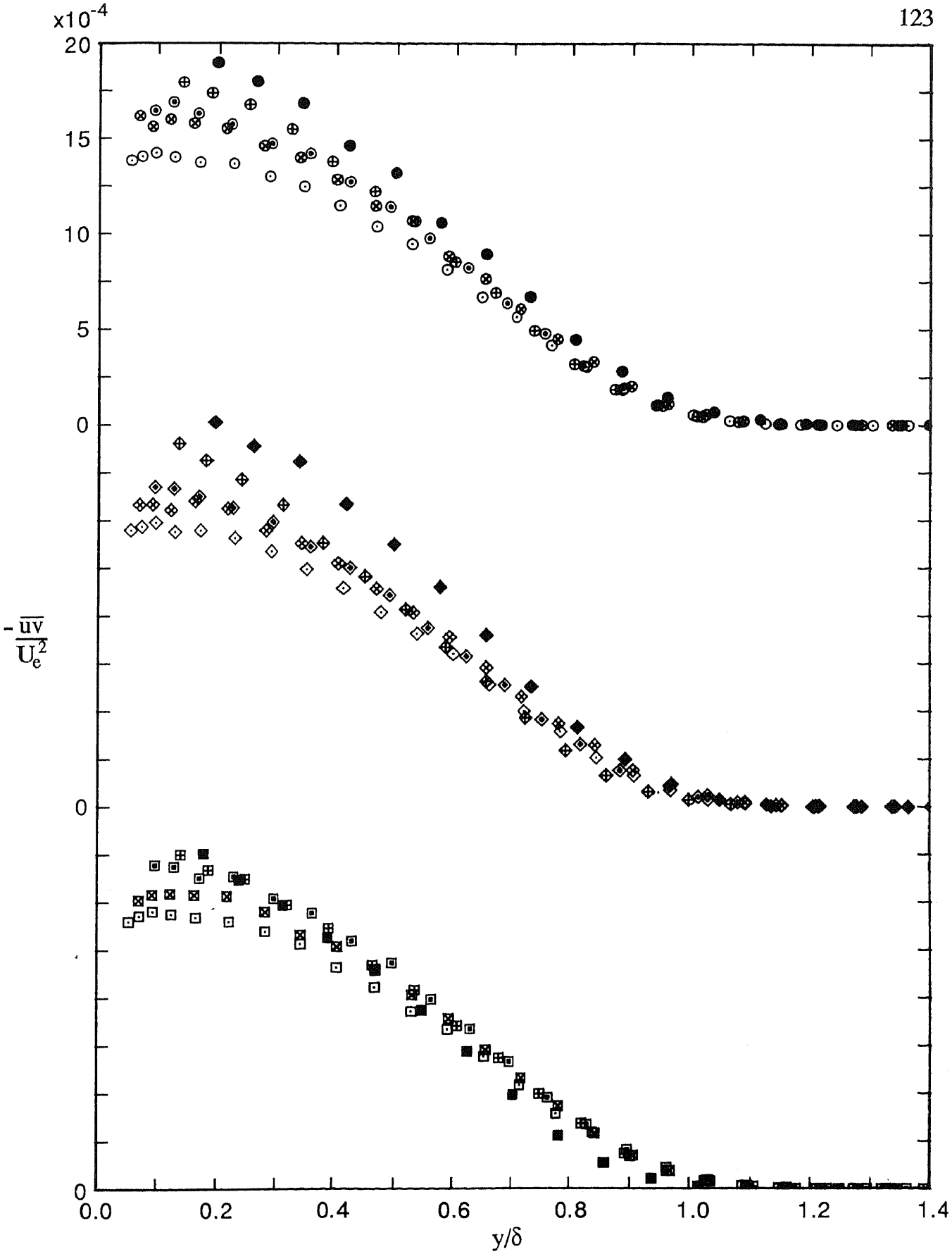

FIGURE 6.20. Profiles of $-\overline{uv}/U_e^2$ versus y/δ for design flows showing effects of R_θ for three devices. Note shift in ordinate.

Wire:	●, R_θ=697;	⊕, 1003;	⊙, 1568;	⊗, 2226;	⊙, 2788.
Grit:	◆, R_θ=706;	⊕, 1042;	◇, 1520;	◈, 2178;	◇, 2730.
2.0 mm pins:	■, R_θ=729;	⊞, 1027;	⊡, 1565;	⊠, 2181;	⊡, 2889.

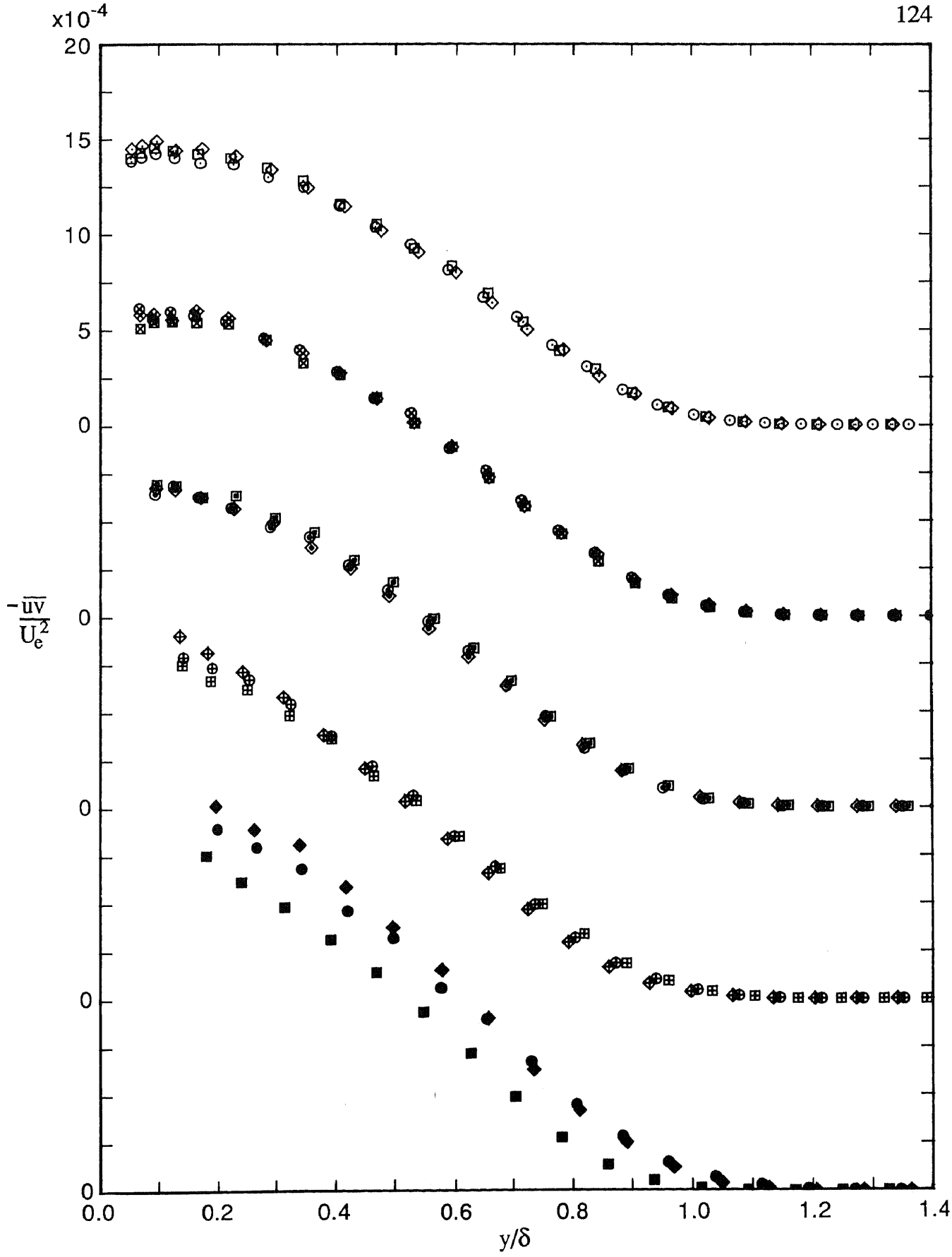

FIGURE 6.21. Profiles of $-\overline{uv}/U_e^2$ versus y/δ for design flows showing effects of device for five nominal values of R_θ. Note shift in ordinate.

Wire:	●, R_θ=697;	⊕, 1003;	⊙, 1568;	⊗, 2226;	⊙, 2788.
Grit:	◆, R_θ=706;	◈, 1042;	◇, 1520;	◈, 2178;	◇, 2730.
2.0 mm pins:	■, R_θ=729;	⊞, 1027;	⊡, 1565;	⊠, 2181;	⊡, 2889.

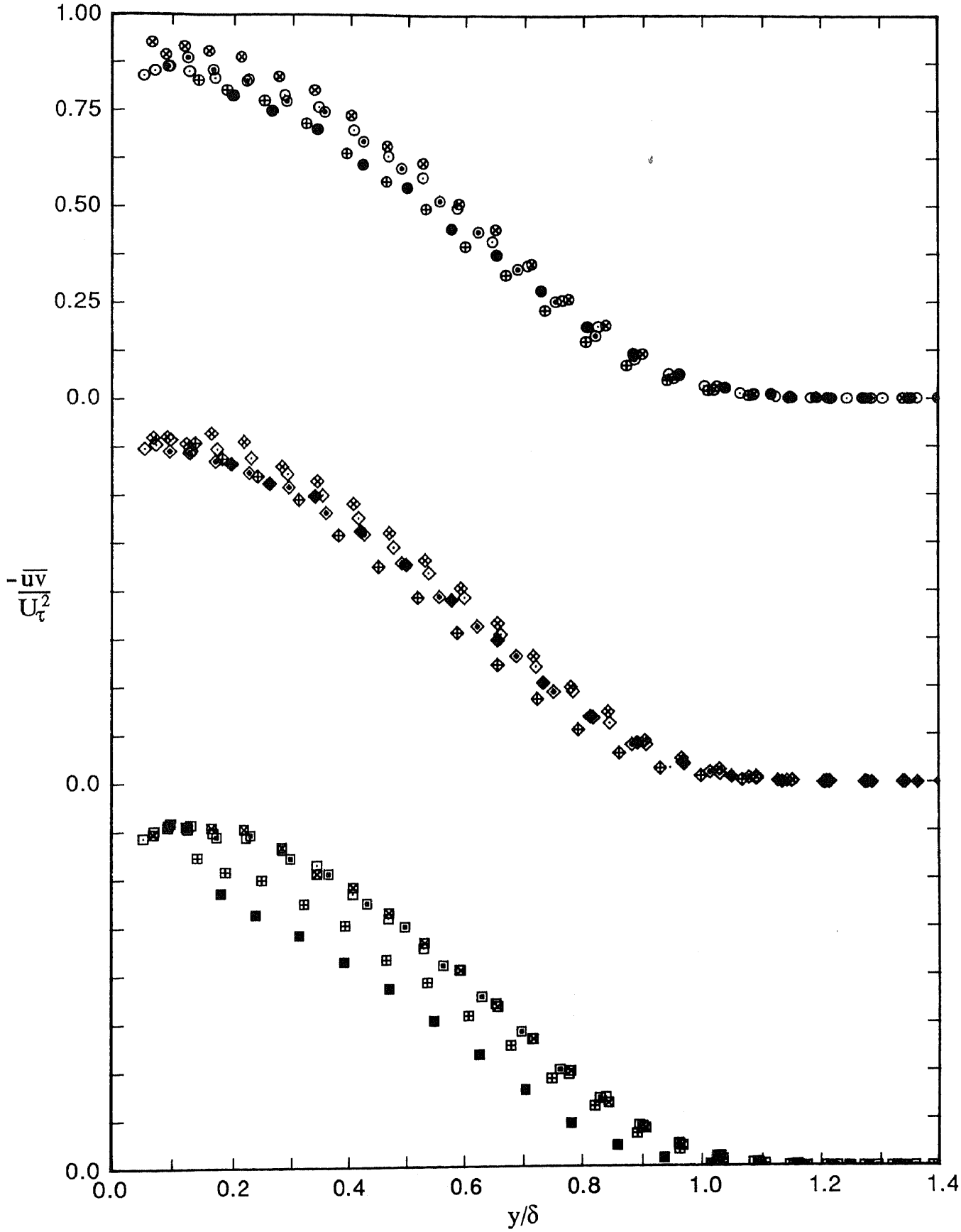

FIGURE 6.22. Profiles of $-\overline{uv}/U_\tau^2$ versus y/δ for design flows showing effects of R_θ for three devices. Note shift in ordinate.

Wire:	●, R_θ=697;	⊕, 1003;	⊙, 1568;	⊗, 2226;	⊙, 2788.
Grit:	◆, R_θ=706;	⊕, 1042;	◇, 1520;	⊗, 2178;	◇, 2730.
2.0 mm pins:	■, R_θ=729;	⊞, 1027;	▣, 1565;	⊠, 2181;	⊡, 2889.

different values of R_θ, are still well below a value of 1.0. Thus it is clear from this figure that for the low Reynolds numbers considered, the viscous shear stresses still have an appreciable magnitude well away from the wall, unlike their behaviour for high Reynolds number flows.

6.3.3 Triple Products

The triple product $\overline{u_i u_j u_k}$ can be interpreted physically as the transport of the quantity $\overline{u_i u_j}$ by the convective action of the velocity fluctuation u_k (see Dean & Bradshaw 1976). A good knowledge of the behaviour of triple products is of importance since they appear in the transport equations used for boundary-layer prediction methods. However, there is still a scarcity of reliable experimental data. For low-Reynolds-number flows, very few measurements of triple products have been published apart from those of Murlis (1975) and Murlis, Tsai & Bradshaw (1982). The $\overline{u^3}$, $\overline{v^3}$, $\overline{u^2v}$ and $\overline{uv^2}$ triple products of the current investigation were each scaled and plotted as in figures 6.4 to 6.6 for the $\overline{u^2}$ normal stresses. Thus all the triple products appearing in the kinetic-energy and shear-stress equations except $\overline{vw^2}$ were measured. In addition, the $\overline{w^3}$ triple products were also measured for the purpose of calculating skewness (see Section 6.3.5). Further discussion on triple products will be given in Section 6.3.6, which deals with energy and shear-stress balances.

Considering firstly the $\overline{u^3}$ triple products, profiles of $-\overline{u^3}/U_e^3$ versus y/δ are shown in figure 6.23. These measurements were all taken with the single-wire probe. As can be seen, the profiles for the three devices depend on R_θ, but the extent of the dependency changes with y/δ. For each of the devices, the dependency on R_θ is greatest for y/δ less than about 0.3. For the three devices, the profiles show a monotonic trend with R_θ, except for the pins for y/δ greater than about 0.7, and the differences between the profiles for $R_\theta \approx 2175$ and $R_\theta \approx 2810$ are reasonably small in each case. All of the profiles can be seen to exhibit two distinct peaks and for each of the devices for virtually all profiles the innermost peaks, as well as the depressions between the two peaks, decrease in magnitude and correspond to successively smaller values of y/δ as R_θ increases. The values of $-\overline{u^3}/U_e^3$ corresponding to the depressions fall to almost zero for $R_\theta \approx 2175$ and $R_\theta \approx 2810$ for each of the devices. Another notable feature of figure 6.23 is the appearance of negative values of $-\overline{u^3}/U_e^3$ for most

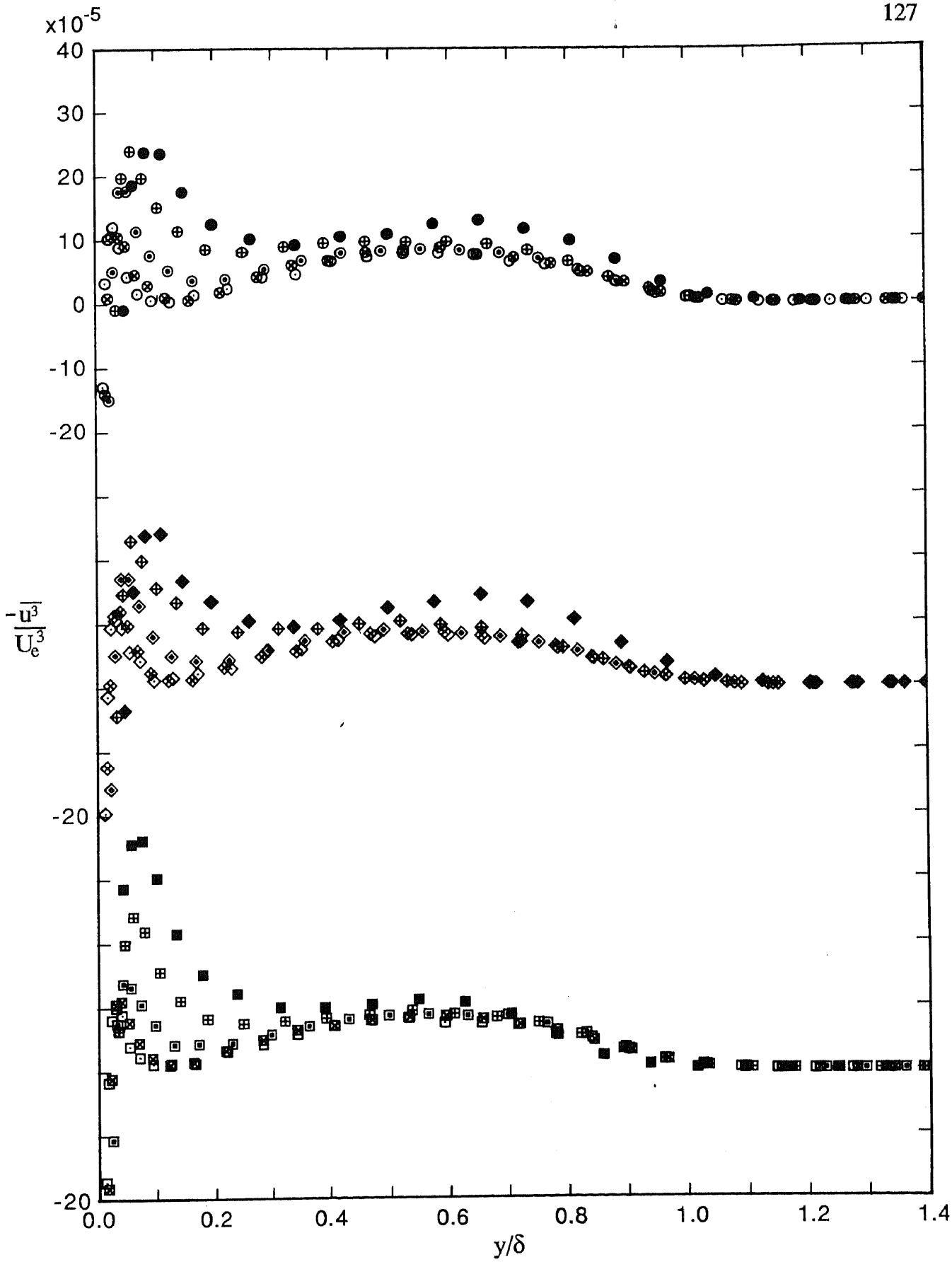

FIGURE 6.23. Profiles of $-\overline{u^3}/U_e^3$ versus y/δ for design flows showing effects of R_θ for three devices. Note shift in ordinate.

Wire:	●, R_θ=697;	⊕, 1003;	⊙, 1568;	⊗, 2226;	⊙, 2788.
Grit:	◆, R_θ=706;	◈, 1042;	◇, 1520;	◈, 2178;	◇, 2730.
2.0 mm pins:	■, R_θ=729;	⊞, 1027;	⊡, 1565;	⊠, 2181;	⊡, 2889.

profiles for low values of y/δ. These negative values of $-\overline{u^3}$ have also been reported in the literature by Barlow & Johnston (1985), (1988) ($R_\theta = 1140$), and also by other researchers in the context of skewness of the u-component fluctuating velocity (see Section 6.3.5).

Figure 6.24 shows profiles of $-\overline{u^3}/U_e^3$ versus y/δ replotted and it is apparent that for $R_\theta \approx 713$, the type of device used can affect the profiles, but for $R_\theta \approx 1020$ and above, the type of device used has very little effect upon the profiles. This behaviour is consistent with that for the corresponding profiles of $\overline{u^2}/U_e^2$ versus y/δ shown in figure 6.5.

Profiles of $-\overline{u^3}/U_\tau^3$ versus y/δ are shown in figure 6.25 and it can be seen that with this scaling, profiles for each of the devices are still dependent on R_θ, especially for y/δ less than about 0.3, as for the $-\overline{u^3}/U_e^3$ profiles shown in figure 6.23. The relative repositioning of the profiles in the vertical direction as a consequence of the new scaling has not altered the trends of the depressions with R_θ, but the heights of the innermost peaks now do not follow monotonic trends with R_θ as well as previously.

Considering now triple-product measurements taken with the crossed-wire probe, profiles of $\overline{v^3}/U_e^3$ versus y/δ are shown in figure 6.26. The profiles do show some scatter, but this is to be expected from triple-product measurements taken with a crossed-wire probe. The profiles for the three devices can be seen to show large variations with R_θ, but once again the extent of the dependency on R_θ varies throughout the y/δ range. For the three devices, there is a general tendency for the profiles to vary monotonically with R_θ, although some exceptions do occur. Also, the profiles for $R_\theta \approx 2175$ and $R_\theta \approx 2810$ for each of the devices agree reasonably closely. As for the $\overline{u^3}$ triple products, the $\overline{v^3}/U_e^3$ profiles exhibit two peaks and a depression and there seems to be a general tendency for the depressions to behave as for the $-\overline{u^3}/U_e^3$ profiles. However, in this case, the values of $\overline{v^3}/U_e^3$ corresponding to the depressions do not fall to almost zero for $R_\theta \approx 2175$ and $R_\theta \approx 2810$. With the crossed-wire probe, measurements could not be taken close enough to the wall to study the behaviour of the innermost peaks and so it is not possible to comment on their behaviour. Also the use of the crossed-wire probe meant that it was not possible to see if negative values of $\overline{v^3}/U_e^3$ occurred, but it is a matter of interest

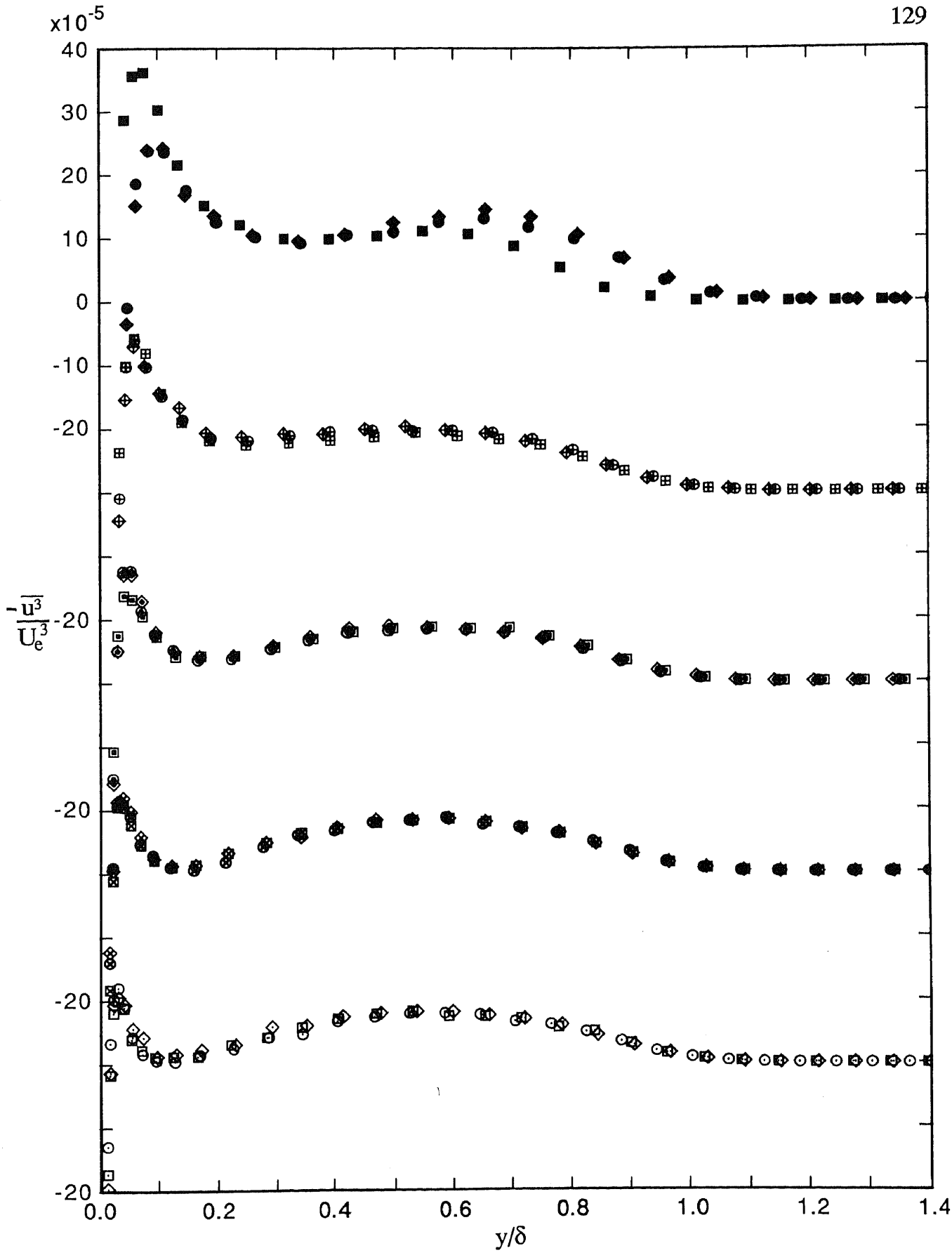

FIGURE 6.24. Profiles of $-\overline{u^3}/U_e^3$ versus y/δ for design flows showing effects of device for five nominal values of R_θ. Note shift in ordinate.

Wire:	●, R_θ=697;	⊕, 1003;	⊙, 1568;	⊗, 2226;	⊙, 2788.
Grit:	◆, R_θ=706;	⊕, 1042;	◇, 1520;	⊗, 2178;	◇, 2730.
2.0 mm pins:	■, R_θ=729;	⊞, 1027;	⊡, 1565;	⊠, 2181;	□, 2889.

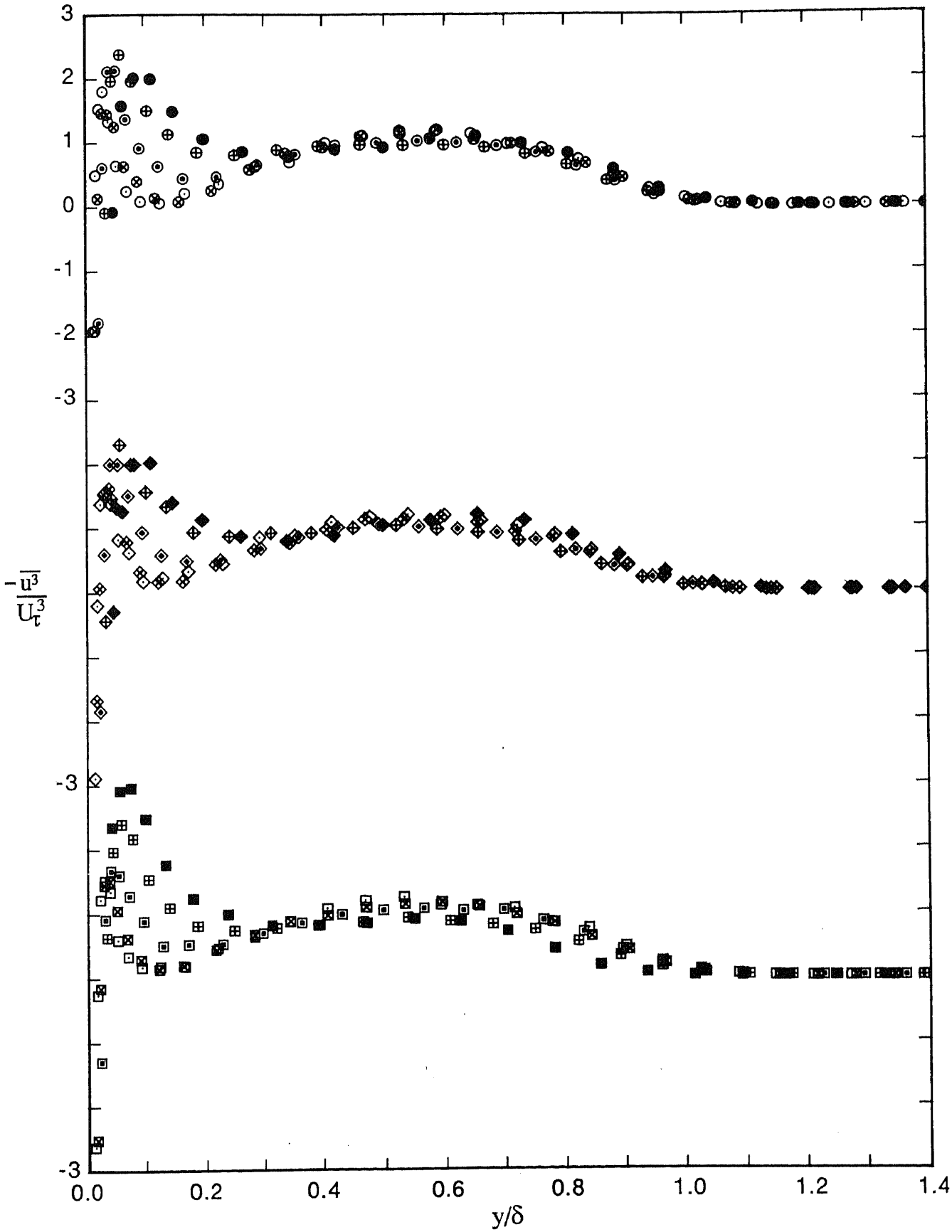

FIGURE 6.25. Profiles of $-\overline{u^3}/U_\tau^3$ versus y/δ for design flows showing effects of R_θ for three devices. Note shift in ordinate.

Wire:	●, R_θ=697;	⊕, 1003;	⊙, 1568;	⊗, 2226;	⊙, 2788.
Grit:	◆, R_θ=706;	◈, 1042;	◇, 1520;	◈, 2178;	◇, 2730.
2.0 mm pins:	■, R_θ=729;	⊞, 1027;	⊡, 1565;	⊠, 2181;	⊡, 2889.

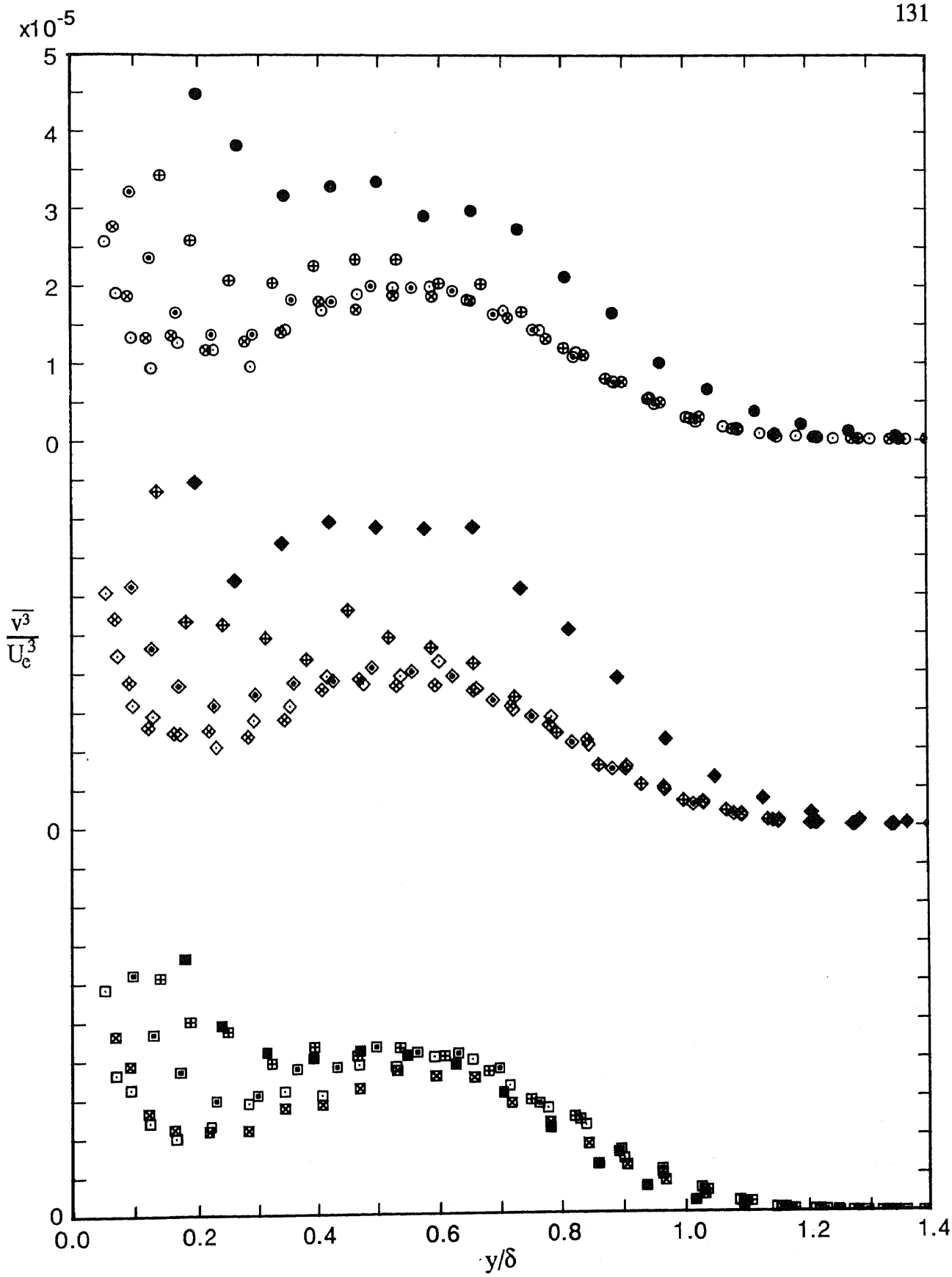

FIGURE 6.26. Profiles of $\overline{v^3}/U_e^3$ versus y/δ for design flows showing effects of R_θ for three devices. Note shift in ordinate.

Wire:	●, R_θ=697;	⊕, 1003;	⊙, 1568;	⊗, 2226;	⊙, 2788.
Grit:	◆, R_θ=706;	⊕, 1042;	◇, 1520;	⊗, 2178;	◇, 2730.
2.0 mm pins:	■, R_θ=729;	⊞, 1027;	⊡, 1565;	⊠, 2181;	⊡, 2889.

that the measurements of Barlow & Johnston (1985), (1988) did in fact show negative values of $\overline{v^3}$ for low-R_θ flows.

The replotted profiles of $\overline{v^3}/U_e^3$ versus y/δ are shown in figure 6.27 and it can be seen that for $R_\theta \approx 713$ the type of device used has a large effect upon the profiles. Although the collapse of the profiles for $R_\theta \approx 1020$ and above is not as good as for the previous broadband-turbulence profiles, the type of device used does not have a significant effect on the profiles if allowances are made for the inevitable scatter.

Figure 6.28 shows profiles of $\overline{v^3}/U_t^3$ versus y/δ and it can be seen that with this scaling, the profiles for each of the devices are strongly dependent on R_θ over the entire boundary layers. For each of the devices, the profiles do not show monotonic trends with R_θ.

Profiles for the $\overline{u^2v}$ triple products are shown in figures 6.29 to 6.31 and profiles for the $\overline{uv^2}$ triple products in figures 6.32 to 6.34. Each of these sets of figures are analogous to figures 6.26 to 6.28 respectively for the $\overline{v^3}$ triple products. As can be seen, the behaviour of the $\overline{u^2v}$ and $\overline{uv^2}$ triple products is very similar to that for the $\overline{v^3}$ triple products considered above and discussion already given for the behaviour of the $\overline{v^3}$ triple products is also applicable to the $\overline{u^2v}$ and $\overline{uv^2}$ triple products and need not be given again. It is only necessary to note that, as for the $\overline{v^3}$ triple products, Barlow & Johnston (1985), (1988) found that the $\overline{u^2v}$ and $\overline{uv^2}$ triple products changed sign near the wall.

It is now desirable to consider the triple-product profiles of Murlis, Tsai & Bradshaw (1982), which are shown reproduced in figures 6.35 (a) to (d). It is immediately apparent that these researchers do not present data for values of y/δ less than about 0.2 for any of their profiles, and for some of their profiles the limiting value of y/δ is as high as about 0.4. Thus their data do not show the details of the peaks closest to the wall or indicate that profiles depend strongly on R_θ in this region. The current data for low values of y/δ are thus especially significant in this respect. In a number of cases, Murlis, Tsai & Bradshaw draw smooth curves to extend their profiles from the innermost points to the wall, and these lines quite obviously disregard the real behaviour. In addition, when the triple-product profiles presented by Murlis, Tsai & Bradshaw (1982) are compared with those presented by Murlis (1975), it is apparent that in some

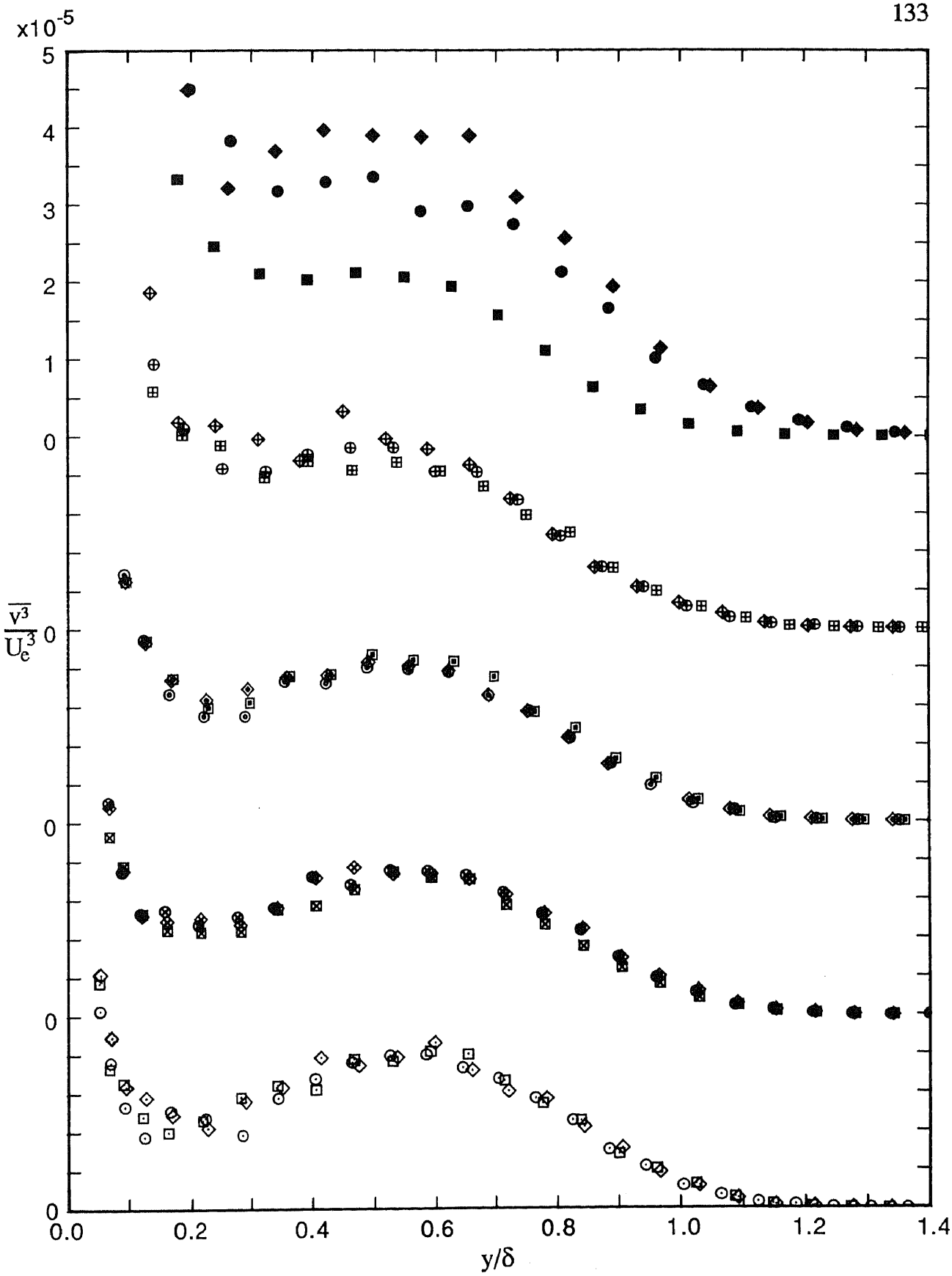

FIGURE 6.27. Profiles of $\overline{v^3}/U_e^3$ versus y/δ for design flows showing effects of device for five nominal values of R_θ. Note shift in ordinate.

Wire: ●, R_θ=697; ⊕, 1003; ⊙, 1568; ⊗, 2226; ⊙, 2788.
Grit: ◆, R_θ=706; ◈, 1042; ◇, 1520; ◈, 2178; ◇, 2730.
2.0 mm pins: ■, R_θ=729; ⊞, 1027; ⊡, 1565; ⊠, 2181; ⊡, 2889.

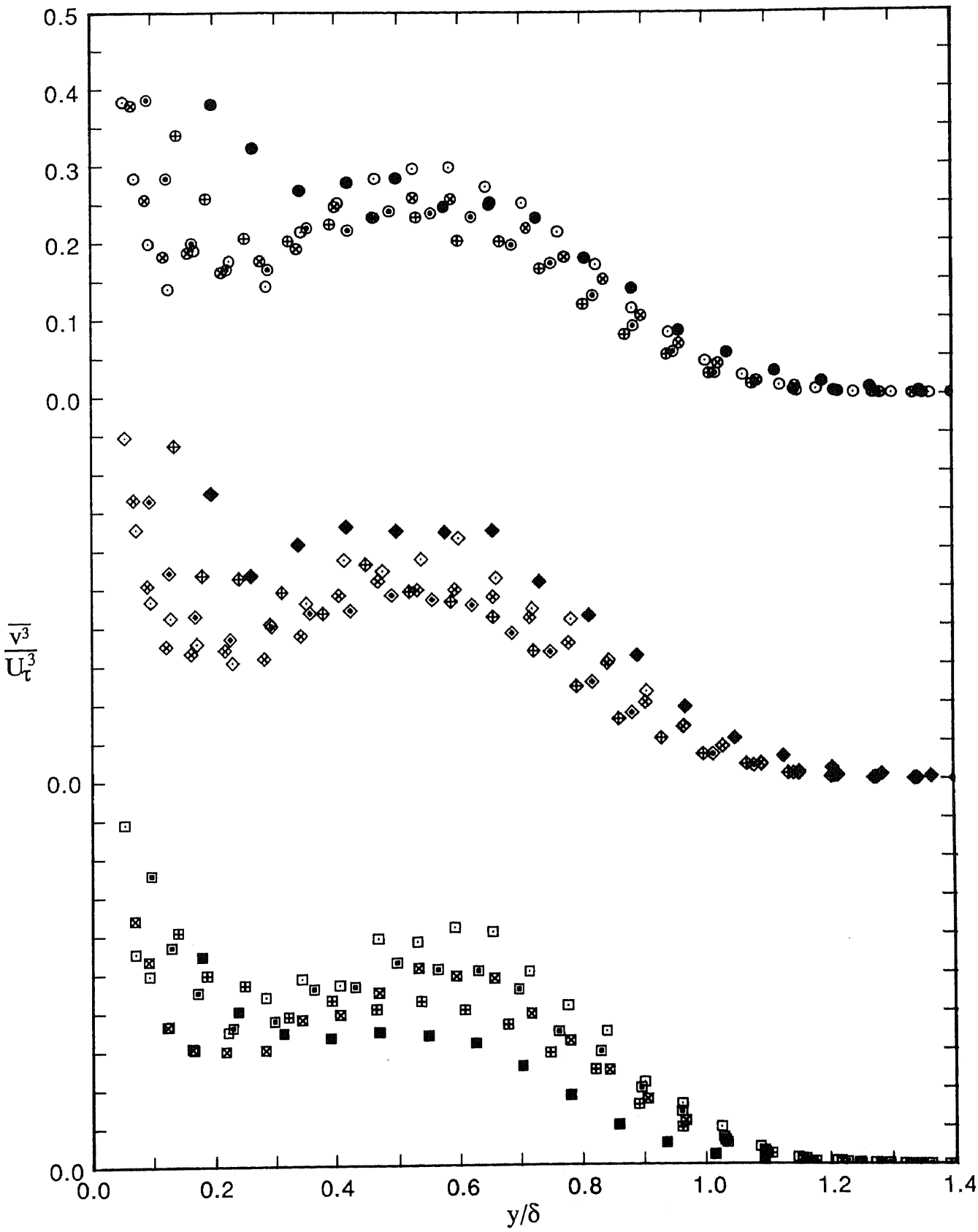

FIGURE 6.28. Profiles of $\overline{v^3}/U_\tau^3$ versus y/δ for design flows showing effects of R_θ for three devices. Note shift in ordinate.

Wire: ●, R_θ=697; ⊕, 1003; ⊙, 1568; ⊗, 2226; ⊙, 2788.
Grit: ◆, R_θ=706; ◈, 1042; ◇, 1520; ◈, 2178; ◇, 2730.
2.0 mm pins: ■, R_θ=729; ⊞, 1027; ⊡, 1565; ⊠, 2181; ⊡, 2889.

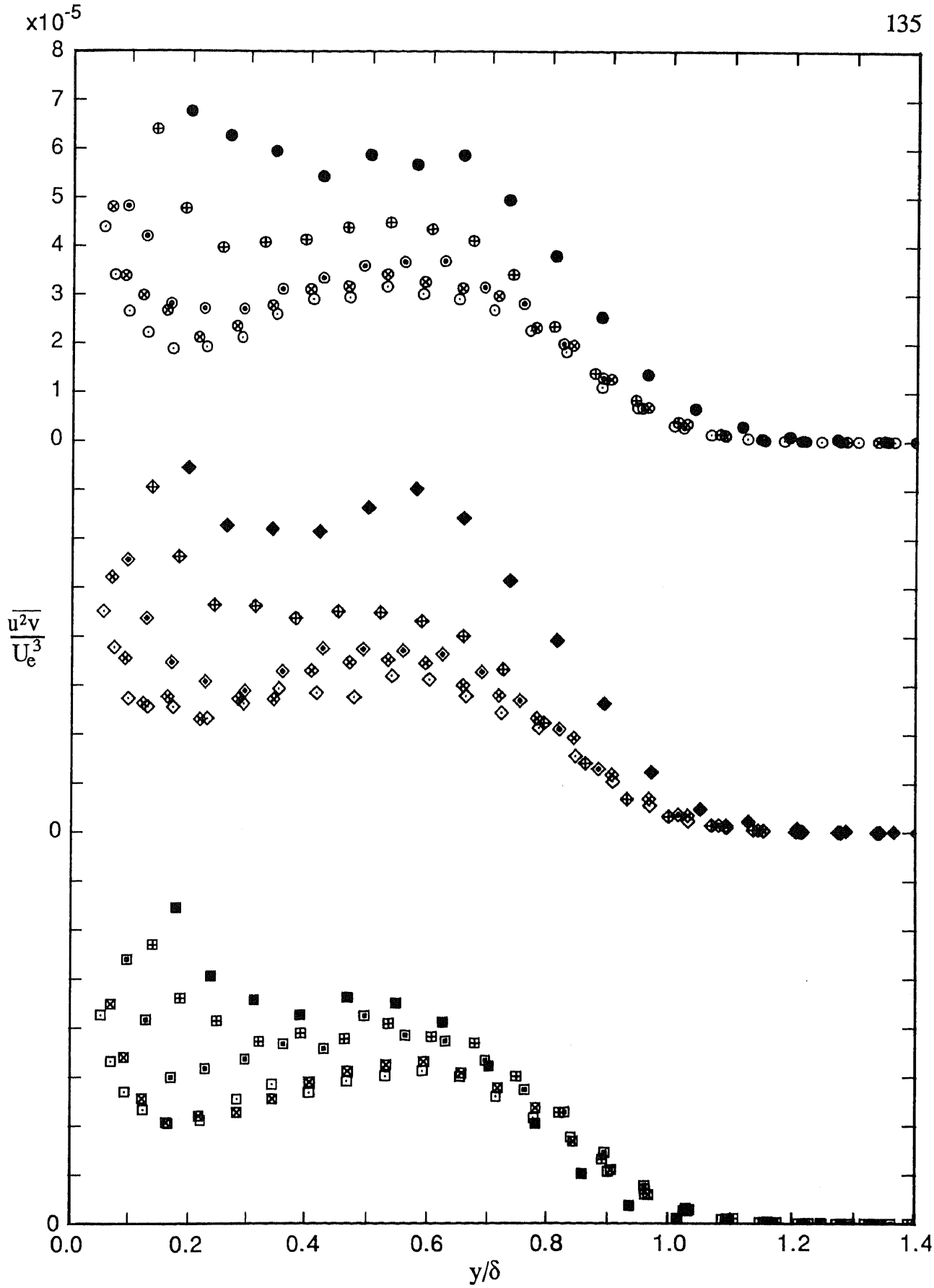

FIGURE 6.29. Profiles of $\overline{u^2v}/U_e^3$ versus y/δ for design flows showing effects of R_θ for three devices. Note shift in ordinate.

Wire:	●, R_θ=697;	⊕, 1003;	⊙, 1568;	⊗, 2226;	⊙, 2788.
Grit:	◆, R_θ=706;	◈, 1042;	◇, 1520;	◈, 2178;	◇, 2730.
2.0 mm pins:	■, R_θ=729;	⊞, 1027;	▣, 1565;	⊠, 2181;	⊡, 2889.

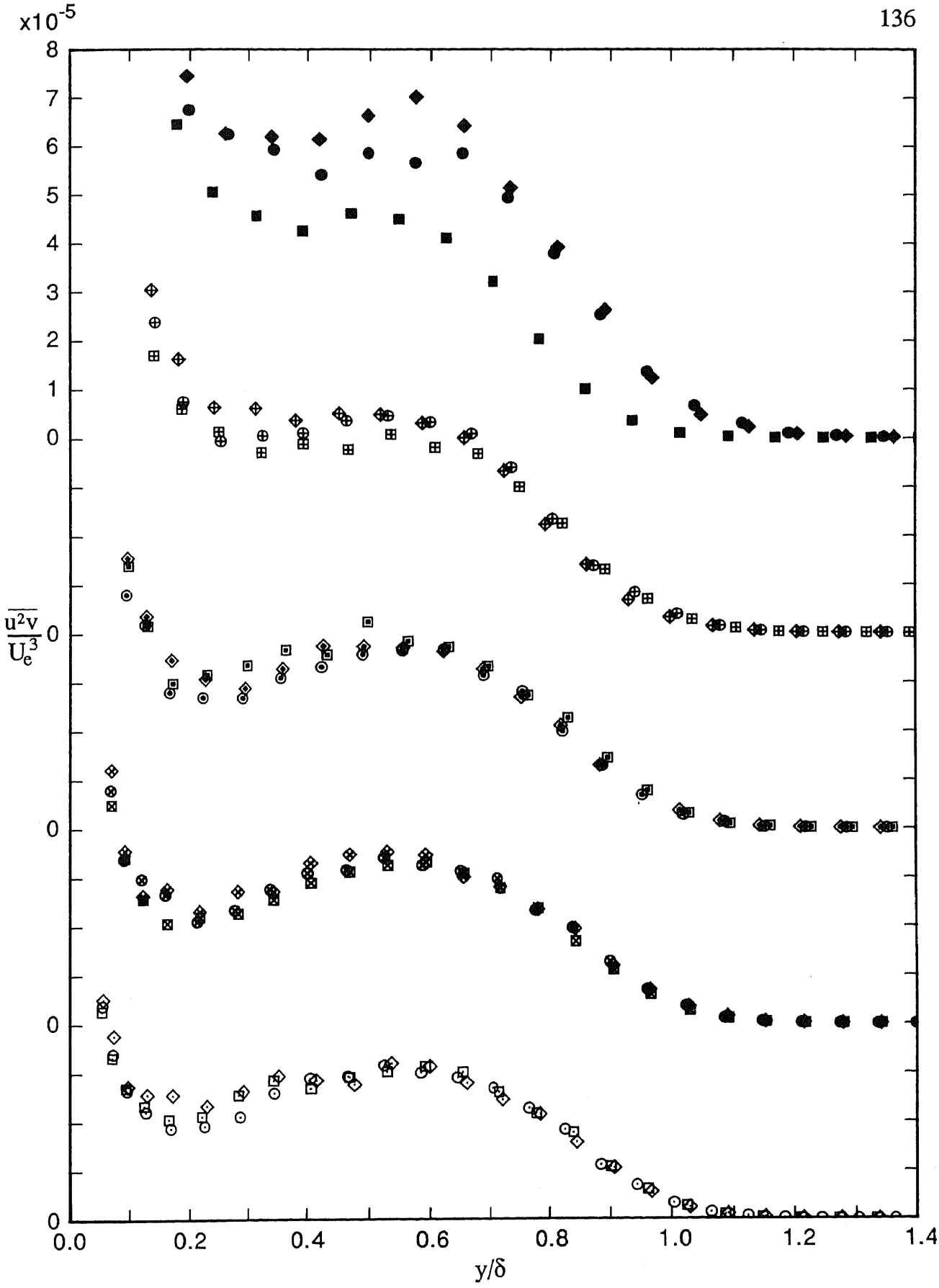

FIGURE 6.30. Profiles of $\overline{u^2v}/U_e^3$ versus y/δ for design flows showing effects of device for five nominal values of R_θ. Note shift in ordinate.

Wire:	●, R_θ=697;	⊕, 1003;	⊙, 1568;	⊗, 2226;	⊙, 2788.
Grit:	◆, R_θ=706;	◈, 1042;	◇, 1520;	◈, 2178;	◇, 2730.
2.0 mm pins:	■, R_θ=729;	⊞, 1027;	⊡, 1565;	⊠, 2181;	⊡, 2889.

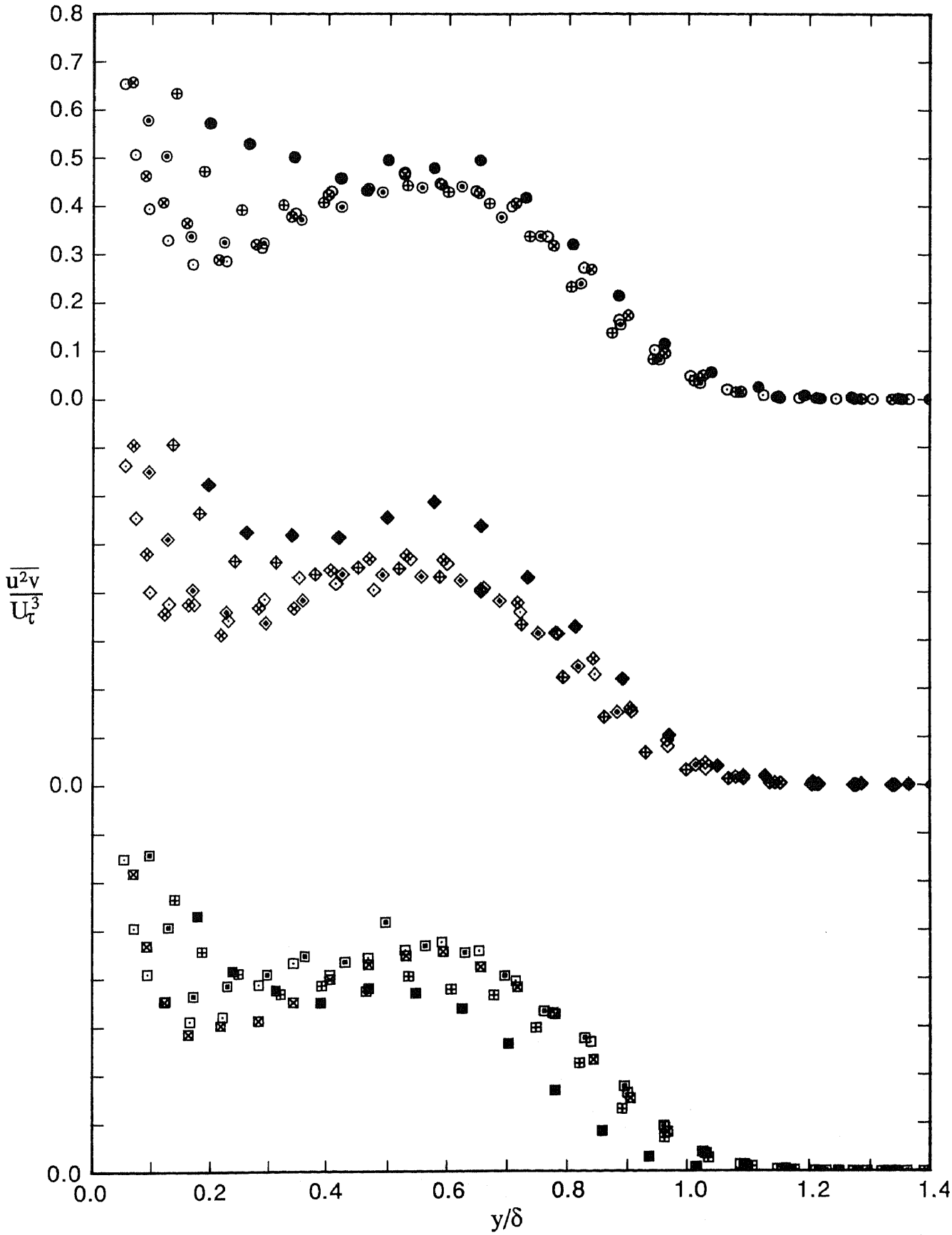

FIGURE 6.31. Profiles of $\overline{u^2v}/U_\tau^3$ versus y/δ for design flows showing effects of R_θ for three devices. Note shift in ordinate.

Wire:	●, R_θ=697;	⊕, 1003;	⊙, 1568;	⊗, 2226;	⊙, 2788.
Grit:	◆, R_θ=706;	◈, 1042;	◇, 1520;	◈, 2178;	◇, 2730.
2.0 mm pins:	■, R_θ=729;	⊞, 1027;	▣, 1565;	⊠, 2181;	⊡, 2889.

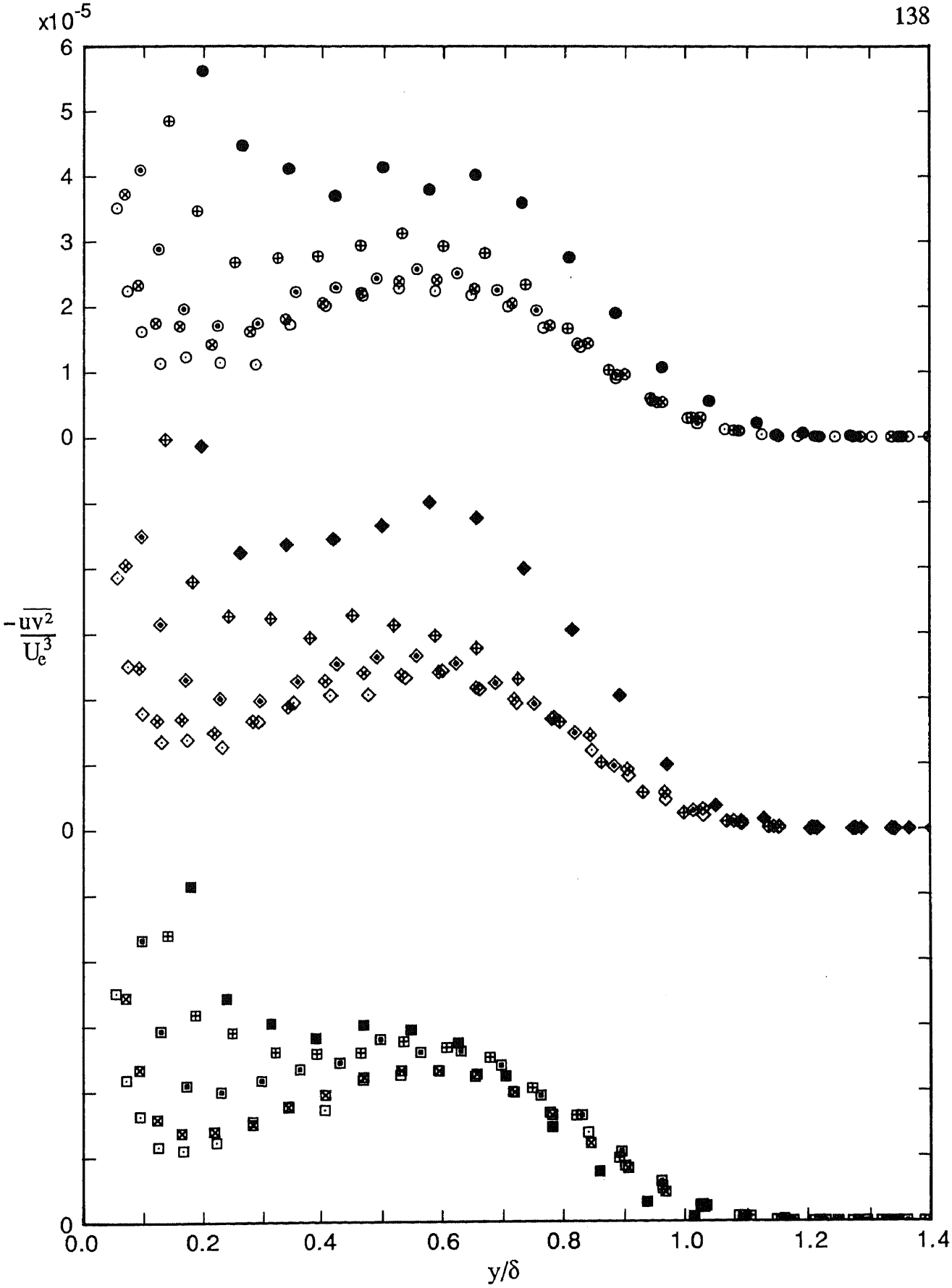

FIGURE 6.32. Profiles of $-\overline{uv^2}/U_e^3$ versus y/δ for design flows showing effects of R_θ for three devices. Note shift in ordinate.

Wire:	●, R_θ=697;	⊕, 1003;	⊙, 1568;	⊗, 2226;	⊙, 2788.
Grit:	◆, R_θ=706;	◈, 1042;	◇, 1520;	◈, 2178;	◇, 2730.
2.0 mm pins:	■, R_θ=729;	⊞, 1027;	⊡, 1565;	⊠, 2181;	⊡, 2889.

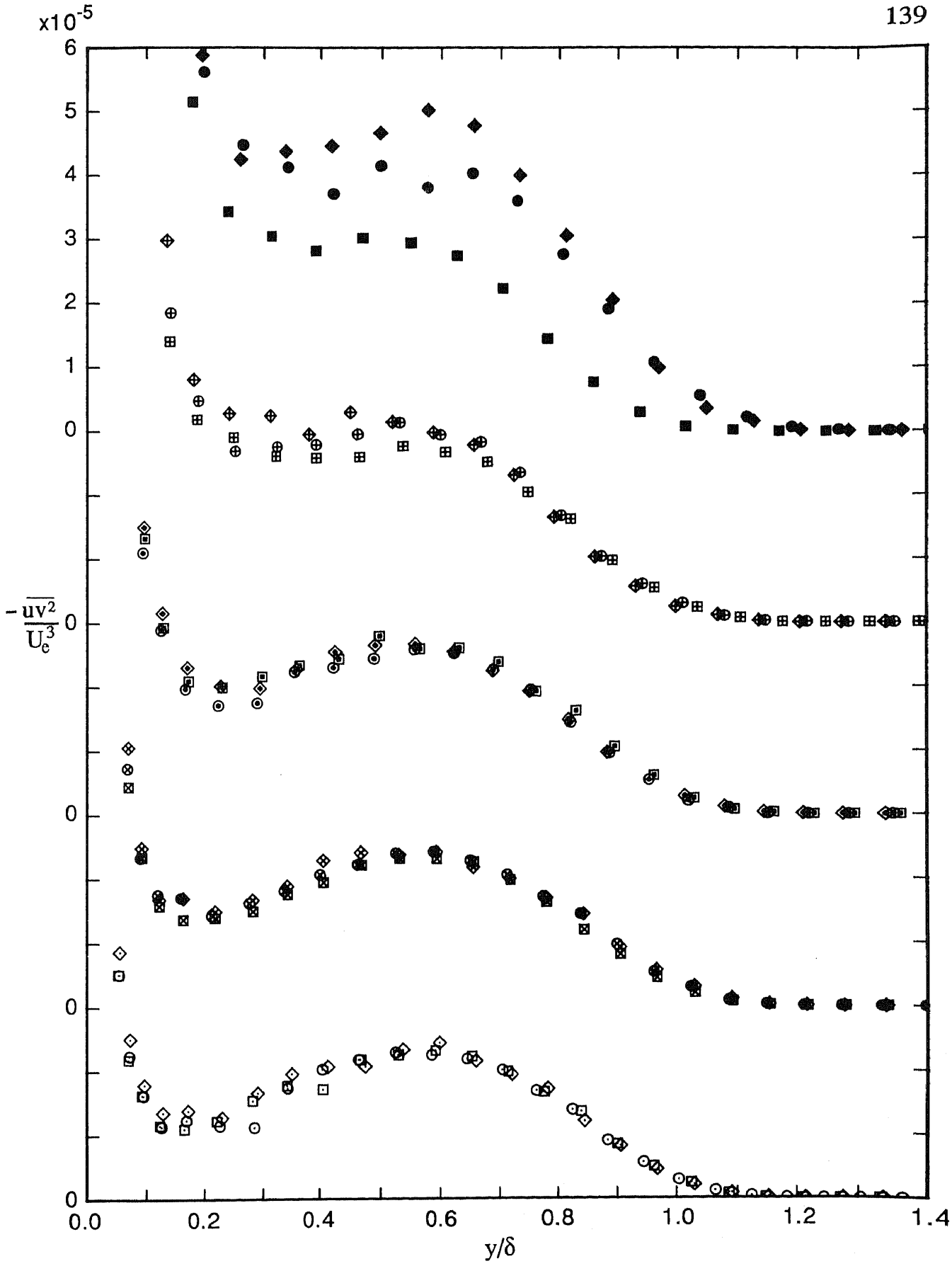

FIGURE 6.33. Profiles of $-\overline{uv^2}/U_e^3$ versus y/δ for design flows showing effects of device for five nominal values of R_θ. Note shift in ordinate.

Wire:	●, R_θ=697;	⊕, 1003;	⊙, 1568;	⊗, 2226;	○, 2788.
Grit:	◆, R_θ=706;	⊕, 1042;	◇, 1520;	⊗, 2178;	◇, 2730.
2.0 mm pins:	■, R_θ=729;	⊞, 1027;	⊡, 1565;	⊠, 2181;	□, 2889.

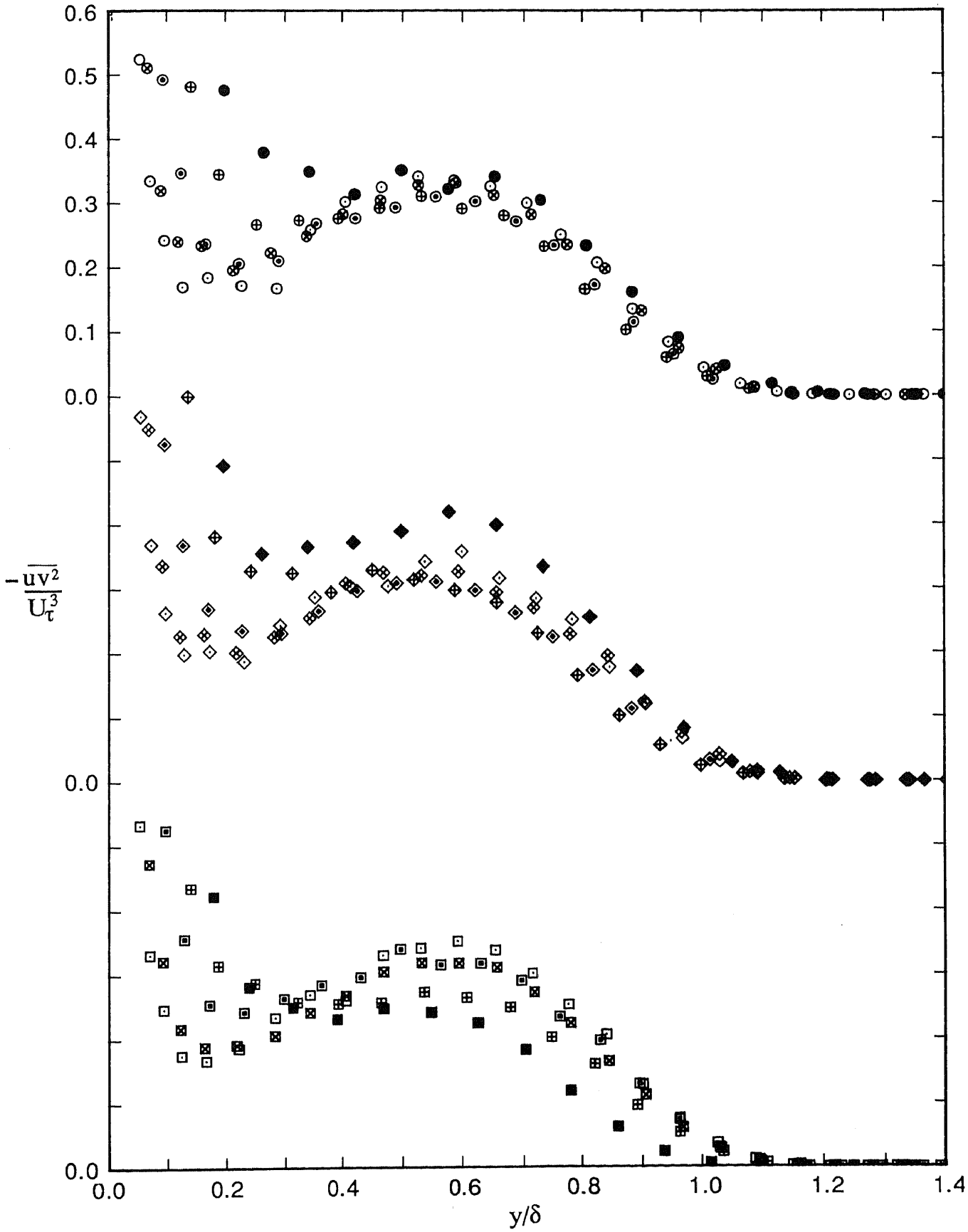

FIGURE 6.34. Profiles of $-\overline{uv^2}/U_\tau^3$ versus y/δ for design flows showing effects of R_θ for three devices. Note shift in ordinate.

Wire:	●, R_θ=697;	⊕, 1003;	⊙, 1568;	⊗, 2226;	⊙, 2788.
Grit:	◆, R_θ=706;	◈, 1042;	◇, 1520;	◈, 2178;	◇, 2730.
2.0 mm pins:	■, R_θ=729;	⊞, 1027;	⊡, 1565;	⊠, 2181;	⊡, 2889.

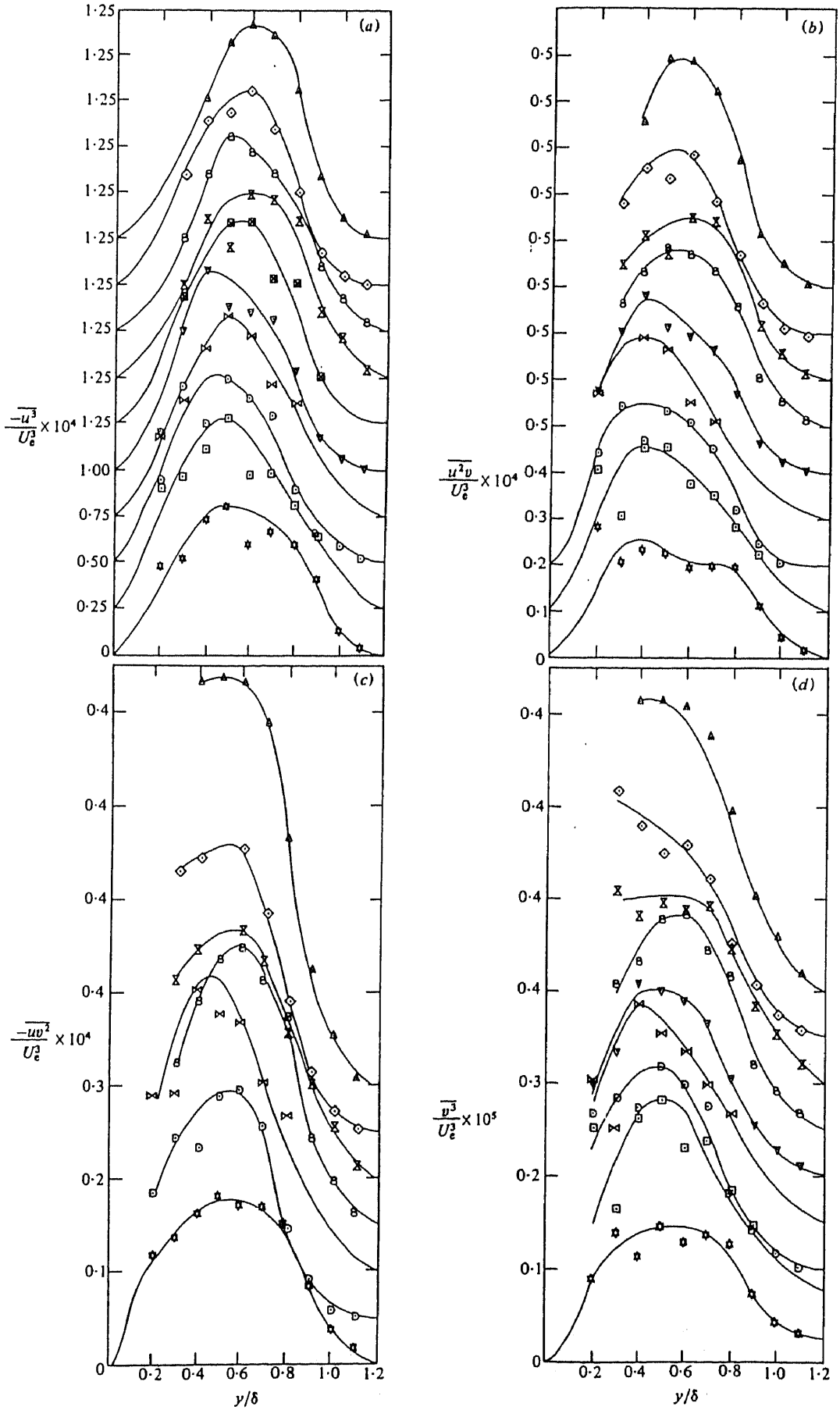

FIGURES 6.35 (a) to (d). Profiles of triple products as given by Murlis, Tsai & Bradshaw (1982). The caption used by Murlis et al. on their figure is shown below:

Triple products, normalized by U_e^3. Values of $U_e\theta/\nu$: △, 791; ◇, 1112; 8, 1368; ⧖, 1640; ⊠, 1900; ▽, 2192; ⋈, 2387; ⊳, 3362; ⊡, 4108; ✡, 4750. (*a*) $-\overline{u^3}$: ordinate scale is for $U_e\theta/\nu = 4750$; other curves successively displaced by 0·25 units. (*b*) $\overline{u^2v}$; ordinate scale is for $U_e\theta/\nu = 4750$; other curves successively displaced by 0·1 units. (*c*) $-\overline{uv^2}$; ordinate scale is for $U_e\theta/\nu = 4750$; other curves successively displaced by 0·05 units. (*d*) $\overline{v^3}$; ordinate scale is for $U_e\theta/\nu = 4750$; other curves successively displaced by 0·05 units.

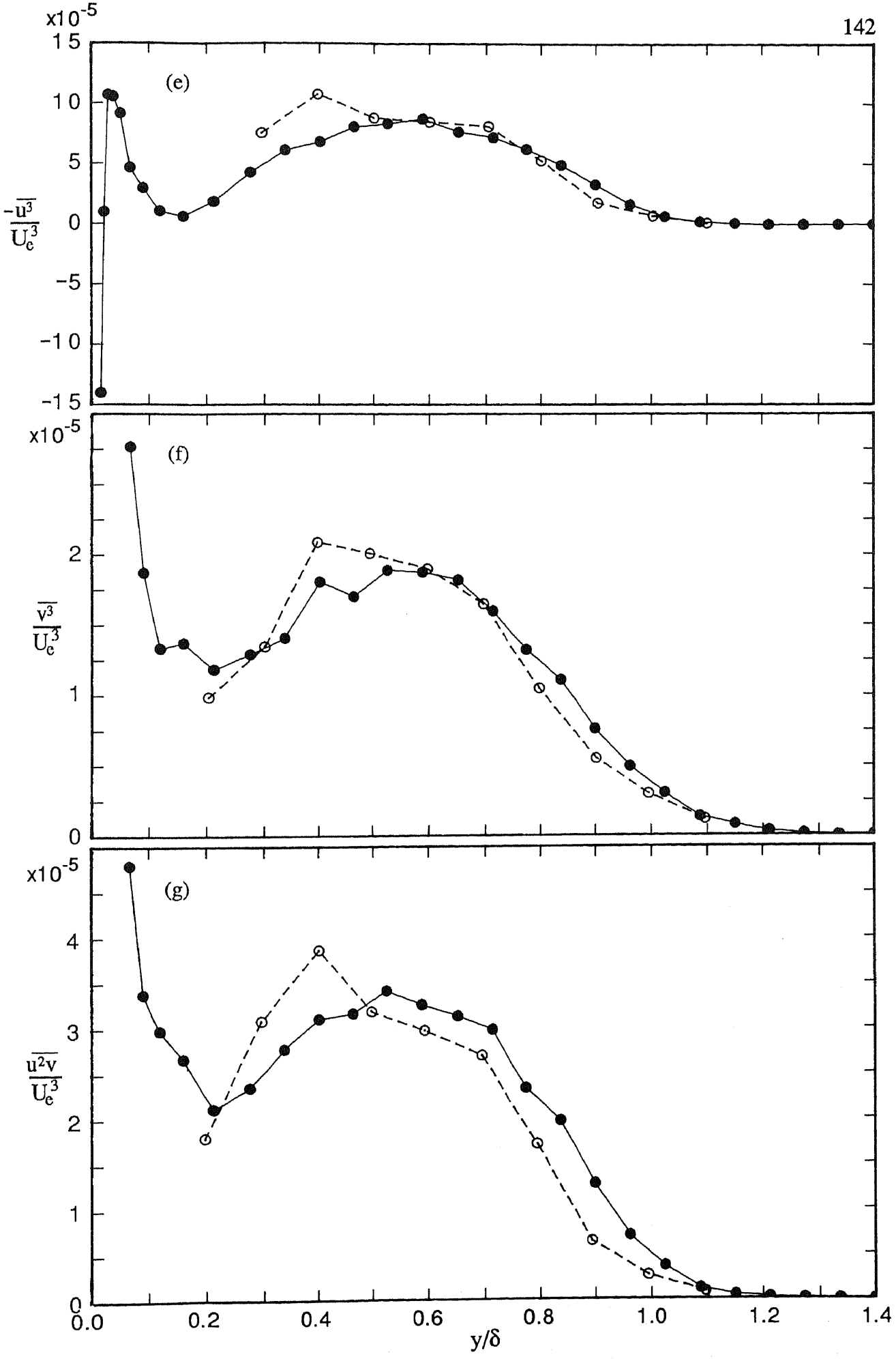

FIGURES 6.35 (e) to (g). Profiles of triple products for current investigation compared with those of Murlis et al. (1982). (e) $-\overline{u^3}/U_e^3$ versus y/δ, (f) $\overline{v^3}/U_e^3$ versus y/δ, (g) $\overline{u^2v}/U_e^3$ versus y/δ. —●—, Data for wire for design flow for $R_\theta = 2226$;--⊙--, Data of Murlis et al. for $R_\theta = 2192$.

cases profiles that appear to be the same have been labeled with different values of R_θ in the two publications. Murlis sometimes used different symbols to denote a given value of R_θ, depending upon the triple product being considered, whereas Murlis, Tsai & Bradshaw reproduced the symbols of Murlis but used the same symbol to denote a given value of R_θ for each of the four triple products. It can be seen from figures 6.35 (a) to (d) that in most cases, the sequence in which the triple-product profiles are plotted by Murlis, Tsai & Bradshaw do not correspond to the sequence of the symbols given in the figure caption. The situation is confusing and it is not possible to resolve adequately this inconsistency.

Difficulties were encountered in comparing the current triple-product data with those of Murlis and Murlis, Tsai & Bradshaw. For the current study, triple products for say the wire were measured for values of R_θ of 697, 1003, 1568, 2226 and 2788. The current data for R_θ = 697, 1003 and 2788 could not be closely matched with data having similar values of R_θ since the variation in R_θ between the two sets of data was at least 10% and was greater than 15% in one case. The current data for R_θ = 1568 could not be compared with that of the above researchers for R_θ = 1640 due to a discrepancy in labeling as discussed above and also the fact that Murlis only presented profiles for one type of triple product for R_θ =1640. The current data for R_θ = 2226 and that of Murlis and Murlis, Tsai & Bradshaw for R_θ = 2192 have Reynolds numbers that differ by only about 1.5%, but these researchers only present $\overline{u^3}$, $\overline{v^3}$ and $\overline{u^2v}$ triple products for this value of R_θ. Notwithstanding this, current data were compared with these data as shown in figures 6.35 (e) to (g). It is encouraging that the two sets of profiles agree reasonably well, given the uncertainties in triple-product measurements, insofar as corresponding profiles can be compared.

Now that the design-flow broadband-turbulence characteristics up to and including triple products have been presented, it is appropriate to discuss the observation that at the lower values of R_θ, the broadband-turbulence characteristics can vary significantly depending upon the device used.

It is known that the three different tripping devices impart different types of disturbances into the flow. Evidence to support this is the transverse C_f measurements for the three devices which are shown in figure 5.16. The

introduction of these three-dimensional disturbances into the flows is inevitable in any low-Reynolds-number turbulent boundary layer that uses a tripping device. It was shown in Chapters 4 and 5 that for $R_\theta \approx 713$, the type of device used had only a small effect upon mean-flow parameters of $\Delta U/U_\tau$ (figure 4.2), C_f (figure 4.5), H (figure 4.6) and G (figure 4.7), as well as mean-flow profiles of U/U_τ versus $\log(yU_\tau/\nu)$ (figure 5.6) and $(U-U_e)/U_\tau$ versus y/δ (figure 5.9). However, in this chapter it has been shown that for $R_\theta \approx 713$, the type of device used can have a significant effect upon Reynolds-stress profiles of $\overline{u^2}/U_e^2$, $\overline{v^2}/U_e^2$, $\overline{w^2}/U_e^2$ and $-\overline{uv}/U_e^2$, versus y/δ (figures 6.5, 6.8, 6.11 and 6.21 respectively), and an even greater effect upon the triple-product profiles of $-\overline{u^3}/U_e^3$, $\overline{v^3}/U_e^3$, $\overline{u^2v}/U_e^3$ and $-\overline{uv^2}/U_e^3$, versus y/δ (figures 6.24, 6.27, 6.30 and 6.33 respectively). The fact that the Reynolds stresses and triple products are more affected by the devices than the mean-flow characteristics is not completely unexpected since any differences between quantities become more pronounced as the order of these quantities increases. For $R_\theta \approx 1020$ and above, the effect of device diminishes and corresponding Reynolds stresses and triple products for the different devices now agree quite closely, as for the mean-flow characteristics for the different devices. This indicates that, for the design flows, the previous history of the flow is now of little consequence as far as these broadband-turbulence characteristics are concerned.

It is apparent from the above that even though mean-flow characteristics for different devices for $R_\theta \approx 713$ may agree reasonably closely, it does not necessarily follow that Reynolds stresses and triple products for different devices will agree at this value of R_θ. Thus, the mere fact that a researcher may choose a device and establish a flow that closely follows Coles' (1962) $\Delta U/U_\tau$-versus-R_θ mean-flow characteristic does not imply that associated broadband-turbulence measurements will be universal within the region of $R_\theta \approx 713$. Such turbulence measurements reported in the literature must therefore be viewed with caution and cannot be regarded as definitive.

The fact that the basic quantities of Reynolds stresses and triple products for the design flows for the different devices agree reasonably closely for $R_\theta \approx 1020$ and above, suggests that parameters derived from these quantities will also not vary appreciably from device to device for these values of R_θ, and that any

variation in derived parameters will primarily be confined to values of R_θ less than about 1020

6.3.4. Anisotropy Parameters

For high Reynolds number flows, structural similarity exists and ratios of various components of the Reynolds stress tensor have fixed values for given flow regions, such as the outer region of a boundary layer. To investigate how the structure of the turbulence changes with R_θ and device for the design flows, a number of anisotropy or structural parameters, viz. $\overline{u^2}/\overline{v^2}$, $-\overline{uv}/(\sqrt{\overline{u^2}}\sqrt{\overline{v^2}}) \equiv R_{12}$ (shear correlation coefficient), and $-\overline{uv}/\overline{q^2} \equiv a_1$, were plotted against y/δ using the method described above. These parameters all tend to 0/0 near the edge of the boundary layer and this can lead to scatter. Consequently, when these parameters are plotted, the limiting values of y/δ will be 1.2 and not 1.4 as previously. The behaviour of each of these parameters will now be analysed in turn.

Profiles of $\overline{u^2}/\overline{v^2}$ versus y/δ for the three tripping devices for different values of R_θ are shown plotted in figure 6.36. For the purpose of determining values of $\overline{u^2}/\overline{v^2}$, the $\overline{u^2}$ normal stresses measured with the crossed-wire probe were used, rather than those measured with the single-wire probe. It is immediately apparent from figure 6.36 that for each of the devices, the structure of the flow, in terms of $\overline{u^2}/\overline{v^2}$, for y/δ greater than about 0.1, shows a moderate dependence on R_θ. However, for the three devices, the profiles do not vary monotonically with R_θ, but instead there is a tendency for the profiles to rise with increasing R_θ up to a maximum at both $R_\theta \approx 1544$ and $R_\theta \approx 2175$, and then to fall again for higher values of R_θ. Murlis, Tsai & Bradshaw (1982) indicate that $\overline{v^2}/\overline{u^2}$ is a crude measure of the efficiency of turbulent mixing. Thus, generally speaking, it can be inferred that the efficiency of turbulent mixing is at a minimum within the region $R_\theta \approx 1544$ to $R_\theta \approx 2175$ but increases as R_θ decreases below this range or increases above this range. For increasing values of y/δ, the values of $\overline{u^2}/\overline{v^2}$ for the different profiles decrease at first and then remain approximately constant between $y/\delta \approx 0.2$ and $y/\delta \approx 0.7$, before decreasing again.

Figure 6.37 shows profiles of $\overline{u^2}/\overline{v^2}$ versus y/δ replotted and it can be seen that the profiles are dependent on device for $R_\theta \approx 713$, but for $R_\theta \approx 1020$ and

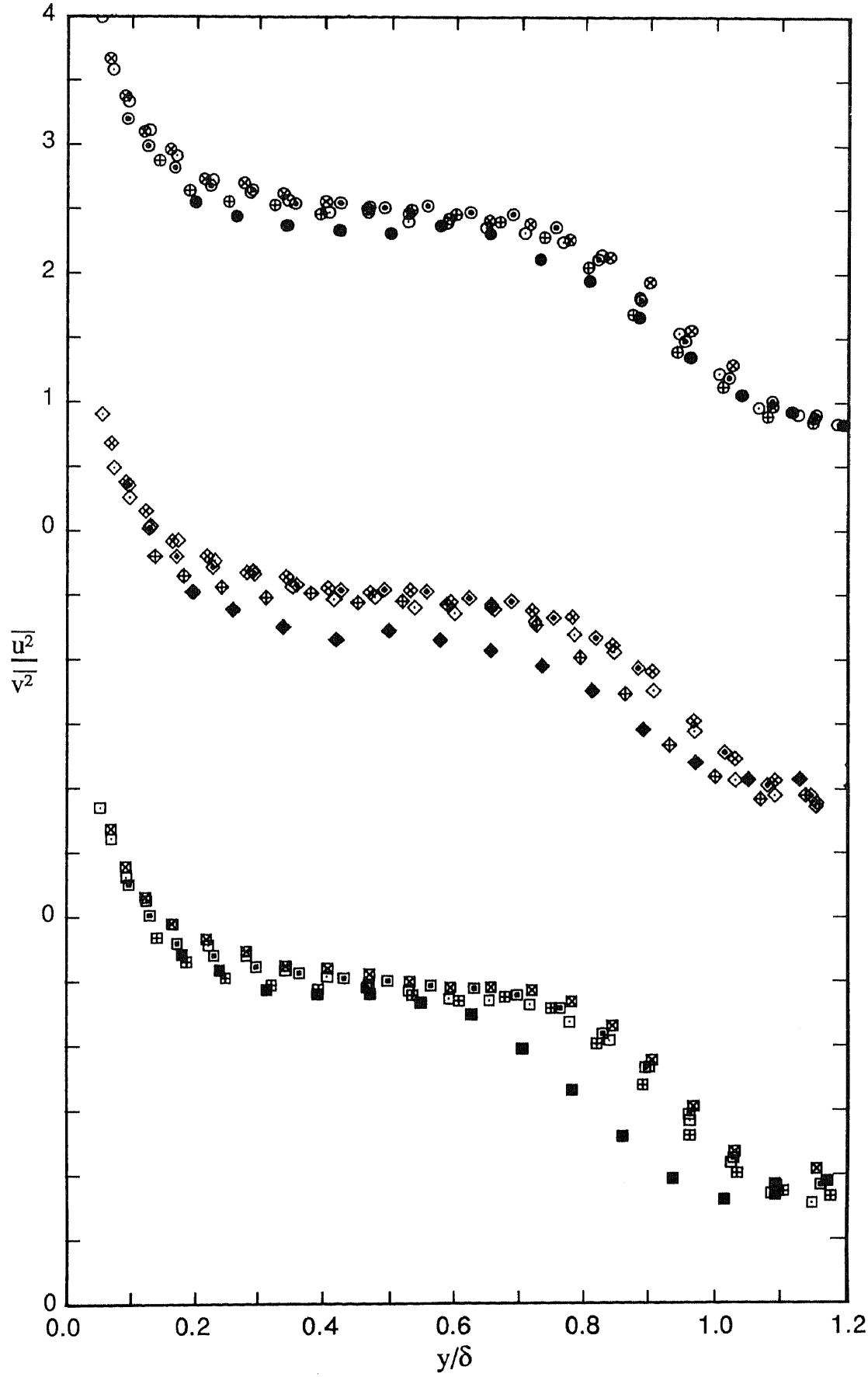

FIGURE 6.36. Profiles of Reynolds-normal-stress ratio, $\overline{u^2}/\overline{v^2}$ versus y/δ, for design flows showing effects of R_θ for three devices. Note shift in ordinate.

Wire: ●, R_θ=697; ⊕, 1003; ⊙, 1568; ⊗, 2226; ⊙, 2788.
Grit: ◆, R_θ=706; ⊕, 1042; ◇, 1520; ◈, 2178; ◇, 2730.
2.0 mm pins: ■, R_θ=729; ⊞, 1027; ⊡, 1565; ⊠, 2181; ⊡, 2889.

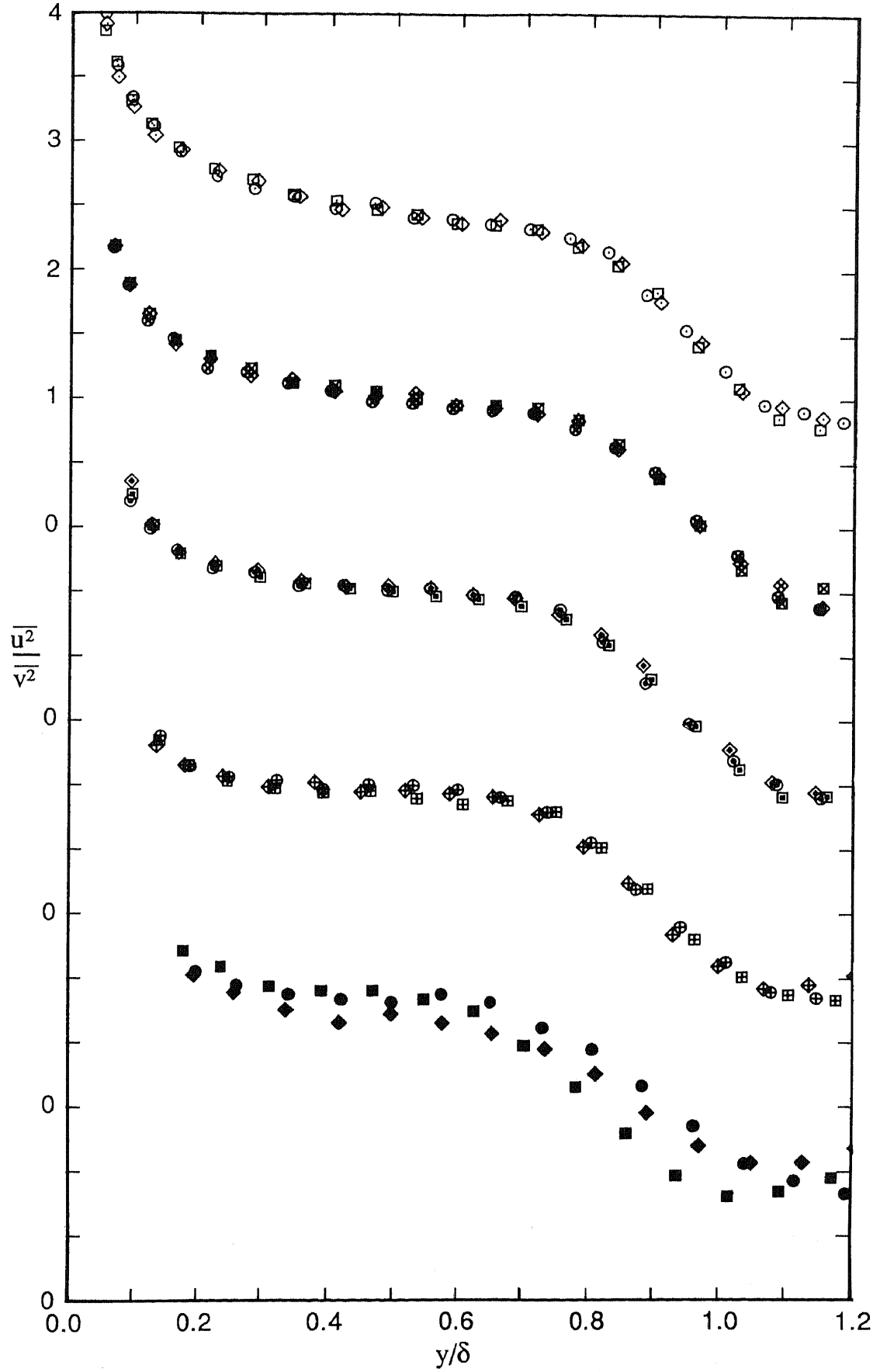

FIGURE 6.37. Profiles of Reynolds-normal-stress ratio, $\overline{u^2}/\overline{v^2}$ versus y/δ, for design flows showing effects of device for five nominal values of R_θ. Note shift in ordinate.

Wire:	●, R_θ=697;	⊕, 1003;	⊙, 1568;	⊗, 2226;	⊙, 2788.
Grit:	◆, R_θ=706;	⊕, 1042;	◇, 1520;	⊗, 2178;	◇, 2730.
2.0 mm pins:	■, R_θ=729;	⊞, 1027;	⊡, 1565;	⊠, 2181;	⊡, 2889.

above, the device used has virtually no effect on the profiles. At $y/\delta = 0.6$, the value of $\overline{u^2}/\overline{v^2}$ for the three devices is about 2.3 for $R_\theta \approx 713$, about 2.5 for $R_\theta \approx 1544$ and $R_\theta \approx 2175$ and about 2.4 for $R_\theta \approx 2810$. This variation of $\overline{u^2}/\overline{v^2}$ with R_θ was not as large as for the corresponding data of Murlis, Tsai & Bradshaw (1982). They found that for $y/\delta = 0.6$, $\overline{u^2}/\overline{v^2}$ was about 1.7 for $R_\theta = 791$, about 2.3 for $R_\theta = 1900$ and about 2.4 for $R_\theta = 4750$. The reasons for the significant difference between the data of the two investigations at the respective lower values of R_θ remain unclear.

Considering now the shear correlation coefficient, profiles of R_{12} versus y/δ are plotted in figure 6.38. The structure of the flow, in terms of R_{12}, shows a moderate dependence on R_θ over the entire y/δ range. Except for the data for the pins for $R_\theta = 729$, the trends of the profiles with R_θ for the three devices are approximately the same as those described above for the $\overline{u^2}/\overline{v^2}$ data. Murlis, Tsai & Bradshaw (1982) indicate that the value of R_{12} is probably a better measure of the efficiency of turbulent mixing than $\overline{v^2}/\overline{u^2}$ and previous discussion on how the efficiency of turbulent mixing varies with R_θ also applies here. For increasing values of y/δ, the values of R_{12} for the different profiles increase at first and then decrease again. Between $y/\delta \approx 0.2$ and $y/\delta \approx 0.7$, the values of R_{12} change by relatively small amounts compared with the changes for the entire profiles.

Profiles of R_{12} versus y/δ are shown replotted in figure 6.39 and it can be seen that for $R_\theta \approx 713$, the profiles are once again dependent on device, and for higher values of R_θ the profiles for the different devices do not collapse as well as for say the corresponding profiles of $\overline{u^2}/\overline{v^2}$ versus y/δ shown in figure 6.37. A possible explanation of this behaviour for the R_{12} profiles for $R_\theta \approx 1020$ and above is that R_{12} is comprised of three terms, compared with two terms for $\overline{u^2}/\overline{v^2}$, and clearly the more terms in a parameter, the more sensitive it will be. At $y/\delta = 0.6$, the value of R_{12} for $R_\theta \approx 713$ is about 0.45 for the wire and grit and about 0.5 for the pins, for $R_\theta \approx 1544$ and $R_\theta \approx 2175$ the value of R_{12} is about 0.48 for all devices and for $R_\theta \approx 2810$ the value of R_{12} is about 0.45 for all devices. Murlis, Tsai & Bradshaw (1982) found that at $y/\delta = 0.6$, the value of R_{12} was 0.42 at $R_\theta = 791$ and 0.45 at $R_\theta = 1900$. If the data for the pins for $R_\theta = 729$ are not considered, then the variation of R_{12} for the current

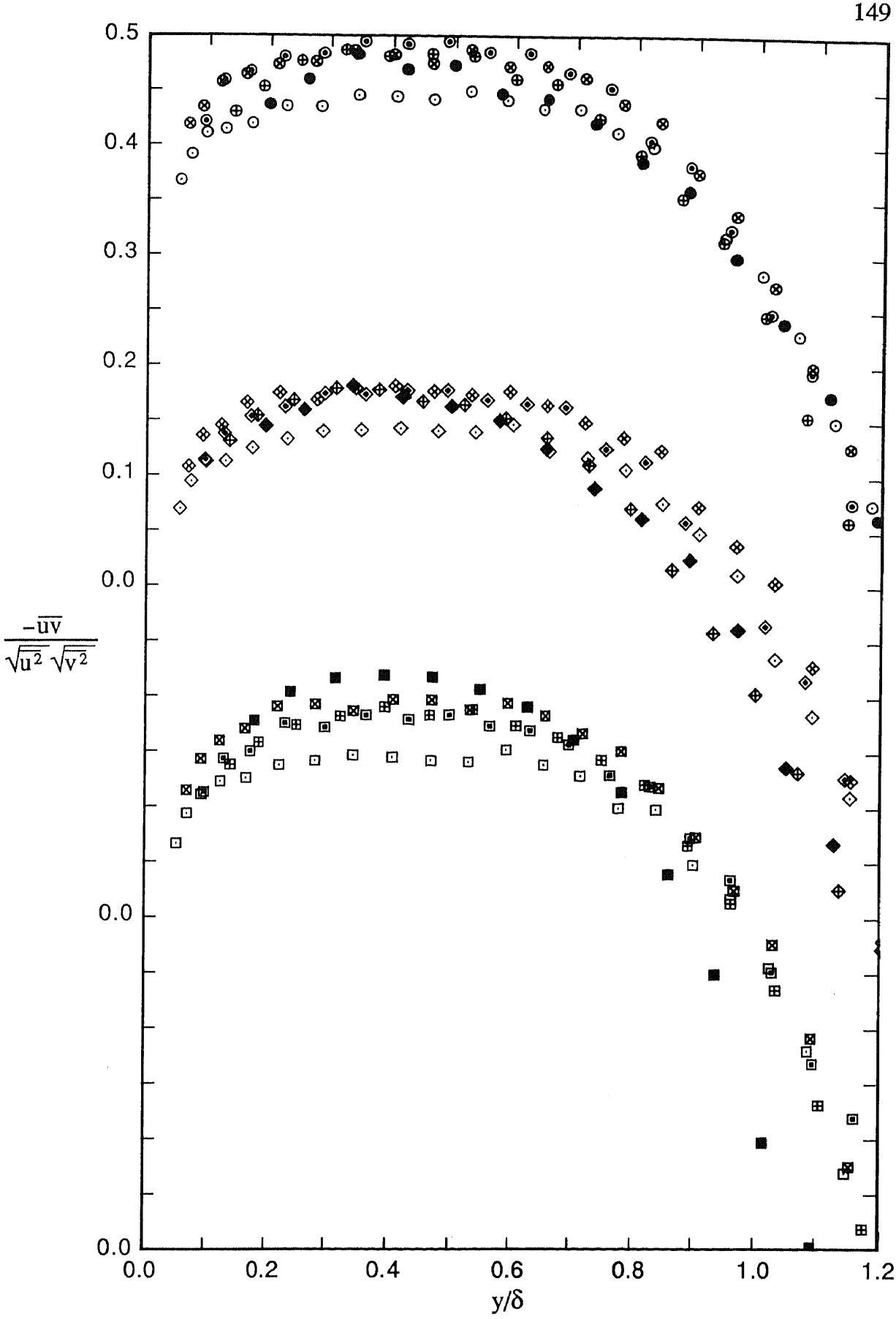

FIGURE 6.38. Profiles of shear correlation coefficient, $-\overline{uv}/(\sqrt{u^2}\sqrt{v^2})$ versus y/δ, for design flows showing effects of R_θ for three devices. Note shift in ordinate.

Wire: ●, R_θ=697; ⊕, 1003; ⊙, 1568; ⊗, 2226; ⊙, 2788.
Grit: ◆, R_θ=706; ⧫, 1042; ◇, 1520; ⧫, 2178; ◇, 2730.
2.0 mm pins: ■, R_θ=729; ⊞, 1027; ⧈, 1565; ⊠, 2181; ⊡, 2889.

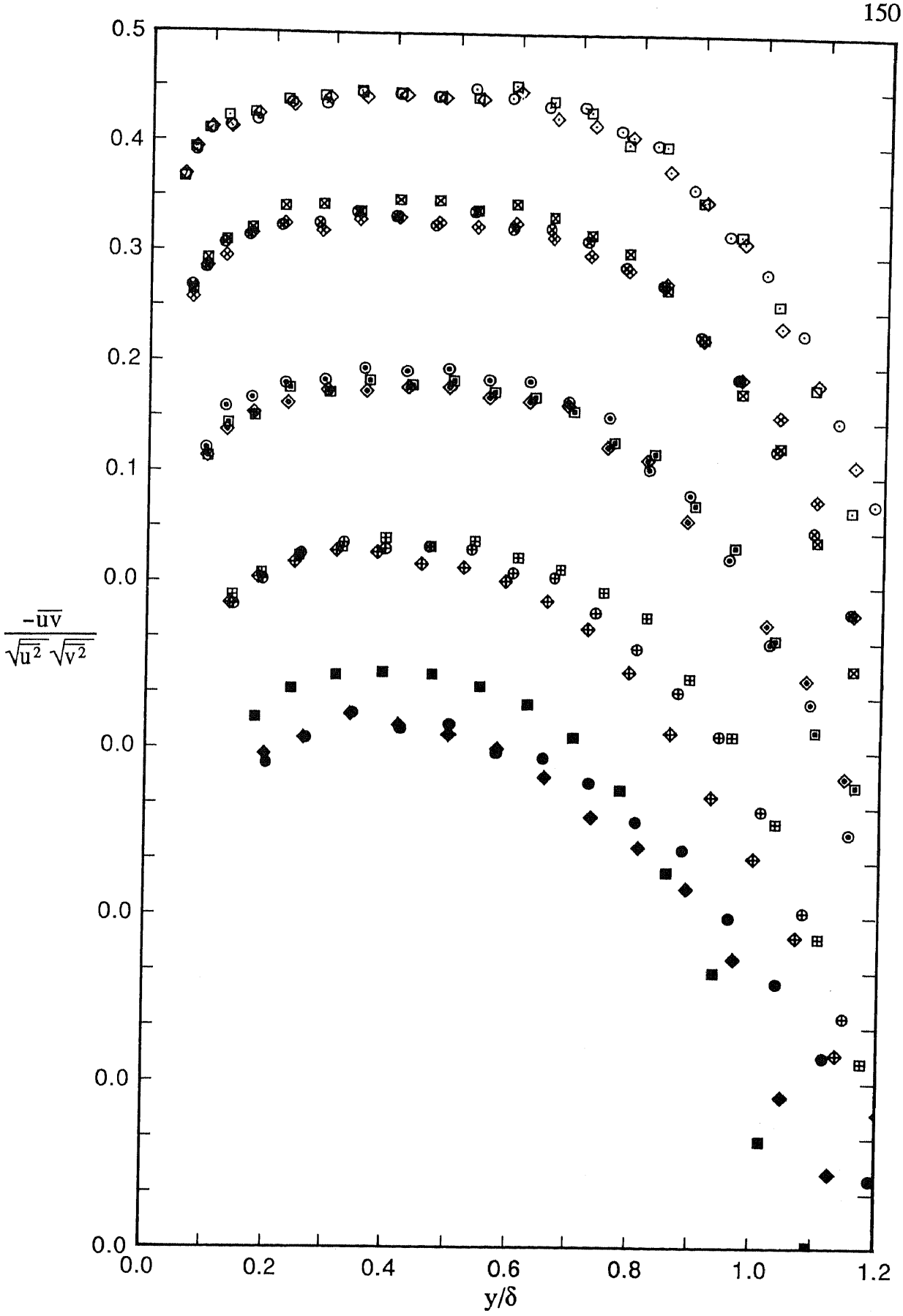

FIGURE 6.39. Profiles of shear correlation coefficient, $-\overline{uv}/(\sqrt{\overline{u^2}}\sqrt{\overline{v^2}})$ versus y/δ, for design flows showing effects of device for five nominal values of R_θ. Note shift in ordinate.

Wire: ●, R_θ=697; ⊕, 1003; ⊙, 1568; ⊗, 2226; ⊙, 2788.

Grit: ◆, R_θ=706; ⊕, 1042; ◇, 1520; ◈, 2178; ◇, 2730.

2.0 mm pins: ■, R_θ=729; ⊞, 1027; ⊡, 1565; ⊠, 2181; ⊡, 2889.

investigation is the same as that for Murlis, Tsai & Bradshaw, although the current values of R_{12} are slightly higher.

Profiles of $a_1 \equiv -\overline{uv}/\overline{q^2}$ versus y/δ are shown in figures 6.40 and 6.41 and these two figures correspond to figures 6.38 and 6.39 respectively for profiles of R_{12} versus y/δ.

A comparison between the two pairs of figures indicates similar behaviour of the a_1 and R_{12} profiles in corresponding cases and discussion already given on the actual profile behaviour for the R_{12} profiles is substantially applicable to the a_1 profiles. At $y/\delta = 0.6$, the value of a_1 for $R_\theta \approx 713$ is about 0.15 for the wire and the grit and about 0.17 for the pins, for $R_\theta \approx 1544$ and $R_\theta \approx 2175$, a_1 is about 0.16 for all devices and for $R_\theta \approx 2810$, a_1 is about 0.15 for all devices. The structural parameter a_1, originally due to Townsend (1961), has been used by Bradshaw, Ferris & Atwell (1967) in their boundary-layer calculation method. In this method, a_1 is taken to have the value 0.15. The current data for $R_\theta \approx 2810$ for values of y/δ varying between about 0.3 and about 0.7 is consistent with this, but if the method of Bradshaw, Ferris & Atwell was to be used for boundary-layer calculations for lower values of R_θ, then allowances would have to be made for variations of a_1 with R_θ.

6.3.5 Skewness and Flatness

The fluctuating velocities occurring at any point in a turbulent flow field can be described using conventional statistical theory. The third moment of the probability density of a fluctuating velocity is a measure of the asymmetry of the distribution and when suitably non-dimensionalised is known as the skewness. The fourth moment of the distribution is a measure of the extent of the skirts of the distribution and when suitably non-dimensionalised is known as the kurtosis or flatness factor. For a Gaussian or normal distribution, the skewness is equal to zero and the flatness factor is equal to 3.0. The definitions used to determine the skewness and the flatness factor for the u-component fluctuating velocity are respectively

$$S_u = \frac{\overline{u^3}}{(\overline{u^2})^{1.5}} \qquad (6.1)$$

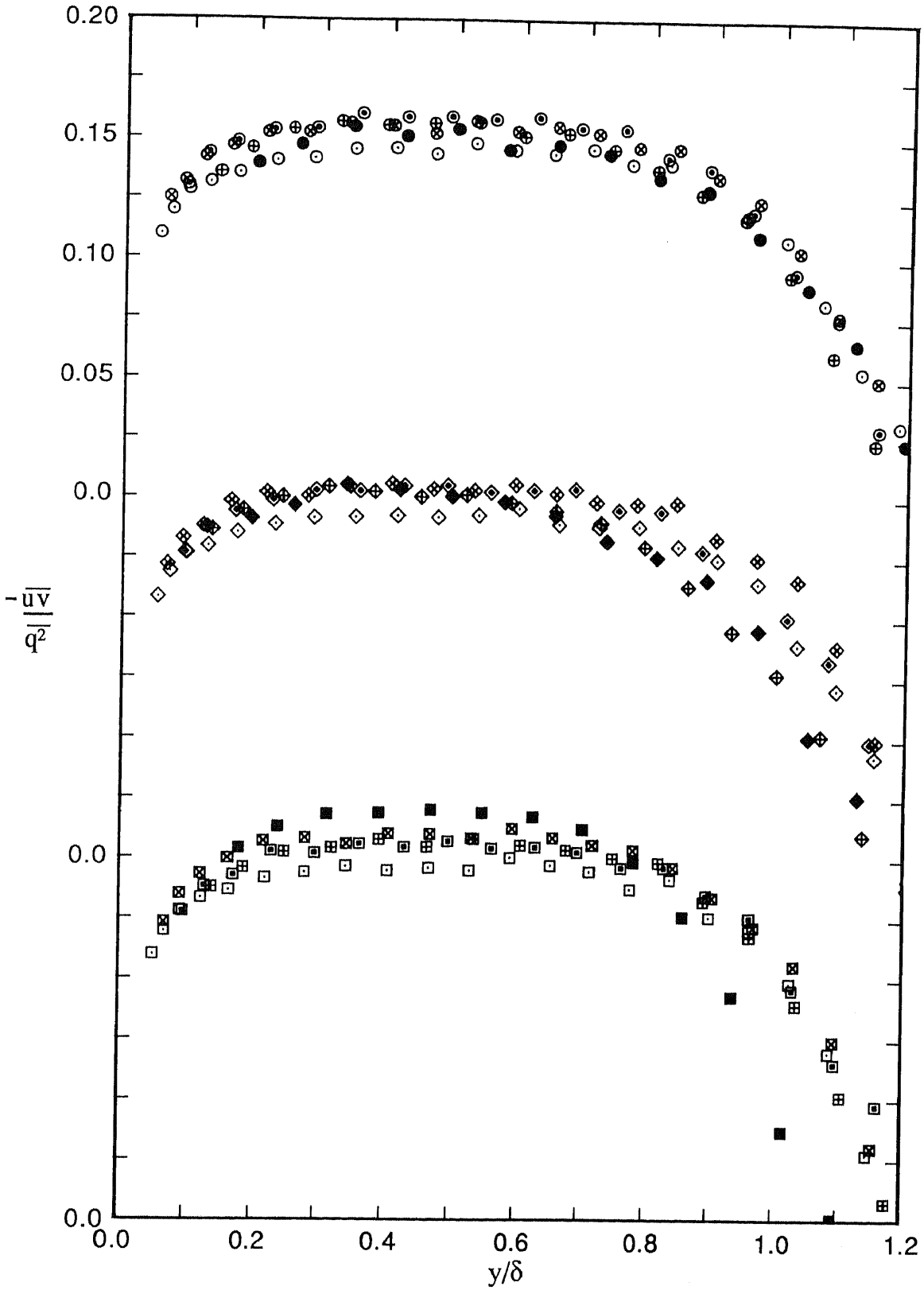

FIGURE 6.40. Profiles of $-\overline{uv}/\overline{q^2}$ versus y/δ for design flows showing effects of R_θ for three devices. Note shift in ordinate.

Wire:	●, R_θ=697;	⊕, 1003;	⊙, 1568;	⊗, 2226;	⊙, 2788.
Grit:	◆, R_θ=706;	◈, 1042;	◇, 1520;	◈, 2178;	◇, 2730.
2.0 mm pins:	■, R_θ=729;	⊞, 1027;	⊡, 1565;	⊠, 2181;	⊡, 2889.

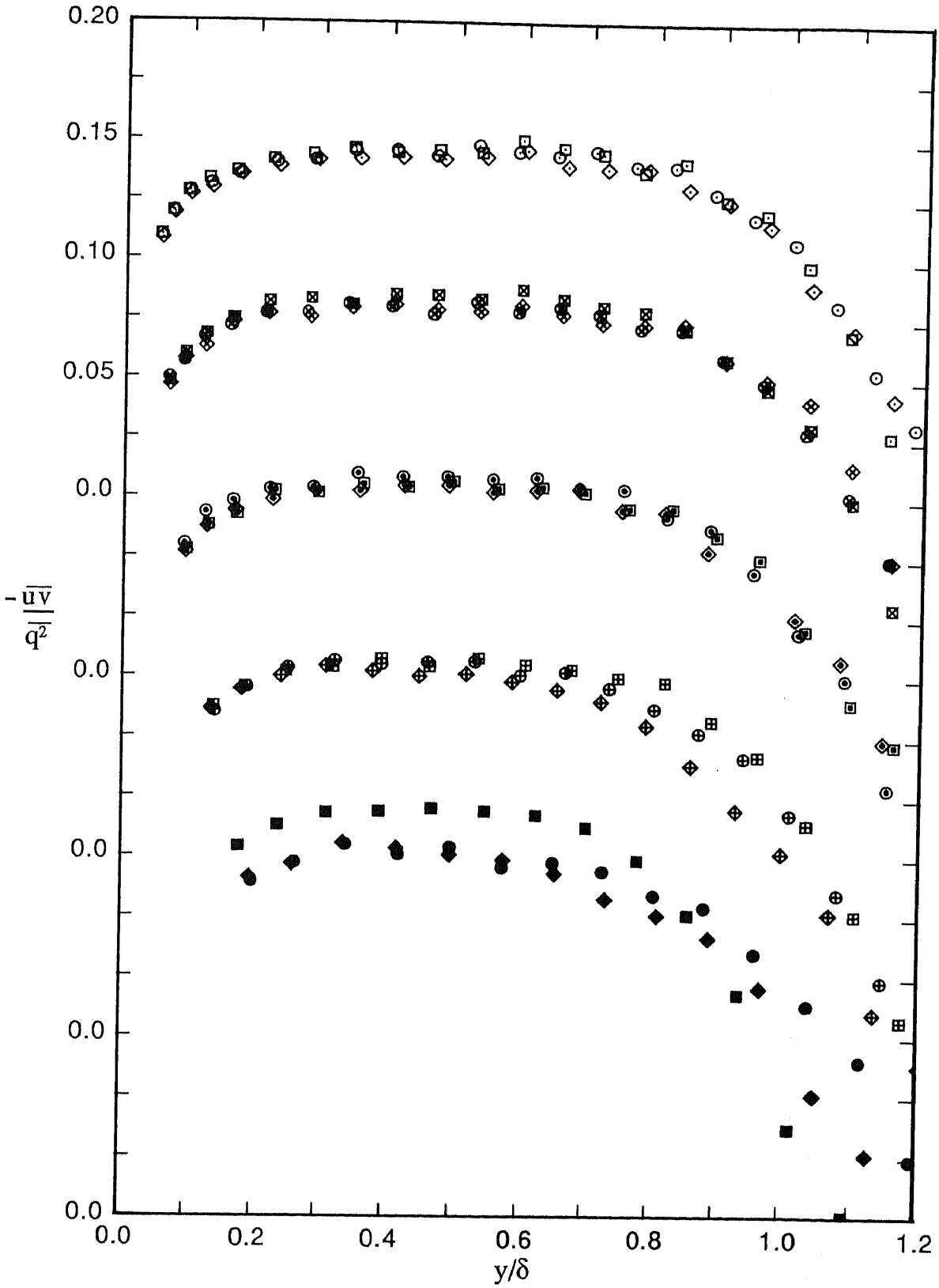

FIGURE 6.41. Profiles of $-\overline{uv}/\overline{q^2}$ versus y/δ for design flows showing effects of device for five nominal values of R_θ. Note shift in ordinate.

Wire: ●, R_θ=697; ⊕, 1003; ⊙, 1568; ⊗, 2226; ⊙, 2788.
Grit: ◆, R_θ=706; ⊕, 1042; ◇, 1520; ◈, 2178; ◇, 2730.
2.0 mm pins: ■, R_θ=729; ⊞, 1027; ⊡, 1565; ⊠, 2181; ⊡, 2889.

and

$$F_u = \frac{\overline{u^4}}{(\overline{u^2})^2} \tag{6.2}$$

and similarly for the v- and w-component fluctuating velocities. Skewness can be either positive or negative, but flatness factor is obviously always positive. Positive skewness means that the instantaneous fluctuating velocity for a given component is more often below its mean value than above it. This implies that large excursions of the instantaneous velocity above its mean value are more common than large excursions below its mean value. The opposite to the above applies for negative skewness.

Plots of S_u versus y/δ for the three devices for different values of R_θ are shown in figure 6.42. These measurements were all taken with the single-wire probe. No figure is given that directly shows the effect of device on the values of S_u for different values of R_θ. Similarly, such figures for other flow characteristics will often not be presented subsequently. From figure 6.42 it can be seen that the values of S_u for the three devices depend moderately on R_θ, except for the pins for R_θ = 729 where the dependency on R_θ is more pronounced. Overall, the general behaviour of the data is as expected. For y/δ less than about 0.3, the values of S_u are reasonably close to zero, especially the data for $R_\theta \approx 2810$, and for increasing values of y/δ the values of S_u become increasingly negative and fall to about -2.5 at $y/\delta \approx 1.0$ before rising again. The limiting values of S_u obtained by Murlis (1975) were about -2.3.

In figure 6.42, the accumulation of data for small values of y/δ for each of the devices makes it difficult to interpret the behaviour of the data in this region. Consequently, to facilitate interpretation, the data of figure 6.42 have been replotted using coordinates of S_u versus $\log(yU_\tau/\nu)$ as shown in figure 6.43. In this figure, points beyond y/δ = 1.2 have been omitted to avoid confusion. This method of presenting skewness is often used in the literature. When the data are plotted in this manner, they shown a far greater variation with R_θ than previously. It is apparent from figure 6.43, that for small values of yU_τ/ν, the values of S_u for the different devices for the different values of R_θ often change sign and become positive. This phenomenon has also been

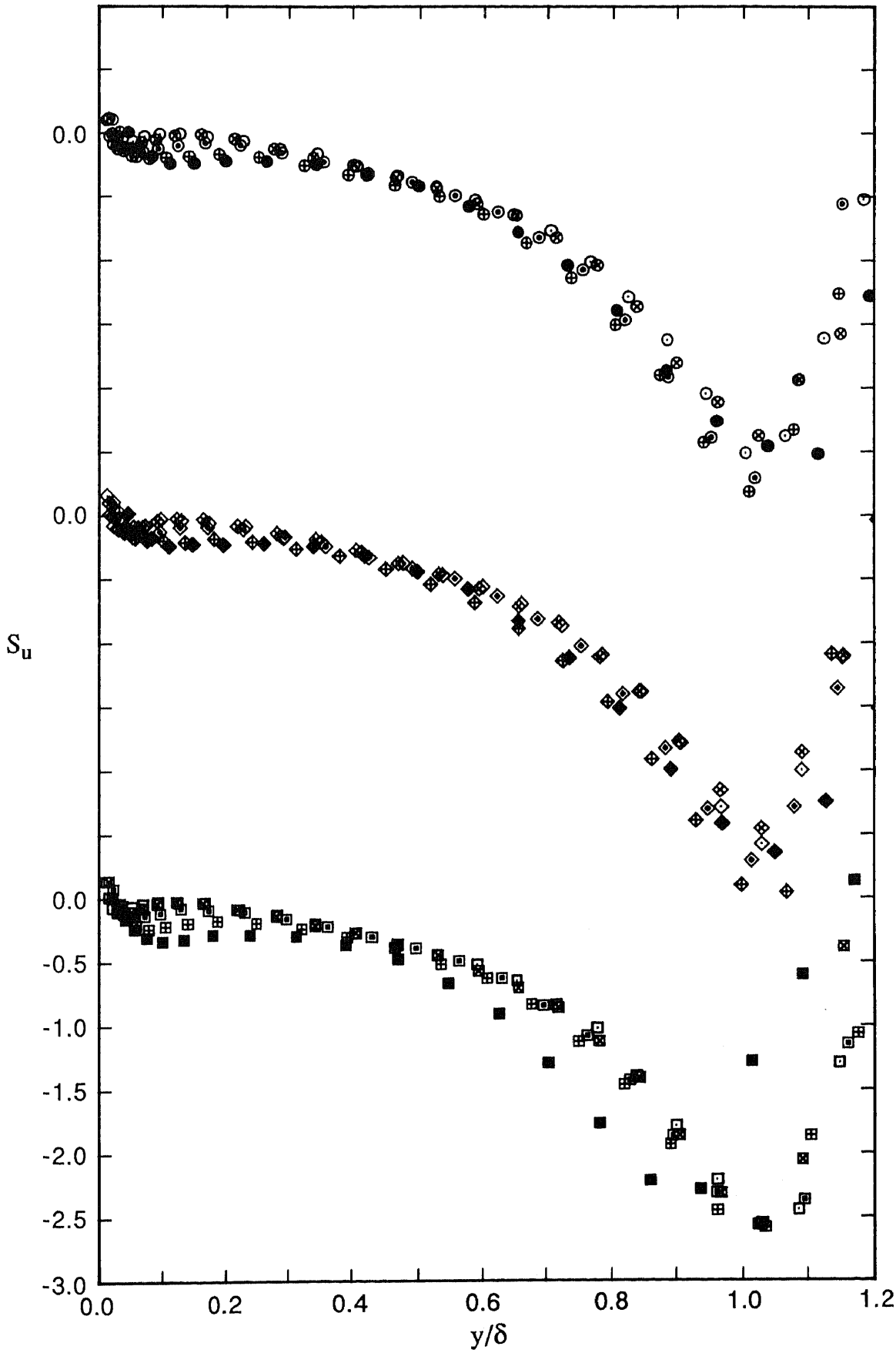

FIGURE 6.42. Profiles of skewness, $\overline{u^3}/(\overline{u^2})^{1.5}$ versus y/δ, for design flows showing effects of R_θ for three devices. Note shift in ordinate.

Wire: ●, R_θ=697; ⊕, 1003; ⊙, 1568; ⊗, 2226; ⊙, 2788.
Grit: ◆, R_θ=706; ⊕, 1042; ◇, 1520; ◈, 2178; ◇, 2730.
2.0 mm pins: ■, R_θ=729; ⊞, 1027; ▣, 1565; ⊠, 2181; ⊡, 2889.

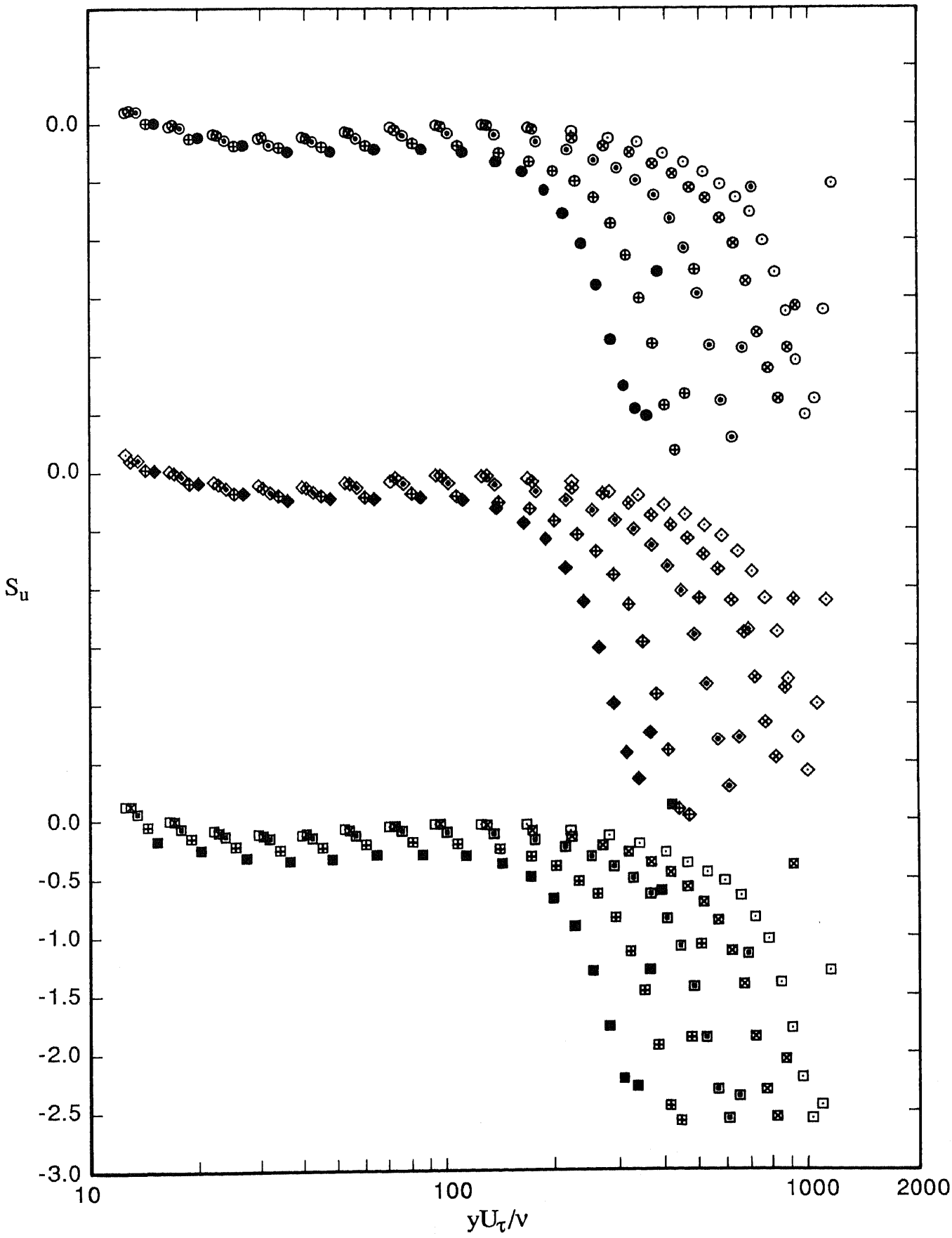

FIGURE 6.43. Profiles of skewness, $\overline{u^3}/(\overline{u^2})^{1.5}$ versus $\log(yU_\tau/\nu)$, for design flows showing effects of R_θ for three devices. Note shift in ordinate.

Wire:	●, R_θ=697;	⊕, 1003;	⊙, 1568;	⊗, 2226;	⊙, 2788.
Grit:	◆, R_θ=706;	⊕, 1042;	◇, 1520;	◈, 2178;	◇, 2730.
2.0 mm pins:	■, R_θ=729;	⊞, 1027;	⊡, 1565;	⊠, 2181;	⊡, 2889.

observed by Gupta & Kaplan (1972) (R_θ = 1900), Ueda & Hinze (1975) (R_θ = 1244), Andreopolous, Durst, Zaric & Jovanovic (1984) (R_θ = 3624) and Barlow & Johnston (1985) (1988) (R_θ = 1140) for low-Reynolds-number turbulent boundary-layer flows. The positive values of S_u correspond to the negative values of $-\overline{u^3}$ shown for example in figure 6.23. Ueda & Hinze showed that S_u becomes zero at $yU_\tau/\nu \approx 15$ and they indicate that this location is where $\sqrt{\overline{u^2}}/U_\tau$ attains its maximum value. The results of Andreopolous et al. as well as those of Barlow & Johnston agreed with this behaviour. Considering the current data shown in figure 6.43, it is apparent that the values of S_u for the different devices for the different values of R_θ become zero at about $yU_\tau/\nu = 15$, and an analysis of figure 6.15 indicates that the corresponding values of $\sqrt{\overline{u^2}}/U_\tau$ in the different cases are, as far as it is possible to tell, close to their maxima.

Figure 6.44 shows plots of S_v versus y/δ for the three devices and the extent of the variation of the data with R_θ is much the same as that for the corresponding plots for S_u shown in figure 6.42. The values of S_v are positive for all values of y/δ, unlike the values of S_u. For increasing values of y/δ, the values of S_v at first decrease slightly towards zero and then rise to about 1.5 at $y/\delta \approx 1.1$ before falling again. As was the case for the S_u measurements, the S_v measurements closest to zero for small values of y/δ correspond to $R_\theta \approx 2810$. The limiting values of S_v obtained by Murlis (1975) are also 1.5.

Since the values of S_v were measured with the crossed-wire probe, it was not possible to obtain values of S_v as close to the wall as for S_u measurements. Consequently the data of figure 6.44 were not replotted using $\log(yU_\tau/\nu)$ as the abscissa as previously. The same obviously also applies to S_w measurements.

Plots of S_w versus y/δ are shown in figure 6.45 for the three devices. Although the spread of the data with R_θ is much the same as that for the S_u and S_v measurements for y/δ less than about 0.6, beyond this range the data for each of the devices show a large variation with R_θ. For a two-dimensional flow, the probability density distributions for the w-component fluctuating velocities are symmetrical, and hence the values of S_w are zero. Thus, the fact that the values of S_w are not zero indicates that the flows are not completely two dimensional. This fact has of course already been established by the transverse measurements

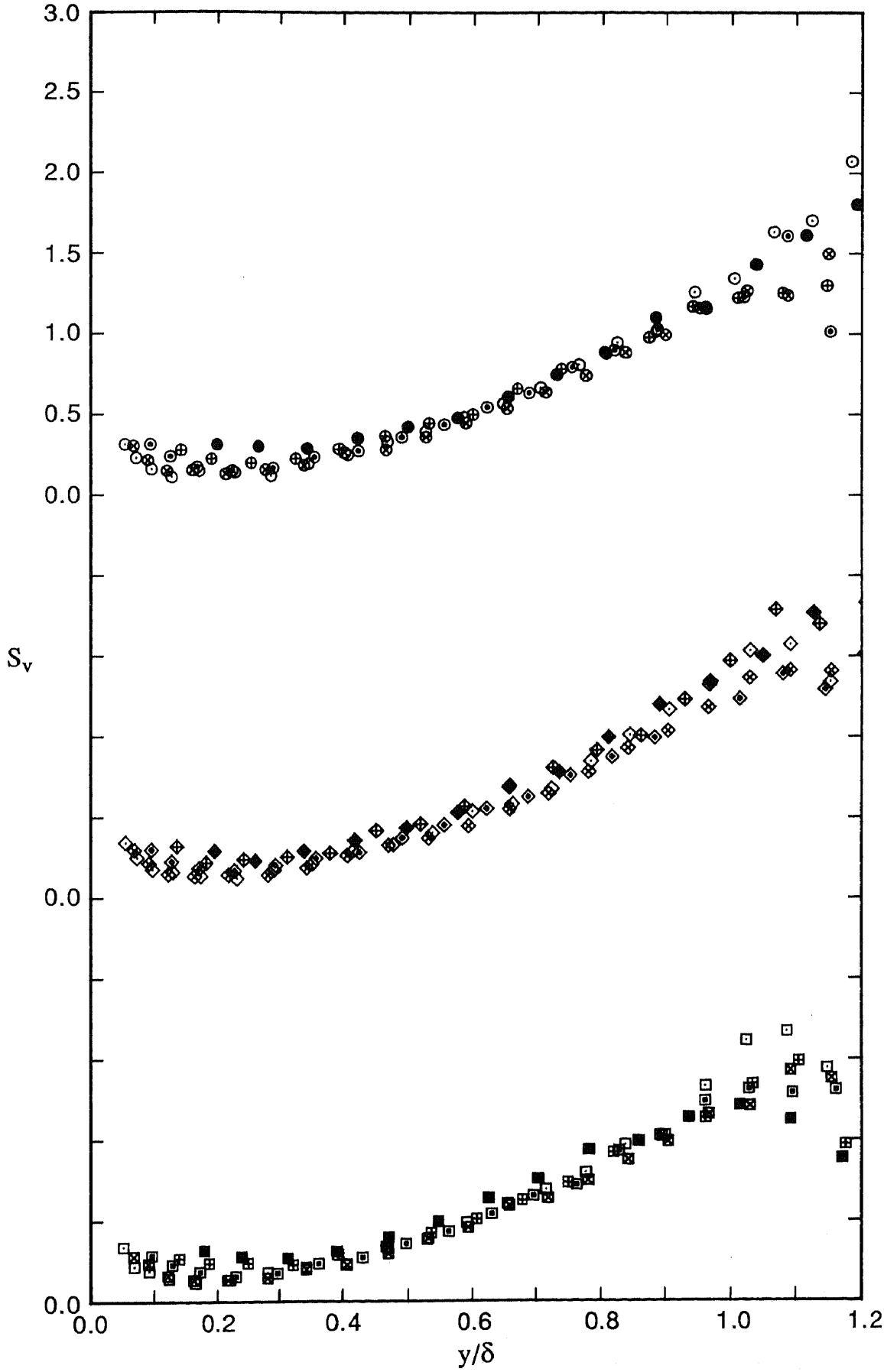

FIGURE 6.44. Profiles of skewness, $\overline{v^3}/(\overline{v^2})^{1.5}$ versus y/δ, for design flows showing effects of R_θ for three devices. Note shift in ordinate.

Wire:	●, R_θ=697;	⊕, 1003;	⊙, 1568;	⊗, 2226;	⊙, 2788.
Grit:	◆, R_θ=706;	◈, 1042;	◇, 1520;	◈, 2178;	◇, 2730.
2.0 mm pins:	■, R_θ=729;	⊞, 1027;	⊡, 1565;	⊠, 2181;	⊡, 2889.

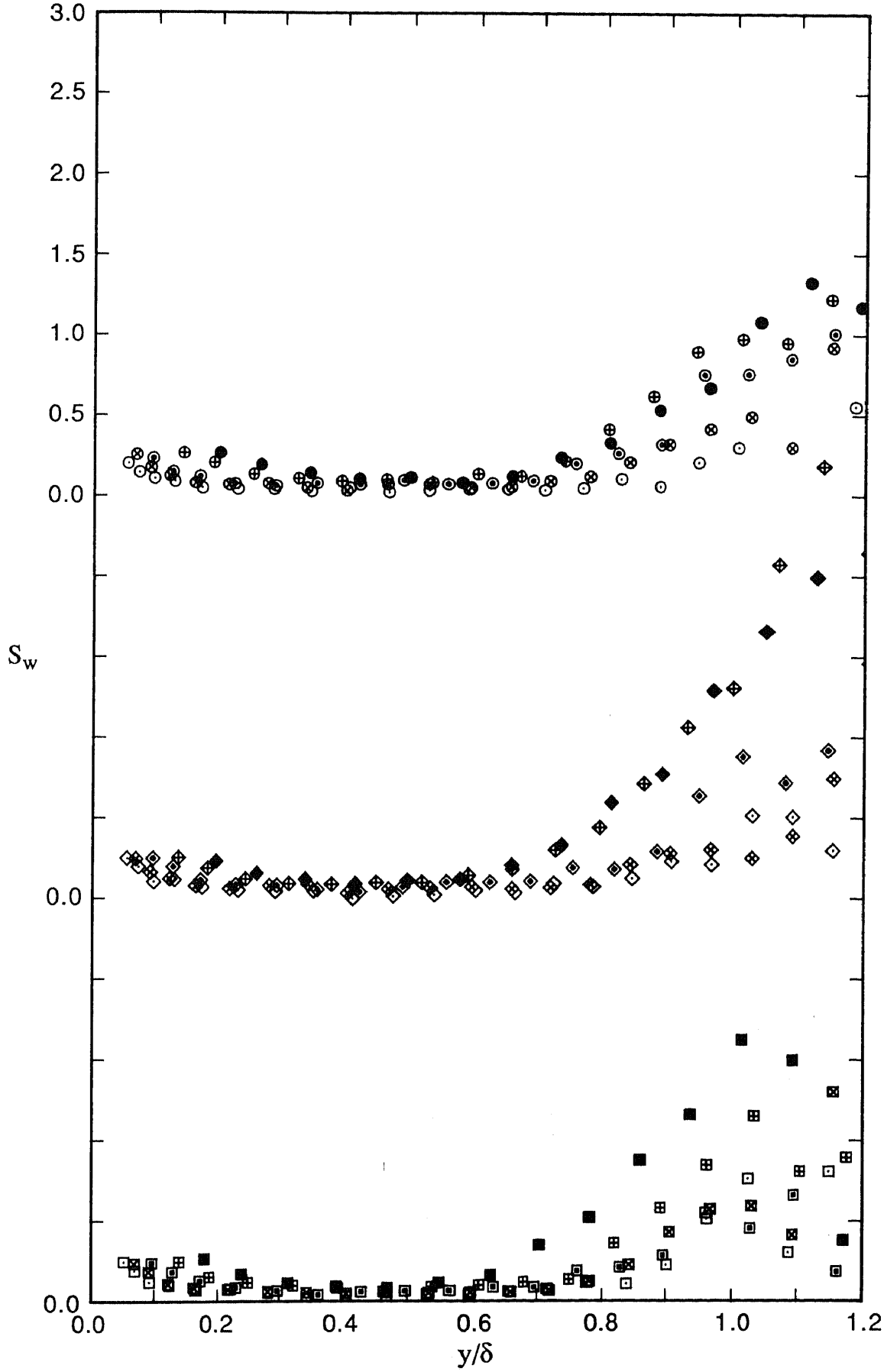

FIGURE 6.45. Profiles of skewness, $\overline{w^3}/(\overline{w^2})^{1.5}$ versus y/δ, for design flows showing effects of R_θ for three devices. Note shift in ordinate.

Wire: ●, R_θ=697; ⊕, 1003; ⊙, 1568; ⊗, 2226; ⊙, 2788.
Grit: ◆, R_θ=706; ⊕, 1042; ◇, 1520; ⊗, 2178; ◇, 2730.
2.0 mm pins: ■, R_θ=729; ⊞, 1027; ⊡, 1565; ⊠, 2181; ⊡, 2889.

of C_f shown in figure 5.16. It is not expected that low-Reynolds-number flows downstream of tripping devices will be two dimensional since it takes the flows some time to recover from the effects of a device. The fact that the values of S_w approach zero as R_θ increases indicates that the flows are becoming more two dimensional as they develop after being tripped and this is consistent with the transverse C_f measurements shown in figure 5.16.

Attention will now be focussed on flatness factors. Plots of F_u versus y/δ for the three devices are shown in figure 6.46. Experimental data points in this and other plots of flatness factors have been joined by straight lines to clarify the behaviour of the data in the regions of the peaks and also to indicate the directions to the next data points beyond $y/\delta = 1.2$. For y/δ less than about 0.6, the data for each of the devices for the different values of R_θ collapse well and, except for the data for y/δ less than about 0.1, the values of F_u are slightly below 3.0, which is the value of F_u for a Gaussian distribution. For y/δ less than about 0.1, the data can be seen to dip slightly and this phenomenon has also been observed by Gupta & Kaplan (1972), Ueda & Hinze (1975), Andreopolous et al. (1984) and Barlow & Johnston (1985), (1988). These researchers also found that closer to the wall, inside the viscous sublayer, the value of F_u rose again appreciably above the Gaussian value of 3.0 (up to about 8.0 for the data of Gupta & Kaplan). Simpson, Chew & Shivaprasad (1981) have indicated that the high values of F_u within the viscous sublayer occur because the inrush phase of the bursting cycle which brings in high velocity fluid from the outer region results in large-amplitude positive u fluctuations and consequently produces a large skirt in the velocity probability distribution. The current data were not taken close enough to the wall to observe any such rises in the values of F_u. Considering now the data in the outer flow regions, it can be seen that beyond $y/\delta \approx 0.6$, the values of F_u rise slowly at first and then more steeply, to peak values of the order of 20 before falling sharply. Simpson, Chew & Shivaprasad have indicated that in this region, intermittent large-amplitude negative u fluctuations occur as a result of the large eddies driving the fluid from the low-velocity regions outwards, which tends to increase F_u. In the region beyond $y/\delta \approx 0.6$, the data for the pins for $R_\theta = 729$ clearly stand alone, but other data do not show a large variation with R_θ and the peak values of F_u for the different values of R_θ occur at $y/\delta \approx 1.1$. A possible reason that the data for the pins for

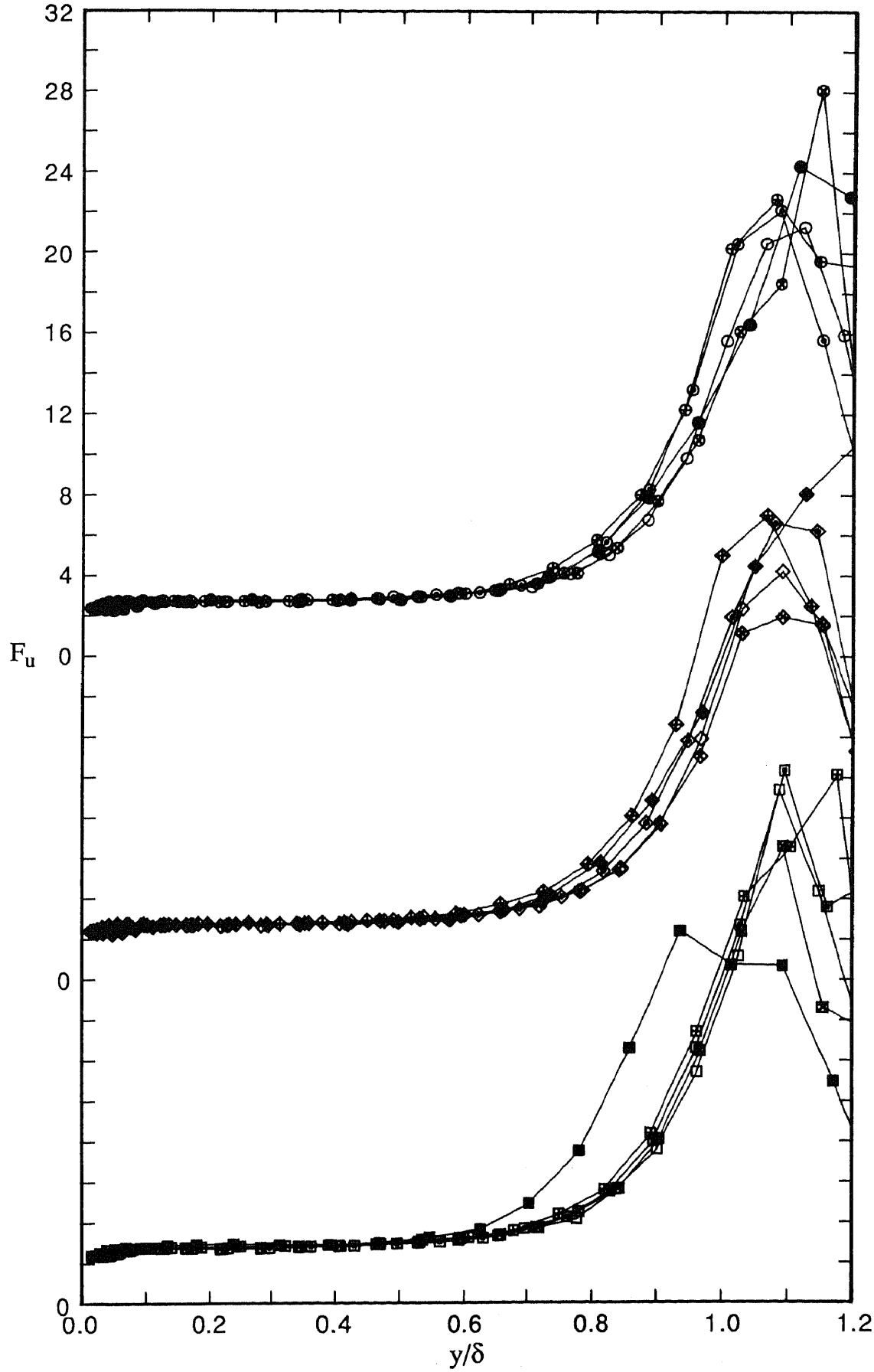

FIGURE 6.46. Profiles of flatness factor, $\overline{u^4}/(\overline{u^2})^2$ versus y/δ, for design flows showing effects of R_θ for three devices. Note shift in ordinate.

Wire: ●, R_θ=697; ⊕, 1003; ⊙, 1568; ⊗, 2226; ⊙, 2788.
Grit: ◆, R_θ=706; ⊕, 1042; ◇, 1520; ◈, 2178; ◇, 2730.
2.0 mm pins: ■, R_θ=729; ⊞, 1027; ⊡, 1565; ⊠, 2181; ⊡, 2889.

R_θ = 729 behave differently is that the associated flow deviates appreciably from being two-dimensional. This explanation is based upon an observation made by Bradshaw & Pontikos (1985). These researchers analysed turbulence measurements on an "infinite" swept wing and indicated that a remarkable feature shared by all three flatness factors is that the region with roughly the "Gaussian" value of 3.0 extends further and further out, as a fraction of the peak location, as the boundary layer becomes more three-dimensional.

Plots of F_v versus y/δ for the three devices are shown in figure 6.47. For each of the devices, the data for y/δ less than about 0.6 collapse well for different values of R_θ, as for the F_u data. For low values of y/δ, values of F_v for different values of R_θ are about 4.0, but for increasing y/δ, the values of F_v decrease to just above the Gaussian value of 3.0 before rising again to peak values and then falling again. The peaks for the F_v data are not as clearly defined as for the F_u data, but generally they are smaller and correspond to slightly larger values of y/δ. The F_v data for the pins for R_θ = 729 can be seen to depart from the trends of the other data, as for the F_u data, but the deviations are not as pronounced as previously.

Finally, plots of F_w versus y/δ for the three devices are shown in figure 6.48. These data have higher peaks than the F_u and F_v data, and accordingly the ordinate of figure 6.48 has been factored by 2 compared with previously. For each of the devices, the data for y/δ less than about 0.6 collapse well for different values of R_θ, as for the F_u and F_v data, and the values of F_w are slightly above 3.0. Beyond $y/\delta \approx 0.6$, the values of F_w increase to their peak values before falling again. Once again the peaks are not as clearly defined as for the F_u data, but generally they are larger and correspond to slightly larger values of y/δ. The F_w data for the pins for R_θ = 729 depart from the trends of the other data, but once again not to the same extent as for the F_u data.

6.3.6 Balances of Energy and Shear Stress

For the equations representing the balances of turbulent kinetic energy and Reynolds shear stress, the distribution between the various terms at a given location and the change of distribution with position in the flow, give the turbulent structure of the flow.

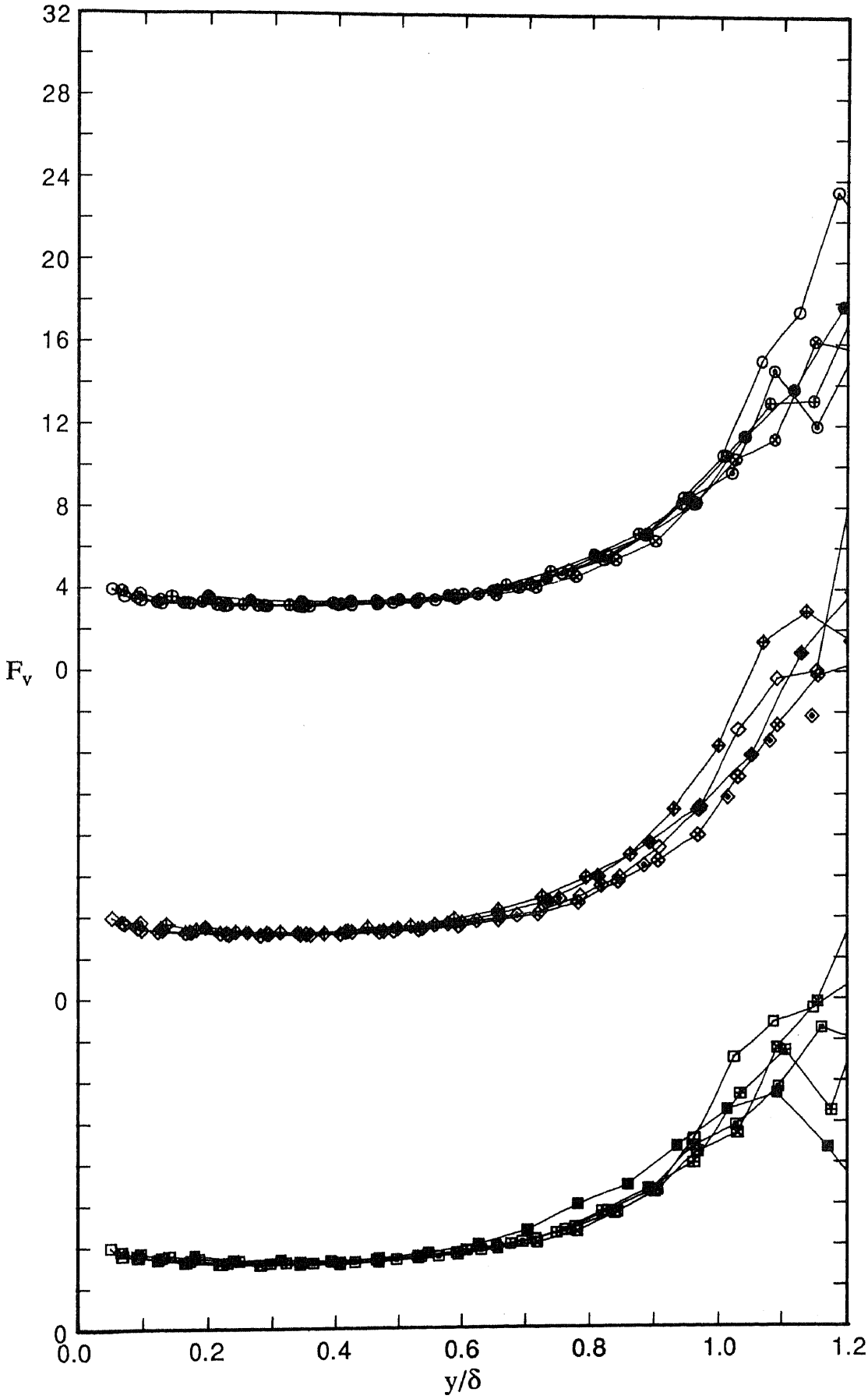

FIGURE 6.47. Profiles of flatness factor, $\overline{v^4}/(\overline{v^2})^2$ versus y/δ, for design flows showing effects of R_θ for three devices. Note shift in ordinate.

Wire:	●, R_θ=697;	⊕, 1003;	⊙, 1568;	⊗, 2226;	⊙, 2788.
Grit:	◆, R_θ=706;	⊕, 1042;	◇, 1520;	⊗, 2178;	◇, 2730.
2.0 mm pins:	■, R_θ=729;	⊞, 1027;	⊡, 1565;	⊠, 2181;	⊡, 2889.

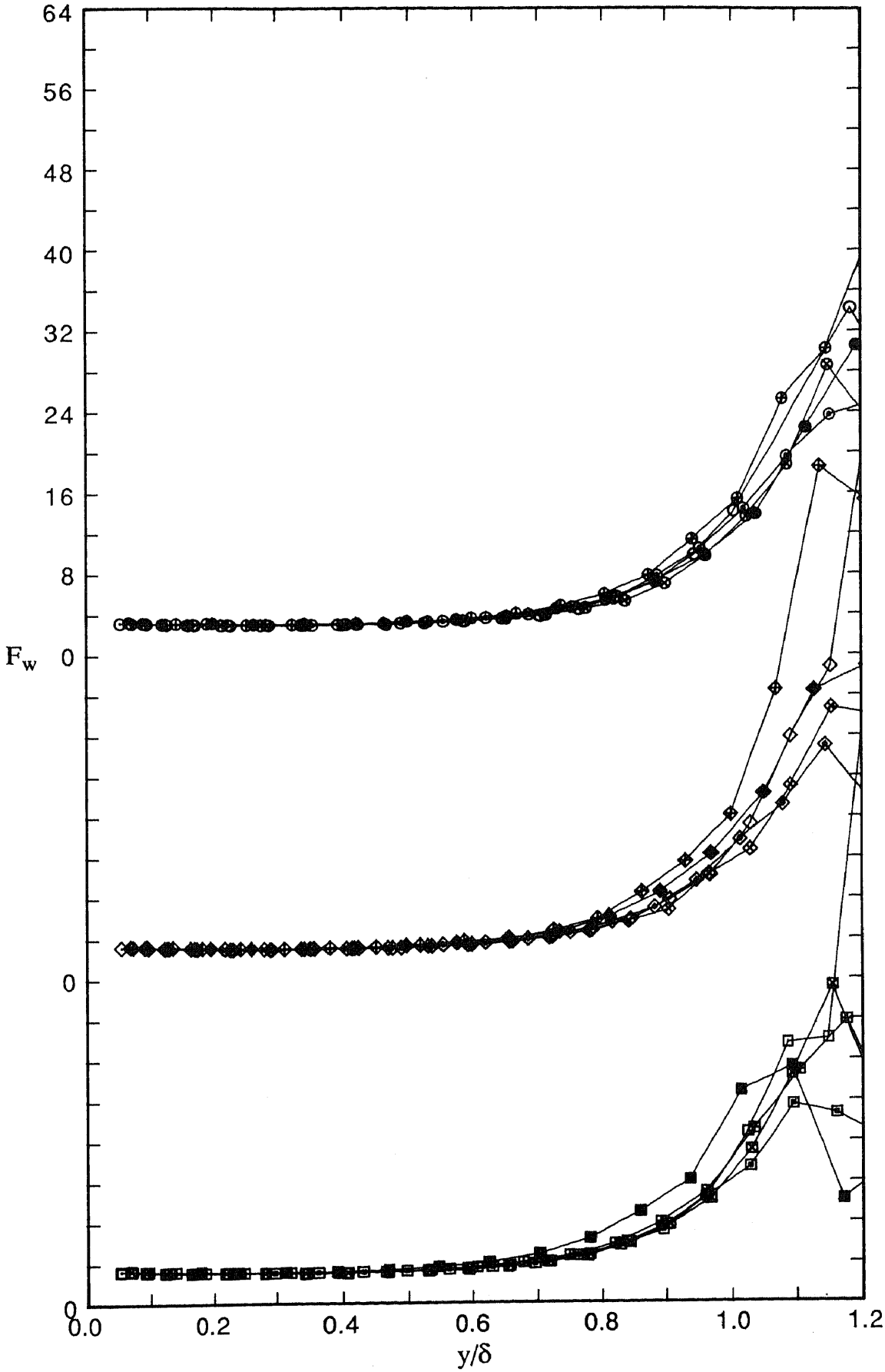

FIGURE 6.48. Profiles of flatness factor, $\overline{w^4}/(\overline{w^2})^2$ versus y/δ, for design flows showing effects of R_θ for three devices. Note shift in ordinate.

Wire: ●, R_θ=697; ⊕, 1003; ⊙, 1568; ⊗, 2226; ⊙, 2788.
Grit: ◆, R_θ=706; ⊕, 1042; ◇, 1520; ◈, 2178; ◇, 2730.
2.0 mm pins: ■, R_θ=729; ⊞, 1027; ⊡, 1565; ⊠, 2181; ⊡, 2889.

Balances of turbulent kinetic energy and Reynolds shear stress were constructed for the three tripping devices for the design flows and for different values of R_θ. The balances are represented mathematically by equations (2.26) and (2.27) respectively given in Section 2.4 and the meanings of the various terms in the balances have been explained in that section. It was indicated that for this investigation, dissipation in the energy balances and redistribution in the shear-stress balances, were determined by difference. For both the energy and shear stress balances, the various terms are normalized by both U_e^3/δ and U_τ^3/δ. The data for the balances of turbulent kinetic energy are plotted in the conventional manner with gains of kinetic energy shown as negative. Likewise, gains in shear stress are shown as positive.

Before the complete range of the current data for the balances of kinetic energy and shear stress are presented, some of the data will be compared with published results to see if they agree. Considering the energy balance, figure 6.49a shows current data for the 1.2 mm wire for the design flow for R_θ = 1568 compared with data given by Murlis (1975), for which R_θ = 1640. The corresponding data for the shear-stress balance are given in figure 6.49b. It can be seen that the balances from both investigations have the same general form and although appreciable differences occur in the advection and diffusion terms as well as the turbulent transport and generation terms, the overall agreement is reasonable given the uncertainty of calculating terms in balances. One advantage of the current data is that the $\overline{w^2}$ Reynolds normal stresses used in the advection term of the energy balance were actually measured, rather than approximated from the $\overline{u^2}$ and $\overline{v^2}$ normal stresses, as was done by Murlis (see Section 2.4). Also, the current data extend to smaller values of y/δ than the data of Murlis.

In this section reference will be made to other published data and these have been reproduced for convenience. Data for an energy balance for R_θ = 1112 as given by Murlis, Tsai & Bradshaw (1982) are shown in figure 6.50. Also, when analysing the current balances to assess the effects of low R_θ, it is desirable to make at least some reference to published data having higher values of R_θ. For this purpose, the data of Klebanoff (1955), as given by Bradshaw (1967), for which $R_\theta \approx 7750$, were used, and these are shown in figure 6.51.

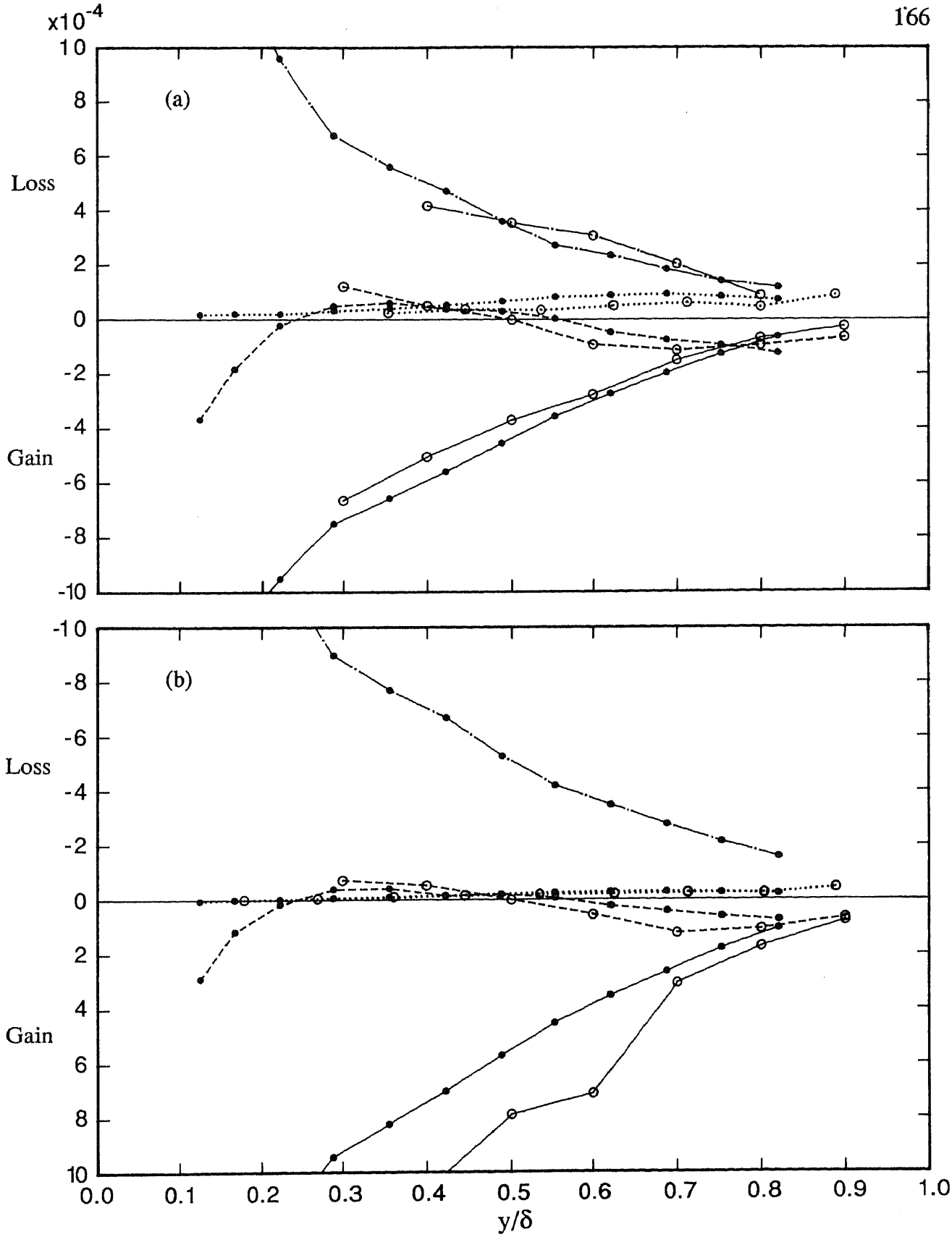

FIGURE 6.49. Balances of turbulent kinetic energy and Reynolds shear stress, normalised by U_e^3/δ, versus y/δ for current investigation and for Murlis (1975).
●, Data for wire for design flow for R_θ=1568; ⊙, Data of Murlis for R_θ=1640.
(a) Energy balance.
·····, advection; ——, production; — — —, diffusion; — · —, dissipation.
(b) Shear stress balance.
·····, mean flow transport; ——, generation; — — —, turbulent transport; — · —, redistribution

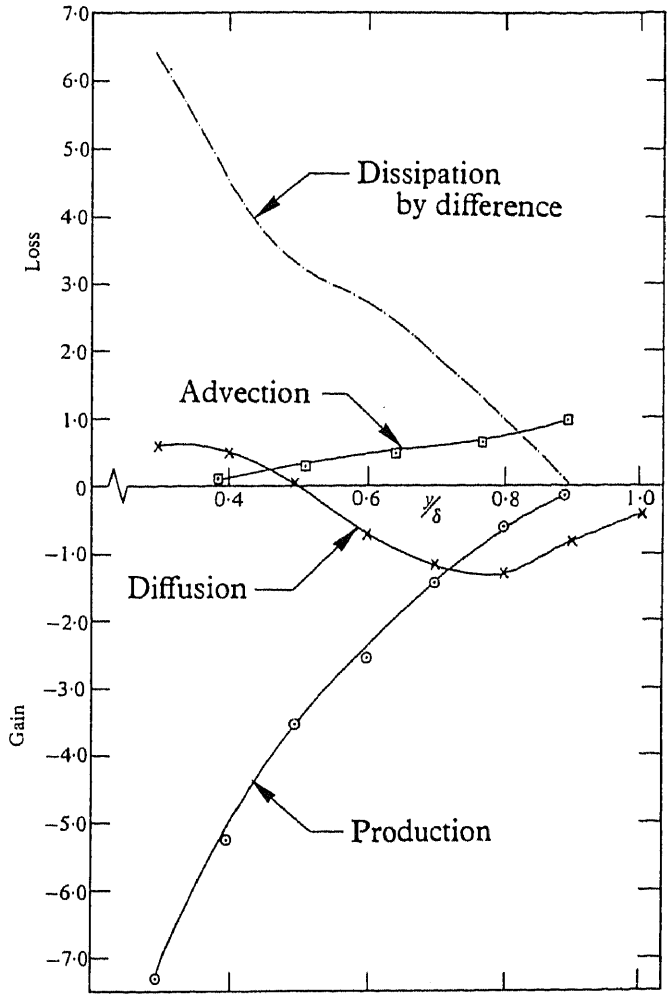

FIGURE 6.50. Balance of turbulent kinetic energy, normalised by U_e^3/δ, versus y/δ as given by Murlis, Tsai & Bradshaw (1982) for $R_\theta = 1112$.

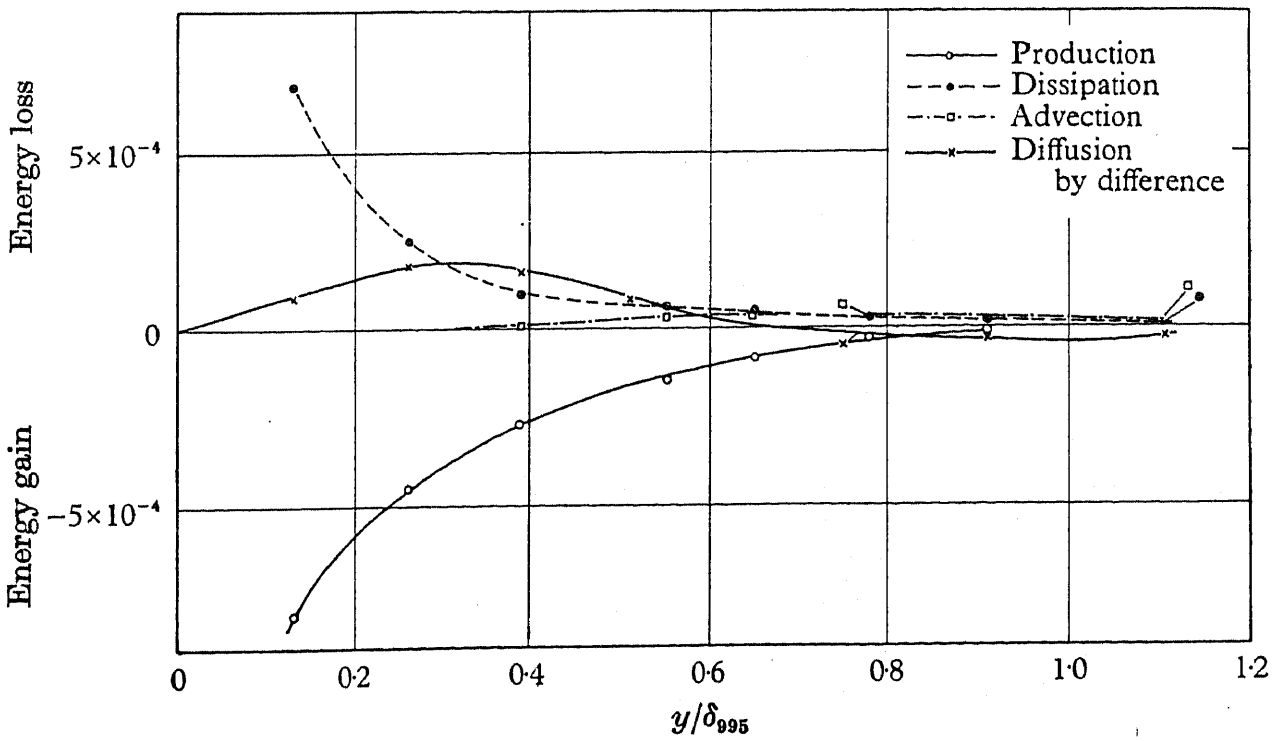

FIGURE 6.51. Balance of turbulent kinetic energy, normalised by U_e^3/δ, versus y/δ from the measurements of Klebanoff (1955), as given by Bradshaw (1967).

Although turbulence profiles were taken for five nominal values of R_θ, as shown in table 5.1, balances are not presented for the two extreme values of R_θ since it was not possible to determine accurately longitudinal gradients of quantities at the extremes. From table 5.1 it can be seen that the limiting nominal values of R_θ at which balances could be constructed are 1020 and 2175, giving an R_θ range of 1155. Murlis (1975) presented energy and shear stress balances for values of R_θ varying between 791 and 4750, but since these two values of R_θ were the extremes at which he took broadband-turbulence measurements, the balances at these two extreme values of R_θ must be viewed with caution. Murlis, Tsai & Bradshaw (1982), who present some of the data of Murlis (1975), indicate that results from the last station that require a differentiation at the end of the range are not very reliable. Thus, the reliable balances presented by Murlis (1975) in fact correspond to values of R_θ varying between 1112 and 2387, giving an R_θ range of 1275, and these numbers are about the same as for the current results. Although the above R_θ range used for the current data may seem somewhat limited, Murlis indicates that for his balances, the largest part of the changes takes place in the Reynolds number range $800 < R_\theta < 2500$.

A problem faced when presenting the energy and shear stress balances for the current data was that some of the terms were often far larger than other terms and it was not possible to choose a plot size that enabled the extremes of the larger terms to be included on the plot and at the same time allowed the smaller terms to be of a sufficient size that they could be interpreted. This problem was overcome in selected cases by firstly presenting all relevant data on a given plot and then presenting some of this data again on a magnified scale on another plot.

Initially the balances of turbulent kinetic energy will be discussed. Figures 6.52a and 6.52b show the various terms of the energy balance plotted against y/δ for the wire for different values of R_θ. In this case, the different terms have been normalized by U_e^3/δ. Data given correspond to actual experimental points and these have been joined by straight lines. As can be seen from figure 6.52b, it is necessary to omit some of the data when the magnified scale is used, but this does not matter since the behaviour of the omitted data is clear from figure 6.52a. Since the behaviour of corresponding data for the grit and the pins

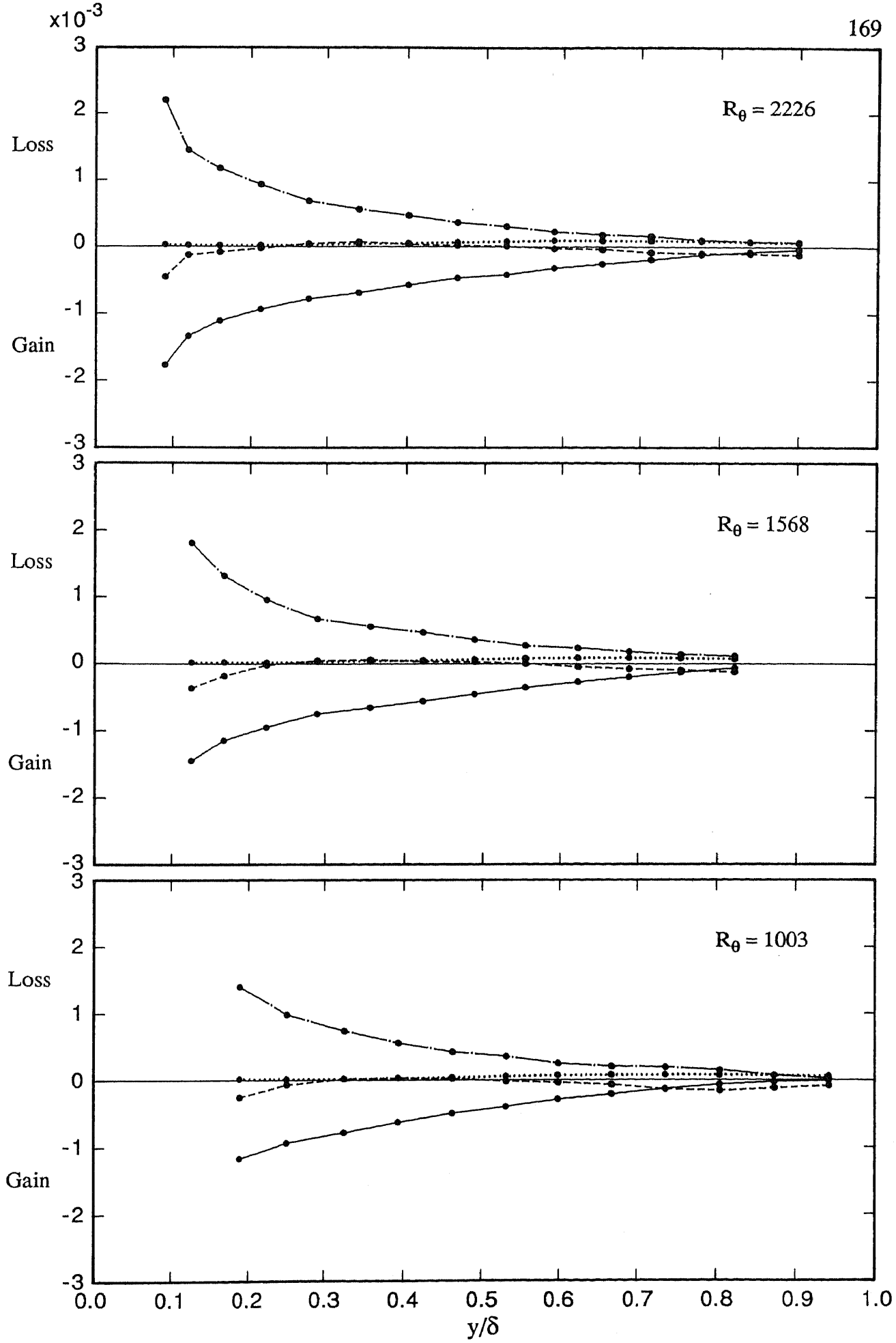

FIGURE 6.52a. Balances of turbulent kinetic energy, normalised by U_e^3/δ, versus y/δ for design flow for wire.

·····, advection; ——, production; – – –, diffusion; — · —, dissipation.

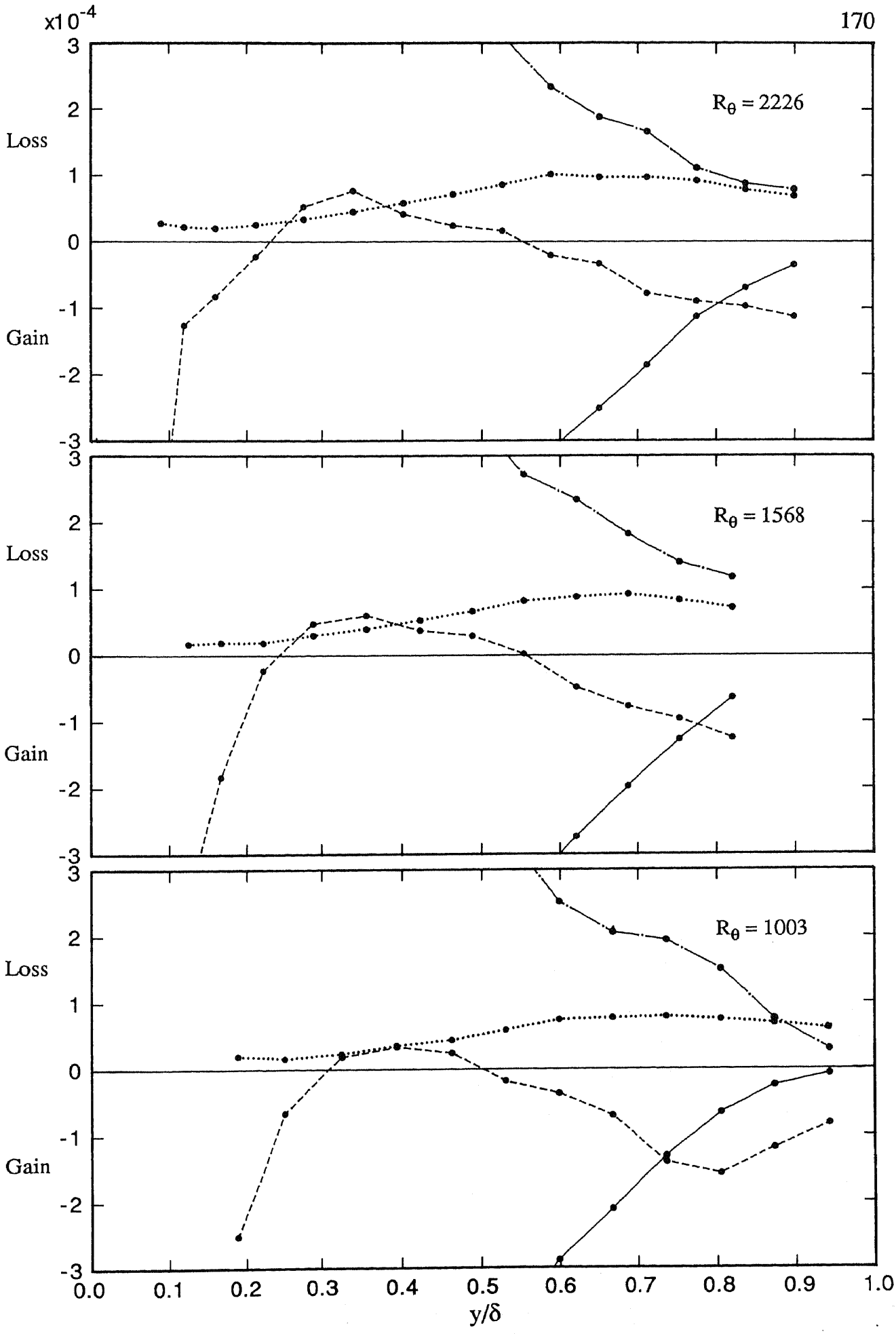

FIGURE 6.52b. Balances of turbulent kinetic energy, normalised by U_e^3/δ, versus y/δ for design flow for wire.

·····, advection; ——, production; – – –, diffusion; — · —, dissipation.

agreed reasonably closely with that for the wire, the balances for the grit and pins have not been presented using a magnified ordinate. Data for the grit, corresponding to the above data for the wire, are shown in figure 6.53 and likewise data for the pins are shown in figure 6.54. Since the behaviour of data for the different devices agreed quite closely, then the above four figures will often be discussed collectively rather than concentrating on figures for individual devices.

In the above balances, as well as others to be presented, it will be seen that the limiting values of y/δ for which data are given are somewhat lower than for other plots presented in this thesis and the reason for this is that it was not possible to determine gradients with respect to x at higher values of y at which measurements were taken since these values of y were beyond the y limits of an upstream profile necessary for determining gradients with respect to x. This problem is particularly noticeable for low-Reynolds-number flows where the boundary layer thickens relatively quickly. When constructing balances, gradients with respect to x and y of various terms were approximated by the gradient of a straight line fitted to three points, viz. the point under consideration as well as those either side of this point.

From figures 6.52 to 6.54 it can be seen that for each of the devices the energy balances maintain the same general form over the given R_θ range. In each case it is particularly noticeable how production and dissipation are the dominant terms over most of the layer, and it is not until y/δ reaches a value in excess of 0.7 that diffusion becomes greater than production. The advection terms for the different cases are very small near the wall and although they become larger for higher values of y/δ, they still remain relatively small throughout the R_θ range. In all cases the advection terms remain positive, indicating a net loss of energy throughout the boundary layers. The diffusion terms, on the other hand, change sign twice over the given y/δ range. The outermost crossover region occurs for values of y/δ within the vicinity 0.5 to 0.6. The behaviour of the diffusion for low values of y/δ will be discussed later in this section.

The way in which the different terms in the energy balances for the wire that are shown in figures 6.52a and 6.52b are affected by changes in R_θ will

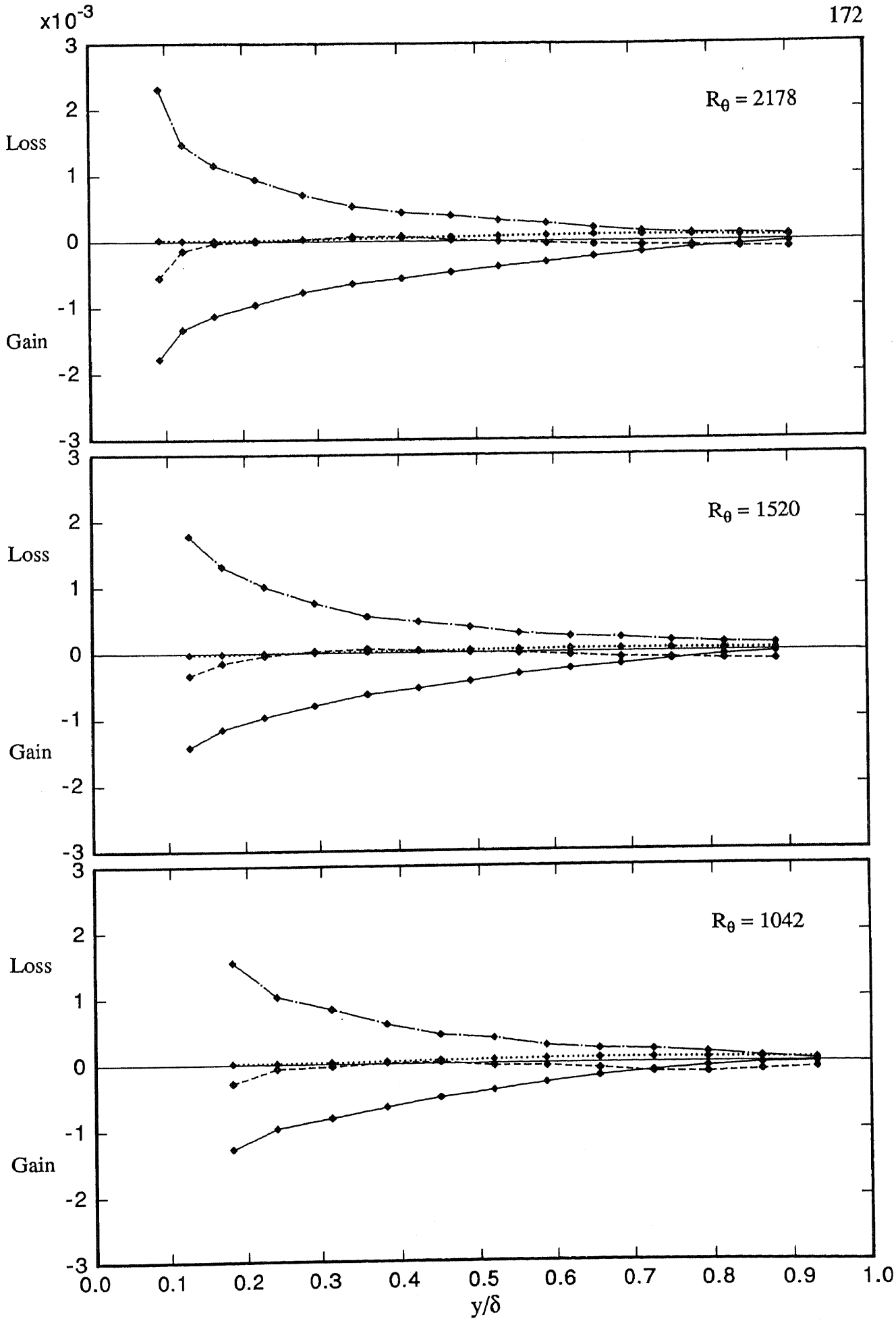

FIGURE 6.53. Balances of turbulent kinetic energy, normalised by U_e^3/δ, versus y/δ for design flow for grit.

....., advection; ——, production; — — —, diffusion; — · —, dissipation.

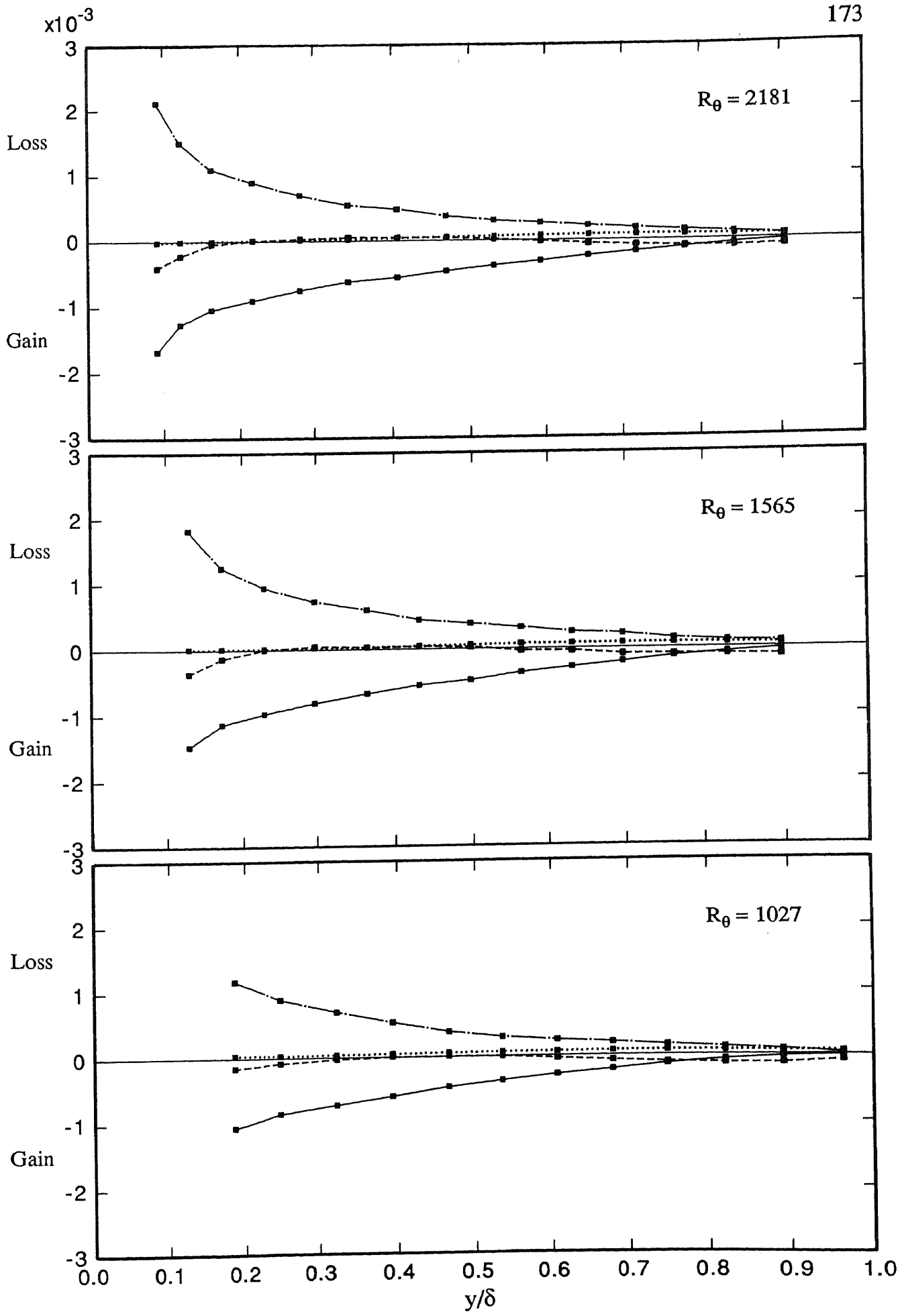

FIGURE 6.54. Balances of turbulent kinetic energy, normalised by U_e^3/δ, versus y/δ for design flow for 2.0 mm pins.

....., advection; ——, production; — — —, diffusion; — · —, dissipation.

now be considered. At $y/\delta \approx 0.7$, the advection term can be seen to increase very slightly with R_θ, but a careful study of Klebanoff's data, shown in figure 6.51, showed that this trend did not continue to $R_\theta \approx 7750$. For the current data, the values of production and dissipation at say $y/\delta = 0.2$, decrease with increasing R_θ and this trend continues to $R_\theta \approx 7750$ for Klebanoff's data. Away from the wall the diffusion can be seen to be relatively strong at low R_θ. For $y/\delta = 0.8$, the diffusion terms for the current data decrease with increasing R_θ and once again this trend continues to $R_\theta \approx 7750$. The location at which diffusion equals production corresponds to increasing values of y/δ as R_θ increases. For the wire, the crossover occurs at $y/\delta \approx 0.73$ for $R_\theta = 1003$ and at $y/\delta \approx 0.8$ for $R_\theta = 2226$, whereas for $R_\theta \approx 7750$ the crossover occurs at $y/\delta \approx 0.81$.

Of particular concern in the energy balances is the behaviour of the diffusion term. It is known (see Bradshaw 1967) that the diffusion must integrate to zero across the boundary layer and for the current data this is clearly not the case, although it must be said that the balances do not extend in any further than $y/\delta \approx 0.1$. Some discussion of the behaviour of the diffusion terms is required. It will be recalled from equation (2.26) in Section 2.4 that the expression for calculating diffusion is $\partial((\overline{pv}/\rho)+0.5\overline{q^2v})/\partial y$. In Section 2.4 it was indicated that when calculating diffusion in the current investigation, the method of Bradshaw (1967) and Murlis, Tsai & Bradshaw (1982) was used. In this method, $\overline{pv}/\rho$ was neglected and it was assumed that $0.5\overline{q^2v} \approx 0.75(\overline{u^2v}+\overline{v^3})$. It was necessary to use simplifications such as these to make the problem tractable. It is possible, however, that the above simplifications may not be completely appropriate to low-Reynolds-number flows. The results of Murlis, Tsai & Bradshaw (1982) for $R_\theta = 1112$, shown in figure 6.50, tend to support this statement, since in this case the diffusion across the boundary layer also does not integrate to zero. It is possible, however, that there is an alternative explanation for the unusual behaviour of the diffusion. The diffusion terms were calculated by determining the gradients with respect to y of the $\overline{u^2v}$ and $\overline{v^3}$ triple products. When the $\overline{u^2v}$ and $\overline{v^3}$ triple product profiles depicted in figures 6.29 and 6.26 respectively are analysed, it is apparent that if the profiles were continued to the wall, then the triple products would decrease sharply towards zero (they could even become negative before rising to zero at the wall) and this

sharp decrease in the triple products would result in positive gradients with respect to y which would cause the diffusion terms to become positive, possibly with large values. If the omitted diffusion data close to the wall had actually been measured and included on the energy balances, then the integration of the diffusion terms across the boundary layers would have been closer to zero. It is noteworthy that the diffusion determined by difference for Klebanoff's (1955) data, as shown in figure (6.51), also does not integrate to zero across the boundary layer, and in fact the trend of the diffusion for low values of y/δ is opposite that of the current data.

Figures 6.55a and 6.55b show energy balances for the wire, with the various terms now normalized by U_τ^3/δ. These two figures correspond to figures 6.52a and 6.52b using the previous scaling. No corresponding balances for the grit and pins using this new scaling are given in this thesis. With this new scaling, the terms in the balances are successively increased with increasing R_θ, compared with the previous scaling, as U_τ decreases with increasing R_θ. From figures 6.55a and 6.55b it can be seen that at $y/\delta \approx 0.7$, the increase of advection with R_θ is now more pronounced than previously. The value of production at $y/\delta = 0.2$ now increases with increasing R_θ, whereas the dissipation at this value of y/δ is now virtually constant for changes in R_θ. At $y/\delta = 0.8$, the diffusion terms still decrease with increasing R_θ. The new type of scaling obviously has no effect upon the crossover regions in the energy balances.

The behaviour of the different terms in the energy balances for both types of scaling shows reasonable agreement with the behaviour found by Murlis (1975) and Murlis, Tsai & Bradshaw (1982) and thus the current data tends to confirm the balances obtained by these researchers. The behaviour of the diffusion data for the current investigation for low values of y/δ was of some concern, but since Murlis and Murlis, Tsai & Bradshaw did not present diffusion data for y/δ less than 0.3, except in one case, where y/δ was 0.2, it was not possible to ascertain whether or not these researchers obtained similar behaviour.

Considering now balances of Reynolds shear stress, the data were plotted in the same way as those for the energy balances considered above. The shear

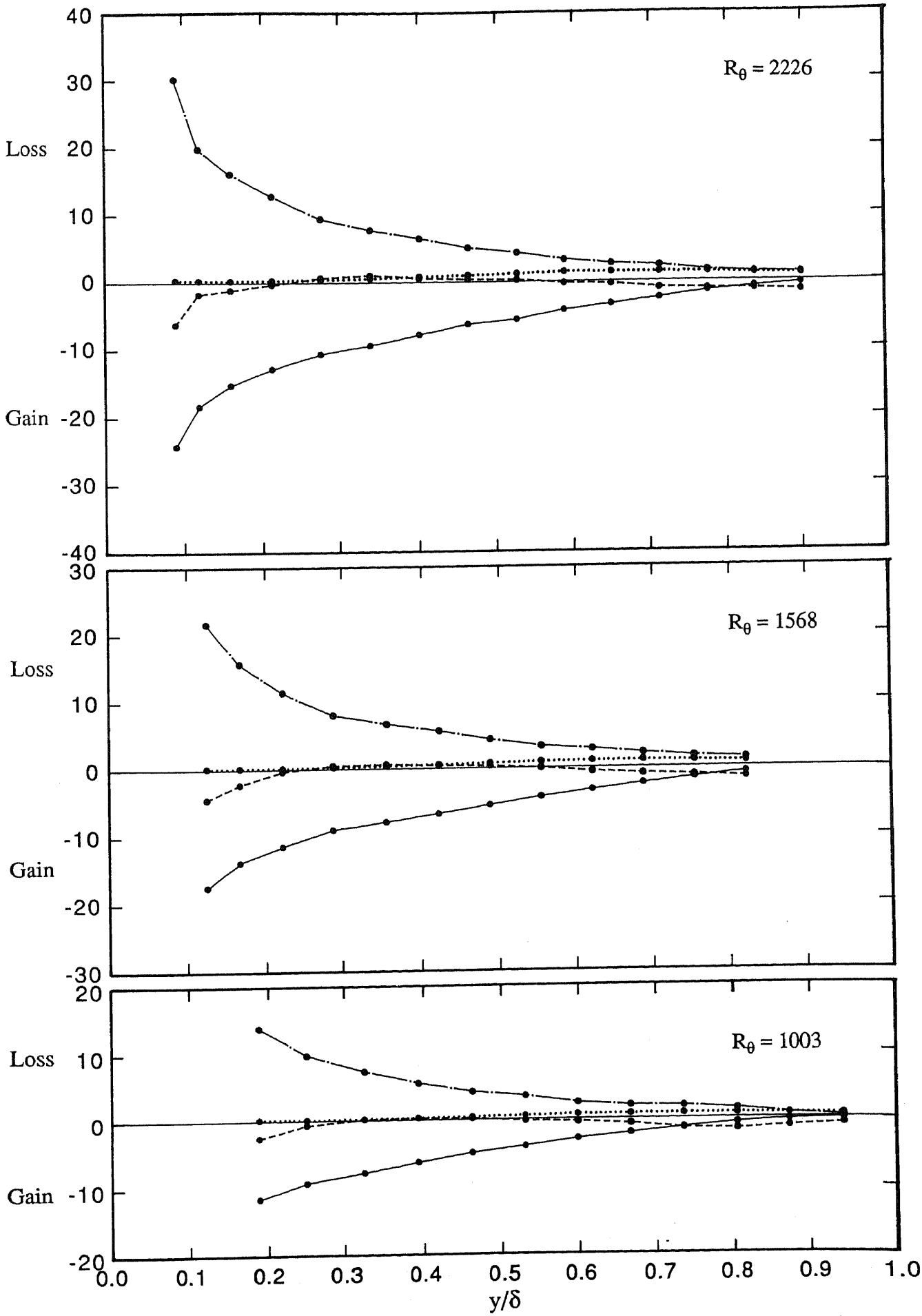

FIGURE 6.55a. Balances of turbulent kinetic energy, normalised by U_τ^3/δ, versus y/δ for design flow for wire.

·····, advection; ——, production; — — —, diffusion; — · —, dissipation.

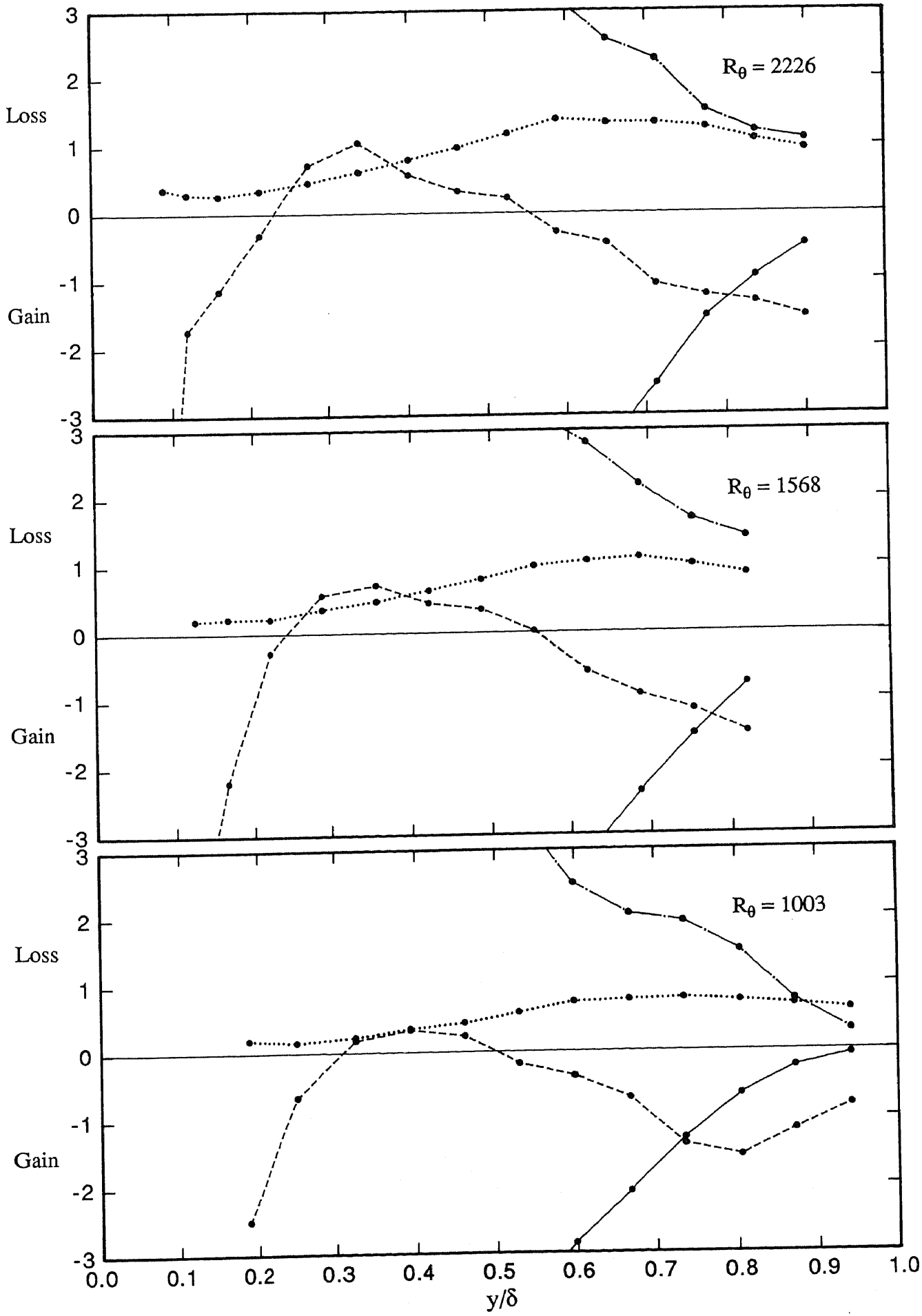

FIGURE 6.55b. Balances of turbulent kinetic energy, normalised by U_τ^3/δ, versus y/δ for design flow for wire.

·····, advection; ——, production; – – –, diffusion; — · —, dissipation.

stress balances are shown in figures 6.56 to 6.59 and these figures correspond to figures 6.52 to 6.55 respectively for the energy balances.

It is apparent from a comparison between the two sets of figures for the energy and shear-stress balances that the general behaviour of corresponding terms is the same in both cases. Consequently it is not necessary to discuss in detail the behaviour of the shear-stress balances, but several aspects of these balances are worth mentioning. The most obvious feature apparent from a comparison between the two types of balances is that the generation and redistribution terms of the shear stress balance are more pronounced than the corresponding production and dissipation terms respectively of the energy balances. As well as this, the mean-flow and turbulent-transport terms of the shear stress balances are noticeably smaller than the corresponding advection and diffusion terms respectively for the energy balances. For the shear-stress balances, the mean-flow transport term sometimes changes sign for small values of y/δ, unlike for the energy balances. In a similar manner to previously, the behaviour of the different terms in the shear-stress balances is similar in most respects to that of Murlis (1975) and Murlis, Tsai & Bradshaw (1982).

6.3.7 Eddy Viscosities and Mixing Lengths

Prediction methods using the concepts of eddy viscosity and mixing length have been widely used in the past. Both these parameters relate the Reynolds shear stress to the mean velocity gradient and are defined by

$$\varepsilon_m = \frac{-\overline{uv}}{\frac{\partial U}{\partial y}} \tag{6.3}$$

and

$$l = \frac{\left(-\overline{uv}\right)^{0.5}}{\frac{\partial U}{\partial y}} \tag{6.4}$$

respectively. The main disadvantage of the concepts of eddy viscosity and mixing length is that they lack generality since they are based on local equilibrium ideas and assume that the transport terms in the governing

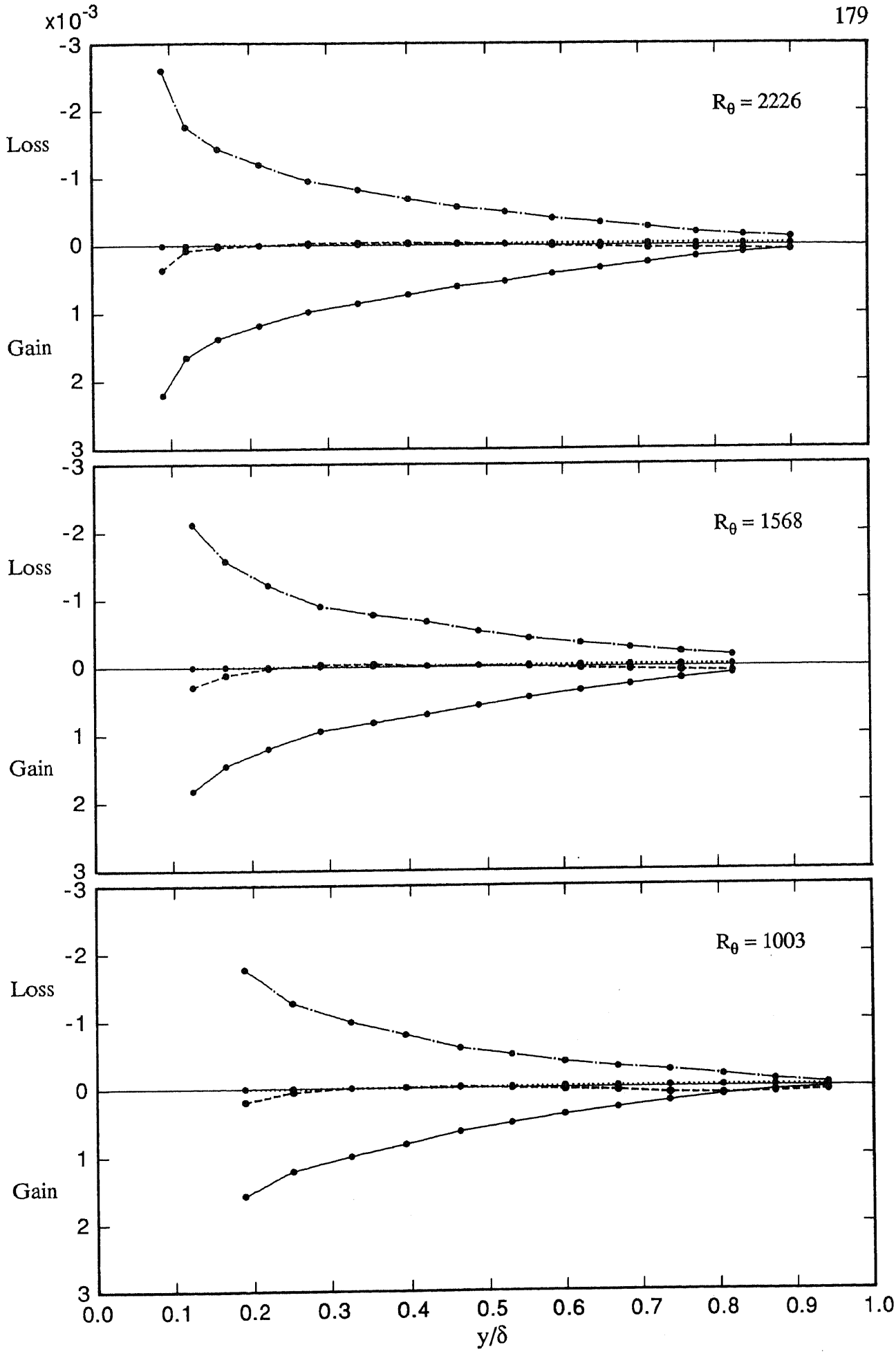

FIGURE 6.56a. Balances of Reynolds shear stress, normalised by U_e^3/δ, versus y/δ for design flow for wire.

·····, mean flow transport; ——, generation; — — —, turbulent transport; — · —, redistribution

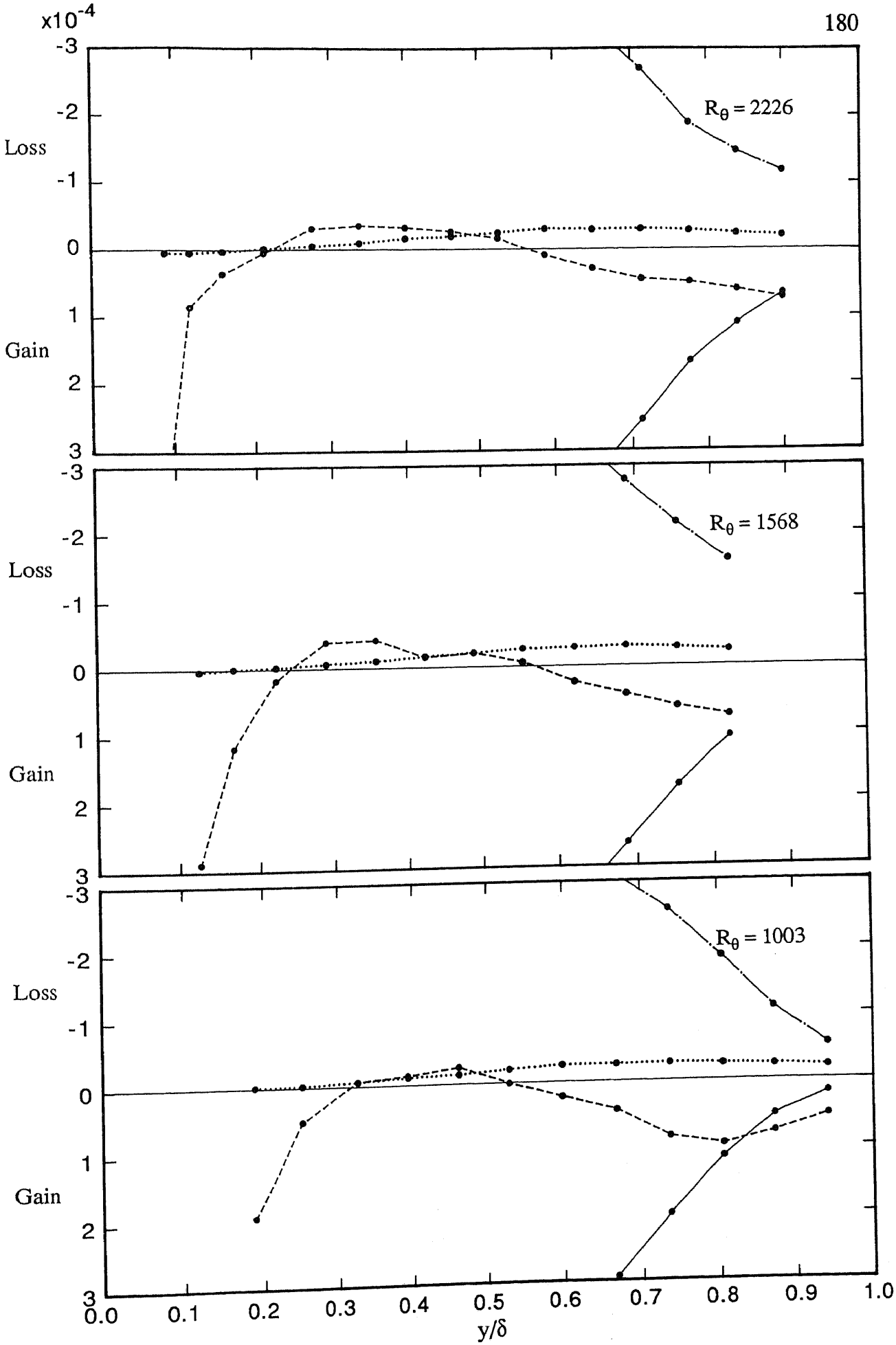

FIGURE 6.56b. Balances of Reynolds shear stress, normalised by U_e^3/δ, versus y/δ for design flow for wire.

....., mean flow transport; ——, generation; — — —, turbulent transport; — · —, redistribution

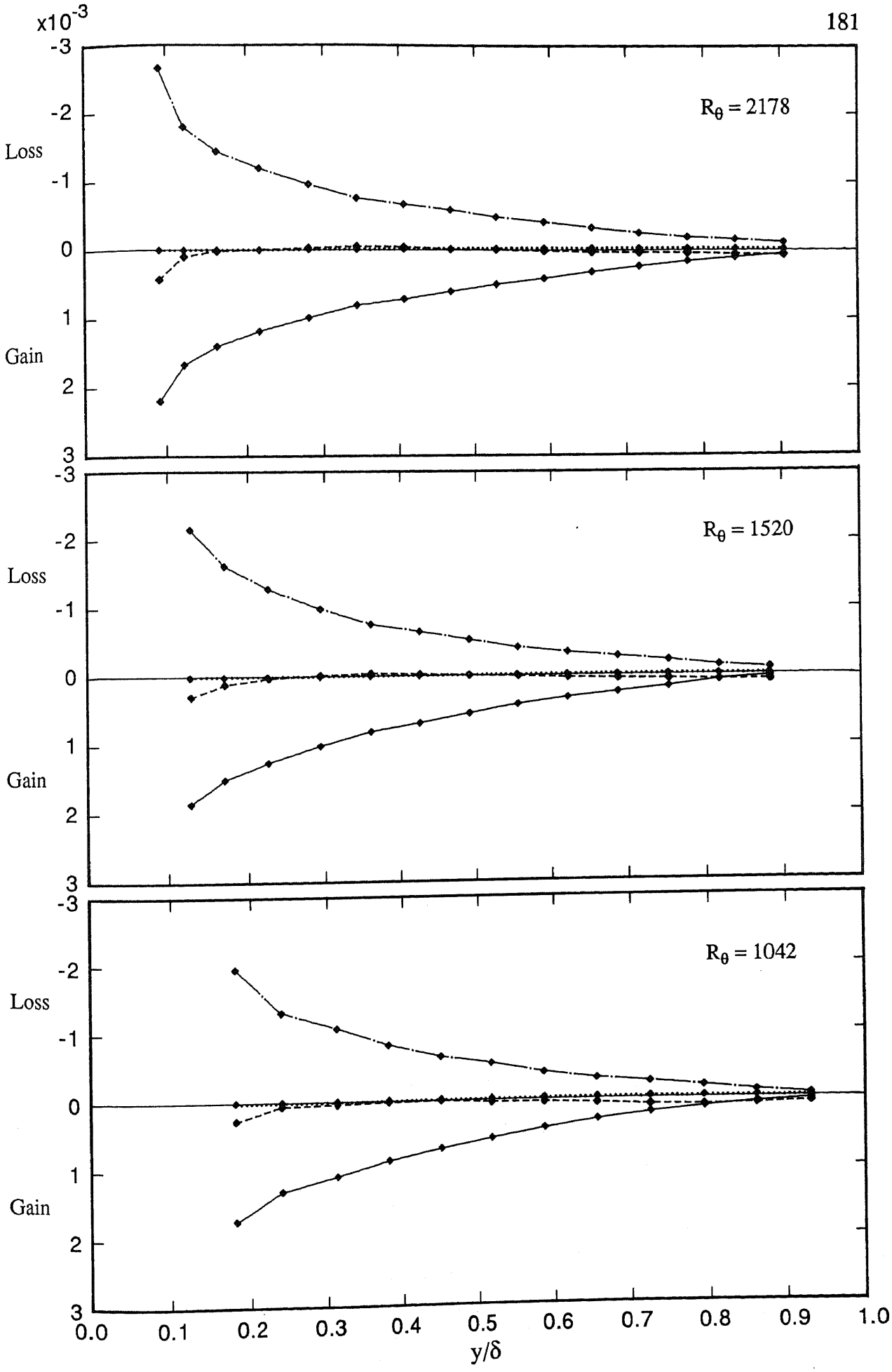

FIGURE 6.57. Balances of Reynolds shear stress, normalised by U_e^3/δ, versus y/δ for design flow for grit.

·····, mean flow transport; ——, generation; – – –, turbulent transport; — · —, redistribution

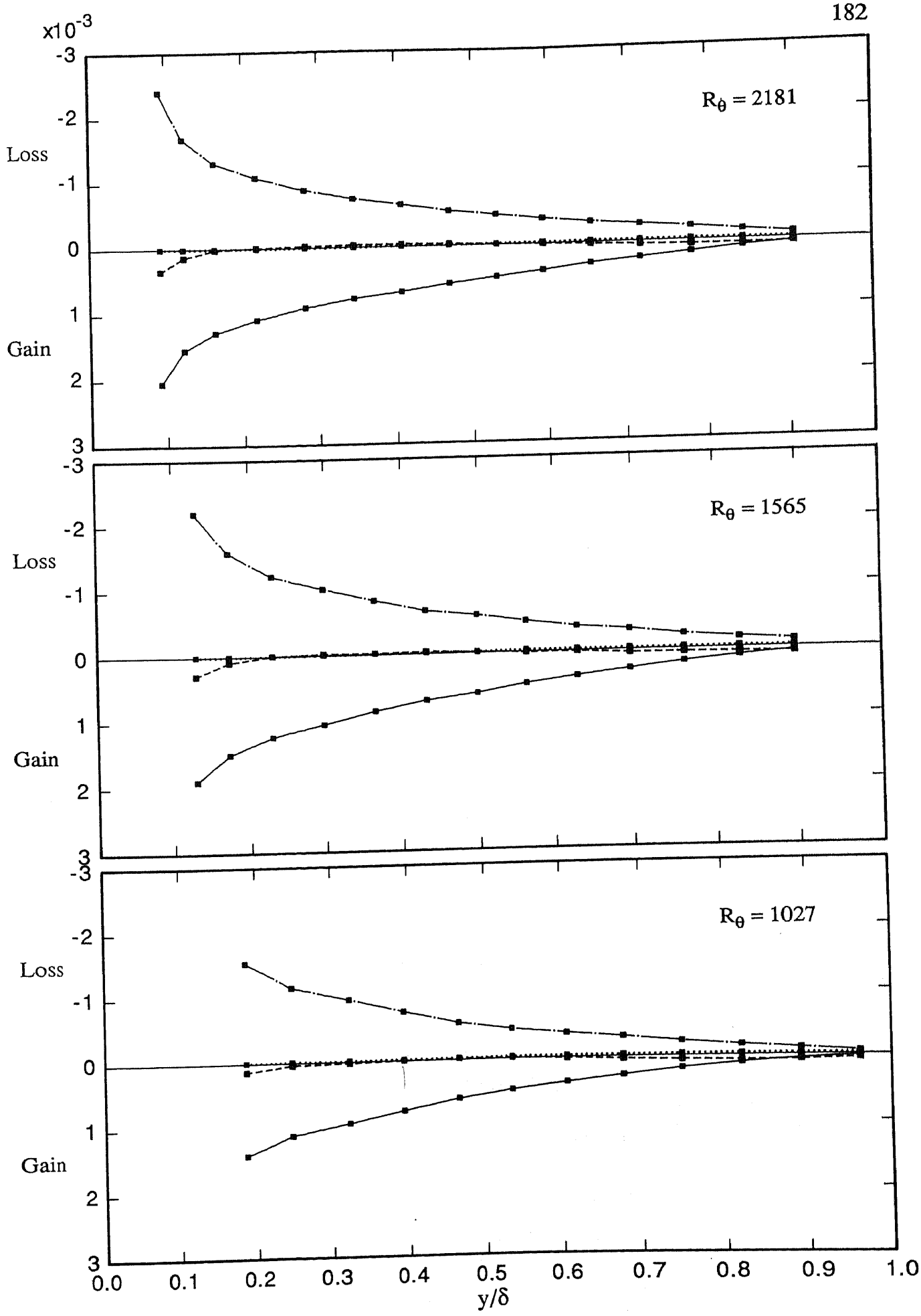

FIGURE 6.58. Balances of Reynolds shear stress, normalised by U_e^3/δ, versus y/δ for design flow for 2.0 mm pins.

....., mean flow transport; ——, generation; – – –, turbulent transport; — · —, redistribution

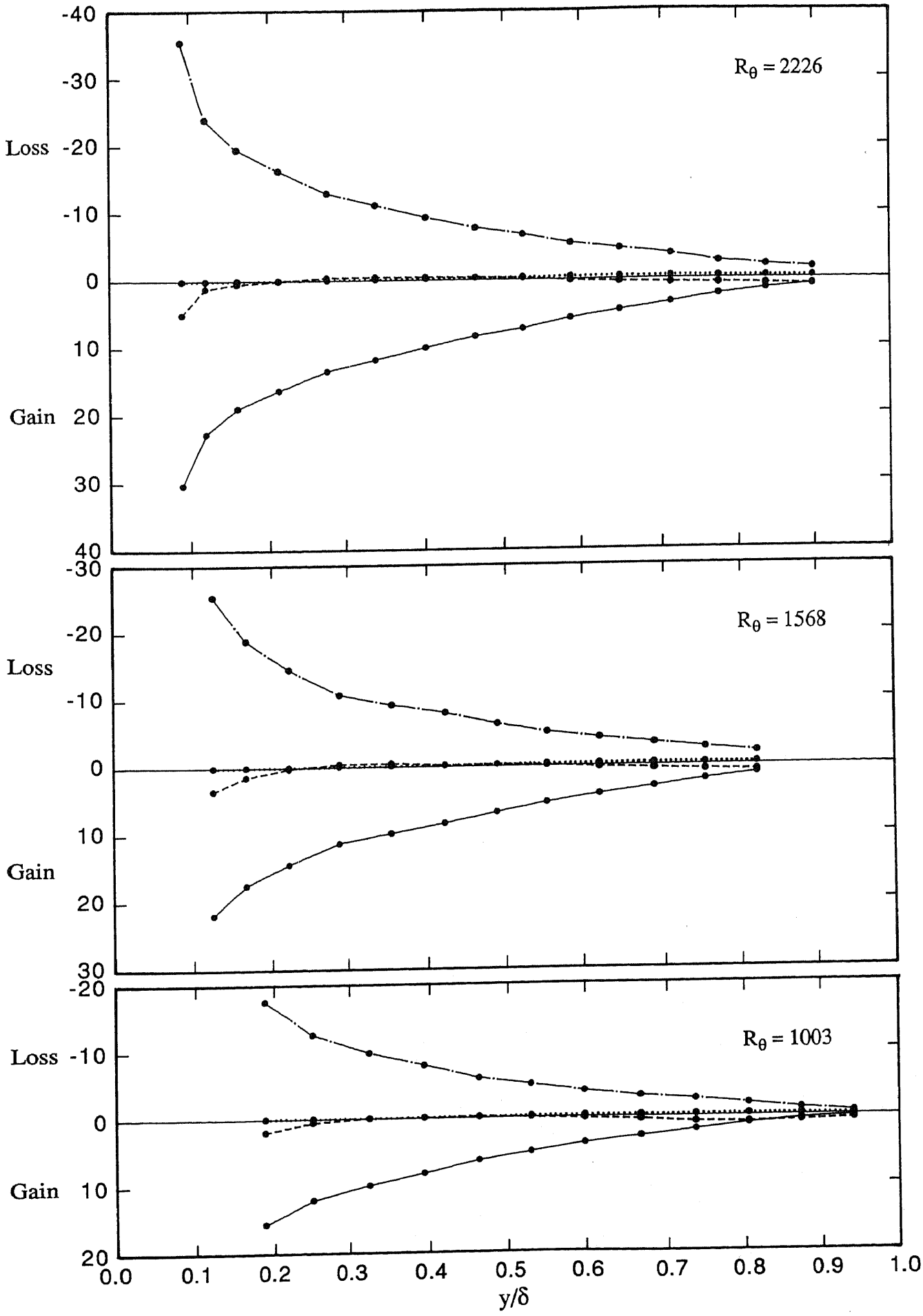

FIGURE 6.59a. Balances of Reynolds shear stress, normalised by U_τ^3/δ, versus y/δ for design flow for wire.

·····, mean flow transport; ——, generation; — — —, turbulent transport; — · —, redistribution

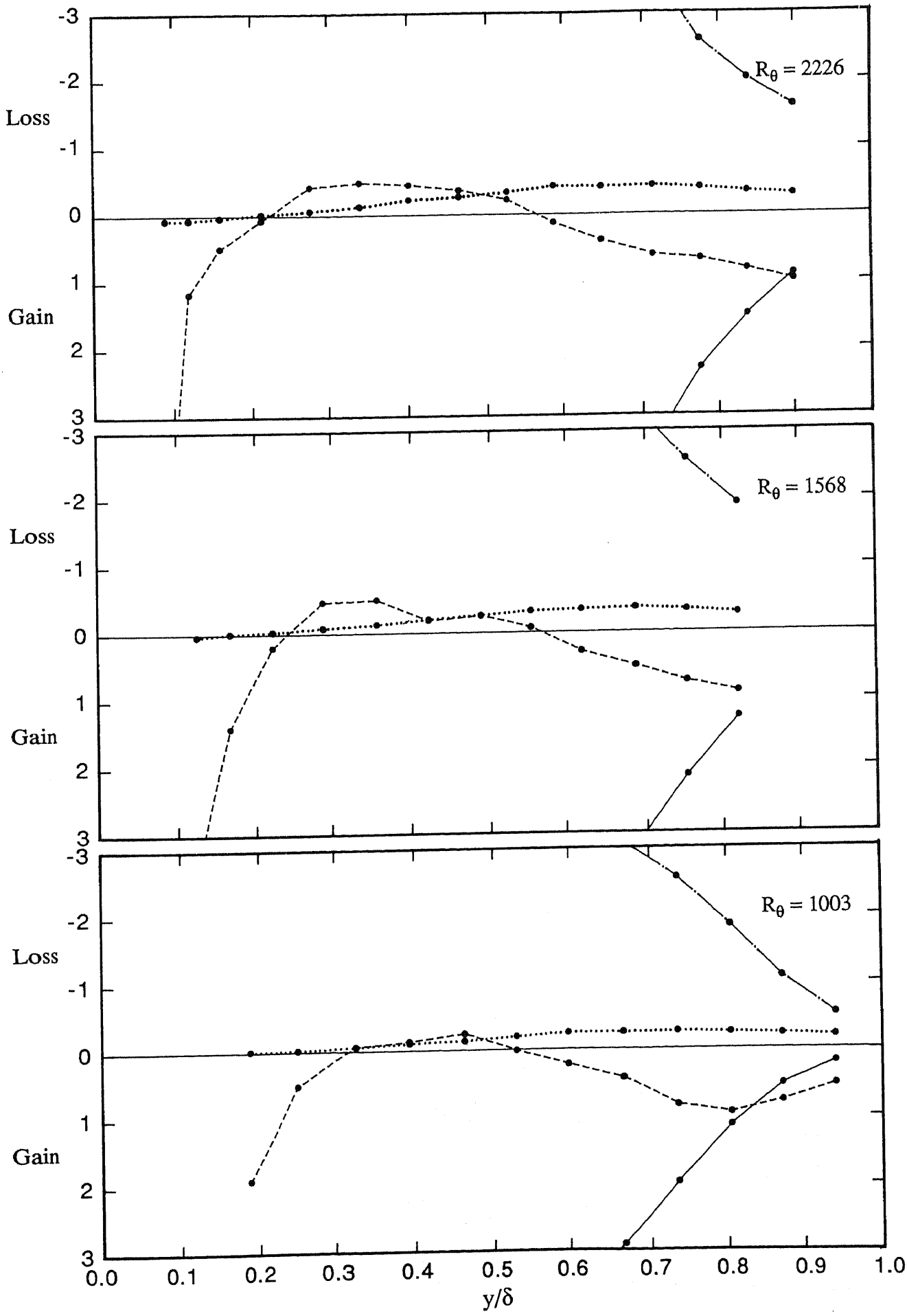

FIGURE 6.59b. Balances of Reynolds shear stress, normalised by U_τ^3/δ, versus y/δ for design flow for wire.

·····, mean flow transport; ——, generation; – – –, turbulent transport; —·—, redistribution

equations are small. Prediction methods based on these concepts have nevertheless proved useful in a restricted number of flow cases.

Eddy viscosities for the three tripping devices for different values of R_θ are shown plotted in figure 6.60 using coordinates of $\varepsilon_m/(U_e\delta^*)$ versus y/δ. It is apparent from figure 6.60, that for each of the devices, the $\varepsilon_m/(U_e\delta^*)$ profiles vary considerably with R_θ over most of the y/δ range. For y/δ greater than about 0.2, there is a general tendency for the values of $\varepsilon_m/(U_e\delta^*)$ to decrease with increasing R_θ, but there are some departures from this trend. For increasing values of y/δ, all profiles rise to a peak at about $y/\delta = 0.3$ or 0.4, before falling again. The values of $\varepsilon_m/(U_e\delta^*)$ corresponding to the peaks are about 0.023 for $R_\theta \approx 713$ and about 0.017 for $R_\theta \approx 2810$. The data of Klebanoff (1954), for which $R_\theta \approx 7750$, peaks at $y/\delta \approx 0.3$, and the value of $\varepsilon_m/(U_e\delta^*)$ at the peak is about 0.02. Beyond $y/\delta \approx 0.2$, the values of $\varepsilon_m/(U_e\delta^*)$ for each of the devices generally decrease with increasing R_θ since for any given value of y/δ, the Reynolds shear stress, $-\overline{uv}$, decreases proportionately more than the velocity gradient, $\partial U/\partial y$, as R_θ increases throughout the low-Reynolds-number range.

Considering now mixing lengths, values of this parameter for the three tripping devices for different values of R_θ are shown plotted in figure 6.61 using coordinates of ι/δ versus y/δ. In each case the ι/δ profiles show a significant variation with R_θ for y/δ greater than about 0.2, and although there is some scatter in the profiles beyond $y/\delta \approx 0.2$, there is a general trend for the values of ι/δ to decrease with increasing R_θ. As y/δ increases, the values of ι/δ rise at first and then tend to level off before rising again near the edge of the boundary layer. In this region the rises are quite sharp due to the smallness of the velocity gradient, $\partial U/\partial y$, in relation to $-\overline{uv}$. In the region where ι/δ changes relatively slowly with changes in y/δ, the values of ι/δ for $R_\theta \approx 713$ are about 0.10 for the wire and the grit and somewhat lower for the pins, and for $R_\theta \approx 2810$ the values of ι/δ are about 0.08 for all devices. For Klebanoff's (1954) data, the corresponding value of ι/δ is between 0.08 and 0.09. The reason that the values of ι/δ tend to decrease with increasing R_θ, for y/δ greater than about 0.2, is the same as that given for the $\varepsilon_m/(U_e\delta^*)$ profiles. On figure 6.61 the line $\iota = \kappa y$ has been drawn and as can be seen, the data merge into this line as for high-Reynolds-number flows. Also, it is a matter of interest that Bushnell, Cary and Holley (1975) found that ι/δ decreased with decreasing Reynolds number in

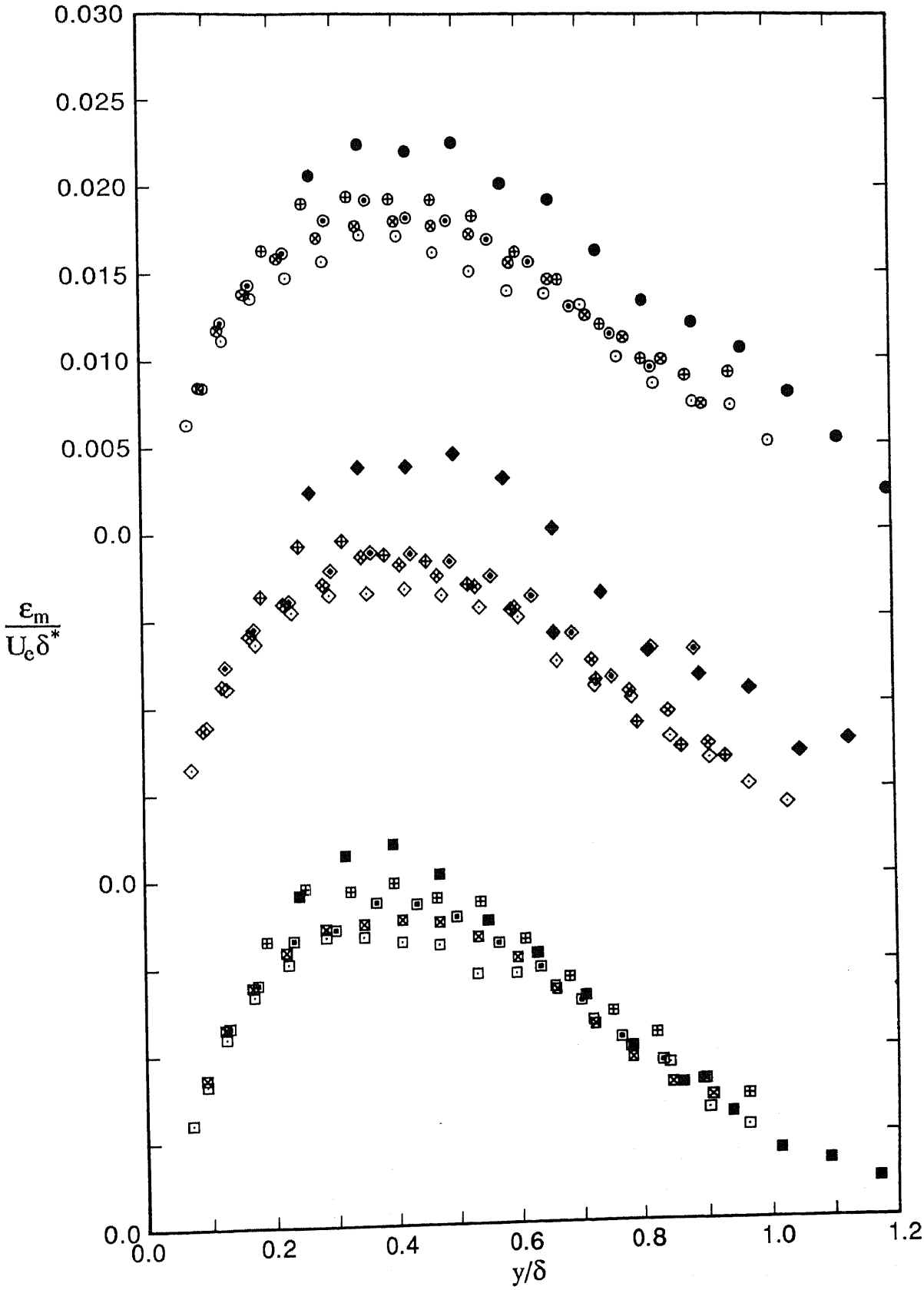

FIGURE 6.60. Profiles of eddy viscosity, $\varepsilon_m/(U_e\delta^*)$ versus y/δ, for design flows showing effects of R_θ for three devices. Note shift in ordinate.

Wire:	●, R_θ=697;	⊕, 1003;	⊙, 1568;	⊗, 2226;	⊙, 2788.
Grit:	◆, R_θ=706;	◈, 1042;	◇, 1520;	◈, 2178;	◇, 2730.
2.0 mm pins:	■, R_θ=729;	⊞, 1027;	▣, 1565;	⊠, 2181;	⊡, 2889.

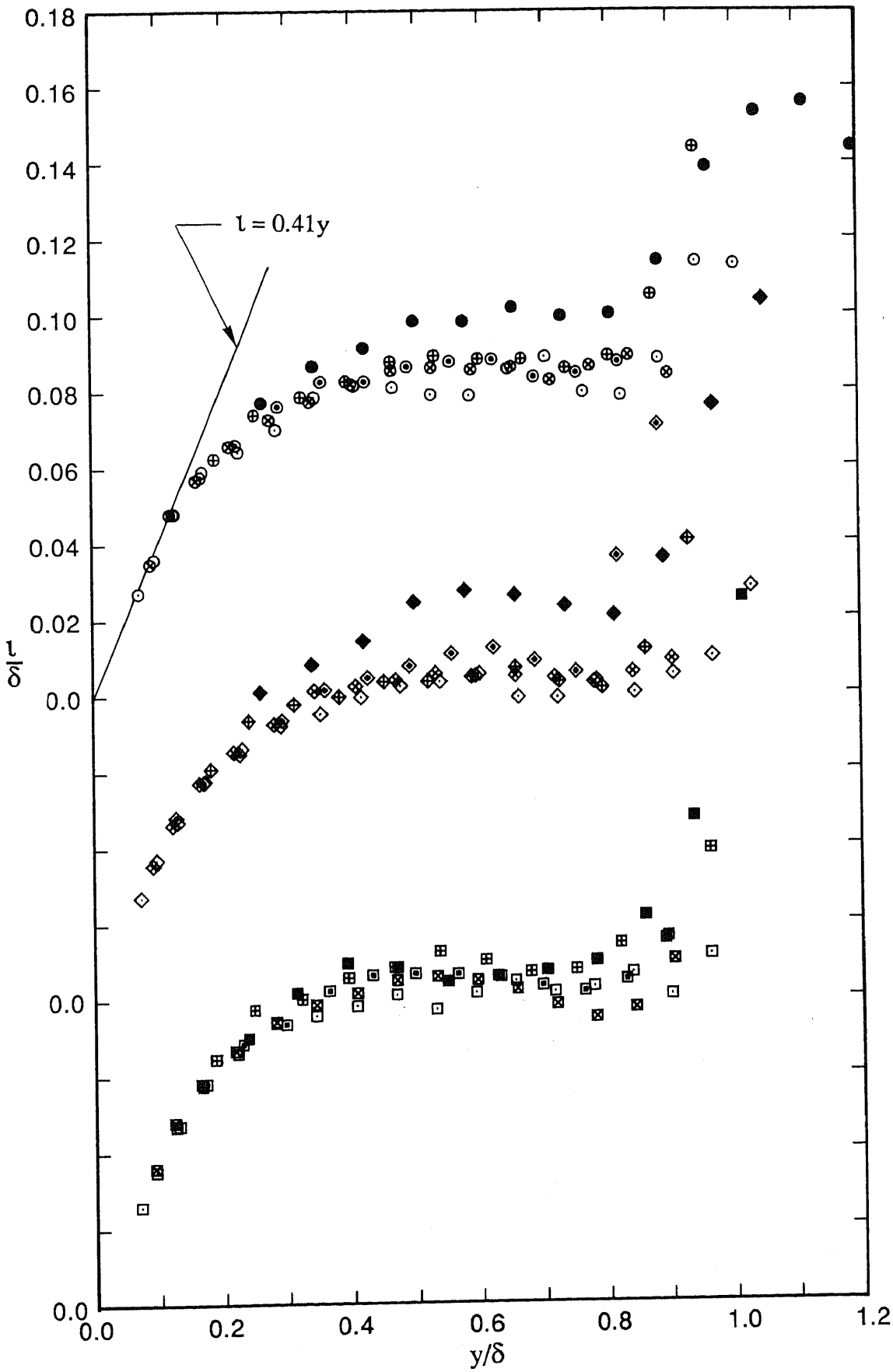

FIGURE 6.61. Profiles of mixing length, l/δ versus y/δ, for design flows showing effects of R_θ for three devices. Note shift in ordinate.

Wire:	●, R_θ=697;	⊕, 1003;	⊙, 1568;	⊗, 2226;	⊙, 2788.
Grit:	◆, R_θ=706;	◈, 1042;	◇, 1520;	◈, 2178;	◇, 2730.
2.0 mm pins:	■, R_θ=729;	⊞, 1027;	▣, 1565;	⊠, 2181;	⊡, 2889.

compressible turbulent boundary layers. However, Inman & Bradshaw (1981) indicate that the effect found by Bushnell, Cary & Holley in their analysis of measurements on supersonic wind tunnel nozzle walls is in fact confined to high Mach numbers.

6.3.8 Dissipation Length Parameters

The dissipation length parameter, L, is defined as

$$L = \frac{(-\overline{uv})^{1.5}}{\varepsilon} \tag{6.5}$$

where ε is the dissipation appearing in the energy balance. L is used by Bradshaw, Ferriss & Atwell (1967) in their boundary-layer prediction method and according to these researchers, L is nearly the same as the "dissipation length parameter" L_ε used by Townsend (1961). Bradshaw, Ferriss & Atwell assumed that L/δ was a function of y/δ, so it is of interest to see how L is affected by changes in R_θ.

Profiles of L/δ versus y/δ for three tripping devices for different values of R_θ are shown in figure 6.62. Only profiles for nominal values of R_θ of 1020, 1544 and 2175 for each device are given, and the reason for this is that the values of ε, used in the calculation of L, could not be determined with acceptable accuracy at the extreme values of R_θ (see Section 6.3.6). The profiles often show considerable scatter but this is not surprising since the calculation of L involved using the dissipation determined as the difference of other terms in an energy balance and high accuracy cannot be expected for such values of dissipation. Thus for the current results the conclusions must be viewed with caution. The profiles for the pins do not show any significant variation with R_θ over the y/δ range whereas for the wire and the grit, the profiles collapse reasonably well up to $y/\delta \approx 0.5$, but beyond this range they show a dependence on R_θ with values of L/δ increasing with increasing R_θ. For increasing values of y/δ, the values of L/δ rise to a peak at $y/\delta \approx 0.5$ before falling again. The scatter in the data makes it difficult to determine precise values of L/δ at the peaks, but for the three devices for the different values of R_θ, the values of L/δ are reasonably close to 0.10. The L/δ profiles shown in figure 6.62 have the same general form as the universal curve given by

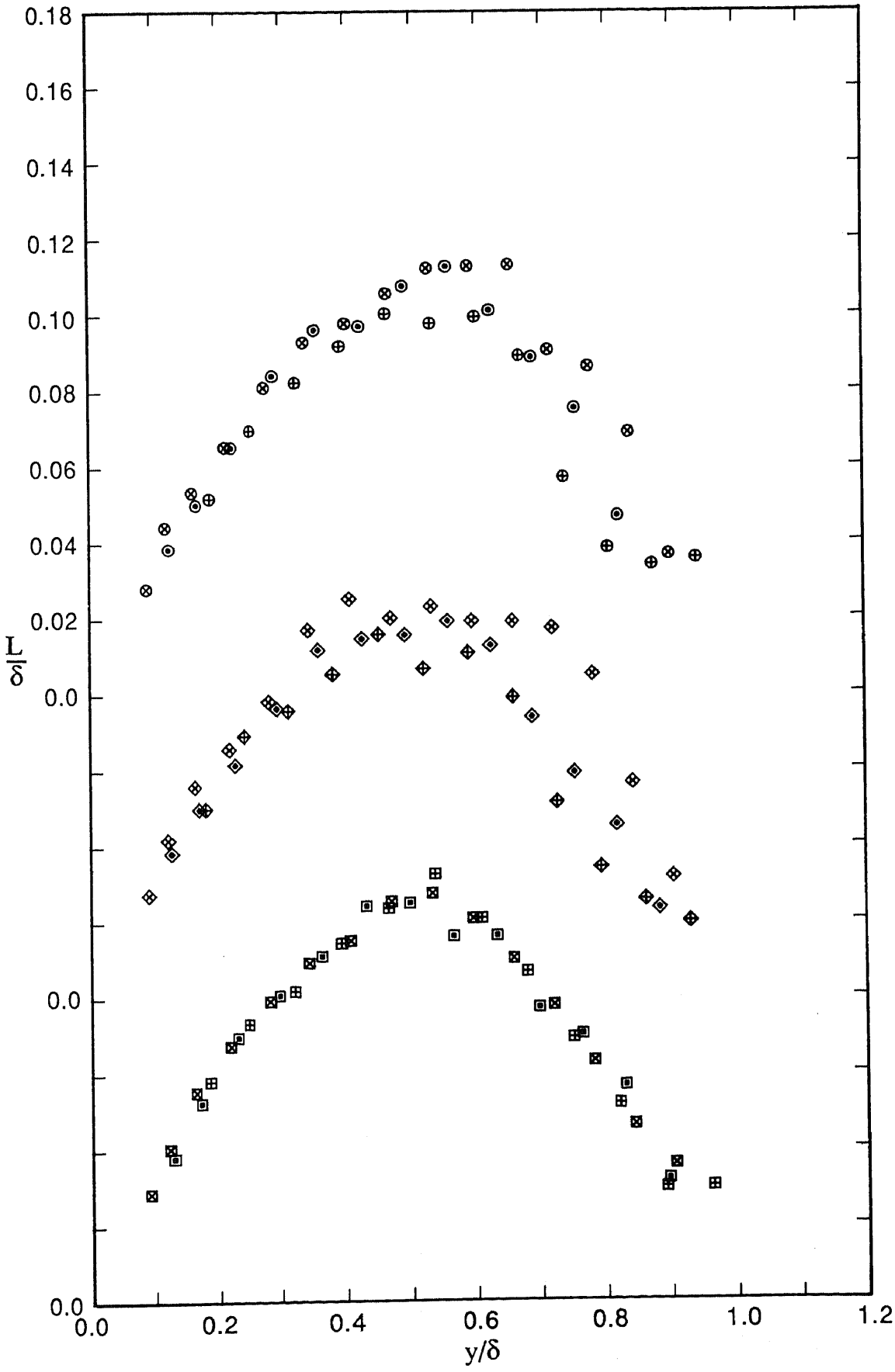

FIGURE 6.62. Profiles of dissipation length parameter, L/δ versus y/δ, for design flows showing effects of R_θ for three devices. Note shift in ordinate.

Wire:	●, R_θ=697;	⊕, 1003;	⊙, 1568;	⊗, 2226;	⊙, 2788.
Grit:	◆, R_θ=706;	⊕, 1042;	◇, 1520;	◈, 2178;	◇, 2730.
2.0 mm pins:	■, R_θ=729;	⊞, 1027;	⊡, 1565;	⊠, 2181;	⊡, 2889.

Bradshaw (1967), which is reproduced in figure 6.63. The maximum value of his curve is about 0.10 and this maximum value occurs at $y/\delta \approx 0.5$. Close to the wall, where dissipation ≈ production, it can be shown that $L \approx \iota$ (this is apparent from equations 6.4 and 6.5 as well as the fact that production ≈ $-\overline{uv}\,\partial U/\partial y$). The ι/δ and L/δ profiles shown in figures 6.61 and 6.62 respectively are plotted to the same scale and a comparison between these two figures shows that close to the wall the above condition that $L \approx \iota$ applies for the current data.

When the current data are compared with those of Murlis, Tsai & Bradshaw (1982), some differences occur in the trends of the data with R_θ. Data for δ/L (not L/δ) versus R_θ for various values of y/δ as given by Murlis, Tsai & Bradshaw are reproduced in figure 6.64 and it can be seen that these data behave in a rather unusual manner. Between $R_\theta \approx 1000$ and $R_\theta \approx 2200$, the values of δ/L increase with increasing R_θ for y/δ less than about 0.7, but decrease with increasing R_θ for $y/\delta = 0.8$. Furthermore, for R_θ greater than about 2000, the trends of the data for $y/\delta = 0.5$ and 0.6 change and the values of δ/L now decrease with increasing R_θ. This author is unable to comprehend the numbers given on the ordinate in figure 6.64. Considering the behaviour of the L/δ versus y/δ characteristic for high Reynolds numbers as given by Bradshaw (1967), which is reproduced in figure 6.63, it is apparent that for values of y/δ varying between 0.4 and 0.6, the value of L/δ is about 0.10, i.e. δ/L is about 10, which does not correspond to the data for $R_\theta = 4750$ given in figure 6.64. Similarly, for $y/\delta = 0.8$, the value of L/δ given by Bradshaw is 0.08, i.e. δ/L = 12.5, which also does not correspond to figure 6.64, even allowing for the fact that in figure 6.64 data for $y/\delta = 0.8$ are only given up to $R_\theta = 2387$. It is worth noting that Murlis, Tsai & Bradshaw specifically state that the results, especially those from the last station (requiring a differentiation at the end of the range to obtain the advection), are not very reliable.

6.3.9 Turbulent Transport Velocities

The turbulent transport terms appearing in the turbulent-kinetic-energy and Reynolds-shear-stress transport equations (equations 2.26 and 2.27 respectively) are often modelled using turbulent transport velocities which are defined respectively as

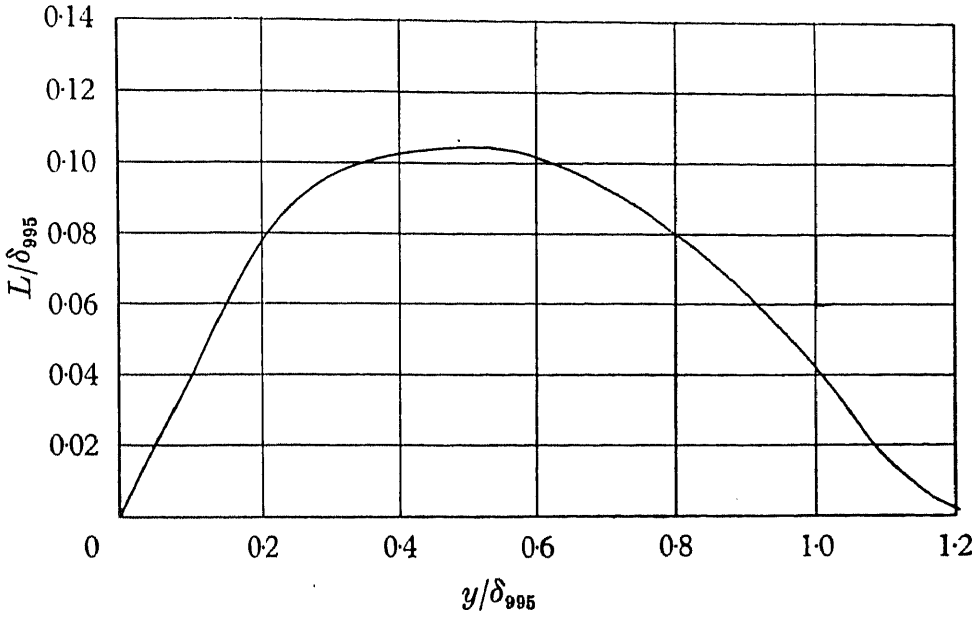

FIGURE 6.63. Dissipation length parameter, L/δ versus y/δ, as given by Bradshaw (1967).

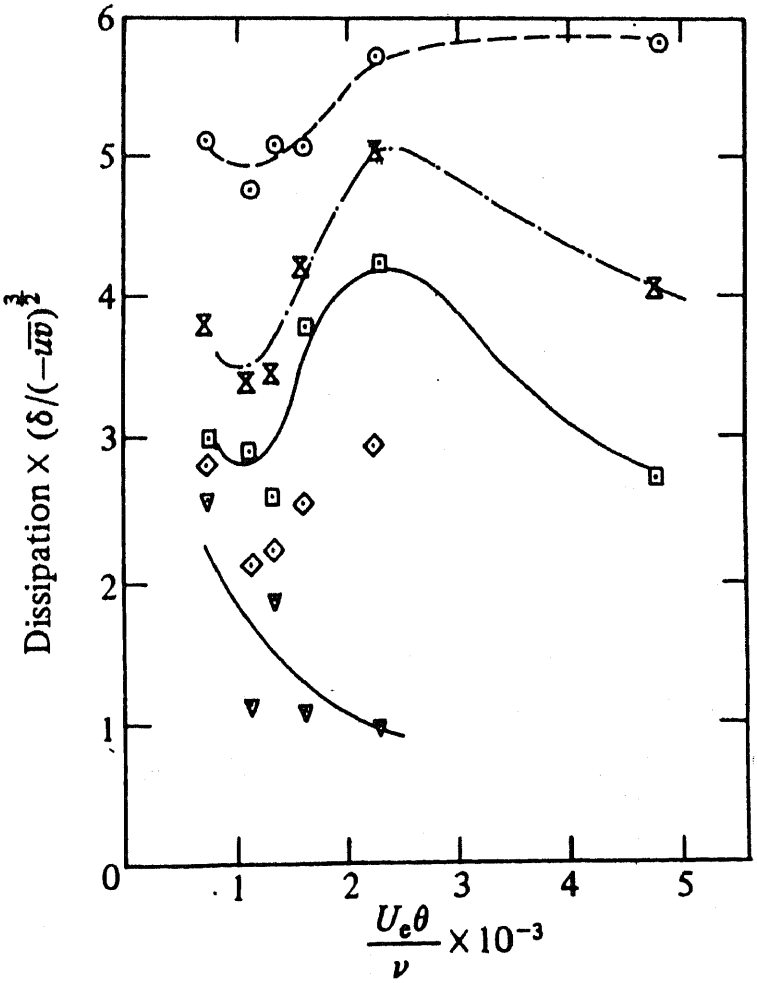

FIGURE 6.64. Variation of δ/L with R_θ for different values of y/δ as given by Murlis, Tsai & Bradshaw (1982).

——⊙— — —, y/δ = 0.4; —·—⧖—·—, 0.5; ——⊡——, 0.6; ◇, 0.7; ——▽——, 0.8.

$$V_q = \frac{\overline{q^2 v}}{\overline{q^2}} \approx \frac{1.5(\overline{u^2 v} + \overline{v^3})}{\overline{q^2}} \qquad (6.6)$$

and

$$V_\tau = \frac{\overline{uv^2}}{\overline{uv}} \qquad (6.7)$$

with transport by pressure fluctuations neglected in each case. In the first of these two equations, it has been necessary to approximate $\overline{vw^2}$, which was not measured and is one of the terms comprising $\overline{q^2 v}$, by $0.5(\overline{u^2 v} + \overline{v^3})$ (see Section 2.4 for background to approximation). V_q and V_τ are the velocities of propagation of turbulent energy and shear stress respectively in the y direction by the large eddies. Equations (6.6) and (6.7) correspond to the "bulk convection" hypothesis for representing turbulent transport processes in the transport equations. This hypothesis was used by Bradshaw, Ferriss & Atwell (1967) in their calculation method.

Figure 6.65 shows profiles of V_q/U_e versus y/δ for the three tripping devices for different values of R_θ. The V_q/U_e profiles for each of the devices can be seen to show large variations with R_θ throughout the entire y/δ range, with the values of V_q/U_e generally decreasing with increasing R_θ at a given value of y/δ. The differences between the profiles for $R_\theta \approx 2175$ and $R_\theta \approx 2810$ are reasonably small in each case except for the pins beyond $y/\delta \approx 0.8$. As y/δ increases, the values of V_q/U_e at first decrease and then increase to a peak value at $y/\delta \approx 0.9$, before falling again. For the data presented, the values of V_q/U_e remain positive in all cases indicating that the transport of energy is always away from the wall. Direct comparisons of the current V_q/U_e profiles with those of other researchers is not always straightforward. Barlow & Johnston (1985), (1988) used $V_q' = (\overline{u^2 v} + \overline{v^3})/(\overline{u^2} + \overline{v^2})$ which is slightly different from the definition used in this investigation, whereas Murlis (1975) did not actually measure $\overline{w^2}$ used in $\overline{q^2}$, but instead approximated it from the measured $\overline{u^2}$ and $\overline{v^2}$ terms. At $y/\delta = 0.5$ and 1.0, the values of V_q/U_e for the current investigation are about 0.011 and 0.020 respectively for all devices for $R_\theta \approx 2810$. The corresponding values of V_q/U_e obtained by Murlis (1975) are about 0.006 and 0.012 respectively for $R_\theta = 4750$. The reason for the differences in the values of V_q/U_e from the two investigations are unclear, but contributing factors could

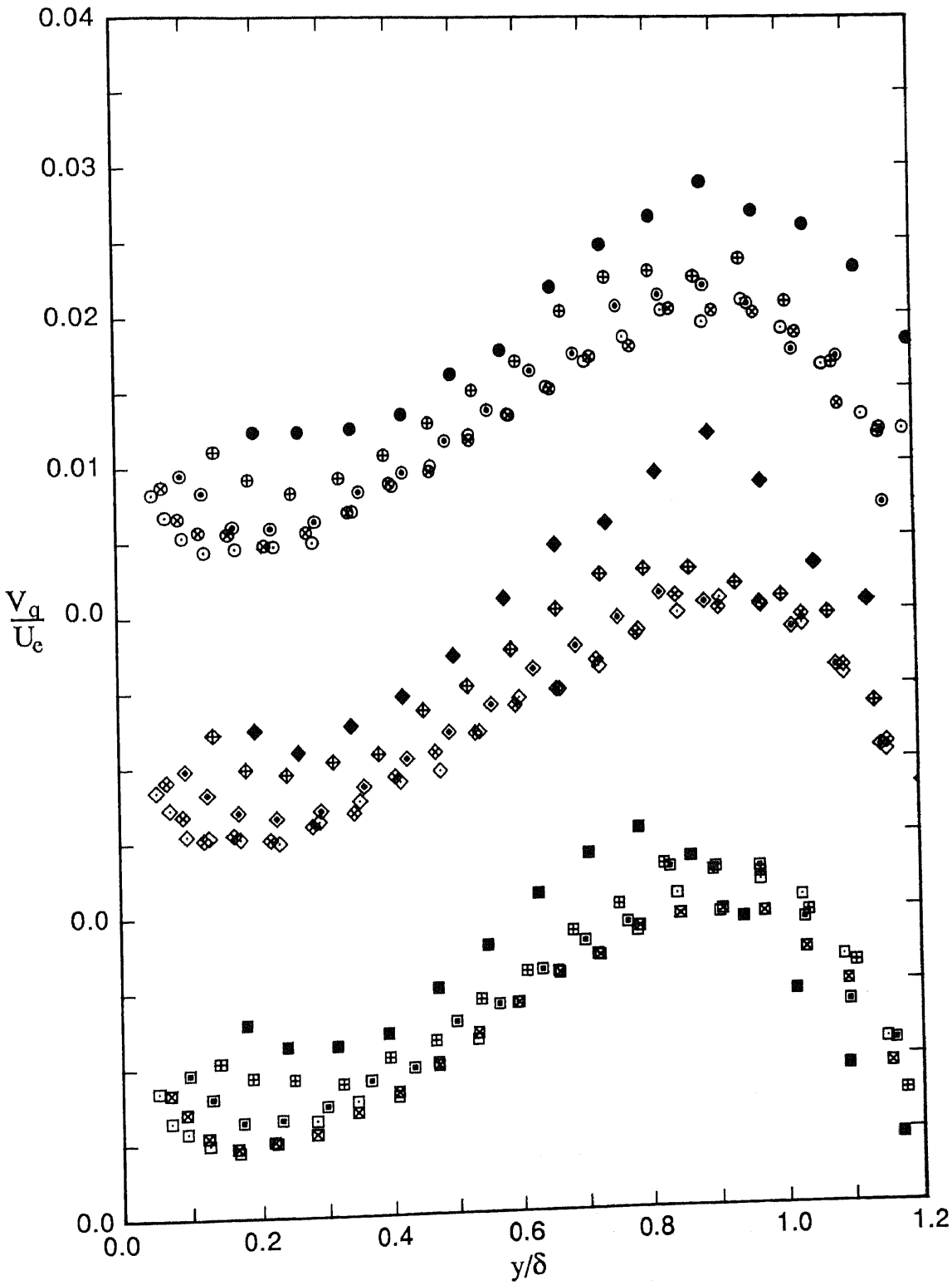

FIGURE 6.65. Profiles of turbulent transport velocity, V_q/U_e versus y/δ, for design flows showing effects of R_θ for three devices. Note shift in ordinate.

Wire:	●, R_θ=697;	⊕, 1003;	⊙, 1568;	⊗, 2226;	⊙, 2788.
Grit:	◆, R_θ=706;	⊕, 1042;	◇, 1520;	⊗, 2178;	◇, 2730.
2.0 mm pins:	■, R_θ=729;	⊞, 1027;	⊡, 1565;	⊠, 2181;	⊡, 2889.

be the approximations used for $\overline{w^2}$, as discussed above, and also differences in the value of R_θ for the two cases.

Profiles of V_τ/U_e versus y/δ are shown in figure 6.66. The behaviour of the V_τ/U_e profiles is similar in many respects to that of the V_q/U_e profiles shown in figure 6.65, so to avoid repetition, only the differences between the two cases will be discussed. For the V_τ/U_e profiles for $R_\theta \approx 713$ for the three devices, data points beyond $y/\delta = 1.0$ have not been plotted since they had considerable scatter and were thus unreliable. For the different devices, the V_τ/U_e profiles vary monotonically with R_θ except for the the profiles for $R_\theta \approx 2810$ for y/δ greater than about 0.4. Also there is a tendency for the values of V_τ/U_e for the different devices to peak at slightly higher values of y/δ compared with previously. At $y/\delta = 0.5$ and 1.0, the values of V_τ/U_e for the current investigation are about 0.024 and 0.056 respectively for $R_\theta \approx 2810$ for all devices. These values of V_τ/U_e compare favourably with corresponding data of Murlis (1975), since his values of V_τ/U_e are about 0.023 and 0.051 respectively. Considering the profiles for both transport velocities, the overall percentage changes in both V_q/U_e and V_τ/U_e for R_θ varying between nominal values of 713 and 2810, are about the same in both cases at $y/\delta = 1.0$.

6.4 Broadband-Turbulence Characteristics For Under and Overstimulated Flows

Since the mean-flow characteristics for different devices had been shown to depend upon the degree of stimulation (see Section 5.5), it was desirable to take a limited number of off-design broadband-turbulence measurements to determine the effects, if any, that under and overstimulation had on the broadband-turbulence behaviour. For this purpose twelve broadband-turbulence profiles were taken and details of these are documented in groups 2 and 4 of table 5.1. The twelve turbulence profiles were all taken with the single-wire probe and consisted of six profiles for understimulated flows (8.0 m/s nominal) and six profiles for overstimulated flows (14.0 m/s nominal).

6.4.1 Reynolds Normal Stresses

For the $\overline{u^2}$ normal stresses, the effects of under and overstimulation for different devices were investigated by simply comparing the normal stresses, at

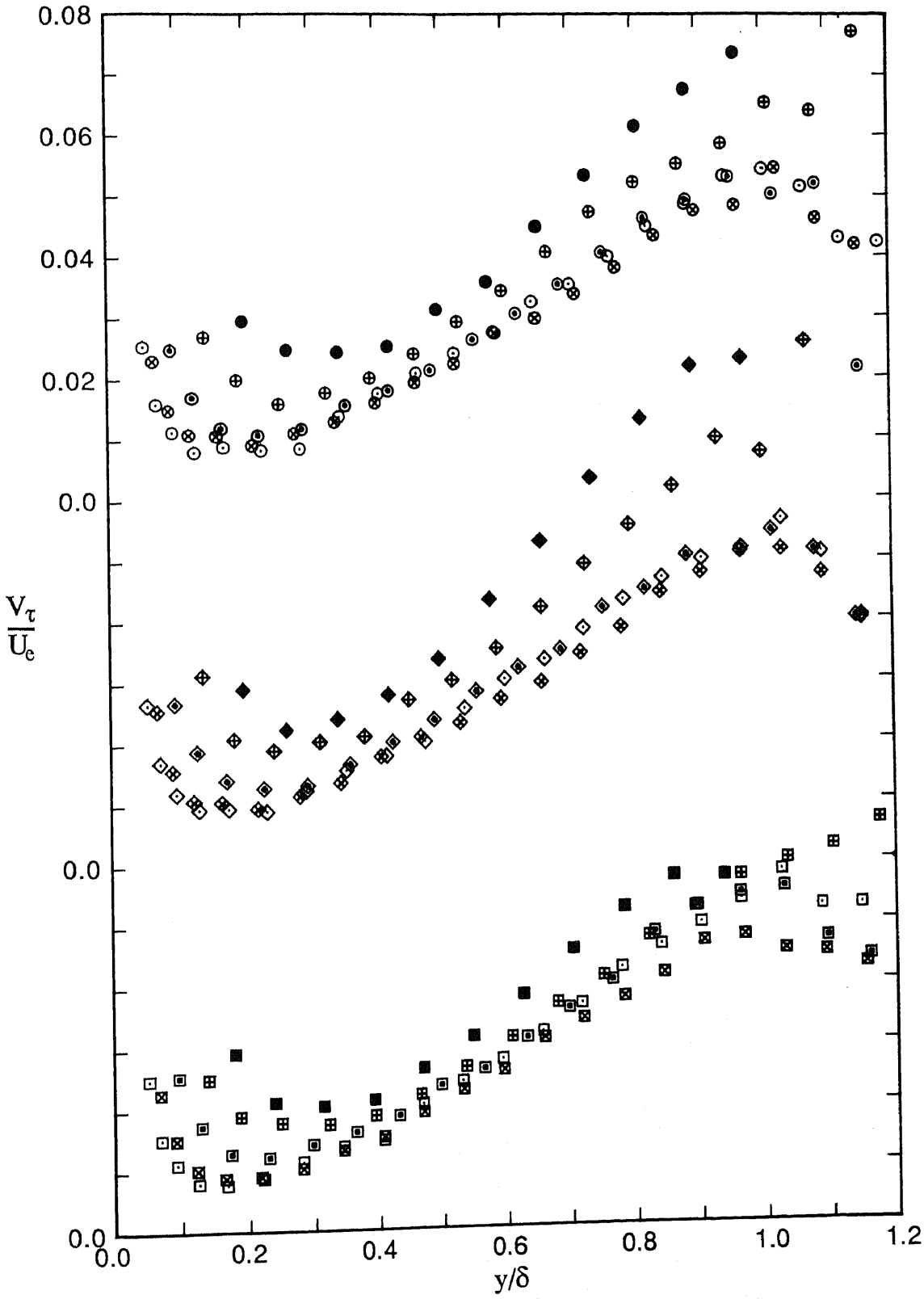

FIGURE 6.66. Profiles of turbulent transport velocity, V_τ / U_e versus y/δ, for design flows showing effects of R_θ for three devices. Note shift in ordinate.

Wire:	●, R_θ=697;	⊕, 1003;	⊙, 1568;	⊗, 2226;	⊙, 2788.
Grit:	◆, R_θ=706;	◈, 1042;	◇, 1520;	◈, 2178;	◇, 2730.
2.0 mm pins:	■, R_θ=729;	⊞, 1027;	⊡, 1565;	⊠, 2181;	⊡, 2889.

both $R_\theta \approx 1020$ and $R_\theta \approx 2175$, for each of the devices for flows having different amounts of stimulation. Profiles of $\overline{u^2}/U_e^2$ versus y/δ used in the comparison are shown in figures 6.67 and 6.68 for $R_\theta \approx 1020$ and $R_\theta \approx 2175$ respectively. These figures are analogous to figures 5.10 and 5.11 for the mean flows.

Considering firstly data for $R_\theta \approx 1020$, shown in figure 6.67, it is apparent that the degree of stimulation can affect the shapes of the $\overline{u^2}/U_e^2$ profiles for all three tripping devices. The profiles for the 2.0 mm pins are affected far more by changes in the degree of stimulation than are the profiles for the wire and the grit, which are affected about equally. Considering data for $R_\theta \approx 2175$, shown in figure 6.68, it can be seen that the profiles for the understimulated and the design flows now collapse well for each of the three devices, but the profiles for the overstimulated flows for each device still do not match their respective design-flow profiles. For $R_\theta \approx 1020$, and at $y/\delta = 0.4$, the maximum values in the overall range of variation of $\overline{u^2}/U_e^2$ for the wire, grit and pins are about 13%, 14% and 33% respectively greater than the corresponding minimum values. Corresponding numbers for $R_\theta \approx 2175$ are 7%, 13% and 9% respectively. It could be argued that some of the differences quoted are within experimental error, but the fact that trends for all devices correspond quite closely suggests that the observed differences are in fact real. Further evidence to support this conclusion is the fact that the profiles of $\overline{u^2}/U_e^2$ versus y/δ for the different devices for the design flows for $R_\theta \approx 1020$ and $R_\theta \approx 2175$, as shown in figure 6.5, show better agreement than the profiles shown in figures 6.67 and 6.68. When the profiles of $\overline{u^2}/U_e^2$ versus y/δ, shown in figures 6.67 and 6.68, are compared with profiles of $(U-U_e)/U_\tau$ versus y/δ, shown in figures 5.12 and 5.13, which are their respective mean-flow counterparts, it is apparent that the flows tend to settle down quicker in terms of the given mean-flow characteristics, rather than the given turbulence characteristics, after being subjected to different degrees of stimulation. It will be recalled from figure 4.3 that the mean-flow behaviour, in terms of $\Delta U/U_\tau$ versus R_θ, depended on the degree of stimulation up to about $R_\theta = 2500$ to 3000. It is uncertain whether or not broadband-turbulence characteristics are still affected by the degree of stimulation at say $R_\theta = 3000$, since measurements were not taken to check this.

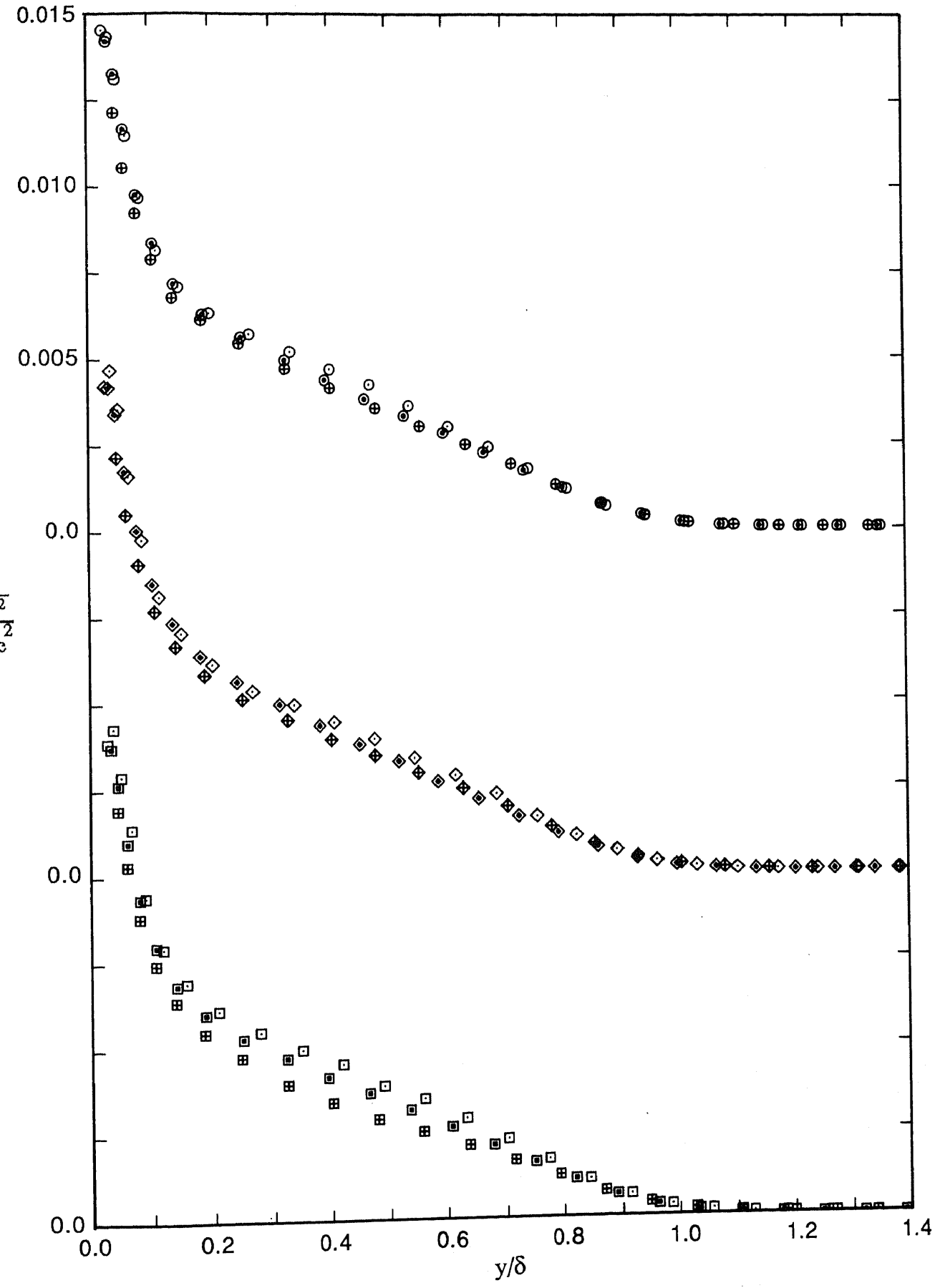

FIGURE 6.67. Profiles of $\overline{u^2}/U_e^2$ versus y/δ for three devices showing effects of different amounts of stimulation. Note shift in ordinate. Velocities given below are nominal values.

Wire:	⊙, 8.0 m/s, R_θ=1017;	⊙, 10.0 m/s, R_θ=1003;	⊕, 14.0 m/s, R_θ=1033.
Grit:	◇, 8.0 m/s, R_θ= 997;	◈, 10.0 m/s, R_θ=1042;	⊕, 14.0 m/s, R_θ=1029.
2.0 mm pins:	⊡, 8.0 m/s, R_θ=1024;	⊞, 10.0 m/s, R_θ=1027;	⊞, 14.0 m/s, R_θ=1013.

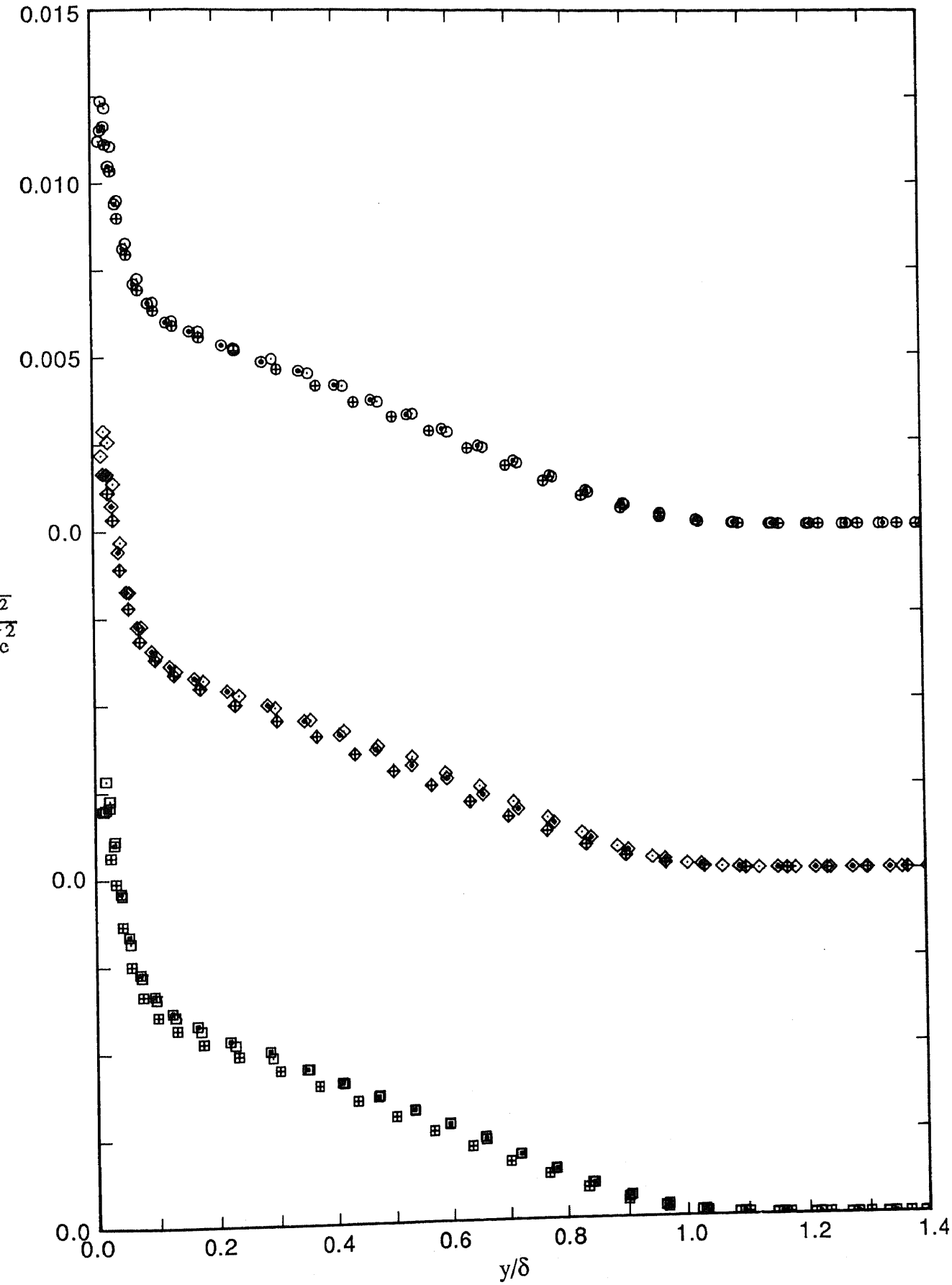

FIGURE 6.68. Profiles of $\overline{u^2}/U_e^2$ versus y/δ for three devices showing effects of different amounts of stimulation. Note shift in ordinate. Velocities given below are nominal values.

Wire:	⊙, 8.0 m/s, R_θ=2151;	⊙, 10.0 m/s, R_θ=2226;	⊕, 14.0 m/s, R_θ=2137.
Grit:	◇, 8.0 m/s, R_θ=2146;	◈, 10.0 m/s, R_θ=2178;	⊕, 14.0 m/s, R_θ=2119.
2.0 mm pins:	⊡, 8.0 m/s, R_θ=2230;	⊞, 10.0 m/s, R_θ=2181;	⊞, 14.0 m/s, R_θ=2169.

The data contained in figures 6.67 and 6.68 are shown replotted in figures 6.69 and 6.70 respectively using coordinates of $\sqrt{\overline{u^2}}/U_\tau$ versus $\log(yU_\tau/\nu)$. An analysis of figures 6.69 and 6.70 indicates that with this scaling, the behaviour of the profiles is similar in many respects to those appearing in figures 6.67 and 6.68 and much of the previous discussion also applies here. The replotted profiles for the different devices show marked variations with the degree of stimulation for both $R_\theta \approx 1020$ and $R_\theta \approx 2175$, and in this case the understimulated flows for the wire and grit do not match their respective design-flow profiles for $R_\theta \approx 2175$. All else that need be noted is that the design-flow profiles for the different devices for $R_\theta \approx 1020$ and $R_\theta \approx 2175$ that can be used as a basis for comparison are shown in figure 6.16.

The fact that significant differences can occur in the above broadband-turbulence profiles for different devices for varying amounts of stimulation, but for given values of R_θ, may not have been fully appreciated by researchers in the past. Most likely researchers would have established a flow by comparing their measured $\Delta U/U_\tau$-versus-R_θ characteristic with that proposed by Coles (1962). However, an examination of the measured $\Delta U/U_\tau$-versus-R_θ characteristics shown in figure 4.3 indicates that in a number of cases a characteristic for under or overstimulated flow could quite easily be assumed to be acceptable if it was the only one measured in an investigation. This point should be borne in mind when assessing published turbulence data on low-Reynolds-number flows.

The reason for measuring turbulence quantities for under and overstimulated flows was not to establish precise forms of profiles, since these would only be of limited use, but instead to see whether or not turbulence quantities were affected by under and overstimulation. Since this was established for each of the devices by the above $\overline{u^2}$ measurements taken with a single-wire probe, there was no point using a crossed-wire probe to measure other broadband-turbulence terms. This is the reason the broadband-turbulence measurements for the under and overstimulated flows were limited to those taken with the single-wire probe. However, since it was possible to determine values of $\overline{u^3}$ without actually taking further turbulence measurements, then it was worthwhile to do this and plot profiles involving these terms to investigate effects, if any, on the profiles of under and overstimulation.

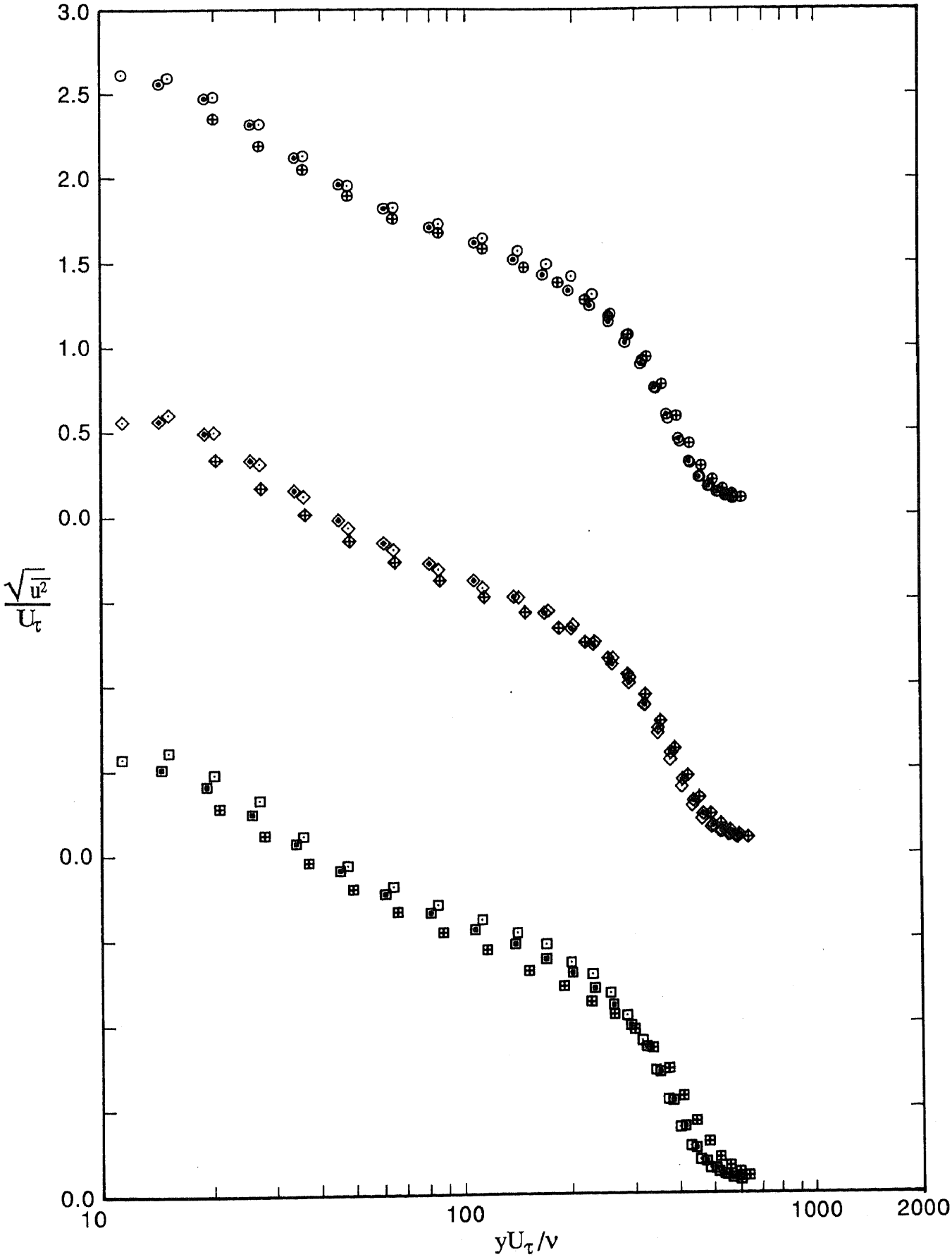

FIGURE 6.69. Profiles of $\sqrt{u^2}/U_\tau$ versus $\log(yU_\tau/\nu)$ for three devices showing effects of different amounts of stimulation. Note shift in ordinate. Velocities given below are nominal values.

Wire:	⊙, 8.0 m/s, R_θ=1017;	⊙, 10.0 m/s, R_θ=1003;	⊕, 14.0 m/s, R_θ=1033.
Grit:	◇, 8.0 m/s, R_θ=0997;	◈, 10.0 m/s, R_θ=1042;	✥, 14.0 m/s, R_θ=1029.
2.0 mm pins:	⊡, 8.0 m/s, R_θ=1024;	▣, 10.0 m/s, R_θ=1027;	⊞, 14.0 m/s, R_θ=1013.

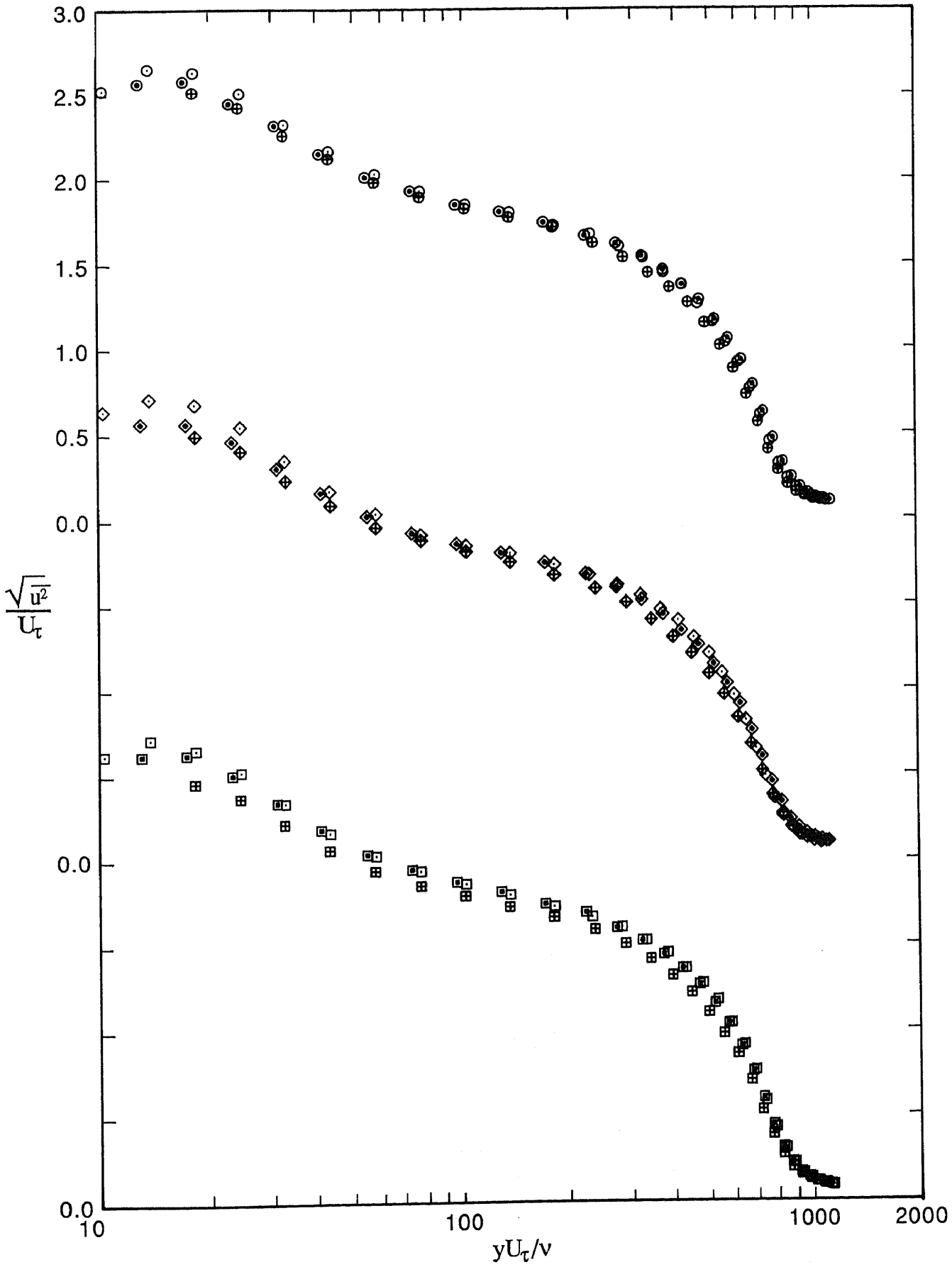

FIGURE 6.70. Profiles of $\sqrt{\overline{u^2}}/U_\tau$ versus $\log(yU_\tau/\nu)$ for three devices showing effects of different amounts of stimulation. Note shift in ordinate. Velocities given below are nominal values.

Wire:	⊙, 8.0 m/s, R_θ=2151;	⊙, 10.0 m/s, R_θ=2226;	⊕, 14.0 m/s, R_θ=2137.
Grit:	◇, 8.0 m/s, R_θ=2146;	◈, 10.0 m/s, R_θ=2178;	⊕, 14.0 m/s, R_θ=2119.
2.0 mm pins:	⊡, 8.0 m/s, R_θ=2230;	▣, 10.0 m/s, R_θ=2181;	⊞, 14.0 m/s, R_θ=2169.

6.4.2 Triple Products

Profiles of $-\overline{u^3}/U_e^3$ versus y/δ for three devices and for different amounts of stimulation are shown plotted in figures 6.71 and 6.72 for $R_\theta \approx 1020$ and $R_\theta \approx 2175$ respectively. Most of these profiles have negative values of $-\overline{u^3}/U_e^3$ for small values of y/δ (similar to those shown in say figure 6.23), but these have been omitted from the plotted profiles. An analysis of figure 6.71 indicates that for $R_\theta \approx 1020$, the degree of stimulation can have a significant effect upon the profiles for the different devices. From figure 6.72 it can be seen that for $R_\theta \approx 2175$, the effect of the degree of stimulation on the profiles for the different devices is now less pronounced. For $R_\theta \approx 1020$ and at $y/\delta = 0.6$, the maximum values in the overall range of variation of $-\overline{u^3}/U_e^3$ for the wire, grit and pins are about 33%, 29% and 61% respectively greater than the corresponding minimum values. Corresponding figures for $R_\theta \approx 2175$ are 7%, 17% and 17% respectively. Although it is difficult to measure triple products accurately, the fact that the profiles for the three devices exhibit similar trends at each of the two nominal values of R_θ suggests that the differences between profiles within each set are real. The design-flow profiles for the different devices for $R_\theta \approx 1020$ and $R_\theta \approx 2175$ that can be used as a basis for comparison are shown in figure 6.24. When making a comparison, it is important to note that the profiles of figures 6.71 and 6.72 have an ordinate that has been magnified by a factor of 2.

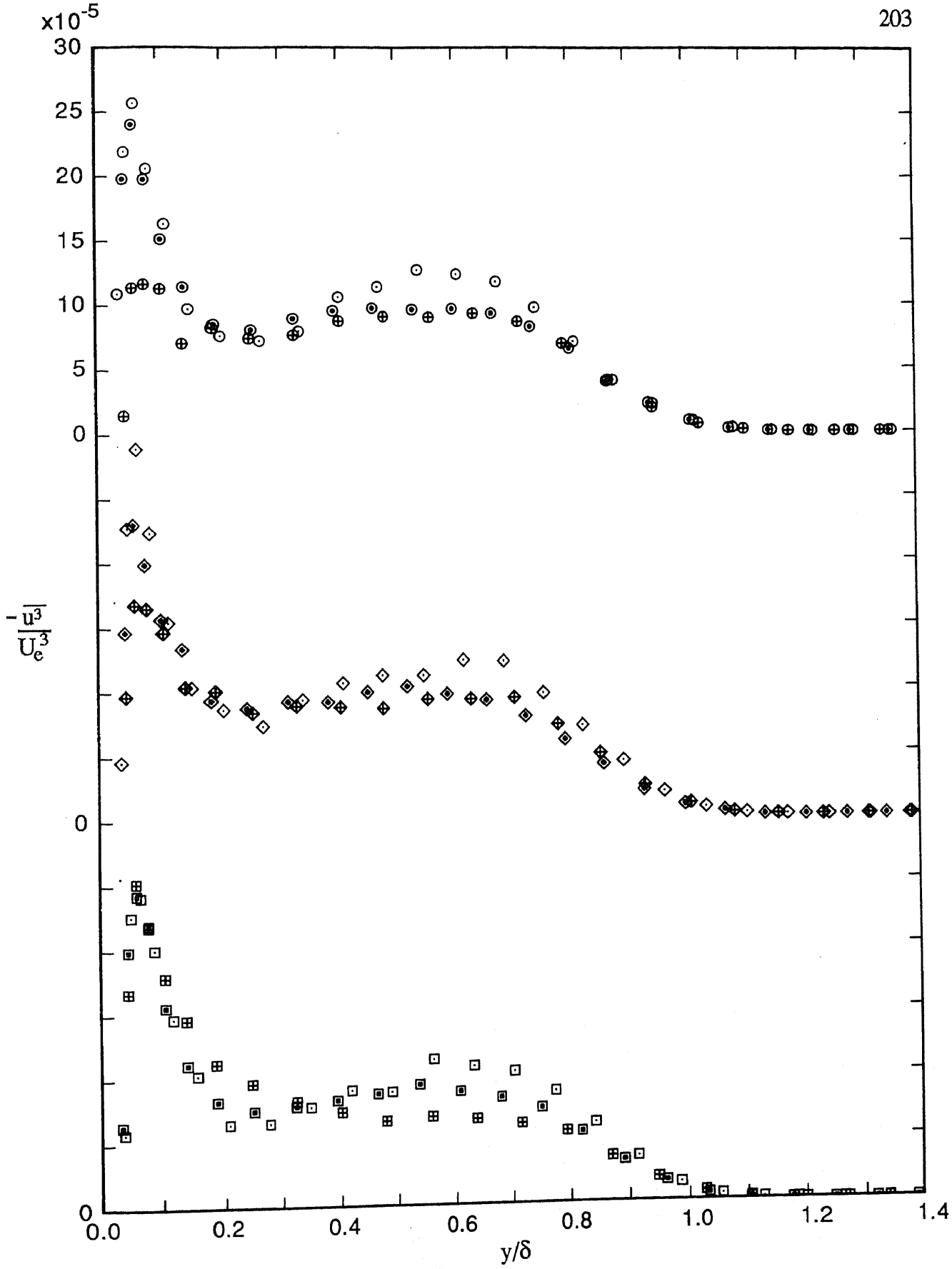

FIGURE 6.71. Profiles of $-\overline{u^3}/U_e^3$ versus y/δ for three devices showing effects of different amounts of stimulation. Note shift in ordinate. Velocities given below are nominal values.

Wire:	⊙, 8.0 m/s, R_θ=1017;	⊙, 10.0 m/s, R_θ=1003;	⊕, 14.0 m/s, R_θ=1033.
Grit:	◇, 8.0 m/s, R_θ=0997;	◈, 10.0 m/s, R_θ=1042;	◈, 14.0 m/s, R_θ=1029.
2.0 mm pins:	⊡, 8.0 m/s, R_θ=1024;	⊞, 10.0 m/s, R_θ=1027;	⊞, 14.0 m/s, R_θ=1013.

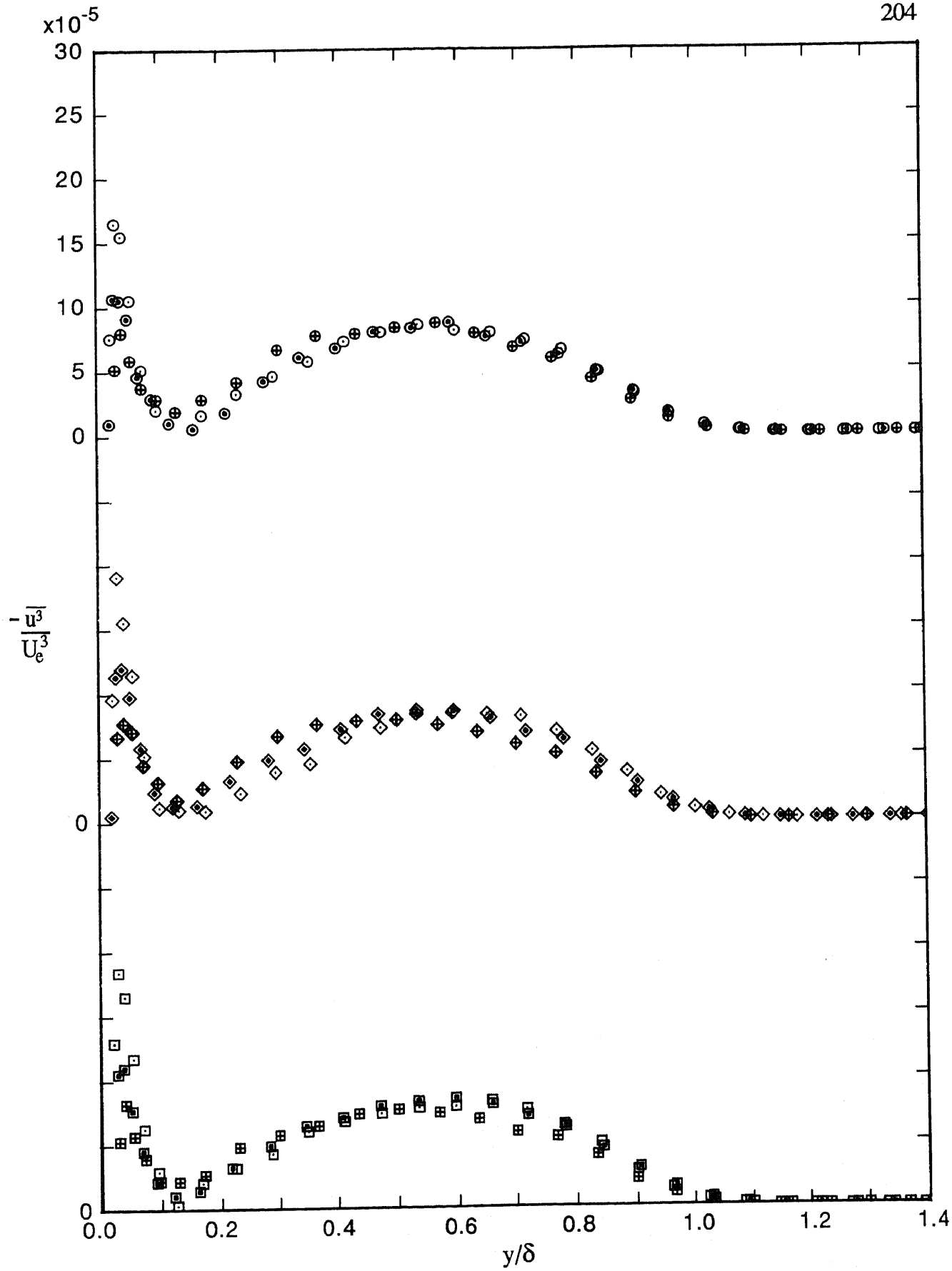

FIGURE 6.72. Profiles of $-\overline{u^3}/U_e^3$ versus y/δ for three devices showing effects of different amounts of stimulation. Note shift in ordinate. Velocities given below are nominal values.

Wire:	⊙, 8.0 m/s, R_θ=2151;	⊙, 10.0 m/s, R_θ=2226;	⊕, 14.0 m/s, R_θ=2137.
Grit:	◇, 8.0 m/s, R_θ=2146;	◈, 10.0 m/s, R_θ=2178;	⊕, 14.0 m/s, R_θ=2119.
2.0 mm pins:	⊡, 8.0 m/s, R_θ=2230;	▣, 10.0 m/s, R_θ=2181;	⊞, 14.0 m/s, R_θ=2169.

CHAPTER 7

ANALYSIS OF SPECTRA

In this chapter spectra are presented and analysed. Spectra were taken for the u, v and w components of the turbulence considered separately, but not products of these components. Details of the technique used to sample and reduce spectra are given in Section 3.12.2.

As was done for both the mean-flow and the broadband-turbulence measurements, the effects on spectra of R_θ, tripping device and amount of stimulation, each considered separately, were investigated. Spectra were systematically taken so that they matched the mean-flow and broadband-turbulence profiles, as shown in table 5.1, and spectra were then compared in the manner outlined in Section 5.3. Spectra for the u component of the turbulence were taken for understimulated, design and overstimulated flows, whereas spectra for the v and w components of the turbulence were limited to the design flows.

7.1 Spectral Theory of Perry, Henbest & Chong

Perry, Henbest & Chong (1986) have recently suggested a number of different ways of scaling spectra and they have also proposed spectral similarity laws associated with some of these different types of scaling. Their analysis is only applicable to high-Reynolds-number, zero-pressure-gradient, flat-plate flows and was mainly applied to the turbulent wall region, which they defined as $\nu/U_\tau << y << \Delta_E$. The parameter Δ_E is an outer-flow length scale that scales with the boundary-layer thickness and has a value close to the 99% boundary-layer thickness. Their analysis was based upon Townsend's (1976) "attached eddy" hypothesis as well as work by Perry & Abell (1977), who used dimensional analysis to explain spectral behaviour, and the work of Perry & Chong (1982), who used a turbulence model based on attached eddies. The dimensional-analysis approach of Perry & Abell was extended to three

dimensions and the model of Perry & Chong was modified so that the attached eddies were now surrounded by detached isotropic fine-scale eddies which are responsible for a Kolmogorov spectral region and for most of the turbulent energy dissipation. Although the theory of Perry, Henbest & Chong was formulated for high-Reynolds-number flows, Spalart (1988) used their suggested scaling laws when plotting his numerical simulations of low-Reynolds-number flows (see Section 2.6 for a brief outline of Spalart's work). Since it was decided to also make use of the theory in the current investigation, a brief description of some of its features is appropriate.

Consider firstly the Townsend (1976) attached-eddy hypothesis. Townsend proposed that the eddies that contribute strongly to the Reynolds shear stress at a given height y above a boundary, scale with that height and are therefore in a sense, attached to the wall. Also, at a distance y from the surface, contributions to u and w will be made by eddies of height of order y and larger, whereas contributions to v will only be made by eddies of height of order y. .

According to Perry, Henbest & Chong, the behaviour of the u spectra in the turbulent wall region for high Reynolds numbers can be separated into three wavenumber regions. Firstly, eddies of height of order Δ_E will contribute energy at low wavenumbers, so at these low wavenumbers the expected "outer-flow" scaling law is of the form

$$\frac{\Phi_{11}[k_1\Delta_E]}{U_\tau^2} = f_1[k_1\Delta_E] \tag{7.1}$$

$\Phi_{11}[k_1\Delta_E]$ is the power spectral density per unit non-dimensional wavenumber, $k_1\Delta_E$, and k_1 is the streamwise wavenumber. Corresponding definitions apply to other power spectral densities having similar forms. With this scaling, spectra can generally be expected to collapse at low wavenumbers. Secondly, eddies of height of order y will contribute energy at moderate to high wavenumbers, so at these wavenumbers the expected "inner-flow" scaling law is of the form

$$\frac{\Phi_{11}[k_1 y]}{U_\tau^2} = f_2[k_1 y] \tag{7.2}$$

With this scaling, spectra can generally be expected to collapse for moderate to high wavenumbers. Thirdly, the fine scale locally isotropic motions will contribute energy at very high wavenumbers. The scaling of the u spectra in this region would be expected to follow the classical Kolmogorov (1941) viscosity-dependent scaling law,

$$\frac{\Phi_{11}[k_1\eta]}{\upsilon^2} = f_3[k_1\eta] \tag{7.3}$$

In this expression η and υ are the Kolmogorov length and velocity scales respectively and these are defined by $\eta = (\nu^3/\varepsilon)^{0.25}$ and $\upsilon = (\nu\varepsilon)^{0.25}$. Both terms can be seen to depend on the turbulent energy dissipation, ε, and the kinematic viscosity, ν. When this scaling is used, spectra can generally be expected to collapse in the very high wavenumber regions.

Equations (7.1) to (7.3) correspond to different u spectral regions over the range of wavenumber k_1, and the theory anticipates two regions of overlap. The first of these is where equations (7.1) and (7.2) both apply simultaneously and in this region the spectra can be expected to collapse onto an inverse power law distribution for both outer-flow and inner-flow scaling. The second region of overlap is where equations (7.2) and (7.3) both apply simultaneously and in this region the spectra can be expected to collapse onto a -5/3 power law distribution for both inner-flow and Kolmogorov scaling provided the Reynolds number of the flow is sufficiently large. This region of overlap is referred to as the inertial subrange and is often interpreted as the region where energy is transferred by an inviscid cascade process from the large-scale anisotropic energy-containing motions to the isotropic fine-scale dissipating motions.

The expected form of the w spectra is similar to that for the u spectra since u and w motions are similar. For the v spectra, no outer-flow scaling law is expected and so there is only the inner-flow and Kolmogorov scaling laws and an overlapping region which is expected to follow a -5/3 power law.

To help clarify the above discussion, diagrams given by Perry, Lim & Henbest (1987) have been reproduced as shown in figure 7.1. These diagrams show the predicted u spectral behaviour (and thus the predicted w spectral behaviour) for the turbulent wall region for both inner-flow and outer-flow scaling and the predicted v spectral behaviour for the turbulent wall region for

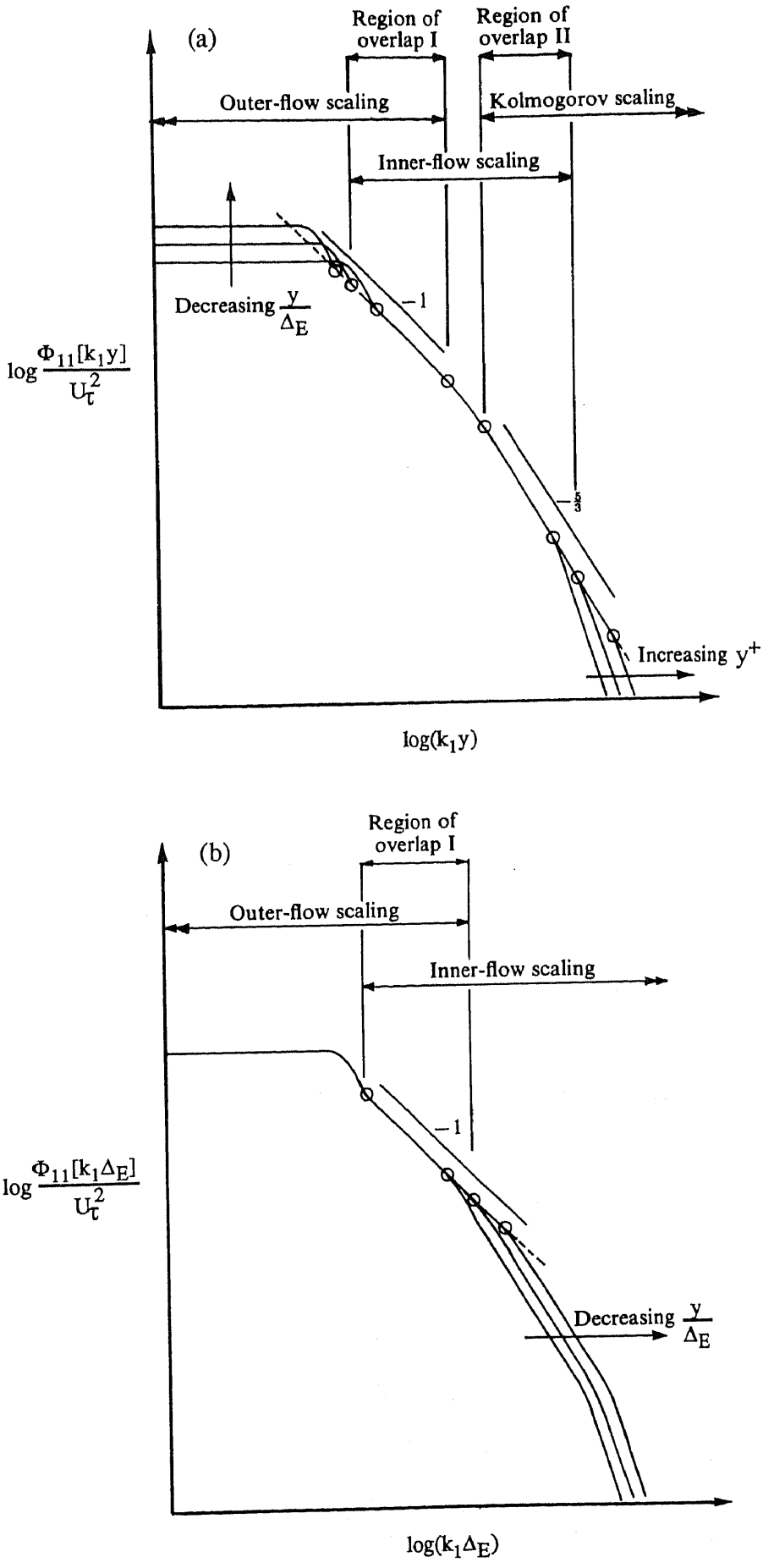

FIGURE 7.1. Predicted spectral behaviour within the turbulent wall region as given by Perry, Lim & Henbest (1986).
(a) u spectra, inner-flow scaling; (b) u spectra, outer-flow scaling; (c) see next page.

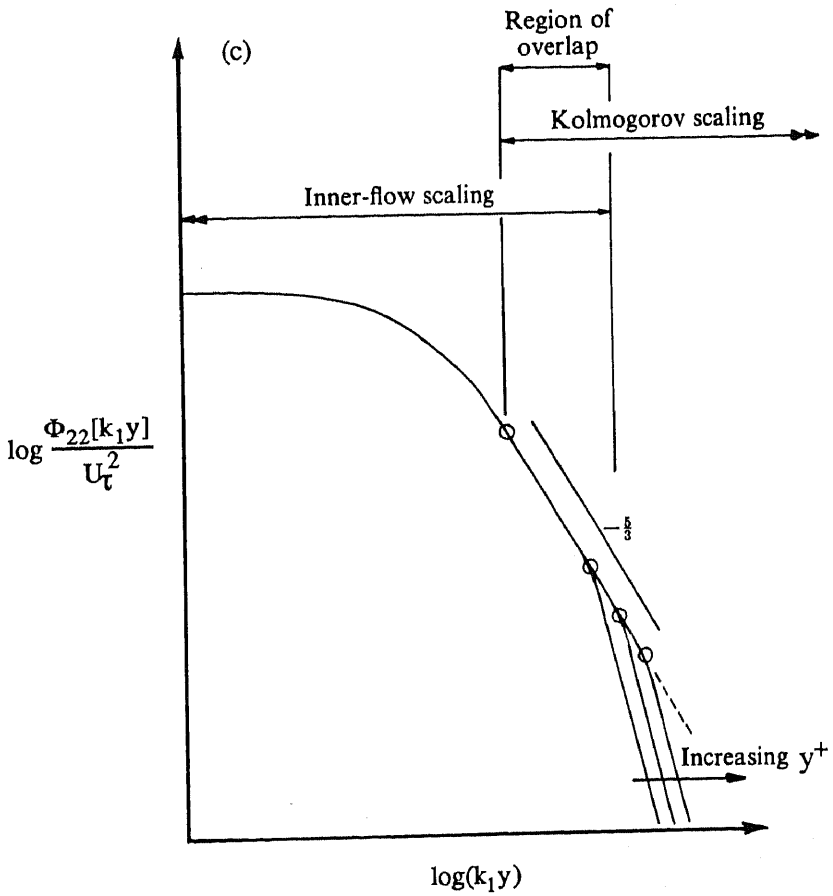

FIGURE 7.1 continued. Predicted spectral behaviour within the turbulent wall region as given by Perry, Lim & Henbest (1986).
(c) v spectra, inner-flow scaling.

inner-flow scaling. Annotations not relevant to the current investigation have been omitted from the diagrams and, where confusion could arise, terminology has been changed to correspond to that used in this thesis. The predicted regions of collapse in the different cases are clearly indicated, as are the predicted -1 and -5/3 regions of overlap. Where appropriate, the order in which the spectra are expected to peel off at the low and high wavenumber ends is also clearly shown.

Perry, Henbest & Chong (1986) also discuss the behaviour of pre-multiplied spectra, in which the power spectral density is multiplied by the terms in its argument, e.g. $\Phi_{11}[k_1 y]$ becomes $k_1 y \Phi_{11}[k_1 y]$. When pre-multiplied spectra are plotted semi-logarithmically, the plots conveniently show the energy contribution over any wavenumber range as an area under the curve.

Perry, Henbest & Chong presented spectral data for turbulent flow in a smooth-walled circular pipe and the data showed support for their model. For this flow, they tentatively defined the turbulent wall region as $yU_\tau/\nu > 140$ and $y/\Delta_E < 0.14$. In a later publication, Perry, Lim & Henbest (1987) presented smooth-wall boundary-layer data and this also showed support for the model. For this flow, the turbulent wall region was tentatively defined as $yU_\tau/\nu > 100$ and $y/\Delta_E < 0.15$.

Perry, Henbest & Chong also consider spectral behaviour in the fully turbulent region, which begins at the outer limit of the buffer zone and extends to the edge of the boundary layer. They indicate that according to the extended Townsend Reynolds number similarity hypothesis, the energy-containing region of the spectra of the u component of the velocity fluctuations should follow

$$\frac{\Phi_{11}[k_1 y]}{U_\tau^2} = q_1[k_1 y, \frac{y}{\Delta_E}] \qquad (7.4)$$

where q_1 is independent of viscosity. Similar expressions hold for the v and w components of the velocity fluctuations.

Pipe flow data of Perry, Henbest & Chong, corresponding to a range of Reynolds numbers, showed that spectra collapsed well at low to moderate wavenumbers, but not at high wavenumbers, for fixed values of y/Δ_E and this behaviour is consistent with equation (7.4). At fixed values of y/Δ_E, the slight

spread of the spectra at low values of k_1y for variations in R_θ was thought to be due to a change in the fractional spread of the convection velocities of the eddies as the Reynolds number varied (see Perry & Abell 1977). Perry, Henbest & Chong used an attached eddy model to predict spectral behaviour for the fully turbulent region and the predictions showed a distinct resemblance with the pipe flow data for low to moderate wavenumbers.

Although the theory of Perry, Henbest & Chong was developed for high Reynolds number flows, the low-Reynolds-number spectra of the current investigation were plotted using their scaling. This was done whether or not any comparison was being made with their model.

7.2 Spectra for Correctly-Stimulated Flows

To determine whether or not the spectra were dependent upon either R_θ or device for the design flows, forty five families of spectra were taken and details of these are given in groups 1 to 5 of table 5.1. The forty five families were comprised of fifteen families of u spectra, fifteen of v spectra and fifteen of w spectra.

It is more instructive to present spectra from different families superimposed on the same set of axes, rather than present complete families of spectra in isolation. However, it is worthwhile to present at least some complete families to show clearly how spectra change across a boundary layer as well as to provide a data base for future research workers. u spectra for $R_\theta \approx 713$ for the three devices, plotted using inner-flow scaling, are shown in figure 7.2 and corresponding u spectra for $R_\theta \approx 2810$ are shown in figure 7.3. These two values of R_θ correspond to the minimum and maximum values respectively listed in groups 1 to 5 of table 5.1. Corresponding v spectra are given in figures 7.4 and 7.5 and corresponding w spectra are given in figures 7.6 and 7.7. Although families of spectra for nominal values of R_θ of 1020, 1544 and 2175 have not been presented, selected spectra from these particular families will be given in subsequent plots.

Perry, Henbest & Chong mention a -5/3 power-law "envelope" for their complete families of spectra at their lower Reynolds numbers and this is clearly evident on some of the complete families of spectra shown in figures 7.2 to 7.7.

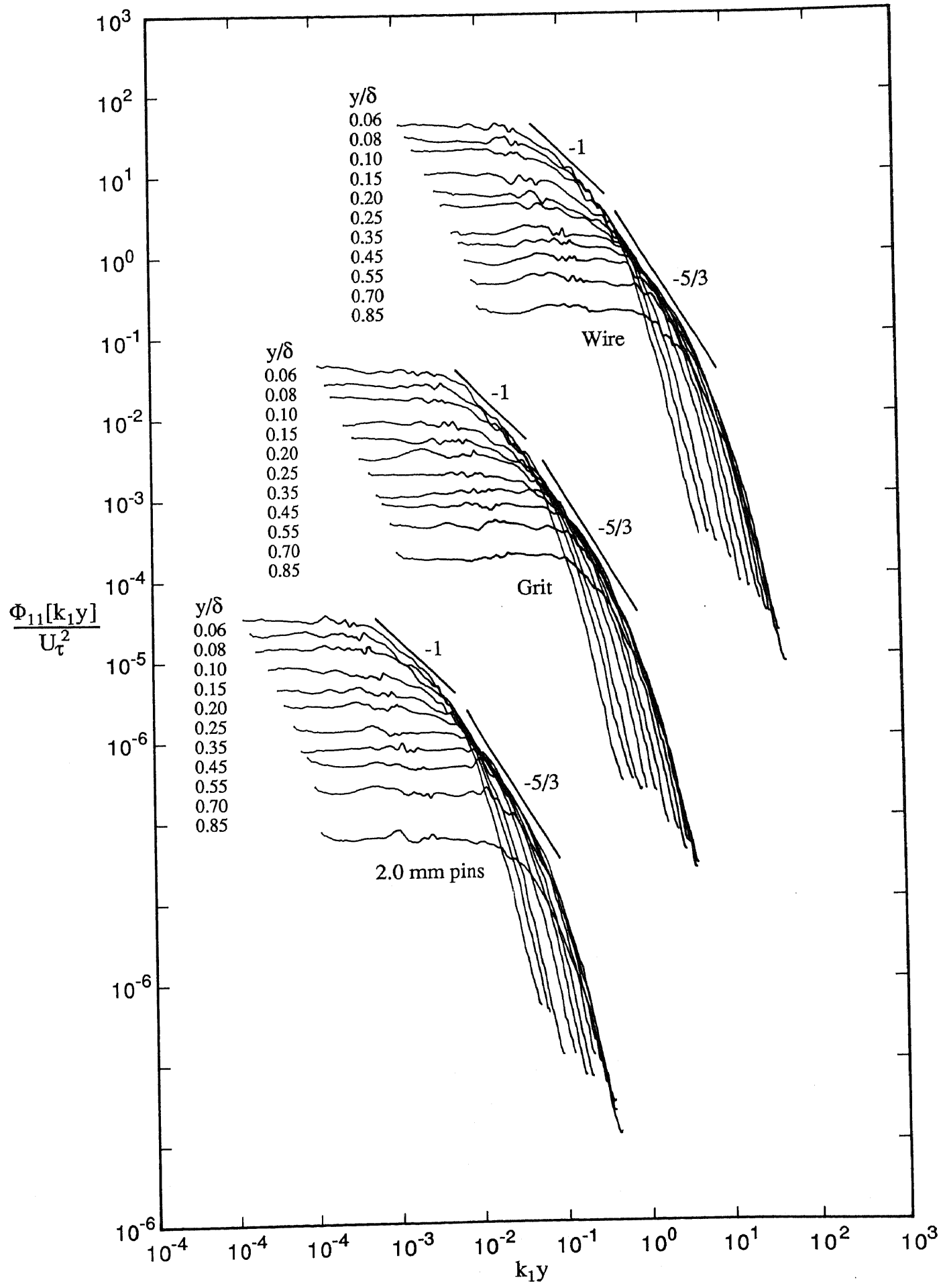

FIGURE 7.2. u spectra for three devices for design flows plotted using inner-flow scaling. Note shift in abscissa and ordinate.
Wire, R_θ= 697; Grit, R_θ=706; 2.0 mm pins, R_θ=729.

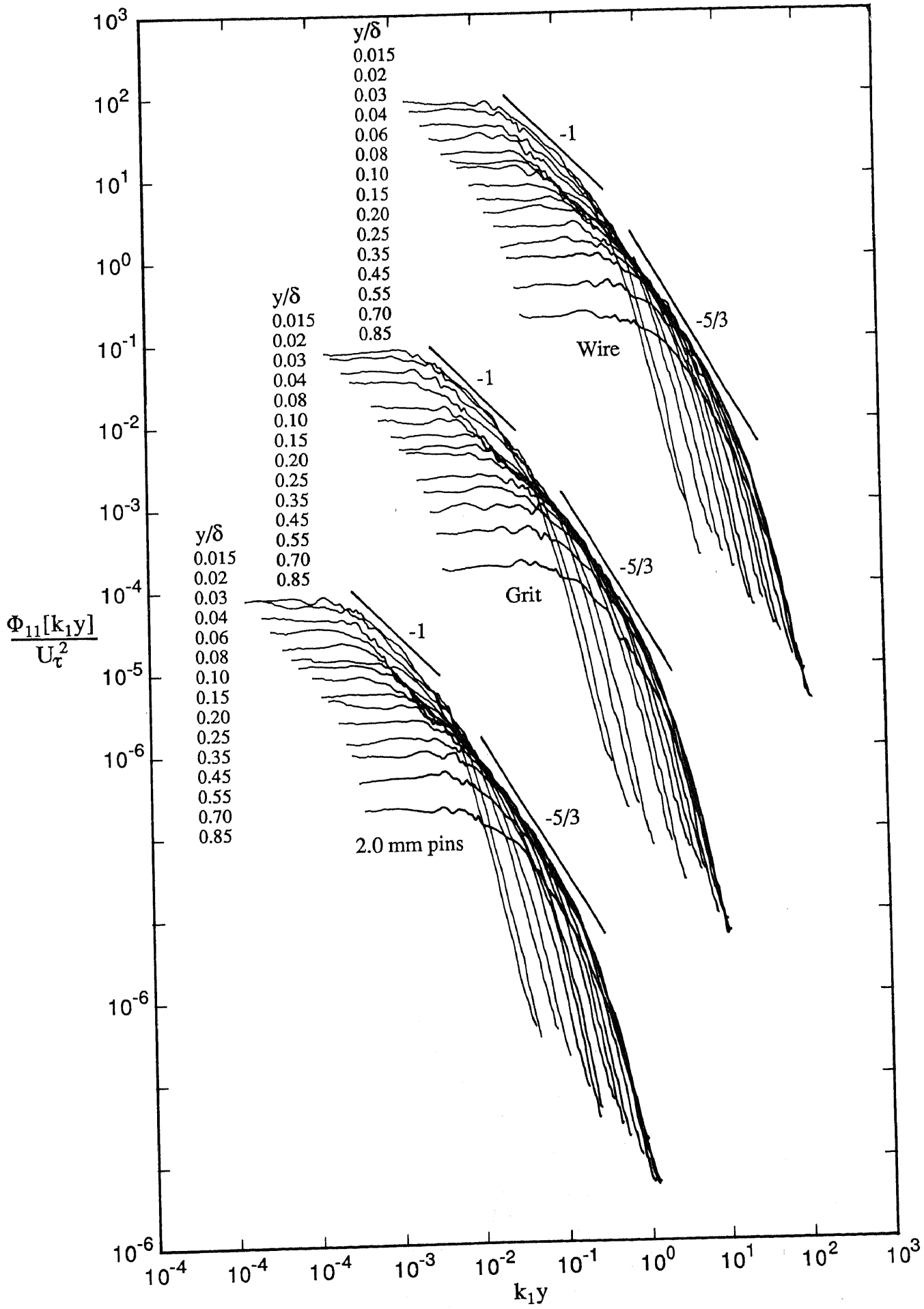

FIGURE 7.3. u spectra for three devices for design flows plotted using inner-flow scaling. Note shift in abscissa and ordinate.
Wire, R_θ=2788; Grit, R_θ=2730; 2.0 mm pins, R_θ=2889.

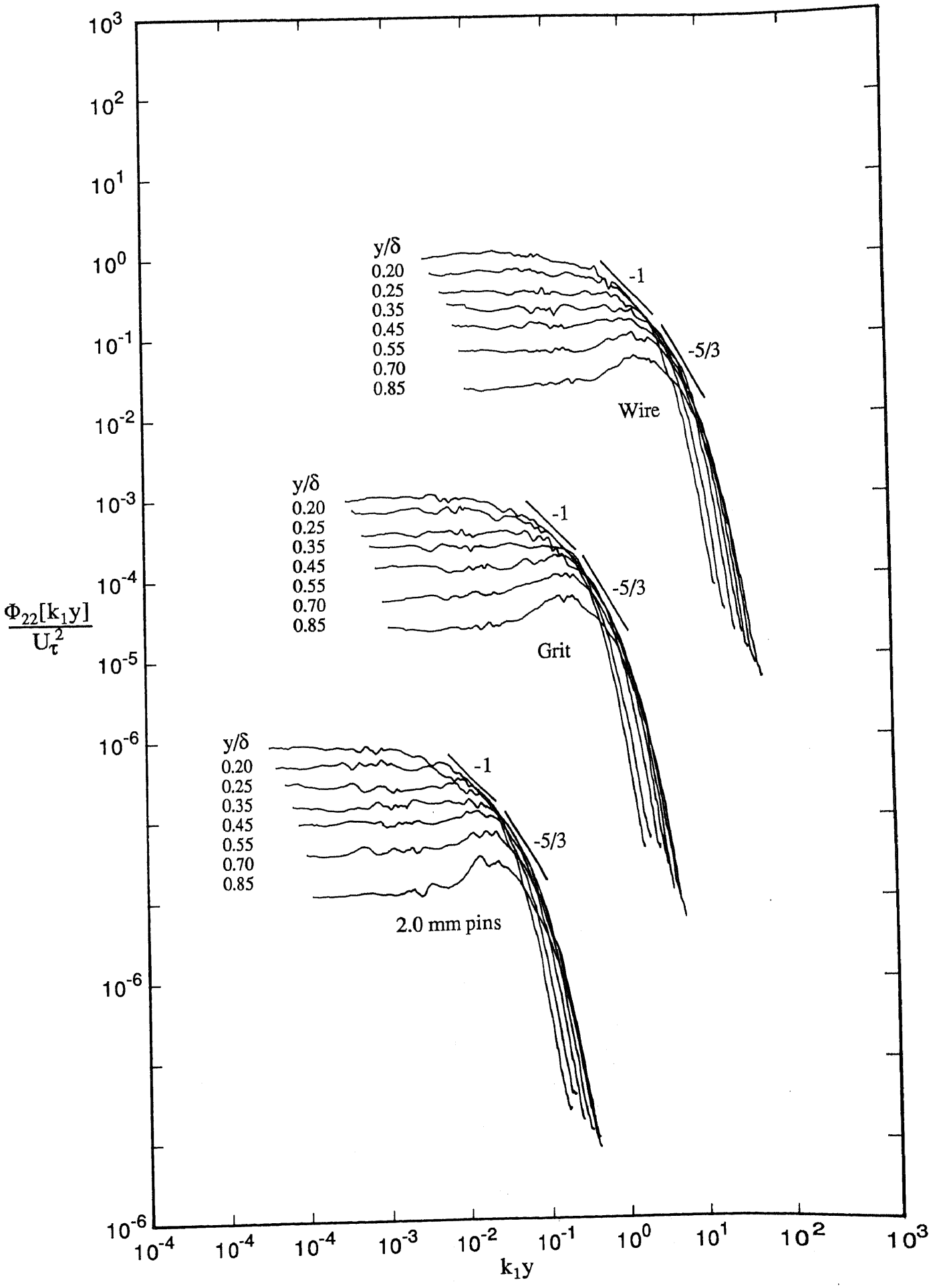

FIGURE 7.4. v spectra for three devices for design flows plotted using inner-flow scaling Note shift in abscissa and ordinate.

Wire, R_θ= 697; Grit, R_θ=706; 2.0 mm pins, R_θ=729.

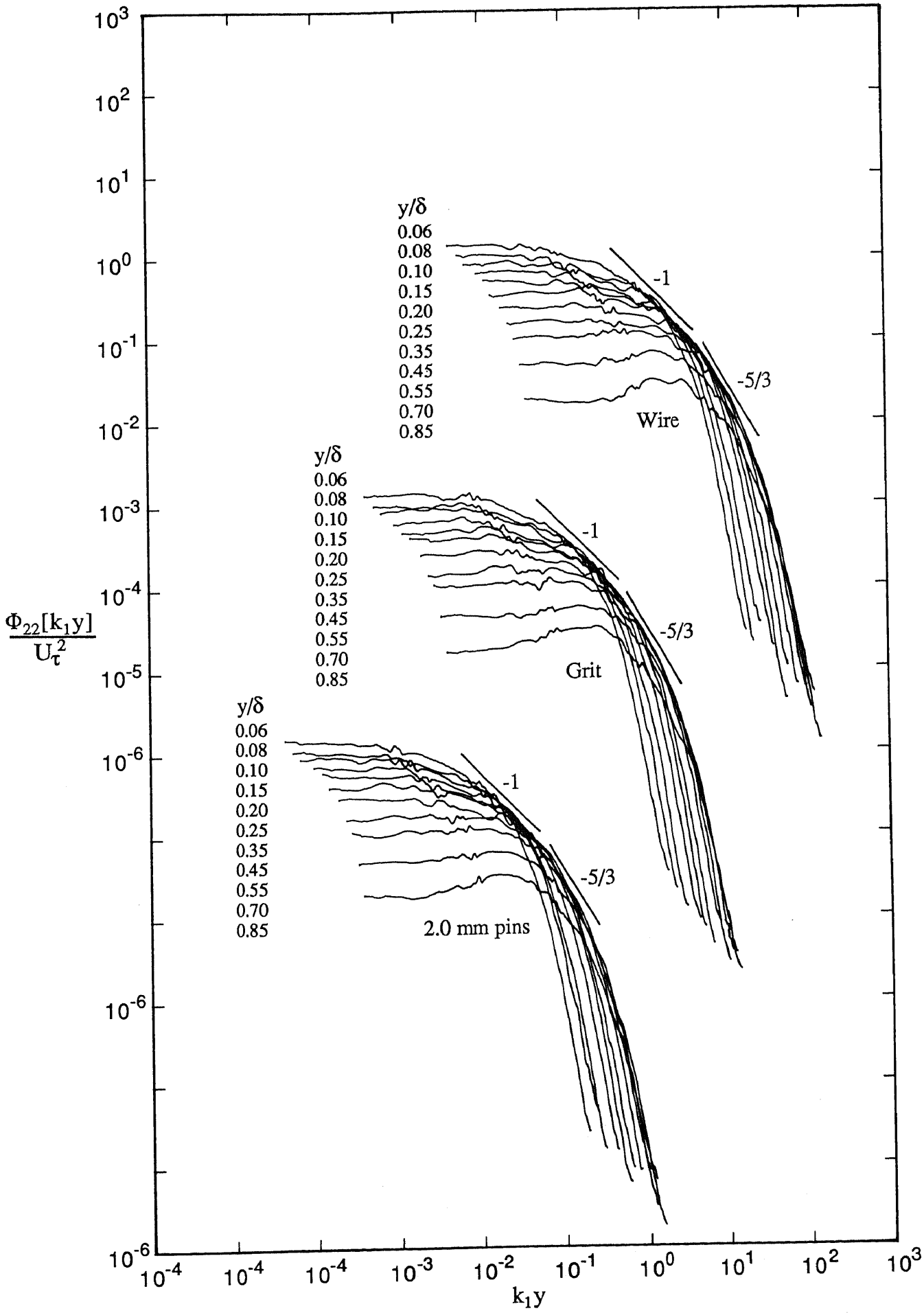

FIGURE 7.5. v spectra for three devices for design flows plotted using inner-flow scaling. Note shift in abscissa and ordinate.
Wire, R_θ=2788; Grit, R_θ=2730; 2.0 mm pins, R_θ=2889.

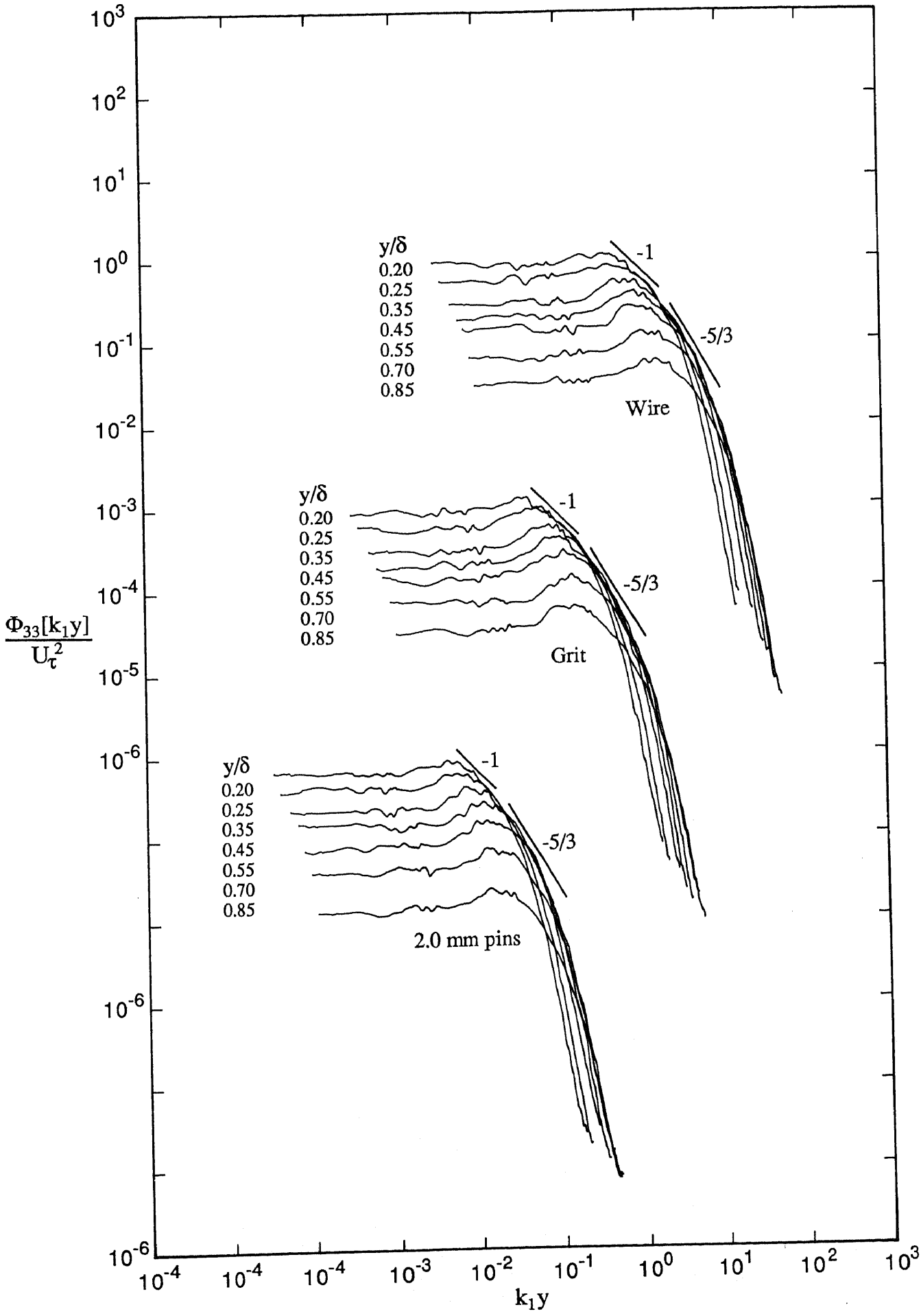

FIGURE 7.6. w spectra for three devices for design flows plotted using inner-flow scaling. Note shift in abscissa and ordinate.
Wire, R_θ= 697; Grit, R_θ=706; 2.0 mm pins, R_θ=729.

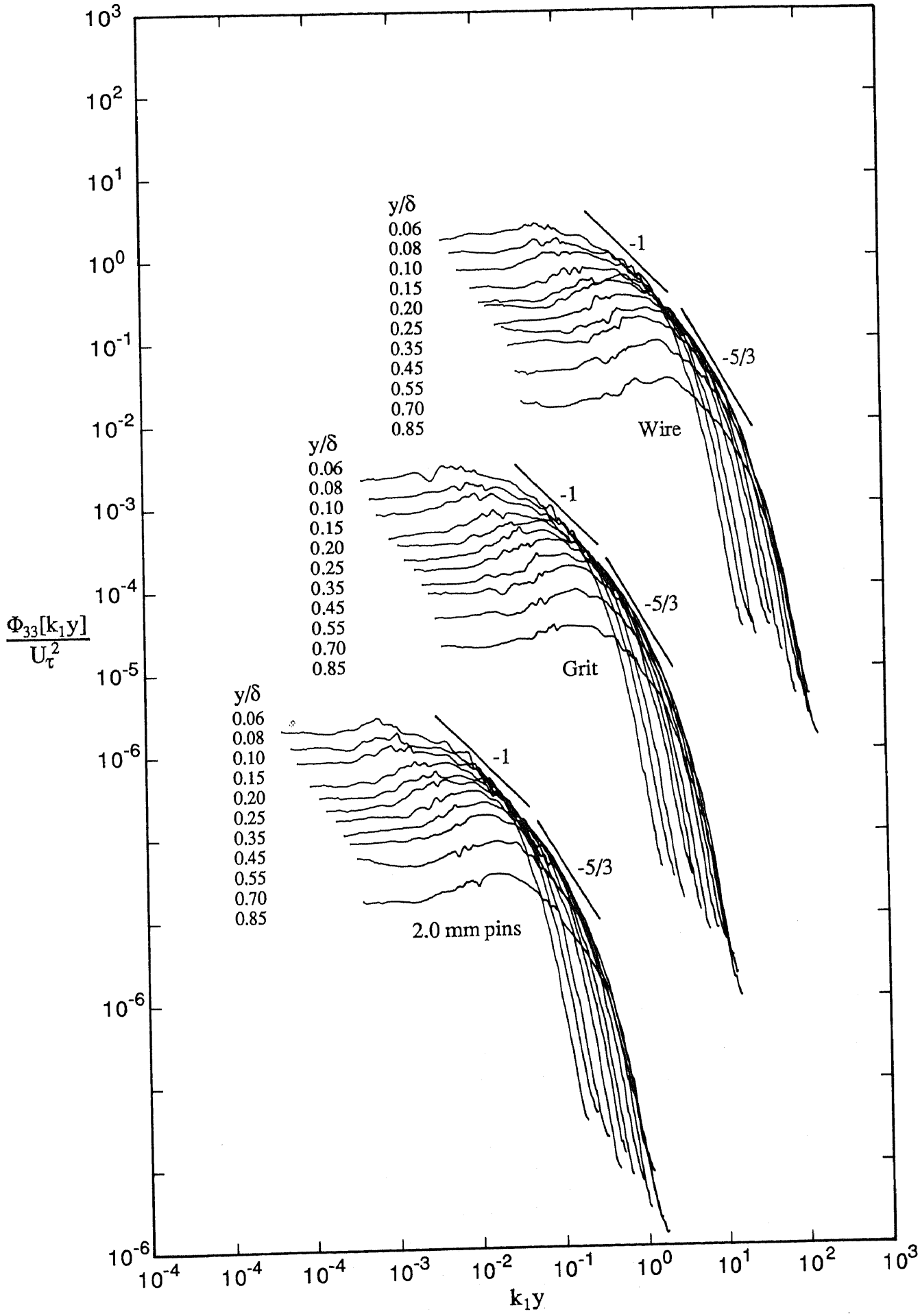

FIGURE 7.7. w spectra for three devices for design flows plotted using inner-flow scaling. Note shift in abscissa and ordinate.
Wire, R_θ=2788; Grit, R_θ=2730; 2.0 mm pins, R_θ=2889.

Initially the measured spectra for the turbulent wall region will be plotted to see if they follow the model of Perry, Henbest & Chong (1986). Since the theory was developed for high-Reynolds-number flows, it is unreasonable to expect it to apply to the current low-Reynolds-number spectra, but nevertheless it is worthwhile to perform checks to see if any agreement exists. After this has been done, the behaviour of spectra in the fully turbulent region will be examined. Once again the theory only applies to high-Reynolds-number flows and comments related to this fact, just given for the turbulent wall region, also apply here. The plots for the fully turbulent region will show whether or not the spectra for the different devices are dependent on R_θ, although spectral behaviour at low values of y/δ, which are outside the fully turbulent region, will not be considered. Finally, spectra will be presented to show the effects on the spectra of the type of device for a number of values of R_θ. In this case, the spectra will correspond to any location across the boundary layer, and will not be confined to the turbulent wall region or the fully turbulent region.

7.2.1 Spectra for the Turbulent Wall Region

As indicated above, Perry, Lim & Henbest (1987) defined the turbulent wall region as $yU_\tau/\nu > 100$ and $y/\Delta_E < 0.15$ when applied to smooth wall boundary-layer flows. An analysis of spectra from the current investigation indicated that for many of the families, the turbulent wall region defined using the above limits, but with Δ_E replaced by δ, the 99.5% boundary-layer thickness, just did not exist. When Spalart (1988) used the theory of Perry, Henbest & Chong (1986), he adopted a less conservative definition for the turbulent wall region, viz. $yU_\tau/\nu > 50$ and $y/\delta < 0.3$, and he indicated from a study of spectra that this definition is not unreasonable. Since difficulties were sometimes encountered in satisfying the limits given by Perry, Lim & Henbest, then for the current investigation it was also necessary to use a less restrictive definition for the turbulent wall region, although not as broad as that used by Spalart. For the current investigation, the turbulent wall region was defined as $yU_\tau/\nu > 60$ and $y/\delta < 0.15$. Thus, only the first of the limits given by Perry, Henbest & Chong was in fact altered. The value of the first limit was chosen so that spectra corresponding to most of the values of R_θ were now accommodated

in the definition of the turbulent region, without the limit being excessively generous.

u spectra for the turbulent wall region for a range of values of R_θ for the three devices for the design flows for outer-flow, inner-flow and Kolmogorov scaling are shown in figures 7.8, 7.9 and 7.10 respectively. Corresponding v spectra are shown in figure 7.11 for inner-flow scaling but no such v spectra for outer-flow scaling are given since, according to the model, no regions of collapse are expected in this case. Corresponding w spectra are shown in figures 7.12 and 7.13 for outer-flow and inner-flow scaling respectively.

Each of these plots will now be discussed in turn to indicate how the spectra fit the model, i.e. whether or not spectra collapse in the required regions and whether or not they peel off as expected. As a visual aid, lines of slope -1 and/or -5/3, corresponding to regions of collapse suggested by the model have been drawn on figures 7.8 to 7.13. The spectra appearing in these figures correspond to nominal values of R_θ of 1020, 1544, 2175 and 2810. No spectra for $R_\theta \approx 713$ are included, since for this value of R_θ the range chosen for the turbulent wall region did not exist.

Considering firstly u spectra plotted using outer-flow scaling, as shown in figure 7.8, it can be seen that for the three devices, the spectra collapse reasonably well onto an inverse power law region as anticipated by the model. Also, at low wavenumbers, the collapse of the spectra is quite good, which is also in accord with the model. According to Perry, Henbest & Chong, any lack of collapse of the spectra at low wavenumbers can possibly be explained in terms of the invalid use of Taylor's (1938) hypothesis of frozen turbulence, which utilizes one single convection velocity for all eddy scales at a fixed point in the flow. They state that it is suspected that the larger-scale coherent attached eddies are convected downstream at a faster rate than the smaller-scale coherent eddies. The other question that must be addressed is whether or not the high wavenumber ends of the spectra peel off from the -1 line in order of decreasing values of y/δ for increasing values of $k_1\delta$, as anticipated by the model. For each of the three devices, a careful analysis of the spectra indicated that this was in fact the case for spectra corresponding to each of the values of R_θ, but for all spectra considered collectively, this behaviour was not consistent.

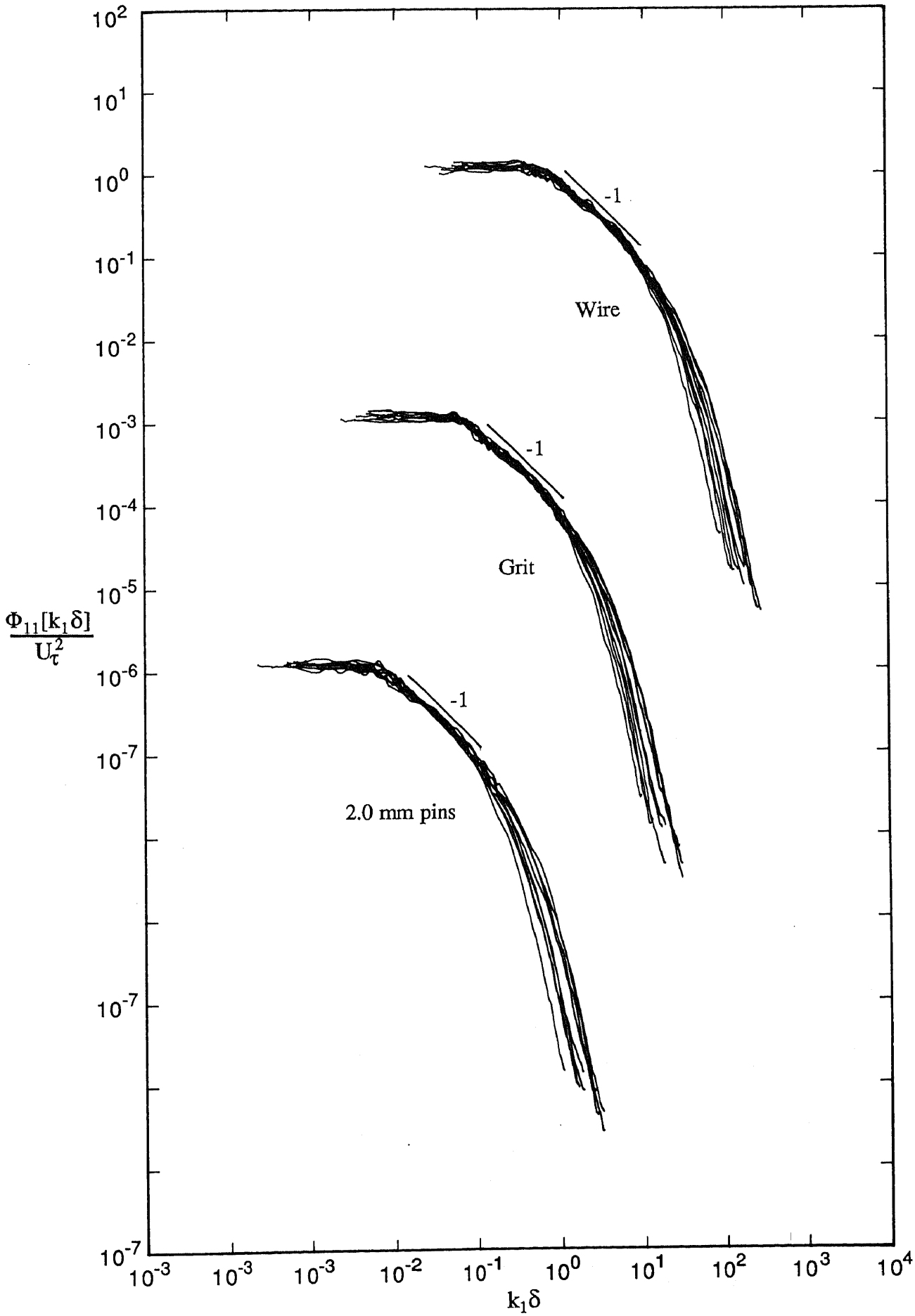

FIGURE 7.8. u spectra for the turbulent wall region for nominal values of R_θ of 1020, 1544, 2175 and 2810 for three devices for design flows plotted using outer-flow scaling. Note shift in abscissa and ordinate.

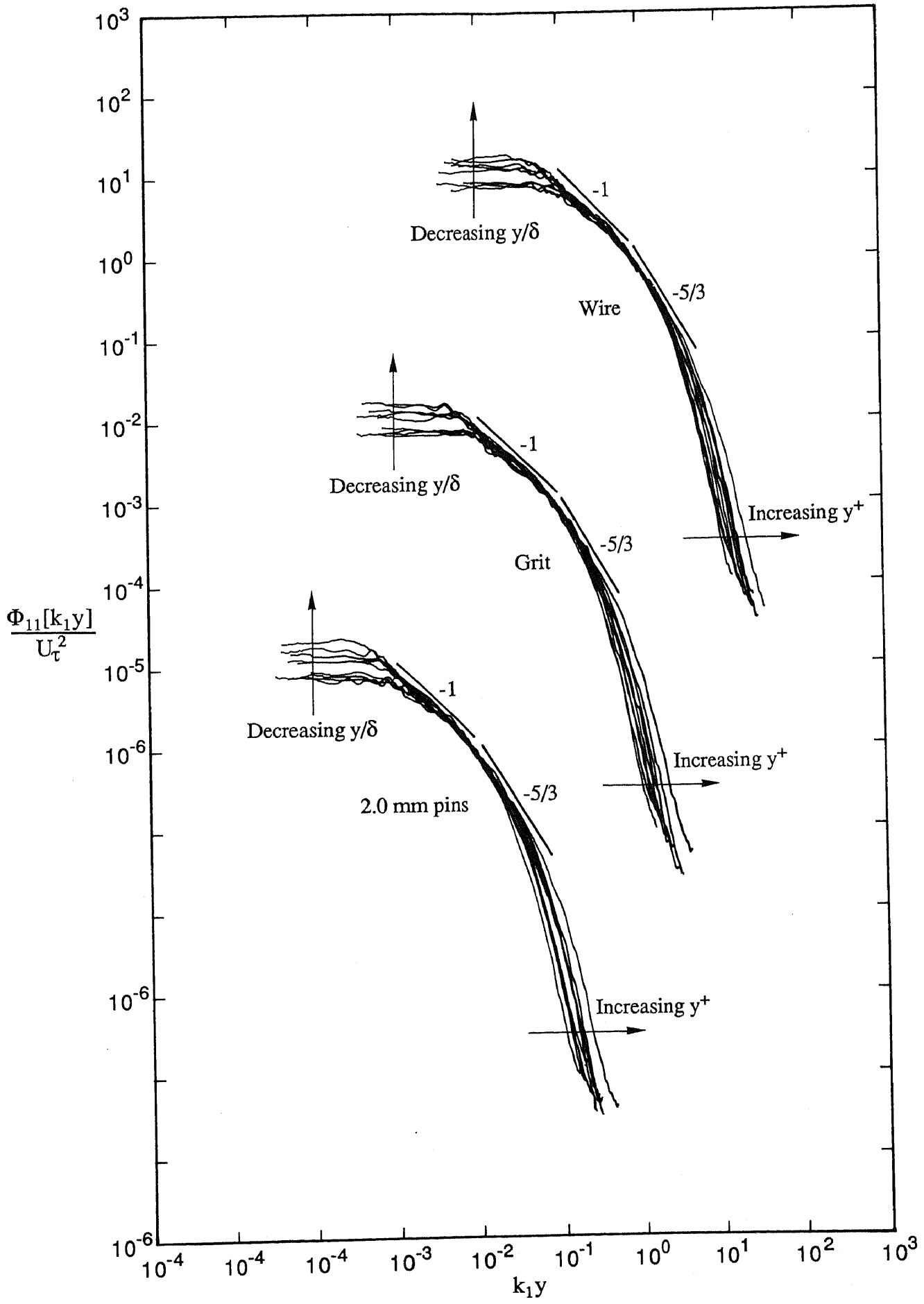

FIGURE 7.9. u spectra for the turbulent wall region for nominal values of R_θ of 1020, 1544, 2175 and 2810 for three devices for design flows plotted using inner-flow scaling. Note shift in abscissa and ordinate.

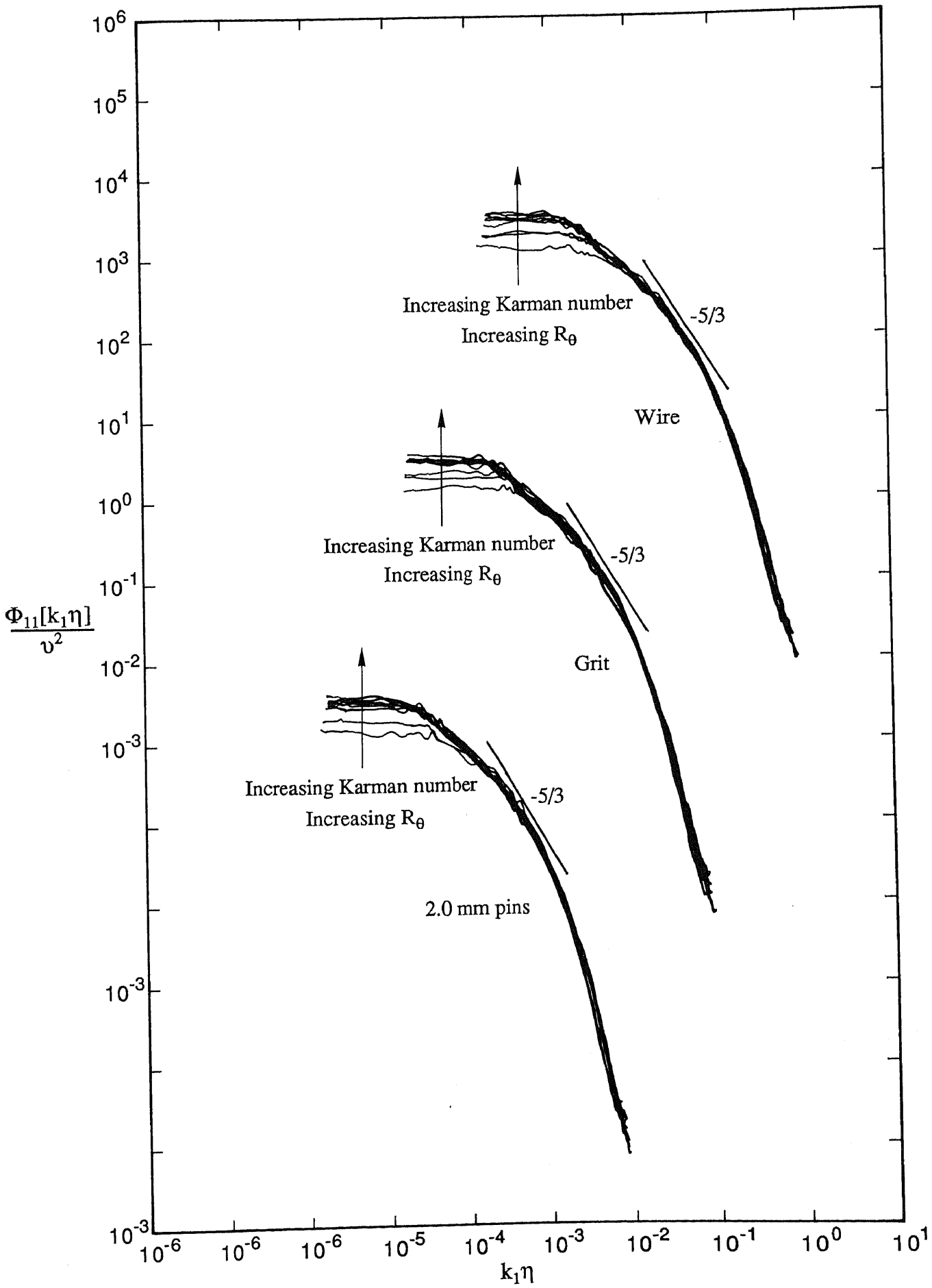

FIGURE 7.10. u spectra for the turbulent wall region for nominal values of R_θ of 1020, 1544, 2175 and 2810 for three devices for design flows plotted using Kolmogorov scaling. Note shift in abscissa and ordinate.

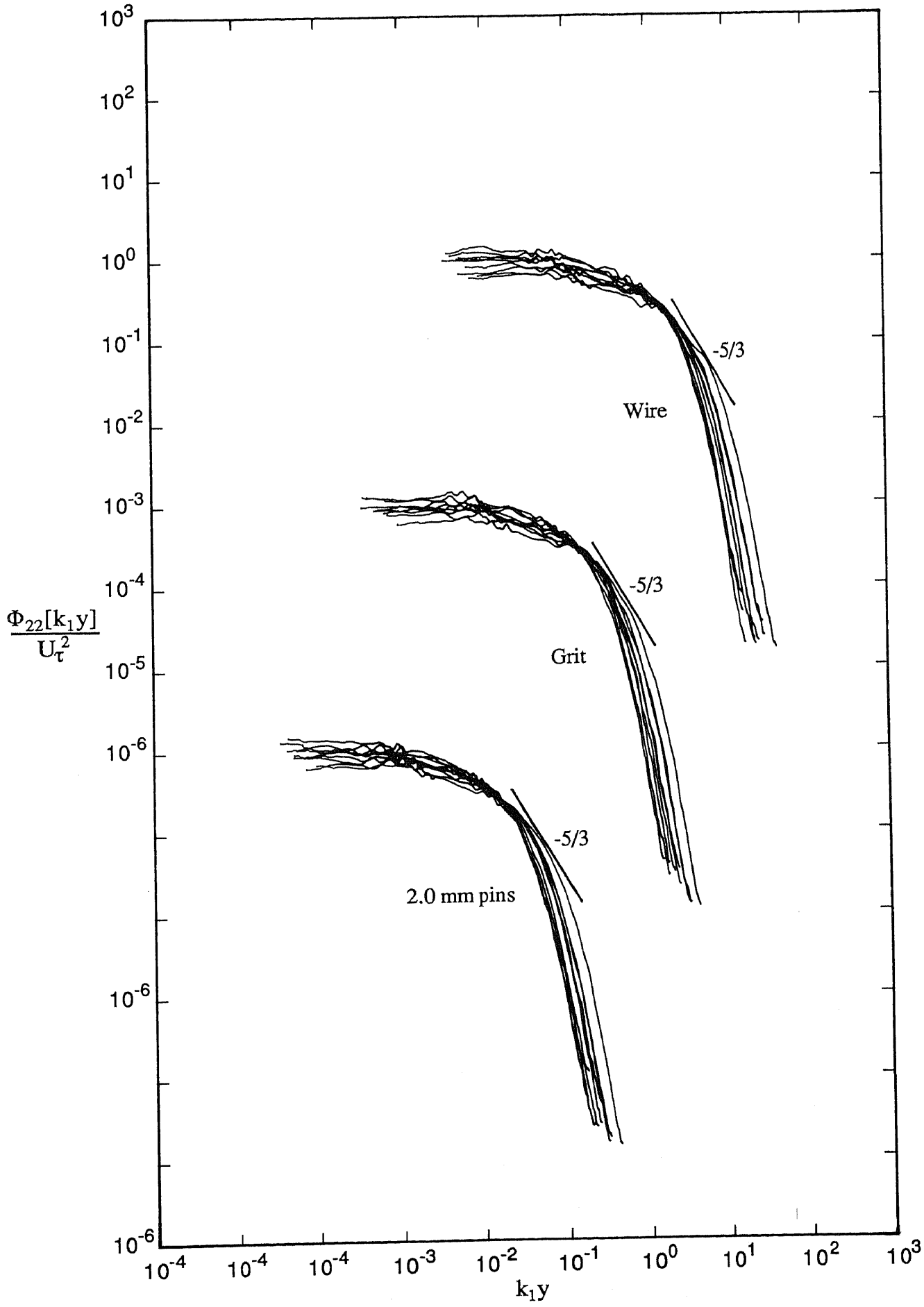

FIGURE 7.11. v spectra for the turbulent wall region for nominal values of R_θ of 1020, 1544, 2175 and 2810 for three devices for design flows plotted using inner-flow scaling. Note shift in abscissa and ordinate.

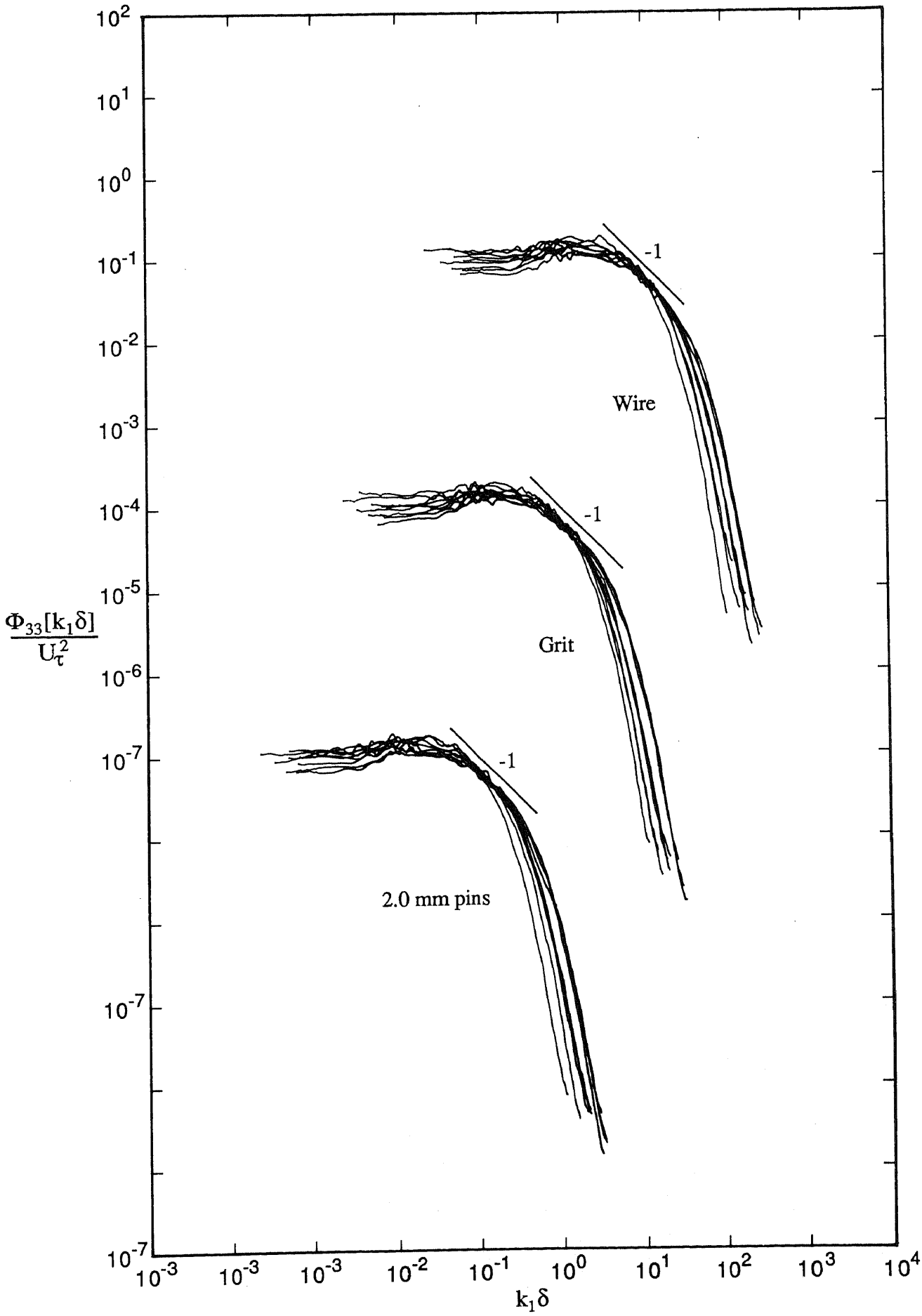

FIGURE 7.12. w spectra for the turbulent wall region for nominal values of R_θ of 1020, 1544, 2175 and 2810 for three devices for design flows plotted using outer-flow scaling. Note shift in abscissa and ordinate.

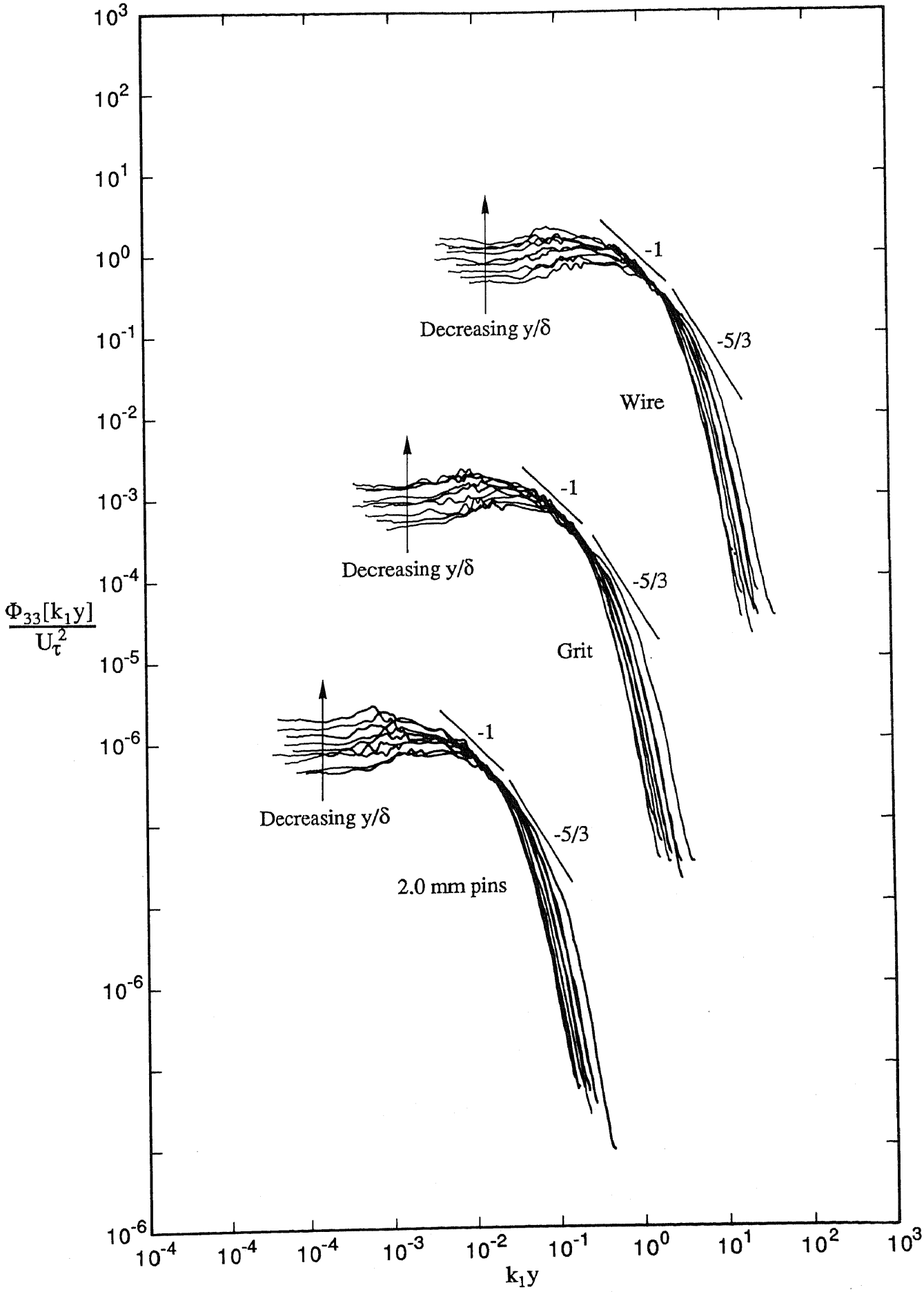

FIGURE 7.13. w spectra for the turbulent wall region for nominal values of R_θ of 1020, 1544, 2175 and 2810 for three devices for design flows plotted using inner-flow scaling. Note shift in abscissa and ordinate.

The u spectra are shown replotted in figure 7.9 using inner-flow scaling, and for each of the devices collapse onto an inverse power law region and a -5/3 inertial subrange is evident, as anticipated by the model. For each of the devices, the low wavenumber ends of the spectra peel off from the -1 line in order of decreasing y/δ for decreasing k_1y, as predicted. Considering the order in which the spectra peel off from the -5/3 line at the high wavenumber end, it is difficult to talk in precise terms because of the closeness of the spectra. However, a careful analysis of the spectra indicated that, with minor exceptions, the spectra peeled off in order of increasing yU_τ/ν for increasing k_1y , as predicted.

The u spectra are shown replotted in figure 7.10 using Kolmogorov scaling. For each of the three devices, the spectra collapse well at high wavenumbers, as expected with this type of scaling. In each case a short region of collapse onto a line of slope -5/3 can be discerned. The spectra at the low wavenumber ends were found to peel off the -5/3 line in order of increasing Karman number, or alternatively increasing R_θ, for decreasing $k_1\eta$, and thus it is apparent that for higher values of R_θ, the extent of the region of collapse onto the line of slope -5/3 would most likely be greater, as was found by Perry, Lim & Henbest (1985) for their flows at higher values of R_θ.

Considering now the v spectra, these are shown in figure 7.11 plotted using inner-flow scaling. The theory anticipates collapse of the spectra at the low wavenumber ends and also collapse onto a line of slope -5/3 in the inertial subrange and for the spectra shown this behaviour clearly does not apply. The v spectra behave in a similar manner to those obtained by Perry, Lim & Henbest (1987) and their explanation of spectral behaviour is possibly also relevant to the current results. They indicate that although the spectra do not follow the model, there are two encouraging features of the plotted spectra. Firstly there is no inverse power law region and secondly the peeling off of the spectra at the low wavenumber ends does not depend on y/Δ_E. They state that the lack of collapse at low wavenumbers cannot be blamed on the spread in convection velocities as only eddies of scale of order y contribute significantly to $\overline{v^2}$ at y. They indicate that the lack of collapse at low wavenumbers is thought to be due to a cross contamination problem, where the matched crossed-wire signals are being influenced by the velocity component normal to the plane of

the wires. They further indicate that the inertial subrange is short because of a spatial-resolution problem of the crossed hot-wire probe.

Considering now w spectra, these are shown plotted in figure 7.12 using outer-flow scaling. According to the model, the behaviour of these spectra should be similar to the behaviour of the corresponding u spectra shown in figure 7.8. For the w spectra, collapse onto an inverse power law region is evident for all devices, but in each case the extent of the collapse is shorter than for the u spectra shown in figure 7.8. The w spectra clearly do not collapse at low wavenumbers, as they should according to the model, and once again this can possibly be explained by the invalid use of Taylor's hypothesis. The spread of the w spectra at low wavenumbers is greater than the spread of the corresponding u spectra shown in figure 7.8, and this behaviour was also observed by Perry, Lim & Henbest. The behaviour of the w spectra at the high wavenumber ends was similar to that for the u spectra shown in figure 7.8.

Finally, w spectra are shown plotted in figure 7.13 using inner-flow scaling and the behaviour of these spectra is expected to be similar to the u spectra shown in figure 7.9. On both figures, the spectra for each of the devices can be seen to collapse onto an inverse power law region, but in each case the extent of this region is less for the w spectra than for the corresponding u spectra, as was found by Perry, Lim & Henbest. Collapse of the w spectra in the inertial subrange is expected, but if collapse does occur, then it is only to a small extent, unlike for the u spectra. Perry, Lim & Henbest found that the inertial subrange was shorter for their w spectra than for their u spectra, and they indicated that this is probably caused by premature peel-off of the spectra caused by a spatial resolution problem, an explanation which could possibly also apply here. With minor exceptions, the low wavenumber ends of the spectra peeled off in order of decreasing y/δ for decreasing k_1y, as predicted.

To complete this section on the turbulent wall region, it is appropriate to comment on how the current u, v and w low-Reynolds-number spectra for this region, plotted using different types of scaling, matched the model proposed by Perry, Henbest & Chong (1986) for high-Reynolds-number flows. It is encouraging that the low-Reynolds-number spectra, corresponding to values of R_θ as low as about 1020, generally showed good agreement with the model, and

where agreement did not occur, at least the spectra showed similar behaviour to those obtained by Perry, Lim & Henbest (1987) in their flat-plate boundary-layer study. The good agreement occurred despite the fact that the limits of the turbulent wall region had to be relaxed slightly to accommodate the low-Reynolds-number spectra.

7.2.2 Spectra for the Fully Turbulent Region

Equation (7.4) predicts that for the fully turbulent region, high-Reynolds-number spectra should collapse in the low to moderate wavenumber energy containing range at each given value of y/δ and if the Reynolds number of the flow is sufficiently large, the spectra for all values of y/δ should collapse onto an inertial subrange at high wavenumbers. It is thus of interest to see whether or not the current low-Reynolds-number spectra follow this law. For each of the devices, any deviations from the law will indicate the effects on spectral behaviour of variations in R_θ.

u spectra for the three devices, corresponding to five values of y/δ and five nominal values of R_θ, are plotted using inner-flow scaling as shown in figure 7.14. For the fully turbulent region, only inner-flow scaling will be used. For each of the devices, the closeness of the spectra at high wavenumbers makes it difficult to interpret spectral behaviour in this region and so to facilitate interpretation, at least for the wire, the spectra corresponding to each of the five values of y/δ for the wire have been replotted on their own set of axes as shown in figure 7.15. In a similar manner, corresponding v spectra are shown in figures 7.16 and 7.17 and corresponding w spectra in figures 7.18 and 7.19. Selected spectra in figures 7.14, 7.16 and 7.18 have been labeled with values of R_θ, for use in the discussion below.

Considering firstly u spectra shown in figure 7.14, it is apparent that at low wavenumbers the spectra within a given set generally show reasonable collapse although in some cases appreciable spread occurs. Perry, Henbest & Chong also found slight spread at fixed values of y/Δ_E in their corresponding plot, and they indicated that this is thought to be due to a change in the fractional spread of the convection velocities of the eddies as the Reynolds number changes. This explanation could possibly also apply to the current spectra and in addition another reason for the spread is the fact that the values of $\overline{u^2}/U_\tau^2$, used when

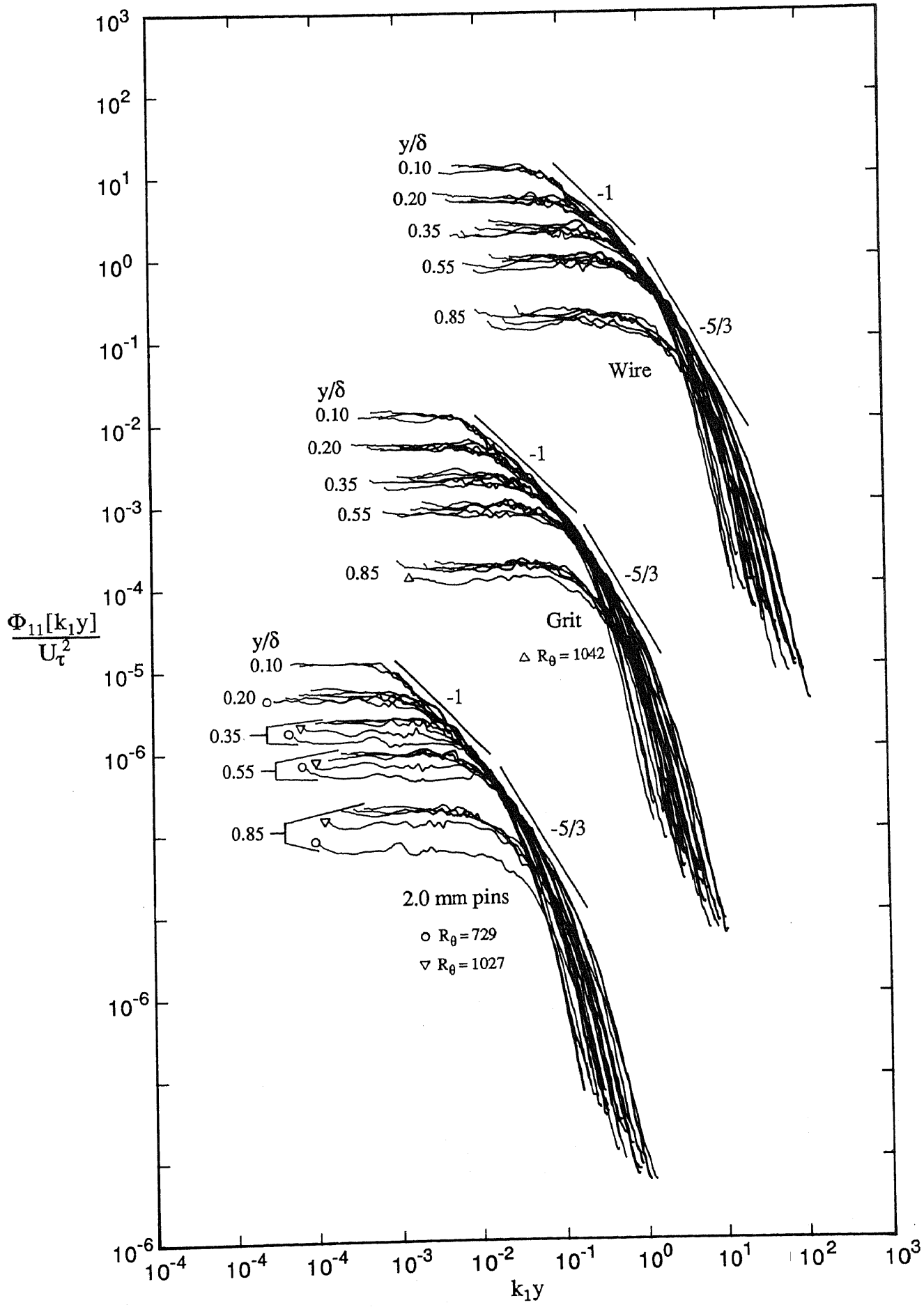

FIGURE 7.14. u spectra for fully turbulent region for nominal values of R_θ of 713, 1020, 1544, 2175 and 2810 for three devices for design flows for various values of y/δ plotted using inner-flow scaling. Note shift in abscissa and ordinate.

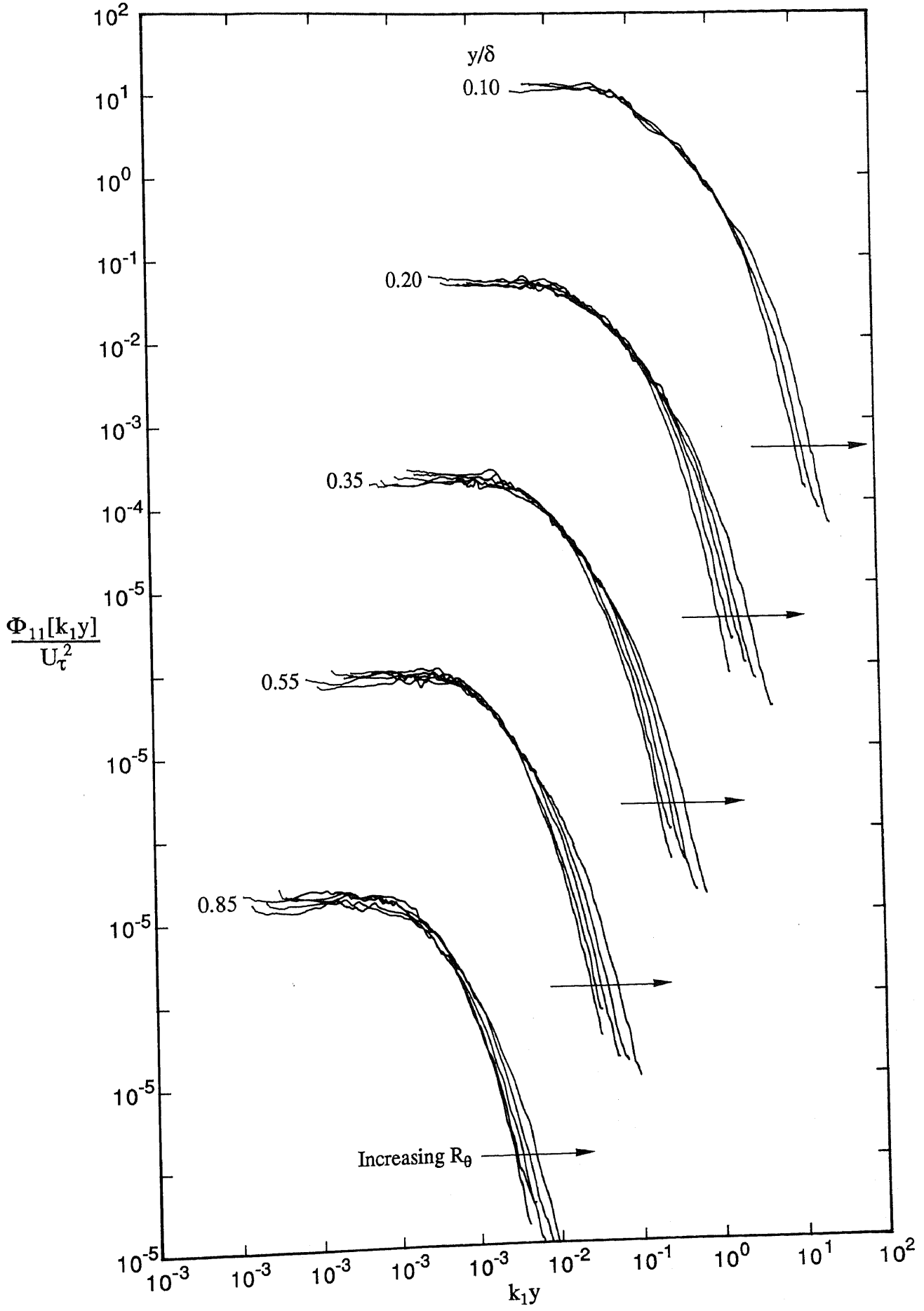

FIGURE 7.15. u spectra for fully turbulent region for values of R_θ of 697, 1003, 1568, 2226 and 2788 for wire for design flow for various values of y/δ plotted using inner-flow scaling. Note shift in abscissa and ordinate.

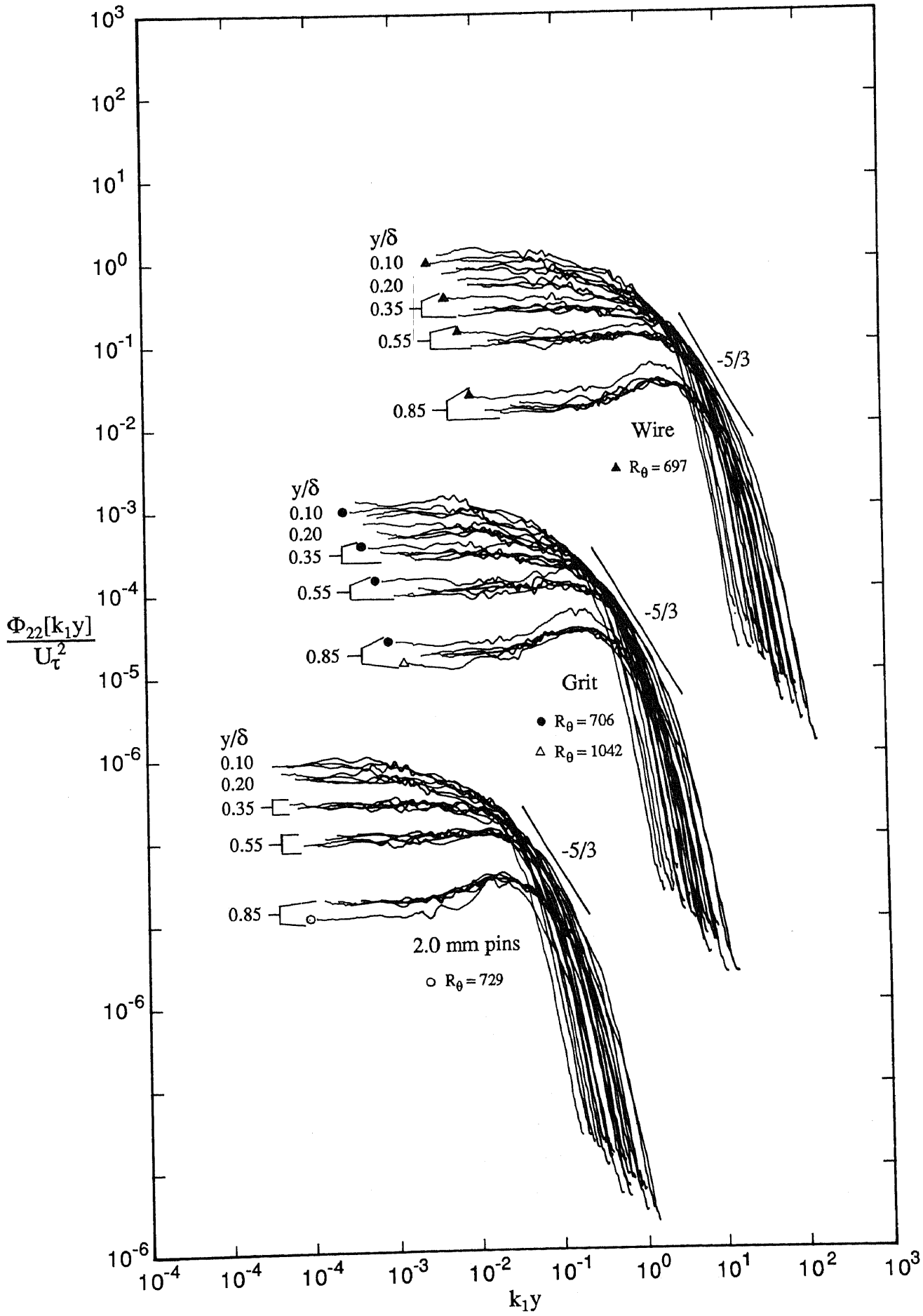

FIGURE 7.16. v spectra for fully turbulent region for nominal values of R_θ of 713, 1020, 1544, 2175 and 2810 for three devices for design flows for various values of y/δ plotted using inner-flow scaling. Note shift in abscissa and ordinate.

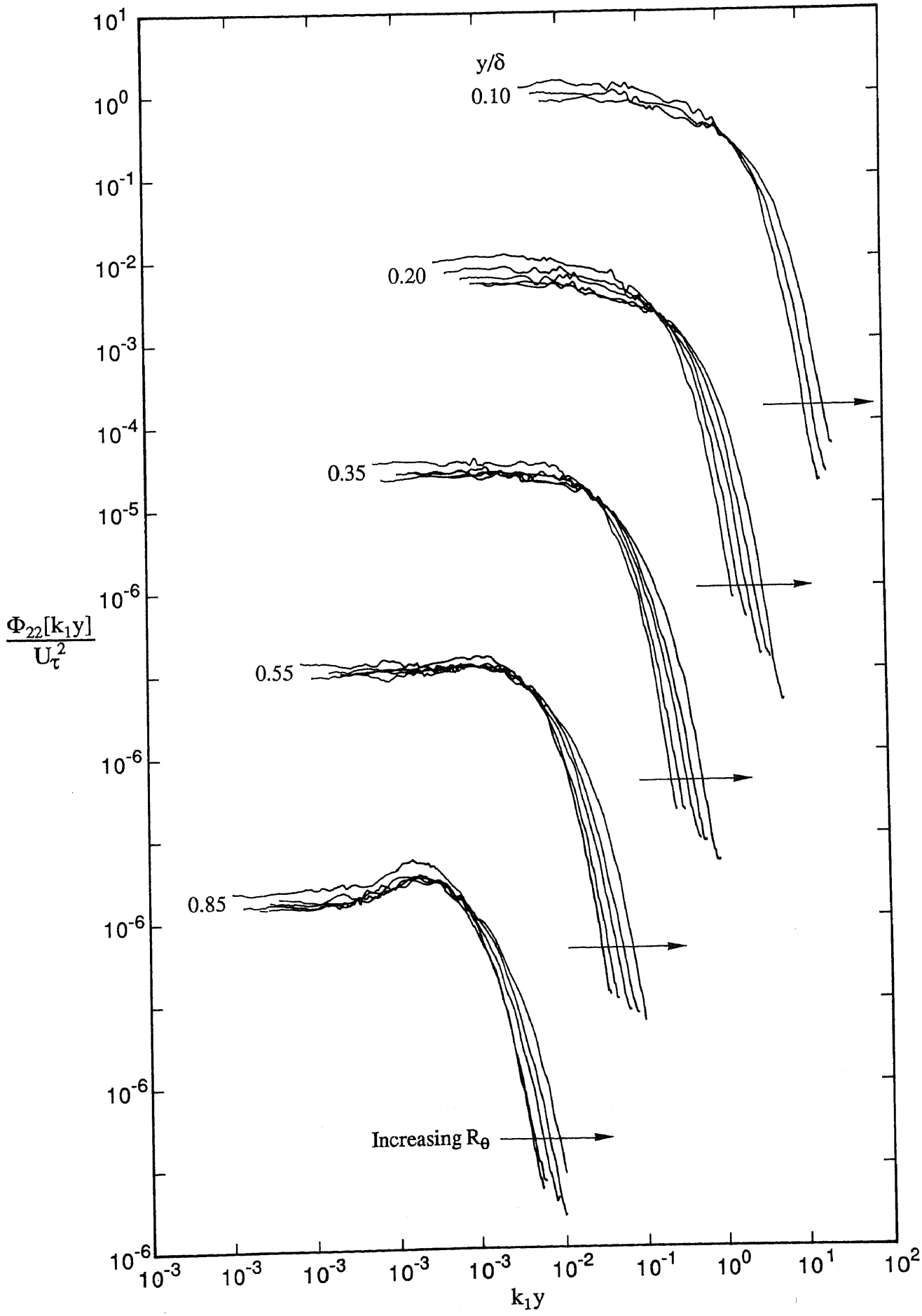

FIGURE 7.17. v spectra for fully turbulent region for values of R_θ of 697, 1003, 1568, 2226 and 2788 for wire for design flow for various values of y/δ plotted using inner-flow scaling. Note shift in abscissa and ordinate.

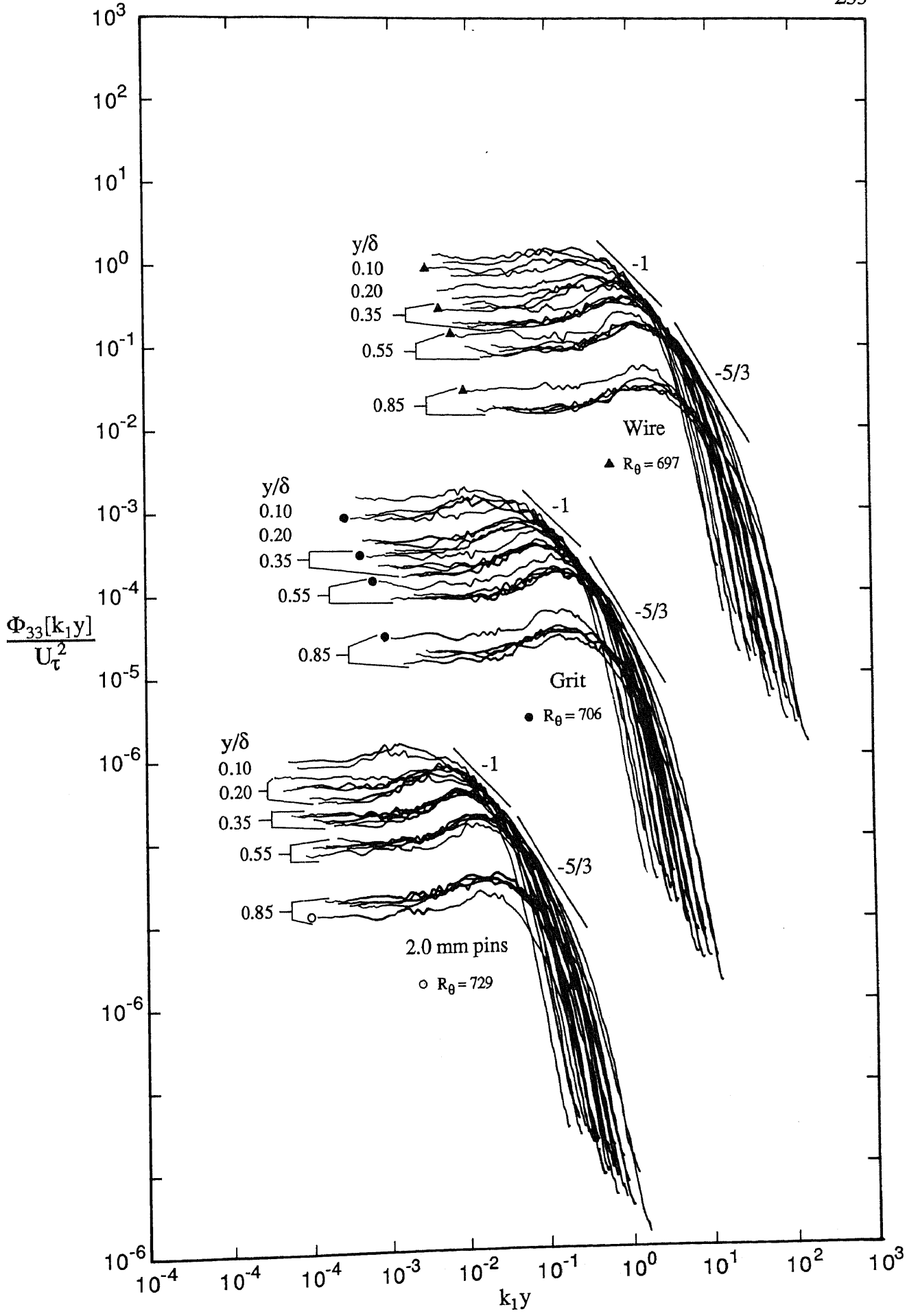

FIGURE 7.18. w spectra for fully turbulent region for nominal values of R_θ of 713, 1020, 1544, 2175 and 2810 for three devices for design flows for various values of y/δ plotted using inner-flow scaling. Note shift in abscissa and ordinate.

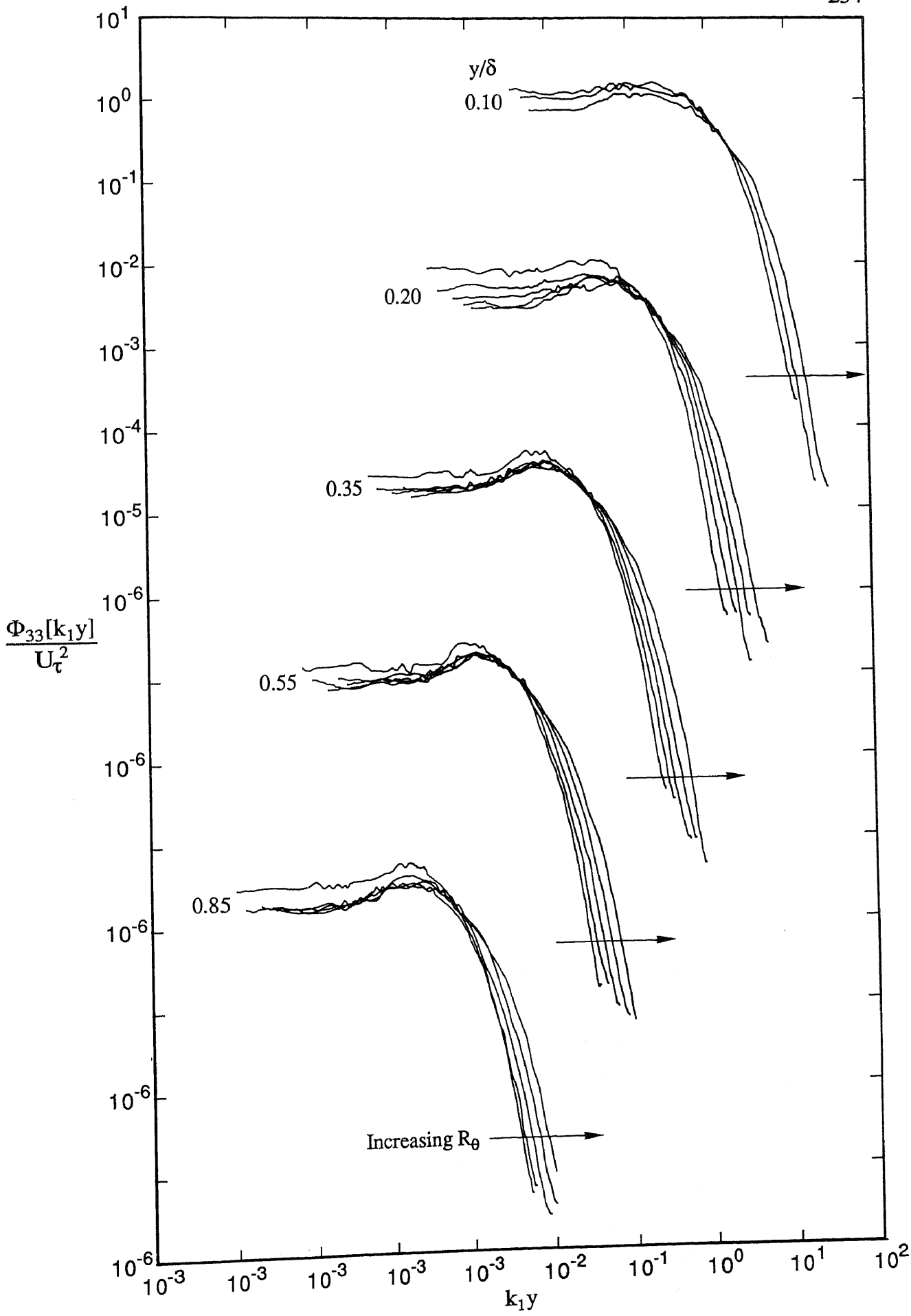

FIGURE 7.19. w spectra for fully turbulent region for values of R_θ of 697, 1003, 1568, 2226 and 2788 for wire for design flow for various values of y/δ plotted using inner-flow scaling. Note shift in abscissa and ordinate.

plotting the spectra, at given values of y/δ, are Reynolds number dependent, as shown in figure 6.6. An analysis of the different sets of spectra shown in figure 7.14 indicates that where spectra at low wavenumbers deviate appreciably from others within a given set, then these spectra correspond to nominal values of R_θ of 713 or 1020. Thus any deviations from predictions are primarily confined to these two nominal values of R_θ. From figure 7.15 for the wire it can be seen that at high wavenumbers, the spectra do not collapse for any of the values of y/δ, but instead peel off in order of increasing R_θ as k_1y increases, a Reynolds number effect also observed by Perry, Henbest & Chong.

The v spectra shown in figures 7.16 and 7.17 and the w spectra shown in figures 7.18 and 7.19 exhibit behaviour similar to the corresponding u spectra, except that the bands of the v and w spectra corresponding to the lower values of y/δ are generally not as clearly defined. The bands corresponding to y/δ = 0.1 and 0.2 generally overlap and when this occurs these bands have not been cleary indicated on figures 7.16 and 17.18 since it would have been too confusing. However, for the wire, these bands have been separated for the v and w spectra in figures 7.17 and 7.19 respectively.

It is apparent from the above that although the low-Reynolds-number spectra of the current investigation tend to follow equation (7.4), appreciable deviations sometimes occur as a consequence of variations in R_θ, as described above.

7.2.3 Effects of Device on Spectral Behaviour

Although spectra for the different devices for the design flows have been presented in a variety of different ways so far in this chapter, there are no spectral plots that directly compare corresponding spectra for different devices at different values of R_θ. This will now be done. u spectra for the three devices for different values of y/δ for nominal values of R_θ of 713, 1020 and 2810 are shown plotted in figure 7.20 using inner-flow scaling. Corresponding v spectra are shown in figure 7.21 and corresponding w spectra in figure 7.22. v and w spectra were not measured for values of y/δ as small as for the u spectra. The scaling of Perry, Henbest & Chong has been used for plotting spectra in figures 7.20 to 7.22, even though no comparison is to be made with their model. This will also apply to subsequent spectral plots in this chapter.

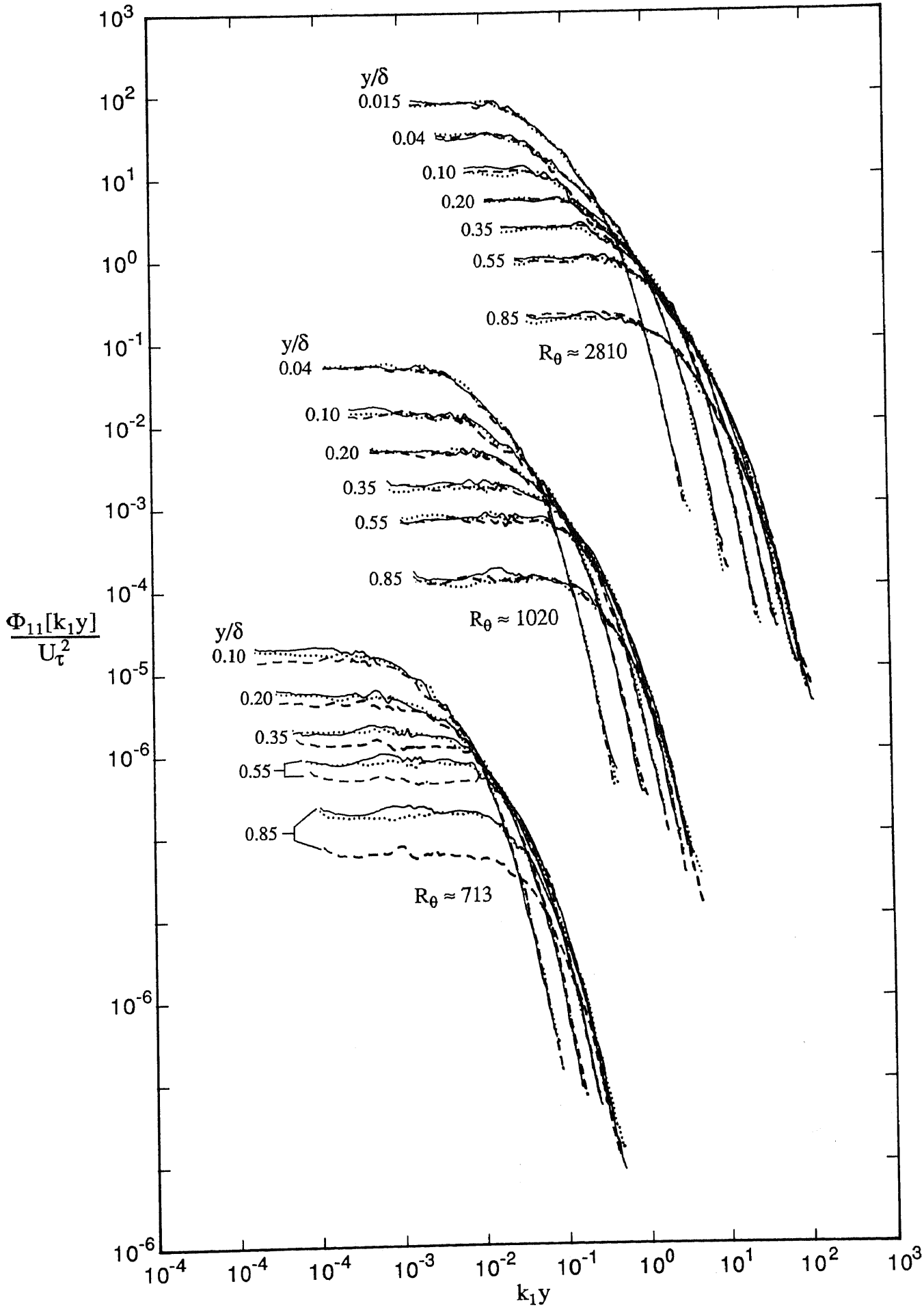

FIGURE 7.20. u spectra for design flows for various values of y/δ plotted using inner-flow scaling showing effects of device for three nominal values of R_θ. Note shift in abscissa and ordinate.

——— wire: ·····, grit; — — —, 2.0 mm pins.

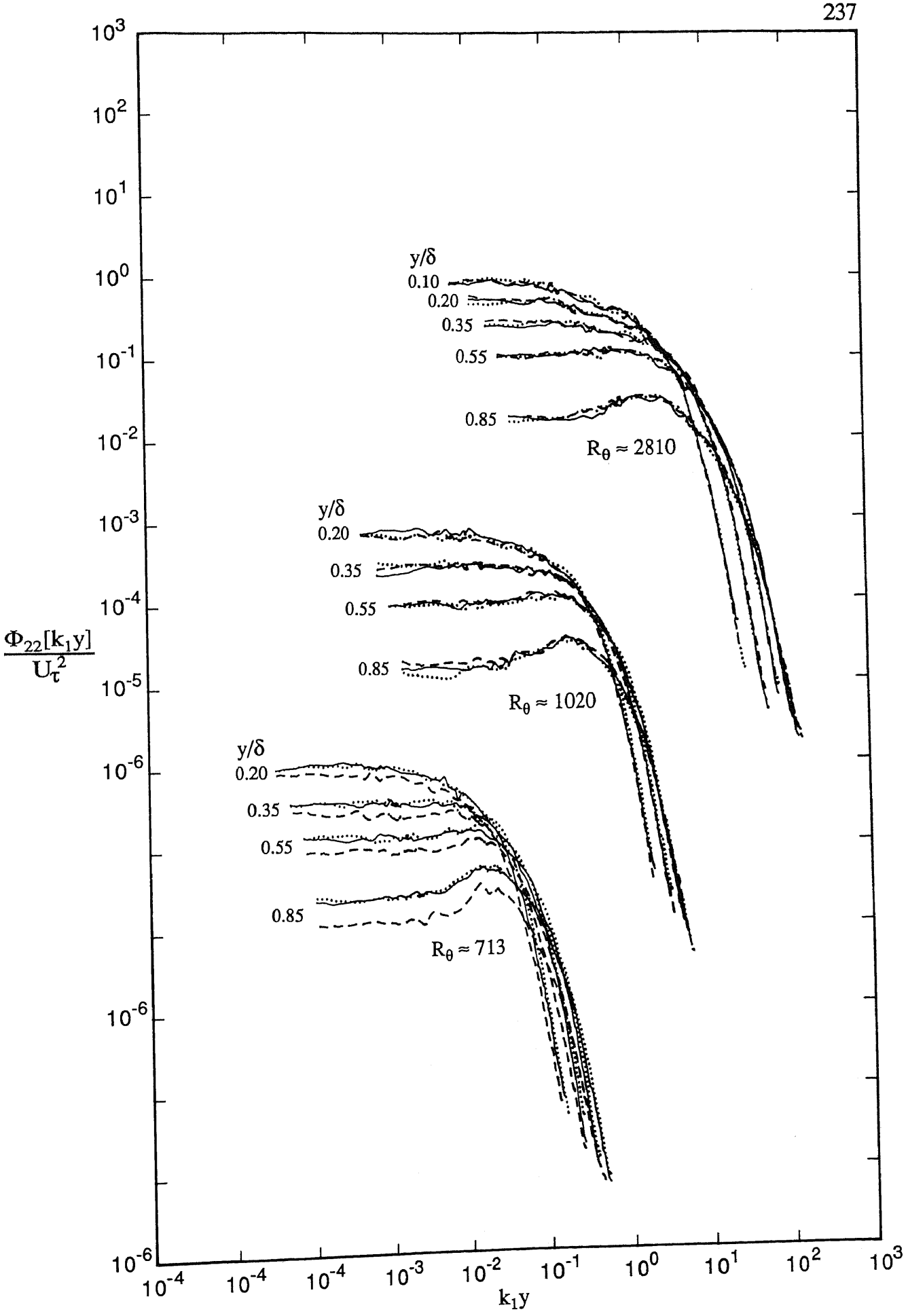

FIGURE 7.21. v spectra for design flows for various values of y/δ plotted using inner-flow scaling showing effects of device for three nominal values of R_θ. Note shift in abscissa and ordinate.

—— wire; ·····, grit; – – –, 2.0 mm pins.

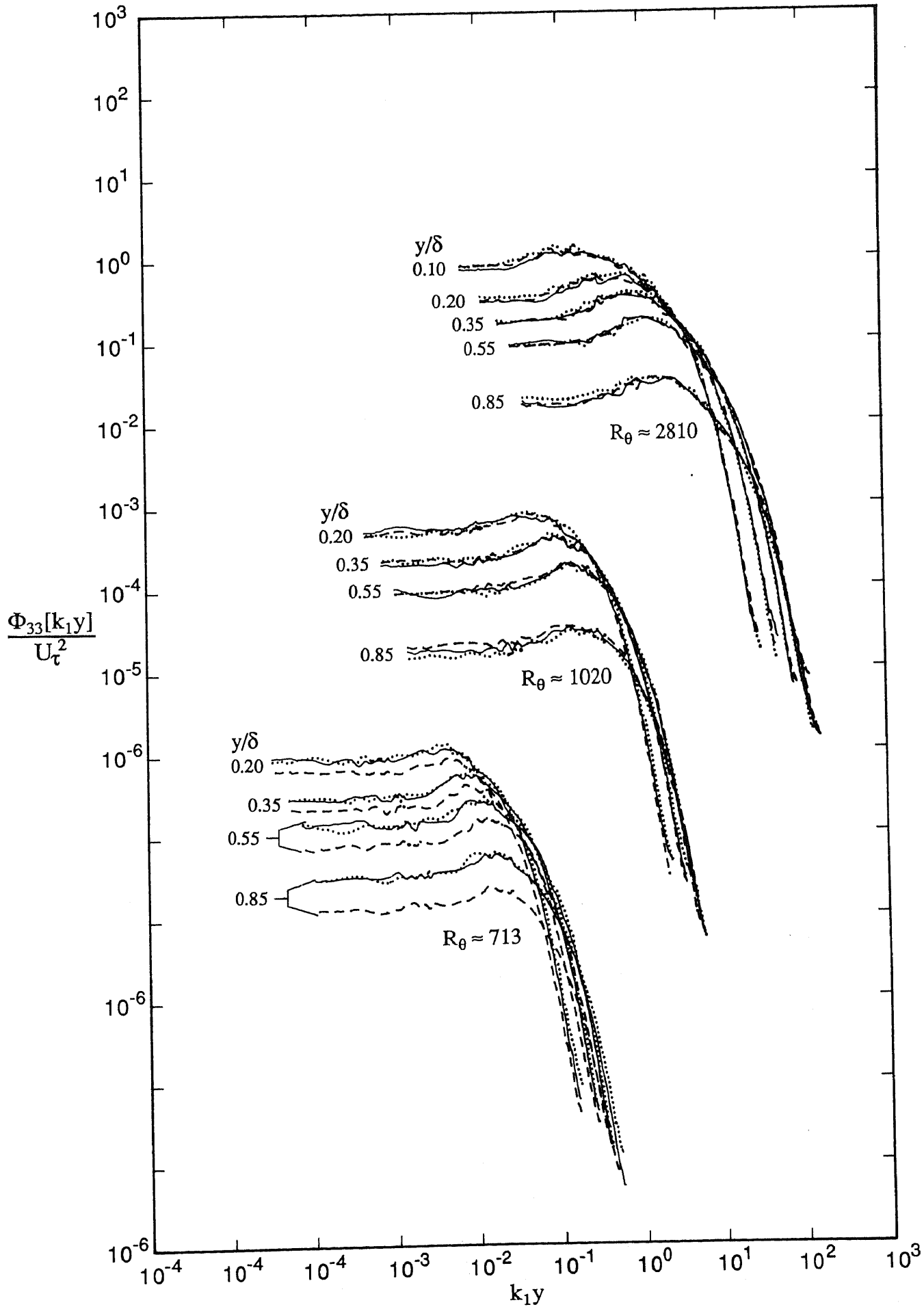

FIGURE 7.22. w spectra for design flows for various values of y/δ plotted using inner-flow scaling showing effects of device for three nominal values of R_θ. Note shift in abscissa and ordinate.

——— wire; ·····, grit; — — —, 2.0 mm pins.

Figures 7.20, 7.21 and 7.22 for the u, v and w spectra respectively, will be discussed collectively. As can be seen from these figures, spectra have only been presented for nominal values of R_θ of 713, 1020 and 2810, i.e. the lowest, the next lowest and the highest nominal value of R_θ. It is immediately apparent that the type of device used can have an appreciable effect upon spectra for $R_\theta \approx$ 713, but for $R_\theta \approx$ 1020 and above, the type of device used does not have a significant effect on the spectra, indicating that, for the design flows, the previous history of the flow is now of little consequence as far as spectral behaviour is concerned. For $R_\theta \approx 713$, the spectra for the wire and the grit agree quite well, but the spectra for the pins differ from these. For the pins, differences can be seen to occur throughout the layer, but they are most pronounced at the higher values of y/δ. At each of the values of y/δ, the differences occur primarily over the low to moderate wavenumber range. The above behaviour is consistent with plots of $\overline{u^2}/U_\tau^2$, $\overline{v^2}/U_\tau^2$ and $\overline{w^2}/U_\tau^2$, versus y/δ, that indicate the effects of device on the Reynolds normal stresses at different nominal values of R_θ. These plots are not given in this thesis, but they have the same general form as corresponding plots normalized by U_e^2, which are shown in figures 6.5, 6.8 and 6.11 respectively.

To help obtain a better understanding of how the spectra are affected by the type of device used, selected spectra from figure 7.20 have been replotted in premultiplied form as shown in figure 7.23. The spectra selected for the replotting cover a wide range of conditions and correspond to $y/\delta = 0.1$ and 0.85 for both $R_\theta \approx 713$ and $R_\theta \approx 2810$. The premultiplied spectra have been plotted such that the area under all spectra is the same. Since the energy contribution over any wavenumber range is represented as an area under a spectrum, then such a presentation gives an indication of the relative distribution of energy over the range of k_1y in the different cases. The region in the vicinity of the peak accounts for most of the area under each spectrum and hence for most of the energy. The peak of each spectrum corresponds to the portion of the raw spectrum having a slope of -1.

From figure 7.23 it is apparent that, for $R_\theta \approx 713$, the question of whether or not the flow is affected by the device used depends upon the value of y/δ. For $R_\theta \approx 713$, the device used has little effect at $y/\delta = 0.1$, but at $y/\delta = 0.85$, the energy-containing range for the pins has shifted towards higher values of

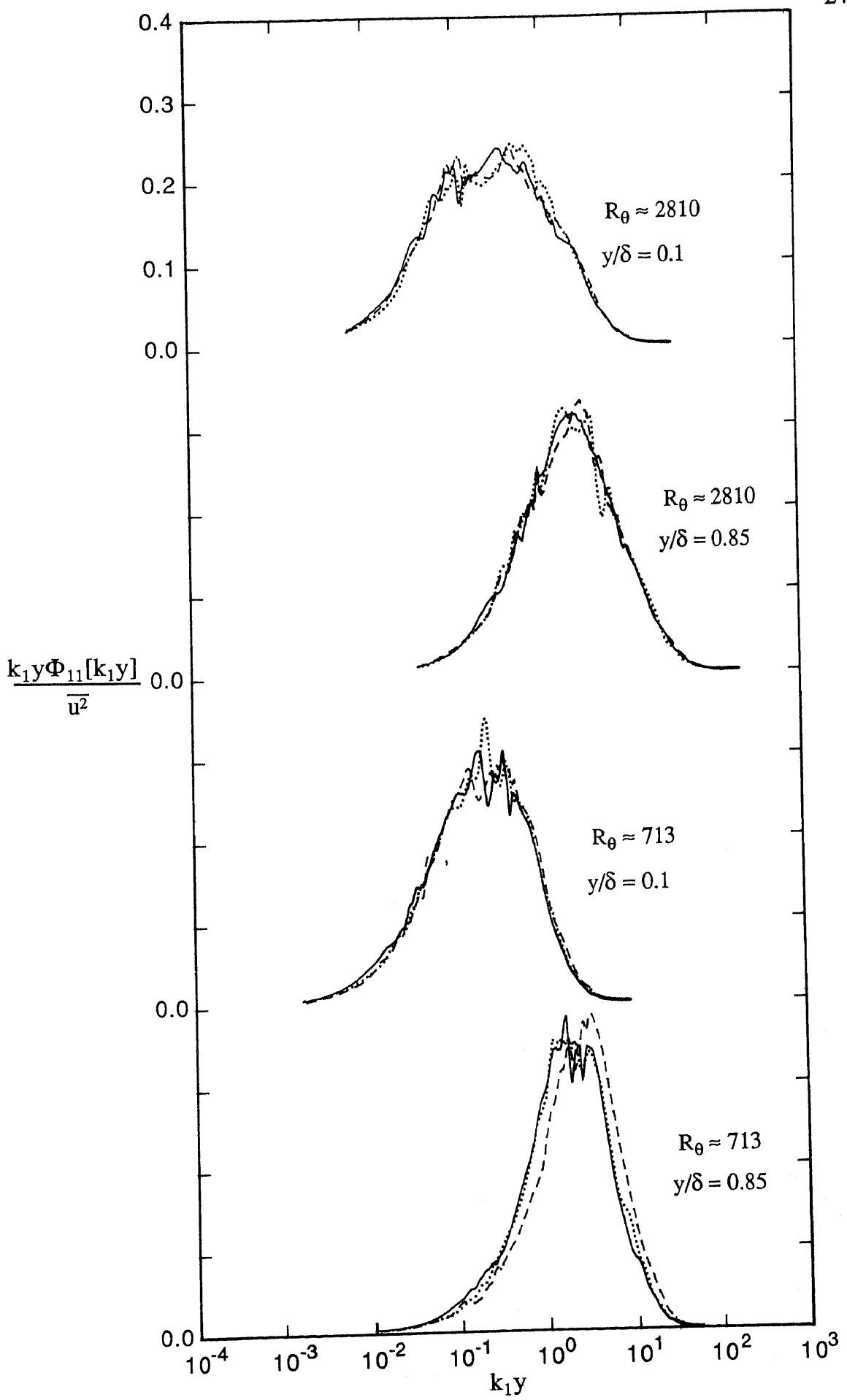

FIGURE 7.23. Pre-multiplied u spectra for design flows for $y/\delta = 0.10$ and 0.85 plotted using inner-flow scaling showing effects of device for nominal values of R_θ of 713 and 2810. Note shift in ordinate.

——— wire; ·····, grit; — — —, 2.0 mm pins.

k_1y, and is thus associated with smaller-scale fluctuations compared with the other two devices. For $R_\theta \approx 2810$, the type of device used can be seen to have little effect on spectral behaviour at both $y/\delta = 0.1$ and $y/\delta = 0.85$, which is in accord with the spectra shown in figure 7.20. For both values of R_θ it can be seen that the energy-containing ranges change significantly with increasing distance from the wall, becoming more peaked and moving to higher values of k_1y

7.3 Spectra for Under and Overstimulated Flows

Since both the mean-flow and the broadband-turbulence characteristics for different devices had been shown to depend upon the degree of stimulation, it was desirable to investigate the effects, if any, that under and overstimulation had on spectral behaviour. Twelve families of u spectra were taken and details of these are given in groups 2 and 4 of table 5.1. These twelve families of spectra were all taken with the single-wire probe and consisted of six families for understimulated flows (8.0 m/s nominal) and six families for overstimulated flows (14.0 m/s nominal). The spectra corresponding to different amounts of stimulation will be analysed for any location across the boundary layer and will only be presented for inner-flow scaling.

The effects on the u spectra of under and overstimulation for different devices were determined by comparing spectra, at both $R_\theta \approx 1020$ and $R_\theta \approx 2175$, for each of the devices for flows having different amounts of stimulation. The u spectra are shown plotted in figures 7.24 and 7.25 for $R_\theta \approx 1020$ and $R_\theta \approx 2175$ respectively.

An analysis of the spectra for $R_\theta \approx 1020$, shown in figure 7.24, indicates that for the three devices, the actual degree of stimulation has a marked effect on the spectra. Differences are quite small at the lower values of y/δ, but tend to increase with increasing y/δ, although for the wire and the pins the differences decrease again at the highest value of y/δ. The effect of the amount of stimulation is most evident at the low wavenumber ends of the spectra.

Considering now the spectra for $R_\theta \approx 2175$, shown in figure 7.25, it can be seen that the effects of the amount of stimulation are now quite small. For low wavenumbers, the spectra corresponding to the different amounts of stimulation

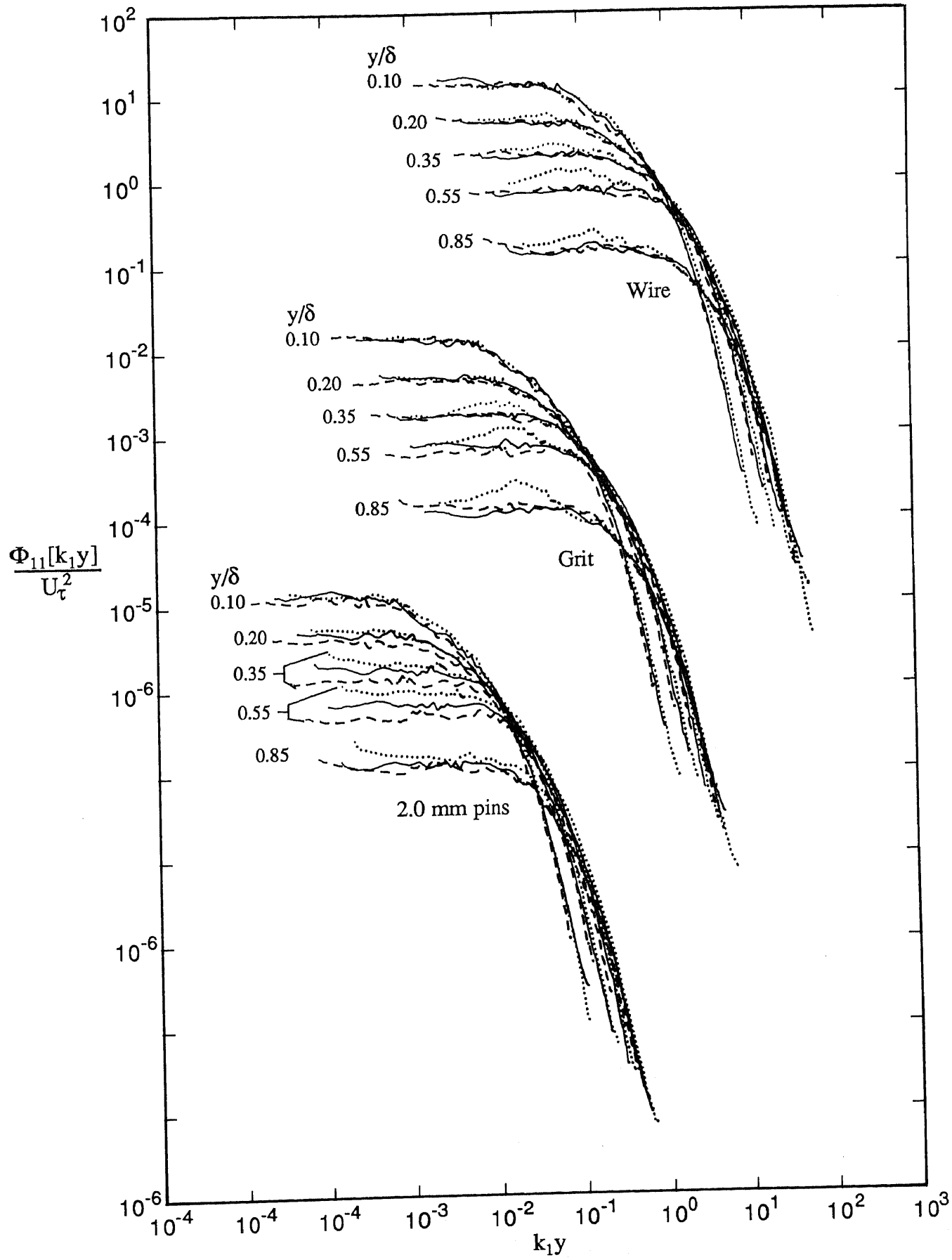

FIGURE 7.24. u spectra for three devices showing effects of different amounts of stimulation at various values of y/δ plotted using inner-flow scaling. Note shift in abscissa and ordinate. Velocities given below are nominal values.

Wire: ·····, 8.0 m/s, R_θ=1017; ——, 10.0 m/s, R_θ=1003; – – –, 14.0 m/s, R_θ=1033

Grit: ·····, 8.0 m/s, R_θ=0997; ——, 10.0 m/s, R_θ=1042; – – –, 14.0 m/s, R_θ=1029

2.0 mm pins: ·····, 8.0 m/s, R_θ=1024; ——, 10.0 m/s, R_θ=1027; – – –, 14.0 m/s, R_θ=1013

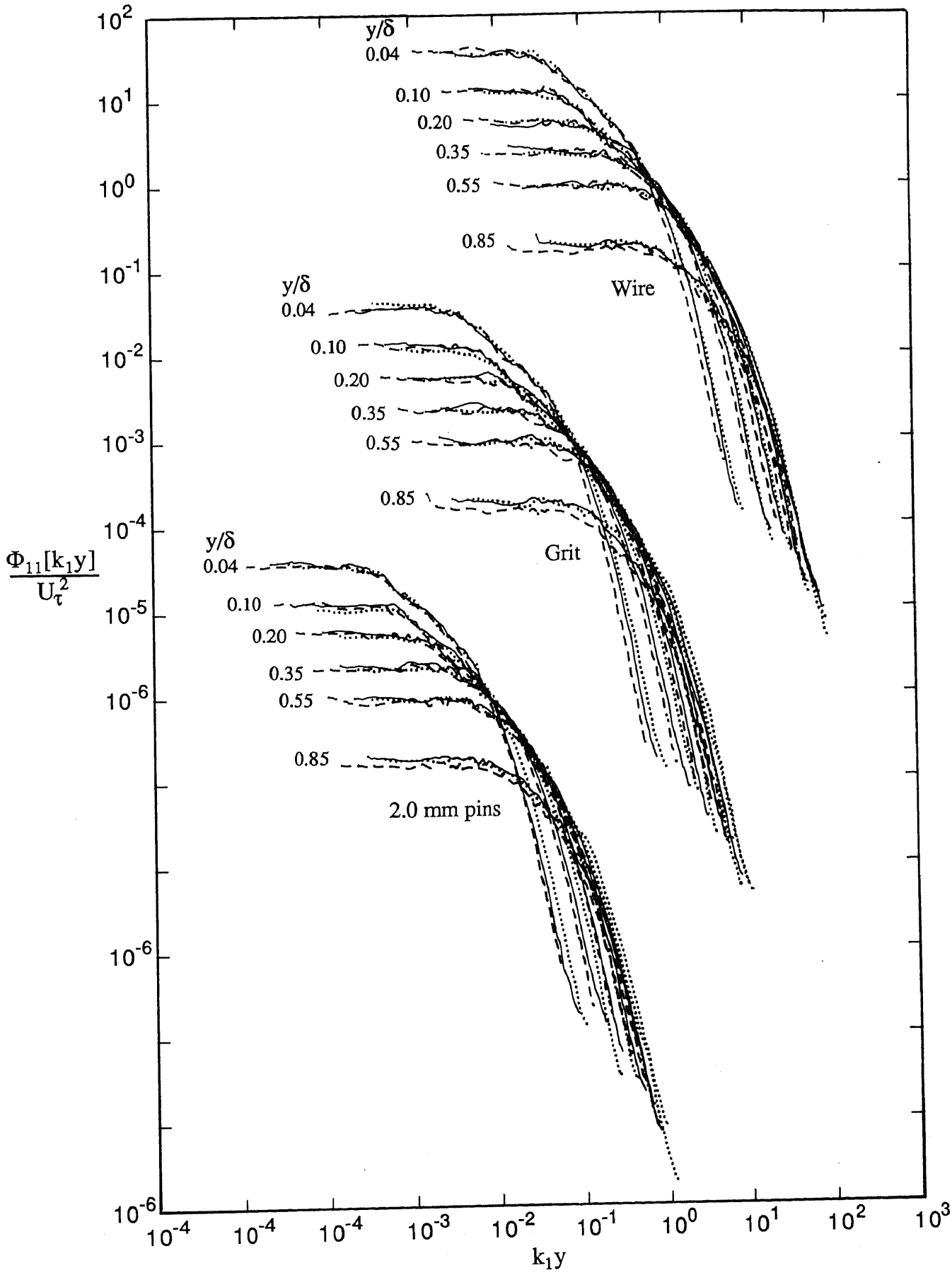

FIGURE 7.25. u spectra for three devices showing effects of different amounts of stimulation at various values of y/δ plotted using inner-flow scaling. Note shift in abscissa and ordinate. Velocities given below are nominal values.

Wire: ·····, 8.0 m/s, R_θ=2151; ——, 10.0 m/s, R_θ=2226; – – –, 14.0 m/s, R_θ=2137

Grit: ·····, 8.0 m/s, R_θ=2146; ——, 10.0 m/s, R_θ=2178; – – –, 14.0 m/s, R_θ=2119

2.0 mm pins: ·····, 8.0 m/s, R_θ=2230; ——, 10.0 m/s, R_θ=2181; – – –, 14.0 m/s, R_θ=2169

now agree quite closely for all values of y/δ, and although some differences showing uniform trends often now occur at the high wavenumber ends of the spectra, the differences are only small.

CHAPTER 8

GENERAL SUMMARY AND CONCLUSIONS

The foregoing investigation was undertaken to improve our understanding of low-Reynolds-number turbulent boundary layers flowing over a smooth flat surface in nominally zero pressure gradients. In practice, such flows generally occur in close proximity to a tripping device and although the actual low value of the Reynolds number was known to have an effect on flow behaviour, it was realised that such flows may also be affected by the type of tripping device used and variations in freestream velocity for a given device. Consequently the experimental programme was devised to investigate systematically the effects of each of these three factors independently.

Three different types of tripping device were chosen and the actual heights of these devices were initially unspecified. The types of devices chosen were a wire, distributed silicon carbide grit of streamwise extent 50 mm and cylindrical pins of diameter 3.0 mm and spacing 9.0 mm. To make meaningful comparisons between the different flows associated with each of the three devices, it was necessary to determine their heights so that they all produced correctly-stimulated flows, i.e. the flows followed Coles (1962) $\Delta U/U_\tau$-versus-R_θ characteristic, at some given nominal design reference velocity, which for these experiments was chosen to be 10.0 m/s. An empirical technique was devised for matching device height and velocity so as to obtain correctly-stimulated flows. Using this technique the heights of the devices were found to be 1.2 mm for the wire, about 1.6 mm for the grit and 2.0 mm for the pins.

For the three devices, low-Reynolds-number measurements were taken at the nominal design reference velocity of 10.0 m/s as well as at nominal reference velocities 8.0 and 14.0 m/s. These latter two velocities were associated with under and overstimulated flow respectively. Thus, the use of three devices at each of three nominal reference velocities meant that nine different flows were studied.

In order that the nine flows could be systematically compared with each other, mean-flow profiles, broadband-turbulence profiles and spectra were taken in each flow for the value of R_θ at which the comparison was to be made. For the three design flows, measurements were taken for nominal values of R_θ of 713, 1020, 1544, 2175 and 2810, whereas for the under and overstimulated flows, measurements were taken for nominal values of R_θ of 1020 and 2175. For all nine flows, additional measurements were also taken for other values of R_θ.

For the design flows, mean-flow profiles, broadband-turbulence profiles and spectra were plotted in two different ways to illustrate two different effects, viz. to indicate the effects on the data of variations in R_θ for different devices and to indicate the effects on the data of variations of device for different nominal values of R_θ. From these latter measurements, it was possible to determine the limiting value of R_θ at which a particular flow characteristic ceased to be affected by the type of device used. The effects that under and overstimulation had on the data for different devices were investigated by simply comparing data at nominal values of R_θ of 1020 and 2175 for each of the devices for flows having different amounts of stimulation. These measurements indicated the way in which the flow at a given nominal value of R_θ was affected by the way in which R_θ was formed.

Mean-flow behaviour, broadband-turbulence behaviour and spectral behaviour have each been dealt with individually in a separate chapter and the important conclusions pertaining to each of these aspects of the flow will now be summarized.

8.1 Mean-Flow Behaviour

The locations of the transition regions from laminar to turbulent flow for the different devices, as expressed in terms of C_f-versus-x relationships, were found to vary with reference velocity. Considering the three devices, the stability of the transition region for the grit was found to be the most affected by changes in the reference velocity and that for the 2.0 mm pins the least affected.

At the nominal design reference velocity of 10.0 m/s, the three $\Delta U/U_\tau$-versus-R_θ characteristics associated with the three tripping devices agreed quite closely with the characteristic proposed by Coles (1962). However, for each of the devices it was found that changes in the reference velocity often had a significant effect upon the shapes of the $\Delta U/U_\tau$-versus-R_θ characteristics. The three characteristics associated with nominal reference velocities of 8.0, 10.0 and 14.0 m/s often differed noticeably at the lower values of R_θ. The characteristic for the 2.0 mm pins was the most sensitive to changes in reference velocity and that for the 1.2 mm wire the least sensitive. This flow behaviour for these two devices was in contrast to that which occurred when the flows were compared on the basis of their C_f-versus-x characteristics, as described above. The nine $\Delta U/U_\tau$-versus-R_θ characteristics associated with the three devices and three velocities showed a general tendency to merge together as R_θ increased so that the differences between the nine characteristics were minimal by the time R_θ had attained a value of about 2500 to 3000. The values of $\Delta U/U_\tau$ associated with the nine flows decreased with reducing R_θ as expected, but they did not actually reach zero at the lower values of R_θ and in almost all cases the values of $\Delta U/U_\tau$ at the lower values of R_θ increased with decreasing R_θ. This phenomenon has also been noticed by Purtell, Klebanoff & Buckley (1981) and they attributed the behaviour to underdevelopment of the flow.

Profiles of U/U_τ versus $\log(yU_\tau/\nu)$ for the design flows were shown to vary monotonically with R_θ for each of the three devices, but as expected the variations were confined to the outer layer. Also, it was found that for the five different nominal values of R_θ, the type of device used had only a very minor effect on the profiles, except perhaps at the very lowest nominal value of R_θ, i.e. $R_\theta \approx 713$. In a similar manner, profiles of $(U-U_e)/U_\tau$ versus y/δ were shown to vary monotonically with R_θ for each of the devices, but in this case the variations occurred over almost the entire y/δ range. Once again it was found that for the five different nominal values of R_θ, the profiles were not affected significantly by the type of device used, except perhaps at $R_\theta \approx 713$.

From the design-flow profiles of U/U_τ versus $\log(yU_\tau/\nu)$ it was found that the lowest value of R_θ at which a logarithmic region was found to exist for a profile whose $\Delta U/U_\tau$-versus-R_θ characteristic followed the trend of Coles' (1962) relationship, was $R_\theta = 581$, and this profile was for the wire. This is

higher than Preston's value of 389, and higher than Landweber's value, which although unspecified by him, is less than that of Preston.

For each of the three devices, profiles of U/U_τ versus $\log(yU_\tau/\nu)$ for flows having different amounts of stimulation were more affected by the degree of stimulation for $R_\theta \approx 1020$ than were the profiles for $R_\theta \approx 2175$, which were affected very little. Any observed differences in the profiles being compared were confined to the outer flows. The behaviour of the profiles of $(U-U_e)/U_\tau$ versus y/δ can be described in a similar manner, except that in this case any observed differences occurred over almost the entire y/δ range.

Velocity profile integral parameters, H and G, for the design flows were found to be in better agreement with the parameters given by Coles (1962) than were those for the understimulated or overstimulated flows.

Transverse measurements of skin-friction coefficients for the above three devices for the design flows showed that the spanwise values of C_f/C_{fm} fluctuated the most rapidly at low values of R_θ, but the fluctuations diminished as R_θ increased. Also, the overall range of variation in the values of C_f/C_{fm} was greatest at low values of R_θ but reduced with increasing R_θ, except perhaps for the wire, where the range of variation of C_f/C_{fm} remained about the same as R_θ changed. At low values of R_θ, the transverse variation of C_f/C_{fm} for the pins showed a strong correlation with pin position but there did not seem to be any pattern in the behaviour of corresponding measurements for the wire and the grit. At high values of R_θ, the lateral distributions of C_f/C_{fm} for the three devices agreed quite closely and the type of device now had little influence on these measurements. Evidence suggested that the non-uniform transverse flow distributions remained stable when considered on a time-averaged basis.

8.2 Broadband-Turbulence Behaviour

Comprehensive broadband-turbulence measurements were taken for the u, v and w components of the turbulence for the design flows and for the u component of the turbulence for the understimulated and overstimulated flows. The measurements included Reynolds normal and shear stresses as well as triple and quadruple products. These basic quantities were used to determine anisotropy parameters, skewness and flatness factors, balances of energy and

shear stress, eddy viscosities and mixing lengths, dissipation length parameters and turbulent transport velocities.

The $\overline{u^2}$, $\overline{v^2}$, $\overline{w^2}$ and $\overline{uv}$ Reynolds stresses for the design flows were plotted using both U_e and U_τ as scaling factors. For both types of scaling, the Reynolds stresses for each of the devices were found to be dependent on R_θ, but the extent of the dependency varied with the location across the boundary layer. When scaled using U_e, there was a general tendency for the Reynolds stresses at a given value of y/δ or yU_τ/ν to decrease with increasing R_θ. When scaled with U_τ, the Reynolds stresses often did not vary monotonically with R_θ.

When the Reynolds stress profiles for the design flows were plotted to determine the effects of device, it was found that the profiles for the three devices often differed significantly at $R_\theta \approx 713$, but for $R_\theta \approx 1020$ and above, the type of device used had only a small effect on the profiles. For $R_\theta \approx 713$, the overall variation of the profiles for the three devices was far greater in percentage terms than that for the corresponding mean-flow profiles.

The $\overline{u^3}$, $\overline{v^3}$, $\overline{u^2v}$ and $\overline{uv^2}$ triple products for the design flows were each scaled and plotted as for the Reynolds stresses. Once again, using both U_e and U_τ as scaling factors, the profiles for the three devices depended on R_θ and the extent of the dependency varied across the boundary layer. There was also a general tendency for the triple products to decrease with increasing R_θ for given values of y/δ when they were scaled using U_e. The profiles did not exhibit monotonic trends with R_θ when scaled using U_τ. With both types of scaling, the triple product profiles exhibited two distinct peaks and the $\overline{u^3}$ triple products changed sign near the wall. The other triple products were not measured close enough to the wall to check whether or not they changed sign.

For each of the four triple products, the profiles for the three devices for the design flows showed large variations at $R_\theta \approx 713$, but for $R_\theta \approx 1020$ and above, the type of device used did not have a significant effect on the profiles if allowances were made for inevitable scatter in triple-product profiles.

It is apparent from the above that even though mean-flow characteristics for different devices for $R_\theta \approx 713$ may agree reasonably closely, it does not necessarily follow that Reynolds stresses and triple products for different devices will agree at this value of R_θ. Thus, the mere fact that a researcher may

choose a device and establish a flow that closely follows Coles' (1962) $\Delta U/U_\tau$-versus-R_θ mean-flow characteristic, does not imply that corresponding broadband-turbulence characteristics will be universal for $R_\theta \approx 713$.

Although some triple products for low-Reynolds-number flows have been reported in the literature, there are no comprehensive measurements of such triple products close to the wall. Murlis, Tsai & Bradshaw (1982) did not present triple products for values of y/δ less than about 0.4 for $R_\theta = 791$ or for values of y/δ less than about 0.2 for $R_\theta = 4750$. Since the triple products often showed large variations with R_θ close to the wall, then the current measurements for low values of R_θ are especially significant in this respect.

A number of different anisotropy or structural parameters were determined for the design flows. The parameters considered were $\overline{u^2}/\overline{v^2}$, $R_{12} \equiv -\overline{uv}/(\sqrt{\overline{u^2}}\sqrt{\overline{v^2}})$ and $a_1 \equiv -\overline{uv}/\overline{q^2}$.

Profiles of $\overline{u^2}/\overline{v^2}$ versus y/δ for the three devices were shown to be moderately dependent on R_θ in the outer flow. However, the variation was not monotonic and there was a tendency for the profiles to rise with increasing R_θ up to a maximum at both $R_\theta \approx 1544$ and $R_\theta \approx 2175$ and then to fall again for higher values of R_θ. Following Murlis, Tsai & Bradshaw (1982), it can be inferred that the efficiency of turbulent mixing is at a minimum within the region $R_\theta \approx 1544$ to $R_\theta \approx 2175$. At $y/\delta = 0.6$, the value of $\overline{u^2}/\overline{v^2}$ for the three devices was about 2.3 for $R_\theta \approx 713$, about 2.5 for $R_\theta \approx 1544$ and $R_\theta \approx 2175$ and about 2.4 for $R_\theta \approx 2810$.

Profiles of R_{12} versus y/δ also showed a moderate dependence on R_θ and, except for the data for the pins for $R_\theta = 729$, the trends of the profiles with R_θ were approximately the same as for the $\overline{u^2}/\overline{v^2}$ data. The above discussion on the efficiency of turbulent mixing is also relevant to the R_{12} data. At $y/\delta = 0.6$, the value of R_{12} for $R_\theta \approx 713$ was about 0.45 for the wire and grit and about 0.5 for the pins, for $R_\theta \approx 1544$ and $R_\theta \approx 2175$, R_{12} was about 0.48 for all devices and for $R_\theta \approx 2810$, R_{12} was about 0.45 for all devices.

The profiles of a_1 versus y/δ behaved in a similar manner to the R_{12} profiles in corresponding cases. At $y/\delta = 0.6$, the value of a_1 for $R_\theta \approx 713$ was about 0.15 for the wire and the grit and about 0.17 for the pins, for $R_\theta \approx 1544$

and $R_\theta \approx 2175$, a_1 was about 0.16 for all devices and for $R_\theta \approx 2810$, a_1 was about 0.15 for all devices.

Considering skewness factors, it was found that for each of the three devices for the design flows, the values of S_u and S_v varied moderately with R_θ in most cases and overall the general behaviour of the data was approximately as expected. Close to the wall the values of S_u and S_v were reasonably small, but near the outer edges of the boundary layers, the values of S_u fell to a lower limit of about -2.5 and the values of S_v rose to an upper limit of about 1.5. Corresponding values of S_w in the vicinity of the outer edges of the boundary layers showed large variations with R_θ and these variations indicated that the flows were not completely two-dimensional.

Considering flatness factors, plots of F_u, F_v and F_w, versus y/δ for each of the devices for the design flows showed good collapse for different values of R_θ for y/δ less than about 0.6, but beyond this range the profiles generally showed a moderate dependency on R_θ. The flatness factors were close to the Gaussian value of 3.0 between $y/\delta \approx 0.1$ and $y/\delta \approx 0.6$, but beyond $y/\delta \approx 0.6$, the flatness factors rose to peak values in the vicinity of the edges of the boundary layers before falling again. The flatness factors for the pins for $R_\theta = 729$ suggested that the flow was three dimensional at this value of R_θ.

Balances of turbulent kinetic energy and Reynolds shear stress were constructed for each of the three devices for the design flows for nominal values of R_θ of 1020, 1544 and 2175. The various terms in the balances were normalized by both U_e^3/δ and U_τ^3/δ. The behaviour of data for the different devices agreed quite closely.

The energy balances maintained the same general form over the above R_θ range. In each case, production and dissipation were the dominant terms over most of the layer. Considering data for the wire, normalized by U_e^3/δ, it was found that near the wall the production and dissipation decreased with increasing R_θ and near the edge of the boundary layer the advection increased and the diffusion decreased with increasing R_θ. When corresponding data were normalized using U_τ^3/δ, the different terms were successively increased with increasing R_θ, so that some of the above trends with R_θ were changed.

For the balances of Reynolds shear stress, it was found that the general behaviour of various terms was the same as that for corresponding terms in the energy balances. The generation and redistribution terms were more pronounced than the corresponding production and dissipation terms respectively and the mean-flow and turbulent transport terms were noticeably smaller than the corresponding advection and diffusion terms respectively.

Considering eddy viscosities, profiles of $\varepsilon_m/(U_e\delta^*)$ versus y/δ for each of the devices for the design flows varied considerably with R_θ over most of the boundary layer. In the outer layer there was a general tendency for the values of $\varepsilon_m/(U_e\delta^*)$ to decrease with increasing R_θ. Profiles rose to peaks at about $y/\delta = 0.3$ or 0.4 and the values of $\varepsilon_m/(U_e\delta^*)$ at the peaks for all devices were about 0.023 for $R_\theta \approx 713$ and about 0.017 for $R_\theta \approx 2810$.

Profiles of mixing length, expressed as ι/δ versus y/δ, for each of the devices for the design flows showed a significant variation with R_θ in the outer layer. In this region there was a general trend for the values of ι/δ to decrease with increasing R_θ. The values of ι/δ over most of the outer layer for $R_\theta \approx 713$ were about 0.10 for the wire and the grit and somewhat lower for the pins, and for $R_\theta \approx 2810$ the values of ι/δ were about 0.08 for all devices.

Profiles of dissipation length parameter, expressed as L/δ versus y/δ, for the three devices for the design flows for nominal values of R_θ of 1020, 1544 and 2175 showed dependency on R_θ to variable extents. The profiles for the pins showed no significant variation with R_θ over the boundary layer, whereas the profiles for the wire and the grit collapsed reasonably well in the inner half of the boundary layers, but beyond this range the profiles showed some dependence on R_θ, with values of L/δ increasing with increasing R_θ. When the data were compared with those of Murlis, Tsai & Bradshaw (1982), some differences occurred in the trends with R_θ.

Considering turbulent transport velocities, profiles of V_q/U_e and V_τ/U_e versus y/δ, for each of the devices for the design flows showed large variations with R_θ throughout the entire y/δ range. The transport velocities at given values of y/δ showed a general tendency to decrease with increasing R_θ, although exceptions did occur. At $y/\delta = 0.5$ and 1.0, the values of V_q/U_e were about

0.011 and 0.020 respectively for all devices for $R_\theta \approx 2810$. Corresponding values of V_τ/U_e were about 0.024 and 0.056 respectively.

Profiles of $\overline{u^2}/U_e^2$ versus y/δ, $\sqrt{\overline{u^2}}/U_\tau$ versus $\log(yU_\tau/\nu)$ and $-\overline{u^3}/U_e^3$ versus y/δ showed that for $R_\theta \approx 1020$, the degree of stimulation generally had a significant effect upon the profiles for each of the devices. Although the effects of the different amounts of stimulation were generally less pronounced for $R_\theta \approx 2175$, appreciable differences often still existed in the profiles being compared. More measurements need to be taken to establish the value of R_θ at which the degree of stimulation no longer has a noticeable effect on the broadband-turbulence characteristics. It was found that the flows tended to settle down quicker in terms of mean-flow characteristics, rather than broadband-turbulence characteristics, after being subjected to different degrees of stimulation.

8.3 Spectral Behaviour

An extensive range of u, v and w spectra were measured and these were plotted using different types of scaling as given by Perry, Henbest & Chong (1986). The plots were for the turbulent wall region and the fully turbulent region, as proposed by the above researchers, and also for any location across the boundary layers.

Perry, Henbest & Chong proposed models of spectral behaviour, and although these models corresponded to high-Reynolds-number flows, the low-Reynolds-number spectra of the current investigation were compared with these models to see if agreement existed. For the current spectra, it was necessary to modify slightly the turbulent wall region to enable a meaningful comparison to be made.

For the turbulent wall region, it is encouraging that the low-Reynolds-number spectra for the design flows, corresponding to nominal values of R_θ as low as 1020, generally showed good agreement with the model. Where agreement did not occur, at least the spectra showed similar behaviour to those of Perry, Lim & Henbest (1987) in their flat-plate boundary-layer study.

Considering the fully turbulent region, it was found that although the current spectra for the design flows tended to obey predictions, some

appreciable deviations were sometimes apparent, due to low-Reynolds-number effects.

When spectra were plotted to assess whether or not they were dependent on device at given values of R_θ, it was found that the type of device could have an appreciable effect for $R_\theta \approx 713$, but for $R_\theta \approx 1020$ and above, the type of device used had little effect on spectral behaviour. For $R_\theta \approx 713$, the spectra for the wire and the grit agreed reasonably closely, but the spectra for the pins differed from these. Differences between the pins and the other two devices occurred throughout the layer, but the differences were larger at the higher values of y/δ. At all locations, the differences occurred mainly for low to moderate wavenumbers.

Spectra were plotted to determine the effects of under and overstimulation and it was found that for each of the devices and for $R_\theta \approx 1020$, the amount of stimulation often had a marked effect on the spectra. The effect varied throughout the layers but at each of the values of y/δ, the effect of the amount of stimulation was most evident at the lower wavenumbers. The spectra corresponding to $R_\theta \approx 2175$ were affected very little by the amount of stimulation.

REFERENCES

ANDREOPOULOS, J., DURST, F., ZARIC, Z. & JOVANOVIC, J. 1984 Influence on Reynolds number on characteristics of turbulent wall boundary layers. Experiments in Fluids. **2**, 7.

BARLOW, R. S. & JOHNSTON, J. P. 1985 Structure of turbulent boundary layers on a concave surface. Report MD-47 Thermosciences Div., Dept. Mech. Eng., Stanford University, California.

BARLOW, R. S. & JOHNSTON, J. P. 1988 Structure of a turbulent boundary layer on a concave surface. J. Fluid Mech. **191**, 137.

BARR, P. K. 1980 Calculation of skin-friction coefficients for low-Reynolds-number turbulent boundary layer flow. M. S. thesis, U. of California, Davis.

BRADSHAW, P. 1965 The effect of wind tunnel screens on nominally two-dimensional boundary layers. J. Fluid Mech. **22**, 679.

BRADSHAW, P., FERRISS, D. H. & ATWELL, N. P. 1967 Calculation of boundary-layer development using the turbulent energy equation. J. Fluid Mech. **28**, 593.

BRADSHAW, P. 1967 The turbulence structure of equilibrium boundary layers. J. Fluid Mech. **29**, 625.

BRADSHAW, P. 1972 The understanding and prediction of turbulent flow. Aero. J. July 1972, 403.

BRADSHAW, P. & PONTIKOS, N. S. 1985 Measurements in the turbulent boundary layer on an "infinite" swept wing. J. Fluid Mech. **159**, 105.

BREDERODE, V. de & BRADSHAW, P. 1974 A note on the empirical constants appearing in the logarithmic law for turbulent wall flows. Imperial Coll. Aero. Rep. 74-03. Imperial Coll., Dept. Aeronaut., London.

BULL, M. K. 1969 Velocity profiles of turbulent boundary layers. Aero. J. Royal Aero. Soc. **73**, 143.

BUSHNELL, D. M., CARY, A. M. & HOLLEY, B. B. 1975 Mixing length in low Reynolds number compressible turbulent boundary layers. AIAA Journal **13**, 1119.

CEBECI, T., & SMITH, A. M. O. 1974 Analysis of turbulent boundary layers. Academic Press, New York.

CEBECI, T. & BRADSHAW, P. 1977 Momentum transfer in boundary layers. Hemisphere Publishing Corp., Washington.

CLAUSER, F. H. 1954 Turbulent boundary layers in adverse pressure gradients. J. Aero. Science **21**, 91.

CLAUSER, F. H. 1956 The turbulent boundary layer. Ed. DRYDEN, H. L. & von KARMAN, T. Advances in applied mechanics. IV, 1. Academic Press Inc., New York.

COLES, D. E. 1956 The law of the wake in the turbulent boundary layer. J. Fluid Mech. **1**, 191.

COLES, D. E. 1962 The turbulent boundary layer in a compressible fluid. Rand Rep. R-403-PR, Appendix A: A Manual of experimental boundary layer practice for low-speed flow.

COLES, D. E. 1968 "The young persons guide to the data", in Proceedings Computation of Turbulent Boundary Layers, AFOSR-IFP-Stanford Conference, Vol. 2, ed. by Coles & Hirst.

ERM, L. P., SMITS, A. J. & JOUBERT, P. N. 1987 Low Reynolds number turbulent boundary layers on a smooth flat surface in a zero pressure gradient. Turbulent Shear Flows 5 Ed. Durst, F., Launder, B. E., Lumley, J. L., Schmidt, F. W. & Whitelaw, J. H., Springer-Verlag, Berlin, see also Proceedings of the Fifth Symposium on Turbulent Shear Flows, Ithaca, New York, August 7-9, 1985.

GIBBINGS, J. C. 1959 On boundary layer transition wires. Aero. Res. Counc. C. P. No. 462.

GRANVILLE, P. S. 1977 Drag and turbulent boundary layer of flat plates at low Reynolds numbers. J. Ship Res. **21**, 30, see also David W. Taylor, Naval Ship Research and Development Centre, Rep. 4682, Maryland, 1975.

GUPTA, A. K. & KAPLAN, R. E. 1972 Statistical characteristics of Reynolds stress in a turbulent boundary layer. Phys. Fluids **15**, 981.

HINZE, J. O. 1959 Turbulence. Mc Graw-Hill Book Co., Inc.

HUFFMAN, G. D. & BRADSHAW, P. 1972 A note on von Karman's constant in low Reynolds number turbulent flows. J. Fluid Mech. **53**, 45.

INMAN, P. N. & BRADSHAW, P. 1981 Mixing length in low Reynolds number turbulent boundary layers. AIAA Journal **19**, 653.

KARMAN, T. von 1930 Nachr. Ges. Wiss. Goett. Math.-Phys. Kl., 58.

KLEBANOFF, P. S. 1954 Characteristics of turbulence in a boundary layer with zero pressure gradient. NACA Tech. note no. 3178

KLEBANOFF, P. S. 1955 Characteristics of turbulence in a boundary layer with zero pressure gradient. NACA Rep. no. 1247.

LANDWEBER, L. 1953 The frictional resistance of flat plates in zero pressure gradient. The Society of Naval Architects and Marine Engineers, Transactions, **61**, 5.

LAWN, C. J. 1970 Diffusion of turbulence energy in flow through axisymmetric ducts. Imperial College Dept. Mech. Eng. Rep.

LAWN, C. J. 1971 The determination of the rate of dissipation in turbulent pipe flow. J. Fluid Mech. **48**, 477.

MACMILLAN, F. A. 1956 Experiments on Pitot-tubes in shear flows. Aero. Res. Counc. R. & M. 3028.

MURLIS, J. 1975 The structure of a turbulent boundary layer at low Reynolds number. Ph.D. thesis, Imperial College, London.

MURLIS, J., TSAI, H. M. & BRADSHAW, P. 1982 The structure of turbulent boundary layers at low Reynolds numbers. J. Fluid Mech. **122**, 13.

PATEL, V. C. 1965 Calibration of the Preston tube and limitations on its use in pressure gradients. J. Fluid Mech. **23**, 185.

PERRY, A. E. & MORRISON, G. L. 1971 Static and dynamic calibrations of constant-temperature hot wire systems. J. Fluid Mech. **47**, 756.

PERRY, A. E. & ABELL, C. J. 1977 Asymptotic similarity of turbulence structures in smooth- and rough-walled pipes. J. Fluid Mech. **79**, 785.

PERRY, A. E. & WATMUFF, J. H. 1981 The phase-averaged large-scale structures in three-dimensional turbulent wakes. J. Fluid Mech. **103**, 33.

PERRY, A. E. 1982 Hot-Wire Anemometry. Oxford University Press, New York.

PERRY, A. E. & CHONG, M. S. 1982 On the mechanism of wall turbulence. J. Fluid Mech. **119**, 173.

PERRY, A. E., LIM, K. L. & HENBEST, S. M. 1985 A spectral analysis of smooth flat-plate boundary layers. Fifth Symposium on Turbulent Shear Flows, Cornell University, Ithaca, New York.

PERRY, A. E., LIM, K. L. & HENBEST, S. M. 1987 An experimental study of the turbulence structure in smooth- and rough-wall boundary layers. J. Fluid Mech. **177**, 437.

PERRY, A.E., HENBEST, S. & CHONG, M. S. 1986 A theoretical and experimental study of wall turbulence. J. Fluid Mech. **165**, 163.

PRANDTL, L. 1933 Z. Ver. Dtsch. Ing. **77**, 105 (trans. as NACA Tech. Mem. 720).

PRESTON, J. H. 1954 The determination of turbulent skin friction by means of Pitot tubes. J. Royal Aero. Soc. **58**, 109.

PRESTON, J. H. 1958 The minimum Reynolds number for a turbulent boundary layer and the selection of a transition device. J. Fluid Mech. **3**, 373.

PURTELL, L. P. 1978 The turbulent boundary layer at low Reynolds number. Ph.D. thesis, University of Maryland.

PURTELL, L. P.,KLEBANOFF, P. S. & BUCKLEY, F. T. 1981 Turbulent boundary layer at low Reynolds number. Phys. Fluids **24**, 802.

ROTTA, J. C. 1962 Turbulent Boundary Layers in Incompressible Flow. In Progress in Aeronautical Sciences, vol. 2, ed. Ferri, A., Kuchemann, D. & Sterne, L. H. G., Pergamon Press, Oxford.

SIMPSON, R. L. 1967 Ph.D. Thesis, Stanford University, California.

SIMPSON, R. L. 1970 Characteristics of turbulent boundary layers at low Reynolds numbers with and without transpiration. J. Fluid Mech. **42**, 769.

SIMPSON, R. L., CHEW, Y. -T. & SHIVAPRASAD, B. G. 1981 The structure of a separating turbulent boundary layer. Part 2. Higher-order turbulence results. J. Fluid Mech. **113**, 53.

SMITS, A. J., MATHESON, N. & JOUBERT, P. N. 1983 Low Reynolds number turbulent boundary layers in zero and favourable pressure gradients. J. Ship Res. **27**, 147.

SPALART, P. R. & LEONARD, A. 1987 Direct numerical simulation of equilibrium turbulent boundary layers. Turbulent Shear Flows 5. Ed. Durst, F., Launder, B. E., Lumley, J. L., Schmidt, F. W. & Whitelaw, J. H., Springer-Verlag, Berlin,

SPALART, P. R. 1988 Direct stimulation of a turbulent boundary layer up to R_θ= 1410. J. Fluid Mech. **187**, 61.

TANI, I. 1969 Boundary-layer Transition. Annual Review Fluid Mechanics, ed. SEARS, W. & VAN DYKE, M. Vol. 1

TAYLOR, G. I. 1938 The spectrum of turbulence. Proc. R. Soc. Lond. A **164**, 476.

TOWNSEND, A. A. 1961 Equilibrium layers and wall turbulence. J. Fluid Mech. **11**, 97.

TOWNSEND, A. A. 1976 The structure of turbulent shear flow. Cambridge University Press, Cambridge.

UEDA, H. & HINZE, J. O. 1975 Fine-structure turbulence in the wall region of a turbulent boundary layer. J. Fluid Mech. **67**, 125.

WATMUFF, J. H., WITT, H. T. & JOUBERT, P. N. 1985 Developing turbulent boundary layers with system rotation. J. Fluid Mech. **157**, 405.

WHITE, B. R. 1981 Low Reynolds number turbulent boundary layers. J. Fluids Engineering **103**, 624.

WILLS, J. A. B. 1962 Correction of hot wire readings for proximity to a solid boundary. J. Fluid Mech. **12**, 388.

WITT, H. T., WATMUFF, J. H & JOUBERT, P. N. 1983 Some effects of rotation on turbulent boundary layers. Fourth Symposium on Turbulent Shear Flows, Sept. 12-14, 1983. Karlsruhe, F. R. Germany.

WITT, H. 1986 Effects of rotation on turbulent boundary layers and wakes. Ph. D. thesis, University of Melbourne.

-U. S. Standard Atmosphere, 1962. Prepared under sponsorship of National Aeronautics and Space Administration, United States Air Force and United States Weather Bureau, Washington, D. C.

APPENDIX 1

DISCUSSION OF FORMULAE FOR DETERMINING HEIGHTS OF TRIPPING DEVICES

In the literature there have been many studies to determine the heights of tripping devices necessary to cause transition to turbulence.

Gibbings (1959) analysed the literature and presented a useful summary of formulae for determining the wire diameter necessary to advance transition to the wire position in incompressible flow, and some aspects of this work will now be briefly outlined. A common criterion for determining a wire size is that the parameter, $U_k k/\nu$, must obtain a specified critical value, where k is the wire diameter and U_k is the velocity in the undisturbed boundary layer at the position of the wire and at a distance k from the surface. Different researchers have proposed different critical values of this parameter and these vary from 200 to 400. Another common criterion is that the parameter $U_e k/\nu$, must obtain a specified critical value, where U_e is the velocity just outside the boundary layer at the element position. For this parameter, the proposed critical values vary from 600 to 1500. Gibbings undertook his own analysis and proposed that the critical value of $U_e k/\nu$ was 826. Tani (1969) presented a comprehensive review article on boundary-layer transition. In this article he discusses the effects of different types of devices on transition, including sandpaper-type distributed roughness and isolated or three-dimensional roughness elements. He indicates that the critical value of $U_k k/\nu$ is about 600 for both sandpaper-type distributed roughness and also a roughness element of height-to-width ratio of one. In this parameter, k for the sandpaper roughness is the probable maximum height of a particle.

When deciding upon the size of tripping devices to use in the current investigation, the situation was confused by the fact that the devices were to be attached to one of the walls of the wind tunnel rather than to a flat plate fixed in the freestream. When devices are attached to the tunnel wall, the boundary

layer has a long development length along the inlet section and through the contraction and may have an appreciable thickness by the time it reaches the device. Criteria developed for isolated flat plates thus may not be applicable in the present situation. It is obvious that the $U_e k/\nu$ criterion has no meaning in the current investigation since this method takes no account of the boundary-layer thickness or amount of prior development at the device. When this method is used to calculate the size of device necessary to cause transition, then the answer is the same for all positions along the developing flow and of course this does not make sense. The fact that the $U_k k/\nu$ criterion, when applied to wires, predicts wire sizes varying by a factor of 2, and when applied to an isolated roughness element, is only applicable to elements having a height-to-width ratio of one, means that the criterion is only of limited use. The above considerations, coupled with the fact that not all of the above criteria were formulated using flat plates, means that the criteria can only be used as a guide when determining the heights of tripping devices

APPENDIX 2

CALCULATION OF DENSITY AND VISCOSITY

For specified values of temperature, T, and pressure, P, of the air, the values of density, ρ, and dynamic viscosity, μ, were determined by using the following formulae, which are given in U.S. Standard Atmosphere (1962).

$$\rho = \frac{MP}{R^*T} \tag{A2.1}$$

$$\mu = \frac{\beta T^{1.5}}{T+S} \tag{A2.2}$$

In these expressions, M is the molecular weight, R^* is the universal gas constant and S is Sutherland's constant. Numerical values of variables are M = 28.9644, $R^* = 8.31432 \times 10^3$ J/(K.kg Mol), $\beta = 1.458 \times 10^{-6}$ kg/(s.m.$K^{0.5}$) and S = 110.4 K.

APPENDIX 3

SPACING OF POINTS ON PROFILES AND SETTING OF PROBE ON WALL

As a starting point to the determination of the spacing of the y values of the points on the profiles it was first necessary to determine the approximate value of δ, the boundary-layer thickness where $U/U_e = 0.995$. To determine δ, the boundary-layer probe was moved well out into the freestream and the dynamic pressure noted. The probe was then moved towards the wall until the dynamic pressure at the new position was 99% of its value in the freestream. The associated value of y at which this occurred was found to correspond very closely to δ.

The probe was then set on the wall for its initial reading. This setting was achieved by pressing the probe lightly against the wall so that the probe tip was deformed very slightly and then traversing the probe by small increments at a time into the freestream until the dynamic pressure showed a sharp increase thus indicating that the probe tip had left the wall. The probe was then reset so that the tip was just on the point of leaving the wall.

Once this had been done all of the values of y to be used in the profile were calculated. The manner in which this was done will be explained by referring to figure A3.1, which is a typical profile plotted semi logarithmically using U/U_τ-versus-yU_τ/ν coordinates. From the beginning of the profile to the approximate end of the logarithmic region, i.e. part AB of the profile, the values of y were determined such that the plotted points had uniform linear spacing in the yU_τ/ν direction when plotted logarithmically. This linear spacing was the same on all velocity profiles, but the value of yU_τ/ν corresponding to point B varied from profile to profile. The location of point B on the different profiles was determined by either estimation or else by using prior knowledge. The y distance between point B and δ was then determined and subdivided into a

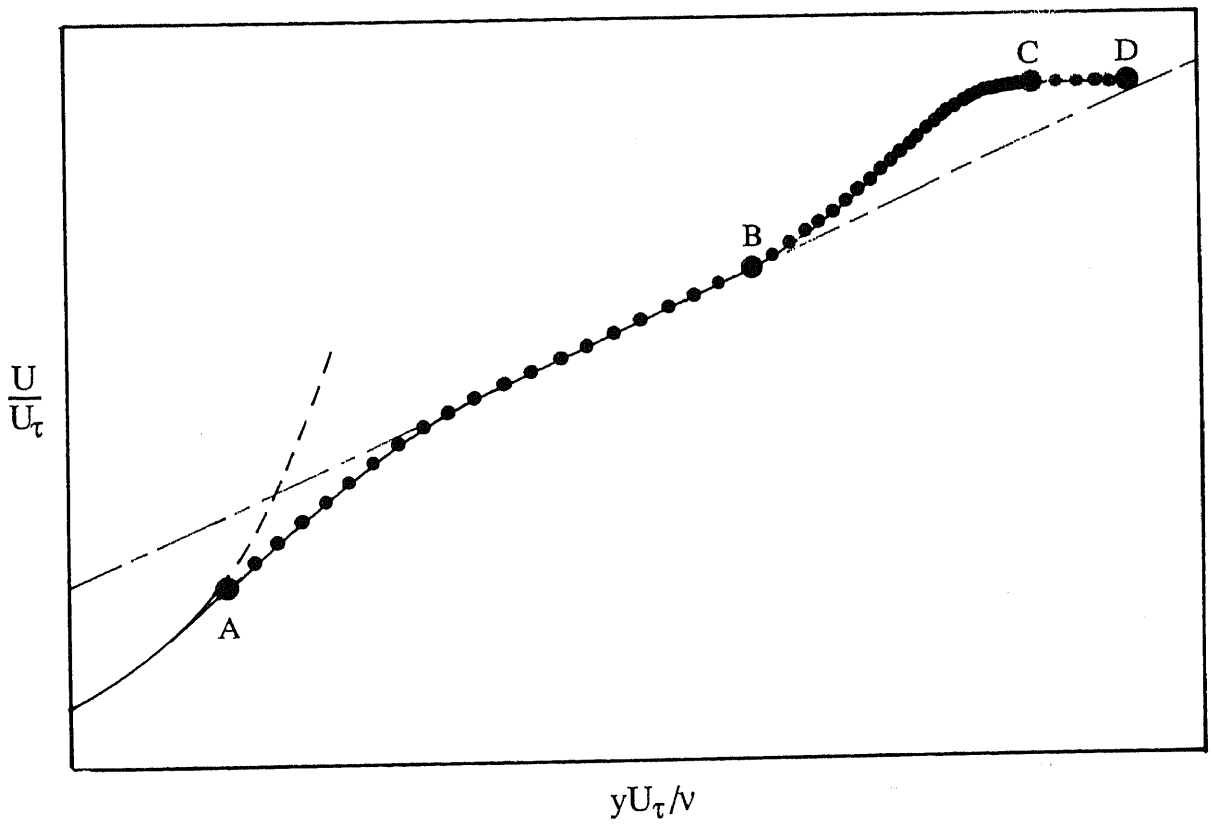

FIGURE A3.1. Typical velocity profile showing spacing of experimental points.

number of parts each of size Δy, such that Δy was equal to or less than the y distance between the last two experimental points in part AB. The y distances for the experimental points beyond point B increased uniformly by Δy up until point C, which was two experimental points beyond δ. Beyond point C, the y distances for the experimental points increased uniformly by $5\Delta y$ for 5 experimental points up until point D, which was well in the freestream.